



TECHNISCHE
UNIVERSITÄT
WIEN



AUSTRIAN INSTITUTE
OF TECHNOLOGY

DISSERTATION

NANOPHOTONIC MATERIALS FOR BIOMEDICAL SENSING

Ausgeführt zum Zwecke der Erlangung des akademischen Grades eines
Doktors der technischen Wissenschaften

Unter der Leitung von

Univ. Prof. Dipl.-Ing. Dr. techn. Markus Valtiner

E134 Institut für Angewandte Physik, TU Wien

und

Dr. Jakub Dostalek, MSc.

Biosensor Technologies, AIT

Eingereicht an der Technischen Universität Wien

Fakultät für Physik

verfasst von

Dipl.-Ing. Stefan Fossati



Wien, Mai 2022

Abstract

Sensitive and rapid detection of chemical and biological species has become a central component in the swiftly emerging fields of information-aided personalized medicine. Currently available technologies are predominantly based on amplification strategies for the analysis of target analytes, such as polymerase chain reaction or other enzymatic reactions. These approaches offer sufficient sensitivity but typically rely on multiple assay steps and purification of the sample that prolong the analysis time and that can only be conducted in a specialized laboratory environment. Alternatively, faster direct detection assays are pursued in order to expand the capability of sensing technology and potentially perform tests closer to the patients. Fluorescence represents a common and established optical readout method in both enzymatic and enzyme-free optical sensors. Nanophotonic surfaces have been developed to boost the sensitivity of fluorescence assays by implementing advanced light management, increasing the fluorescence emission strength, improving optical collection efficiency and reducing the background. However, these efforts rarely found practical applications as nanophotonic structures are more commonly prepared only for research purposes by complex manufacturing processes. This work presents nanostructured optical materials that can be prepared by scaled-up fabrication means that support novel multimodal biosensor concepts and increase the sensitivity upon optical readout. In particular, it focuses on tailoring surface plasmonic resonances on metallic nanostructures for optical spectroscopy amplification in conjunction with the development of dedicated optical readers. Plasmonic nanostructure architectures and an optical instrument are developed that provide the large field of view required for multiplexing and parallelized kinetics measurements. The combination offers improved collection efficiency of fluorescence light emitted by the selectively excited molecules on the sensor surface. The work is organized in three parts, starting with the exploration of nanophotonic 2D materials by numerical simulation, their lab-scale preparation, and characterization. The optical properties of architectures composed of periodic arrays of nanoparticles, nanomeshes, holographic gratings, and combinations of such elements are

studied. Furthermore, thermo-responsive hydrogel elements are introduced to the architectures, serving as a binding matrix for affinity reactions and as an actively tunable optical component. In the second part, new instruments are developed to take advantage of the optical properties of these surfaces. An epifluorescence reader is presented for the simultaneous observation of affinity binding events by fluorescence spectroscopy and direct monitoring of associated refractive index changes. Moreover, a label-free refractive index sensing modality using surface plasmon resonance is integrated with a novel instrument with an electrolyte-gated field-effect transistor and used for simultaneous and time-resolved observation of surface mass deposition and reorganization of polymer assembly at the common sensor surface. The final section deals with the utilization of light management and surface plasmon-enhanced fluorescence to push forward the sensitivity of fluorescence heterogeneous assays. A sensor for the continuous monitoring of low molecular weight chemical analytes based on a hairpin aptamer and fluorophore quenching at a metallic surface is presented. Finally, there is developed a multi-resonant plasmonic substrate that provides fluorescence enhancement by a factor of 300 while maintaining compatibility with scaled-up industrial manufacturing processes. Together with a newly developed imaging reader, this fluorescence enhancement is achieved by utilizing plasmonically enhanced excitation and surface plasmon-mediated emission of fluorescence. The system is employed for the highly multiplexed observation of immunoassay binding kinetics on a large surface area with a low femtomolar limit of detection (LOD).

Concluding, nanophotonic 2D materials have been implemented in novel biosensor concepts that push forward the sensitivity and open door for combined sensor modalities providing additional insights into surface processes, beyond state-of-the-art methods.

Kurzfassung

Der empfindliche und schnelle Nachweis chemischer und biologischer Spezies ist zu einer zentralen Komponente in den sich rasch entwickelnden Bereichen der informationsgestützten personalisierten Medizin geworden. Die derzeit verfügbaren Technologien beruhen überwiegend auf Amplifikationsstrategien für die Analyse von Analyten wie der Polymerase-Kettenreaktion oder anderen enzymatischen Reaktionen. Diese Ansätze bieten eine ausreichende Empfindlichkeit, erfordern aber in der Regel mehrere Testschritte und eine Aufreinigung der Probe, welche die Analysezeit verlängern und nur in einer speziellen Laborumgebung durchgeführt werden können. Alternativ dazu werden schnellere direct-detection-Assays angestrebt, um die Möglichkeiten der Sensortechnologie zu erweitern und potenziell Tests näher am Patienten durchzuführen. Fluoreszenz ist eine gängige und etablierte optische Auslesemethode sowohl bei enzymatischen als auch bei enzymfreien optischen Sensoren. Nanophotonische Oberflächen wurden entwickelt, um die Empfindlichkeit von Fluoreszenztests zu erhöhen, indem ein fortschrittliches Lichtmanagement implementiert, die Fluoreszenzemissionsstärke erhöht, die optische Erfassungseffizienz verbessert und der Hintergrund reduziert wurde. Diese Bemühungen fanden jedoch nur selten praktische Anwendungen, da nanophotonische Strukturen in der Regel nur für Forschungszwecke durch komplexe Herstellungsprozesse hergestellt werden. In dieser Arbeit werden nanostrukturierte optische Materialien vorgestellt, die durch skalierte Herstellungsverfahren hergestellt werden können, die neuartige multimodale Biosensorkonzepte unterstützen und die Empfindlichkeit der optischen Auslesung erhöhen. Insbesondere geht es um die Anpassung plasmonischer Oberflächenresonanzen auf metallischen Nanostrukturen zur Verstärkung der optischen Spektroskopie in Verbindung mit der Entwicklung spezieller optischer Lesegeräte. Es werden plasmonische Nanostrukturen und ein optisches Instrument entwickelt, die ein großes Sichtfeld bieten, das für Multiplexing und parallelisierte kinetische Messungen erforderlich ist. Die Kombination bietet eine verbesserte Erfassungseffizienz von Fluoreszenzlicht, das von den selektiv angeregten Molekülen auf der Sensoroberfläche emittiert wird. Die Arbeit ist in drei Teile gegliedert, beginnend mit der Erforschung von nanophotonischen 2D-Materialien durch numerische Simulation, deren Herstellung und Charakterisierung im

Labormaßstab. Die optischen Eigenschaften von Architekturen, die aus periodischen Anordnungen von Nanopartikeln, Nanomesches, holographischen Gittern und Kombinationen solcher Elemente bestehen, werden untersucht. Darüber hinaus werden thermoreagierende Hydrogelelemente in die Architekturen eingebracht, die als Bindungsmatrix für Affinitätsreaktionen und als aktiv abstimmbare optische Komponente dienen. Im zweiten Teil werden neue Instrumente entwickelt, um die optischen Eigenschaften dieser Oberflächen zu nutzen. Es wird ein Epifluoreszenz-Reader vorgestellt, mit dem Affinitätsbindungsereignisse durch Fluoreszenzspektroskopie und die direkte Überwachung der damit verbundenen Brechungsindexänderungen gleichzeitig beobachtet werden können. Darüber hinaus wird ein markierungsfreies Verfahren zur Messung des Brechungsindex unter Verwendung der Oberflächenplasmonenresonanz in ein neuartiges Instrument mit einem elektrolytgesteuerten Feldeffekttransistor integriert und zur gleichzeitigen und zeitaufgelösten Beobachtung der Ablagerung von Oberflächenmasse und der Reorganisation der Polymeranordnung an der gemeinsamen Sensoroberfläche verwendet. Der letzte Abschnitt befasst sich mit der Nutzung von Lichtmanagement und oberflächenplasmonenverstärkter Fluoreszenz, um die Empfindlichkeit von fluoreszenzheterogenen Assays voranzutreiben. Es wird ein Sensor für die kontinuierliche Überwachung chemischer Analyten mit niedrigem Molekulargewicht vorgestellt, der auf einem Haarnadel-Aptamer und der Löschung von Fluorophoren an einer Metalloberfläche basiert. Schließlich wird ein plasmonisches Multi-Resonanz-Substrat entwickelt, das die Fluoreszenz um den Faktor 300 verstärkt und gleichzeitig mit industriellen Herstellungsprozessen im Maßstab 1:1 kompatibel ist. Zusammen mit einem neu entwickelten bildgebenden Instrument wird diese Fluoreszenzverstärkung durch plasmonisch verstärkte Anregung und oberflächenplasmonisch vermittelte Emission von Fluoreszenz erreicht. Das System wird für die hochparallelisierte Beobachtung der Bindungskinetik von Immunoassays auf einer großen Oberfläche mit niedriger femtomolarer Nachweisgrenze (LOD) eingesetzt.

Zusammenfassend lässt sich sagen, dass nanophotonische 2D-Materialien in neuartige Biosensorkonzepte implementiert wurden, die die Empfindlichkeit erhöhen und die Tür für kombinierte Sensormodalitäten öffnen, die zusätzliche Einblicke in Oberflächenprozesse bieten, die über den Stand der Technik hinausgehen.

Ich erkläre an Eides statt, dass ich die vorliegende Dissertation selbstständig und ohne fremde Hilfe unter der Betreuung von Dr. Jakob Dostalek und Univ. Prof. Dipl.-Ing. Dr. techn. Markus Valtiner verfasst habe. Es wurden keine anderen als die angegebenen Quellen und Hilfsmittel benutzt bzw. die wörtlich oder sinngemäß entnommenen Stellen als solche kenntlich gemacht.

Wien, am 12.05.2022

Acknowledgments

Experimental research in an interdisciplinary field is a collaborative effort, and the work presented in this thesis has been no exception. It could not have been carried out successfully without the support of many people over the last couple of years.

First, I want to express my deepest gratitude to Dr. Jakub Dostalek for offering me the opportunity to carry out my research in his group, his advice, fruitful discussions, and helping hand in the lab. My appreciation also goes to Prof. Wolfgang Knoll for assembling this wonderful group of people that constitutes the BST group.

Furthermore, I want to thank Prof. Markus Valtiner for offering his help as my supervisor at the TU Wien.

I can't thank Simone Hageneder enough, who became the heart and soul of the lab and somehow managed to work with instruments that barely reached prototype status in many joint projects. Thank you for the countless hours we spent together in the lab, your positive, and caring attitude, and the always open ear, I appreciate it.

To the members of the BST group, who became true friends and made this journey an unforgettable experience. Khulan, Agnes, Daria, Nestor, Jakob, Patrik, Priya, Simone (2), Ciril, Bernadette, Johannes, Ulrich, Anil, Chiara, Vanessa, Roger, Yevhenii, Katharina, Erika, Nico, David, Nitya, Imran, Martin and all the other members I met over the years: thank you for the inspiring discussions, the fruitful joint work and the terrific memories created.

Special thanks go to my family, to my mother, my brother, and particularly to my grandparents, whose love and dedication enabled me to go on this wonderful journey.

Vienna, May 2022 12 May 2022

Stefan.

Content

Abstract.....	I
Kurzfassung.....	III
Acknowledgments.....	IX
Content.....	X
List of Figures.....	XII
List of Abbreviations.....	XV
List of Publications.....	XVI
1. Introduction.....	1
1.1. Biosensors	2
1.2. Surface Plasmon Resonance	8
1.2.1. Electromagnetic Theory of the Surface Plasmon Polaritons	8
1.2.2. Excitation of Surface Plasmon Polaritons	10
1.2.3. Localized Surface Plasmons	12
1.3. Plasmonic Nanostructures.....	13
1.4. Fluorescence	18
1.4.1. Fluorophores at Interfaces	
1.4.2. Plasmon Enhanced Fluorescence - PEF	21
1.5. Plasmonic Biosensors and Plasmon-Enhanced Spectroscopy	24
1.6. Research Aims	26
1.7. Methodology.....	29
1.7.1. Numerical Simulations	30
1.7.2. Nanostructure Preparation and Characterization	32
2. Results.....	36
2.1. Surface Plasmon Modes of Nanomesh-on-Mirror Nanocavities prepared by Nanosphere Lithography	38
2.2. Actuated Plasmonic Nanohole Arrays for Sensing and Optical Spectroscopy Applications.....	48
2.3. UV-Laser Interference Lithography for Local Functionalization of Plasmonic Nanostructures with Responsive Hydrogel	63

2.4. Multi-diffractive Grating for Surface Plasmon Biosensors with Direct Back-side Excitation.....	74
2.5. Dual Monitoring of Surface Reactions in Real Time by Combined Surface Plasmon Resonance and Field-Effect Transistor Interrogation.....	87
2.6. Plasmon Field-Enhanced Fluorescence Energy Transfer for Hairpin Aptamer Assay Readout.....	97
2.7. Biosensor Platform for Parallel Surface Plasmon-Enhanced Epifluorescence and Surface Plasmon Resonance Detection.....	107
2.8. Multiresonant Plasmonic Nanostructure for Ultrasensitive Fluorescence Biosensing	116
3. Summary and Outlook.....	133
4. References.....	139
5. Appendix.....	151
5.1. Supporting Information – Surface Plasmon Modes of Nanomesh-on-Mirror Nanocavities prepared by Nanosphere Lithography	152
5.2. Supporting Information – Actuated Plasmonic Nanohole Arrays for Sensing and Optical Spectroscopy Applications.....	165
5.3. Supporting Information – UV-Laser Interference Lithography for Local Functionalization of Plasmonic Nanostructures with Responsive Hydrogel.....	167
5.4. Supporting Information – Dual Monitoring of Surface Reactions in Real Time by Combined Surface Plasmon Resonance and Field-Effect Transistor Interrogation	172
5.5. Supporting Information – Plasmon Field-Enhanced Fluorescence Energy Transfer for Hairpin Aptamer Assay Readout.....	199
5.6. Supporting Information – Multiresonant Plasmonic Nanostructure for Ultrasensitive Fluorescence Biosensing.....	207
Curriculum Vitae.....	223

List of Figures

Figure 1 Schematic illustration of the main components of a biosensor.	3
Figure 2 Illustration of key sensor parameters in a dose-response curve.	6
Figure 3: Spatial field distribution of the electrical field component perpendicular to the surface E_{\perp} for a surface plasmon mode on a gold - water interface, at a frequency equivalent to light with a wavelength of 633 nm in vacuum. a) The evanescent field perpendicular to the propagation direction shows exponential decay, and b) attenuation of a SPP propagating along the surface.	10
Figure 4 a) Illustration of prism coupling in the Kretschmann configuration and b) phase matching between the light line in the prism (blue) with the SPP dispersion curve (black).	11
Figure 5 a) Schematic illustration of diffraction coupling by scattering on periodical surface features. b) Excitation of SPPs by multiple superimposed gratings on a metal-dielectric interface, observed as absorption lines in angular resolved reflectivity spectra, reproduced with permission from reference 92.	12
Figure 6 a) Polarization of an isolated metallic particle under illumination. b) Optical extinction cross section of Au nanoparticles embedded in dielectric media with different refractive index n_d . Image adapted from reference 97.	13
Figure 7: Advanced plasmonic 2D architectures: a) Multi-diffractive corrugated gold layer as published in reference 38, b) Nanohole array in Au layer reproduced from reference 110 with permission the Royal Society of Chemistry, c) Gold nano-mushroom architecture reproduced from reference 108 with permission from Springer Nature and d) Nanomesh-on-mirror architecture adopted from reference 102. The scalebar length is 1 μm in b and d and 200 nm in c.	15
Figure 8 a) The phase transition of thermoresponsive pNIPAAm hydrogel from the hydrophilic state at low temperatures to the hydrophobic state at high temperatures is reflected as sudden change in the swelling ratio (black line) and the refractive index (blue line). b) The change of material properties is observed as SPR shift in angular spectroscopy.	

Adapted from reference 119 under a CC-BY license, Copyright © 2013 American Chemical Society..... 17

Figure 9 Jablonski diagram of excitation and decay processes in molecular fluorescence. (Figure by Steve Pawlizak, 2009.).....

Figure 10 Cross section of averaged angular fluorescence intensity for a) a fluorophore on a water-glass interface and b) a water-gold interface. Collection cone for NA=0.2 is indicated as dashed line and the calculated collection efficiency is shown. Figure adapted from reference ¹²⁹ with permission from Optica Publishing Group..... 21

Figure 11 Schematic illustration of a) a laser interference lithography device in Lloyd's mirror configuration, reproduced from reference ¹⁷² with permission from the Royal Society of Chemistry and b) a UV-NIL process. (Graphic by Jakub Dostalek) 34

List of Abbreviations

AFM	Atomic force microscopy
ATR	Attenuated total reflection
EBL	Electron beam lithography
EM	Electromagnetic
FDTD	Finite difference time domain
FET	Field effect transistor
gFET	graphene field effect transistor
IC	Internal conversion
ISC	Inter system crossing
LBL	Layer-by-layer assembly
LIL	Laser interference lithography
LoD	Limit of detection
LSP	Localized surface plasmon
MIM	Metal-insulator-metal (architecture)
NIL	Nanoimprint lithography
PCR	Polymerase chain reaction
PEF	Plasmon enhanced fluorescence
PMMA	Poly(methyl methacrylate)
RE	(Bio-) recognition element
SARS	Severe acute respiratory syndrome
SEM	Scanning electron microscopy
SP	Surface plasmon
SPP	Surface plasmon polariton
SPR	Surface plasmon resonance
SR	Swelling ratio
QCM	Quartz crystal microbalance

List of Publications

Following publications have been published within this work and are included as sections in chapter 2.

First author publication:

1. **Stefan Fossati**, Simone Hageneder, Samia Menad, Emmanuel Maillart und Jakub Dostalek Multiresonant plasmonic nanostructure for ultrasensitive fluorescence biosensing. *Nanophotonics* **9**, 3673–3685 (2020). <https://doi.org/10.1515/nanoph-2020-0270>

Co-Authored publications:

2. Christian Stelling, **Stefan Fossati**, Jakub Dostalek and Markus Retsch Surface plasmon modes of nanomesh-on-mirror nanocavities prepared by nanosphere lithography. *Nanoscale* **10**, 17983–17989 (2018). <https://doi.org/10.1039/c8nr05499a>
3. Daria Kotlarek, **Stefan Fossati**, Priyamvada Venugopalan, Nestor Gisbert Quilis, Jiří Slabý, Jiří Homola, Médéric Lequeux, Frédéric Amiard, Marc Lamy de la Chapelle, Ulrich Jonas and Jakub Dostálek Actuated plasmonic nanohole arrays for sensing and optical spectroscopy applications. *Nanoscale* **12**, 9756–9768 (2020). <https://doi.org/10.1039/d0nr00761g>
4. Nestor Gisbert Quilis, Simone Hageneder, **Stefan Fossati**, Simone K. Auer, Priyamvada Venugopalan, Anil Bozdogan, Christian Petri, Alberto Moreno-Cencerrado, Jose Luis Toca-Herrera, Ulrich Jonas, and Jakub Dostalek UV-Laser Interference Lithography for Local Functionalization of Plasmonic Nanostructures with Responsive Hydrogel. *J. Phys. Chem. C* **124**, 3297–3305 (2020). <https://doi.org/10.1021/acs.jpcc.9b11059>
5. Simone Hageneder, **Stefan Fossati**, Nicolas-Guillermo Ferrer, Batuhan Güngörmez, Simone K. Auer, and Jakub Dostalek Multi-diffractive grating for surface plasmon biosensors with direct back-side excitation. *Opt. Express* **28**, 39770 (2020). <https://doi.org/10.1364/oe.410416>

6. Patrik Aspermaier, Ulrich Ramach, Ciril Reiner-Rozman, **Stefan Fossati**, Bernadette Lechner, Sergio E. Moya, Omar Azzaroni, Jakub Dostalek, Sabine Szunerits, Wolfgang Knoll, and Johannes Binterger Dual Monitoring of Surface Reactions in Real Time by Combined Surface-Plasmon Resonance and Field-Effect Transistor Interrogation. *J. Am. Chem. Soc.* **142**, 11709–11716 (2020). <https://doi.org/10.1021/jacs.9b11835>
7. Khulan Sergelen, **Stefan Fossati**, Aysegül Turupcu, Chris Oostenbrink, Bo Liedberg, Wolfgang Knoll, and Jakub Dostálek Plasmon field-enhanced fluorescence energy transfer for hairpin aptamer assay readout. *ACS Sensors* **2**, 916–923 (2017). <https://doi.org/10.1021/acssensors.7b00131>
8. Agnes T. Reiner, **Stefan Fossati**, Jakub Dostalek Biosensor platform for parallel surface plasmon-enhanced epifluorescence and surface plasmon resonance detection. *Sensors Actuators, B Chem.* **257**, 594–601 (2018). <https://doi.org/10.1016/j.snb.2017.10.116>

1. Introduction

Highly sensitive and specific detection of biochemical substances is vital in a wide range of applications, including food safety, environmental monitoring, and medical diagnostics, which has been addressed by the rapidly evolving field of biosensing. For instance, the importance of medical testing capabilities became painstakingly obvious in the COVID-19 pandemic, when efficient tests for the corona virus SARS-CoV-2 needed to be developed and brought to global application in the shortest time. Merely weeks after the first genetic sequences of the virus were published, polymerase chain reaction (PCR) test kits had been rolled out, followed by lateral flow antigen tests and antibody tests within a few months.^{1,2} Frequently, the target analytes are also present in a complex matrix, like nasopharyngeal mucosa, blood, or urine in low concentrations, ranging down to a few particles per milliliter.^{3,4} The detection of such low concentrations thus requires highly targeted detection schemes that suppress unspecific background signal and/or time-consuming purification steps before the actual detection can be performed. Novel direct detection biosensor approaches seek to rapidly obtain results by overcoming the need for time-consuming amplification as well as integrating and automating purification steps. This allows to bring the diagnostic devices out of the specialized laboratories and closer to the patient, supporting the rapidly emerging topic of point-of-care diagnostics.⁵

Among the sensor technologies explored, optical biosensors stand out for their versatility and the ability to take advantage of optical components developed in other fields, such as telecommunications, optical spectroscopy, and microscopy. Numerous optical techniques were developed for the direct label-free observation of molecular and their affinity interactions, for example, using optical waveguides,^{6,7} photonic crystals,^{8,9} or surface plasmon resonance^{10,11} (SPR). For high sensitivity measurements, labeling steps can be integrated into the assay to boost the output signal strength by orders of magnitude.^{12,13} Furthermore, by choosing an imaging format, spatial multiplexing of the detection from several to large sets of analytes on a small footprint becomes possible.¹⁴ While optical methods have demonstrated the ability to resolve single molecules present in a small

volume or attached to a surface, achieving similar sensitivity in a biosensor for the analysis of trace amounts of target molecules in a complex sample with realistic volume remains an unsolved challenge. Nanophotonic surface architectures, particularly plasmonic surfaces have been successfully employed in sensitive fluorescence sensors at the research stage.¹⁵⁻¹⁷ However, the transfer of these, often complex, surface geometries to practical applications has proven difficult. It is, therefore, crucial to consider limitations imposed by scalable manufacturing technologies already in the design phase.

1.1. Biosensors

According to the IUPAC (International Union of Pure and Applied Chemistry) definition, a chemical sensor is a self-contained device that transforms chemical information, like concentration or the total composition of a sample into a measurable physical signal. Biosensors are chemical sensors that use a biological recognition element. The devices are kept compact, for the most prevalent applications require portable or even handheld sensors. Frequently, the readout mechanism is integrated with an electronic module and the assay is implemented by using a microfluidic device to minimize material waste.

The most successful example of biosensors in commercial applications are glucose sensors for diabetes treatment, which are a daily companion for many diabetes patients,¹⁸ pregnancy tests,¹⁹ and other lateral flow tests for a large range of applications,²⁰⁻²² including recently the detection of the SARS-COV-2 virus.^{23,24}

While paper-based lateral flow assays are strictly single-use, continuous monitoring sensors are under development, particularly for glucose sensing applications.²⁵ Combined with an insulin pump, such sensor technology would allow the implementation of automatic insulin regulation, mimicking the natural function of the pancreas.²⁶

A typical biosensor is comprised of two distinct parts:

1. The biointerface is the contact region of the sensor with the sample and carries the **recognition element (RE)** which serves as a specific receptor and is responsible for the specific interaction with the target analyte. Depending on the analyte, a wide range of biomolecules can serve as recognition elements: antibodies, enzymes, proteins, peptides, or recently aptamers have been used. Furthermore, the interface

is modified with molecular architectures to prevent undesired interaction of the sample with the transducer, while enabling the recognition elements to work effectively, also referred to as antifouling coating.

2. The **transducer** converts the change of a physical or chemical property induced by the interaction of the analyte with the RE to a measurable signal. The most frequently used modalities include electrical, electrochemical, optical, calorimetry, or measuring mass change. The output is most commonly an electrical or optical signal that can be digitized and further processed.

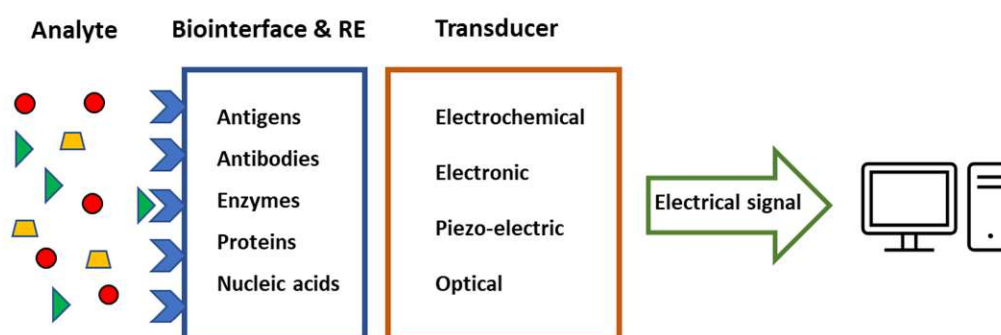


Figure 1 Schematic illustration of the main components of a biosensor.

Signal processing finally extracts the chemical parameters from the obtained sensor data. Some optical sensors, particularly colorimetric sensors, can be qualitatively read by the naked human eye (e.g. pH test strips, lateral flow assays). However, most commonly the transducer provides an output that is digitized and electronically processed. Comparison with reference data then allows quantification of the result.

Let us now have a more detailed look at the components that a biosensor is comprised of and the functions they fulfill in the sensing process.

Biointerface with the recognition element, RE

As the contact point of the analyte-containing liquid with the solid surface of a sensor device, the biointerface serves a twofold role. Firstly, it carries the RE, the chemical compound specifically interacting with the target analyte. It provides the appropriate environment for the RE to work at high efficiency. Particularly, controlling the density of the binding sites to avoid steric hindrance and surface charge effects are to be considered. Furthermore, the biointerface prevents the unspecific adhesion of compounds present in

biological samples to the surface. This unspecific interaction is also called fouling. Among the numerous types of chemical and physical interactions driving fouling, the most important are van der Waals forces, charge interaction, hydrophilic interaction, and osmotic pressure. The topic is still subject of intense research^{27,28} and a large variety of polymer 2D²⁹⁻³¹ and 3D³²⁻³⁴ architectures have been studied. A detailed introduction to biointerface architectures can be found in recent literature.^{35,36}

The RE can specifically bind the analyte at the surface that is probed by the transducer. Compounds used as RE expose at least one binding site specific to the analyte. Different naturally occurring and also synthetic compounds have been used as RE, including antibodies,^{37,38} enzymes,³⁹ peptides,⁴⁰ aptamers,⁴¹ and molecularly imprinted polymers.⁴² Interactions of these REs with the target analyte can often be described by the Langmuir adsorption model and characterized by their binding affinity, defined as the analyte concentration in the liquid sample, at which half the binding sites are occupied in equilibrium.⁴³ The affinity between receptor and ligand thus plays a vital role in achievable sensitivity and dynamic range of the sensor and the density of recognition elements within the biointerface defines the maximum signal change observed for a saturated sensor. The receptor affinity should be chosen to match the expected analyte concentration, for the best sensor performance in terms of sensitivity and dynamic range. In the case of continuous monitoring, as discussed later in chapter 2.6, a compromise must be found between sensitivity and the system response time to changes of analyte concentration to achieve reversibility.

Transducers

The transducer converts the physicochemical changes induced by the captured analyte to a measurable signal. Different transducers respond to different physical or chemical properties of the analyte present in the analyzed medium. Furthermore, the sensitivity and dynamic range of the transduction mechanisms can vary greatly. While most sensor approaches use a single transducer, the combination of different transducing mechanisms can offer the advantage of extending the dynamic range,⁴⁴ improving sensitivity^{12,45} or gaining additional insight into surface processes by observing complementary properties and will be explored in this work.

Most of the commonly employed transducers fall into four categories:

Electrochemical sensors utilize the electrochemical reaction between a moiety, frequently an enzyme, anchored at the sensor surface and the analyte present in the analyzed liquid sample.⁴⁶ The electrical current occurring upon the reaction is directly proportional to the analyte concentration. The sensors are thus well suited for quantitative and continuous monitoring applications.⁴⁷

Electronic sensors observe the change of the charge transfer properties of parts of the sensor device upon analyte binding. In potentiometric sensors, a constant potential is applied across the sensor surface. A change of conductivity upon analyte binding is then observed as a change of current. Another important implementation of electrical sensors are field-effect transistors, where the conductivity of a semiconducting channel is controlled by a gate voltage.⁴⁸ The capture of charged moieties on gate or channel surface has a similar effect as additional voltage and modulates the measured channel conductivity.

Piezo-electric sensors respond to the accumulation of mass on the sensor interface. The most prominent example is the quartz crystal microbalance (QCM).⁴⁹ These sensors are based on the mechanical oscillation of electrically driven piezo crystals where the resonance frequency is changed by the weight of the captured analyte.

Optical biosensors utilize light to determine the presence of the analyte. They can be roughly split into two categories: Transducers that directly modulate the properties of electromagnetic waves and approaches that employ optically active dye molecules as part of the assay. Examples for the first category are interferometric waveguide sensors,⁵⁰ ellipsometry,⁵¹ or surface plasmon resonance (SPR) sensors,⁵²⁻⁵⁴ all sensitive to the change of refractive index on the sensor surface. Such direct-detection methods are also referred to as *label-free* and the strength of the sensor response is directly proportional to the mass of the captured target analyte.⁵² The second class of sensors employs an additional labeling step to enhance the sensitivity if the molecular weight or the concentration of the analyte are not high enough to induce a measurable refractive index change. Frequently, this additional labeling step also includes an additional recognition element, consequentially increasing the specificity of the assay. For those labels, three main enhancement strategies can be pursued: First, a high molecular mass molecule, usually an antibody, can be used as secondary RE, specifically binding to the analyte and thus increasing the output of mass-sensitive sensors.⁵⁵ To further amplify the surface-mass gain, the secondary RE can be conjugated with nanoparticles.^{13,56} Alternatively, by using a secondary RE conjugated with

an assay element that absorbs or emits light, a visual color change^{57,58} or the emission of fluorescence light⁵⁹ can be induced. Such a label effectively acts as an amplifier for optical transducers, as a single label can interact with a large number of photons, which can be detected with high efficiency.^{60,61} Most common labels employed in analytical assays are metallic nanoparticles^{62,63} (for their large absorption cross section and mass) and fluorescent^{60,61} dyes. Another interesting approach is the use of enzymes as labels, which over time generate reaction products that can be detected by increased surface mass⁶⁴ and color change⁶⁵ or fluorescence⁶⁶. Optical sensors are unique among transducer technologies as they can be read out by the naked human eye without conversion to an electronic signal. Such approaches thus have been successfully implemented for a wide range of point-of-care applications, for example, lateral flow assays for pregnancy tests or viral antigen tests.

At this point, it is worth to briefly consider the key performance parameters of biosensors:

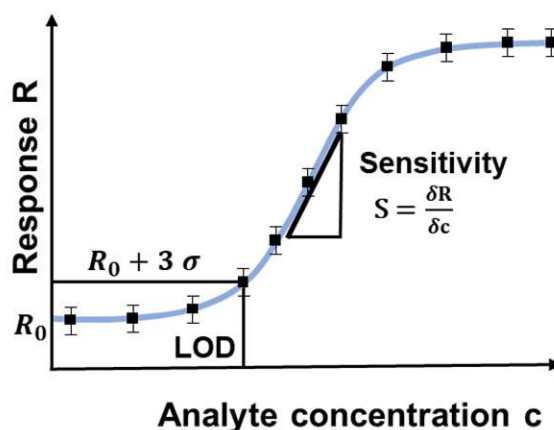


Figure 2 Illustration of key sensor parameters in a dose-response curve.

The response R of a biosensor is typically represented as a calibration curve as schematically shown in Figure 2. During measurements without analyte, the sensor generates the blank signal R_0 with a standard deviation σ . For very small concentration of analytes, any change of response is hidden within the blank signal. The **limit of detection (LOD)** is characterized as the concentration that can reliably be distinguished from the blank signal.⁶⁷ The definition of the LOD depends on the desired confidence interval and in this work, this is defined as $R_{LOD} = R_0 + 3\sigma$, at which point the analyte can be discriminated from the background with 99.7% certainty for Gaussian statistics. Practically, sensors are used in the **operational range**, where the sensor response is a linear function of the analyte

concentration, with the proportionality factor **sensitivity** $S = \frac{\delta R}{\delta c}$. The maximum of this range is limited by two factors: the **binding capacity** of the biointerface and the **dynamic range** of the transducer. Chemical sensors, that rely on the affinity binding of analyte by the RE, saturate when a large portion of the available binding sites are occupied. Furthermore, the dynamic range of the transducer is limited by the background signal and the maximum output signal obtainable by the transducer and the electronic subsystem. At high concentrations, the output signal thus becomes independent of the analyte concentration; the sensor reaches **saturation**.

Practical biosensor applications require the detection of analytes that occur in a broad range of concentrations from few molecules per milliliter (for example, when screening for specific mutations of tumor DNA present in circulating blood⁶⁸) to grams per liter (for albumin or immunoglobulins⁶⁹) and in a large variety of complex media including blood, saliva or urine. The challenge in sensor design is finding the balance between sensitivity, specificity, and dynamic range suitable for the analyte in a particular medium. This becomes especially challenging when designing multiplexed sensors for multiple analytes, where concentration differences can be orders of magnitude.

Among the transducer technologies, optical methods, particularly those involving surface plasmon resonance, stand out for their versatility and sensor properties well suited for the detection of biomedical analytes. The small probing volume with a thickness of several 10 nm to a few 100 nm from the biointerface is well-matched with the size of typical biomolecules and allows measurements with reduced influence from the analyte carrying medium. The technology allows label-free, continuous, and quantitative observation of biochemical reactions. In case the sensitivity of the direct detection approach is insufficient, labeled assays can be employed, which also can be boosted by the interaction with the surface plasmons. SPR has thus been chosen as the platform for the biosensor applications presented in this work.

The following chapters will briefly introduce the concepts behind plasmonic biosensors and their implementations. Furthermore, enhancement strategies relying on surface plasmon optics for sensors based on fluorescence assays and the integration of actively tunable materials into the sensor architectures will be discussed.

1.2. Surface Plasmon Resonance

Plasmons are collective charge oscillations of the electron density and the associated electromagnetic (EM) field. Surface plasmons (SP), also referred to as surface plasmon polaritons (SPP), are surface electromagnetic waves propagating on a metal-dielectric interface. First discovered by Wood in 1902 as dark absorption lines in the reflectance spectra of metallic gratings,⁷⁰ Fano in 1942 attributed these observations to the excitation of electromagnetic surface waves in his theoretical work.⁷¹ With their pioneering work in 1968, Otto, as well as Kretschmann and Raether, introduced convenient, prism-based coupling strategies for the optical excitation of these surface waves from the far field.^{72,73} In the following years, the effect gained importance for the characterization of thin films.⁷⁴ With a short propagation length in the range of 1 μm – 100 μm at optical frequencies and the possibility to work with subwavelength structures, SPP later attracted strong interest as an active mechanism in nanophotonic components^{75–77}, electrooptic modulators^{78–81} and have been particularly successfully employed to study biochemical reactions in biosensors.^{82–84} The method, referred to as surface plasmon resonance (SPR) biosensor, is well suited for the investigation of biomolecular processes on surfaces, as the probing depth of the SPPs is in the order of 100 nm, significantly smaller than the wavelength used for illumination and comparable to the size of common biomolecules. As the method is surface mass sensitive, SPR delivers the best sensitivity for analytes with high molecular weight.

1.2.1. Electromagnetic Theory of the Surface Plasmon Polaritons

This section will introduce the basic concepts and terminology used to describe SPPs. It does not aim to be a comprehensive introduction to the field or present the detailed theoretical derivation. Excellent literature for the introduction to the physics of surface plasmon has already been published by Maier⁸⁵ and Homola⁵².

SPPs originate from the coupled oscillation of the electromagnetic field and the density of the electron plasma on a metal-dielectric interface. They are a guided wave solution to the Maxwell equations, where the real part of the metal permittivity is $\text{Re}\{\epsilon_m\} < 0$. Solved for a single metal-dielectric interface, the wavevector of the SPP is expressed as

$$k_{spp} = k_0 \sqrt{\frac{\epsilon_m \cdot \epsilon_d}{\epsilon_m + \epsilon_d}}, \quad (1)$$

where k_{spp} is the wavenumber of the SPP and $k_0 = \frac{2\pi}{\lambda} = \frac{\omega}{c}$ is the vacuum wavenumber, with the angular frequency ω , wavelength λ and speed of light in vacuum c . The complex permittivity of the metal $\varepsilon_m = \varepsilon'_m + i \varepsilon''_m$ and dielectric $\varepsilon_d = \varepsilon'_d + i \varepsilon''_d$ are material properties and in general dispersive, this means functions of the frequency $\varepsilon_m(\omega)$. Consequently, also k_{spp} is a complex, dispersive quantity. It is worth noting that $k_{spp} = \frac{2\pi}{\lambda_{spp}}$ and thus the wavelength of the surface plasmon at a given frequency only depends on the material properties. Under the assumption that the dielectric has negligible dampening ($\varepsilon''_d = 0$) and that $\varepsilon''_m < |\varepsilon'_m|$, k_{spp} can be rewritten as⁵²

$$k_{spp} = k'_{spp} + i k''_{spp}, \quad (2)$$

$$k'_{spp} = \pm k_0 \sqrt{\frac{\varepsilon'_m \cdot \varepsilon_d}{\varepsilon'_m + \varepsilon_d}}, \quad (3)$$

$$k''_{spp} = k_0 \left(\frac{\varepsilon'_m \cdot \varepsilon_d}{\varepsilon'_m + \varepsilon_d} \right)^{\frac{3}{2}} \frac{\varepsilon''_m}{2(\varepsilon'_m)^2}. \quad (4)$$

The propagation length of the SPP is then defined as the distance along the surface, where the field intensity of the electric field is reduced by a factor of $1/e$:

$$L_p = \frac{1}{2 k''_{spp}}. \quad (5)$$

The factor 2 in this equation originates from the fact that the field intensity is proportional to the square of the field strength.

Perpendicular to the interface plane, the electric field amplitude decays exponentially into the metal and dielectric. The penetration depth d_p , also called skin depth, into metal and dielectric is given by:⁸⁵

$$d_{p,d} = \text{Re} \left\{ \left(k_{spp}^2 - \varepsilon_d k_0^2 \right)^{\frac{1}{2}} \right\}^{-1}, \quad (6)$$

$$d_{p,m} = \text{Re} \left\{ \left(k_{spp}^2 - \varepsilon_m k_0^2 \right)^{\frac{1}{2}} \right\}^{-1}. \quad (7)$$

To illustrate the properties of SPPs, let us consider a standard surface employed in biosensing: the gold-water interface under illumination with a HeNe laser with a wavelength of 633 nm. At this wavelength, water has a refractive index⁸⁶ $n_D = 1.332$ and thermally deposited gold⁸⁷ has a complex refractive index of $n_m = n'_m + i \kappa = 0.18344 + i 3.4332$, where κ is the extinction coefficient. The relation between the permittivity and

the refractive index is given by $\varepsilon = n^2 = (n' + (i\kappa))^2$. Solving equations (3) - (7) with these material properties shows that the SPP at this frequency travels along the surface with a periodicity of $\lambda_{spp} = \frac{2\pi}{k_{spp}} = 438 \text{ nm}$ and a propagation length of $L_p = 3.6 \mu\text{m}$. The SPP exhibits a penetration depth into water of $d_{p,d} = 180 \text{ nm}$ and $d_{p,m} = 27 \text{ nm}$ into the metal. These results are illustrated in Figure 3.

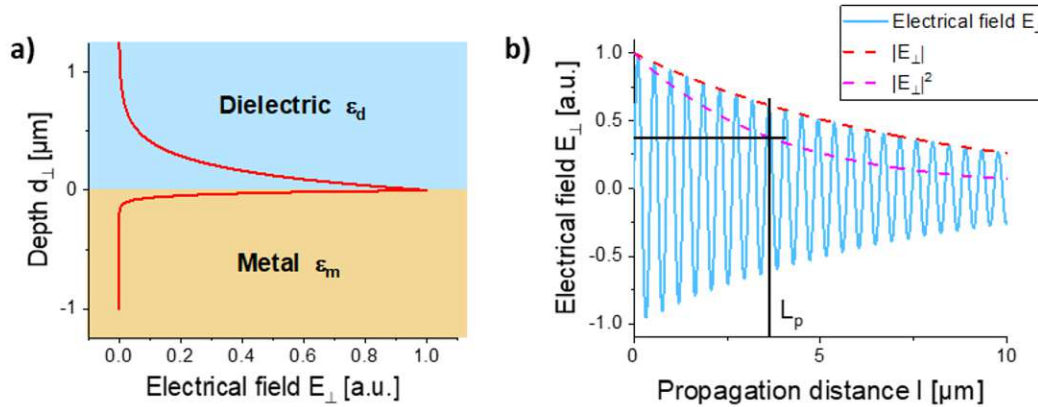


Figure 3: Spatial field distribution of the electric field component perpendicular to the surface E_{\perp} for a surface plasmon mode on a gold-water interface, at a frequency equivalent to light with a wavelength of 633 nm in vacuum. a) The evanescent field perpendicular to the propagation direction shows exponential decay and b) attenuation of a SPP propagating along the surface.

1.2.2. Excitation of Surface Plasmon Polaritons

Equation (3) shows that the real part of the wave vector $Re\{k_{spp}\}$ of a SPP at a given frequency ω is always larger than that of the light propagating in the dielectric medium ($k_d = k_0 \cdot n_d = k_0 \sqrt{\varepsilon_d}$) and can thus not couple to SPPs on a flat metal film, see Figure 4b. The SPP dispersion curve approaches the light cone for low frequencies whereas at high frequencies it approaches the cutoff frequency $\omega_m = \omega_p / \sqrt{1 + \varepsilon_d}$. This means, that these waves cannot directly couple to the far field. Additional momentum Δk needs to be provided by a coupling mechanism to achieve phase matching and enable the efficient transfer of energy from the far field to SPP modes.

Two methods have been established as practical coupling mechanisms. As already discovered by Wood in the first observation of SPPs, diffractive or *grating coupling* utilizes a periodic corrugation of the metallic surface to provide additional momentum and allows the launching of SPPs from the dielectric side of the interface. Secondly, *prism coupling* has been established as the primary means of coupling in commercial SPR biosensor systems.

There, the momentum matching is realized by embedding a thin metallic film between two dielectrics with different refractive indices, where the propagating waves on the high refractive index side can be matched to surface plasmons on the lower refractive index side by resonant tunneling through the metallic film. While these are the main methods used for sensing applications, for the sake of completeness, it should be mentioned that surface plasmons can also be launched by other methods, including irradiation with a focused electron beam,⁸⁸ near field coupling,⁸⁹ and matched modes of a dielectric waveguide^{13,90} and by scattering on individual particles.⁹¹

Prism coupling

In prism coupling, SPPs are excited by the evanescent field of light reflected at the base of an optical prism by attenuated total reflection (ATR). In the Kretschmann configuration,⁷³ as shown in Figure 4a, a thin metallic film is attached to the prism base. When the wave vector component parallel to the surface matches with the SPP wave vector on the metal-dielectric interface:

$$\text{Re}\{k_{spp}\} = k_0 \cdot n_p \cdot \sin\theta, \quad (8)$$

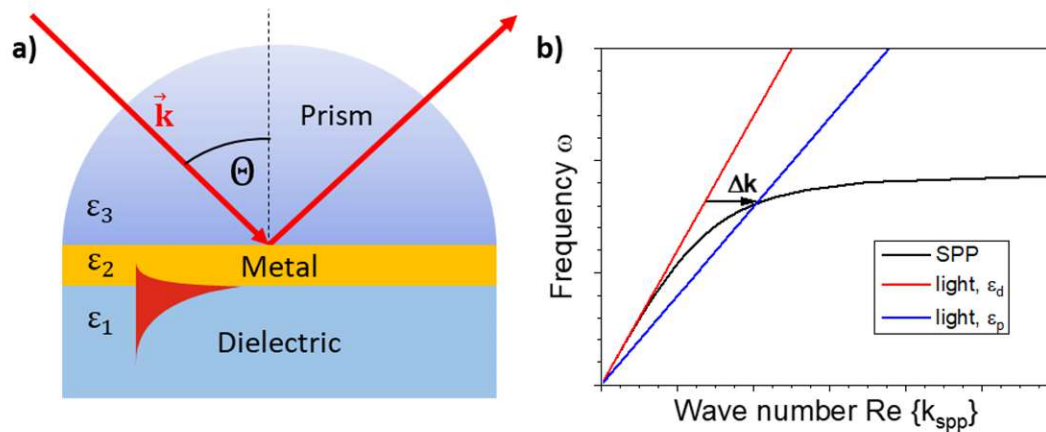


Figure 4 a) Illustration of prism coupling in the Kretschmann configuration and b) phase matching between the light line in the prism (blue) with the SPP dispersion curve (black).

the transfer of energy between the incident propagating wave and the SPP can occur. The refractive index $n_p = \sqrt{\epsilon_p}$ of the prism in such a configuration must be larger than the refractive index of the dielectric $n_p > n_d$ and θ refers to the angle of incidence with respect to the surface normal.

Diffractive coupling

A periodic corrugation of a metallic surface allows the diffractive coupling to SPPs, as illustrated in Figure 5a. The coupling condition is fulfilled when SPPs originating from scattering on the periodic structures with a period Λ form a standing wave pattern. This can be expressed using the grating vector $G = 1/\Lambda$ as

$$k_0 n_d \sin\theta + m G = \pm \text{Re}\{k_{spp}\} \quad (m = 0, \pm 1, \pm 2, \dots), \quad (9)$$

where the integer m is the diffraction order. Diffraction coupling, also called grating coupling, allows the excitation of SPPs from the dielectric side and thus also on bulk metal. It is worth noting that, despite the coupling to propagating modes, the electric field intensity is not homogeneously distributed over the surface but forms localized hot spots. It should be pointed out that surfaces structured with multiple superimposed diffractive features allow the independent excitation of surface plasmons at different wavelengths,⁹² as exemplarily shown in Figure 5b.

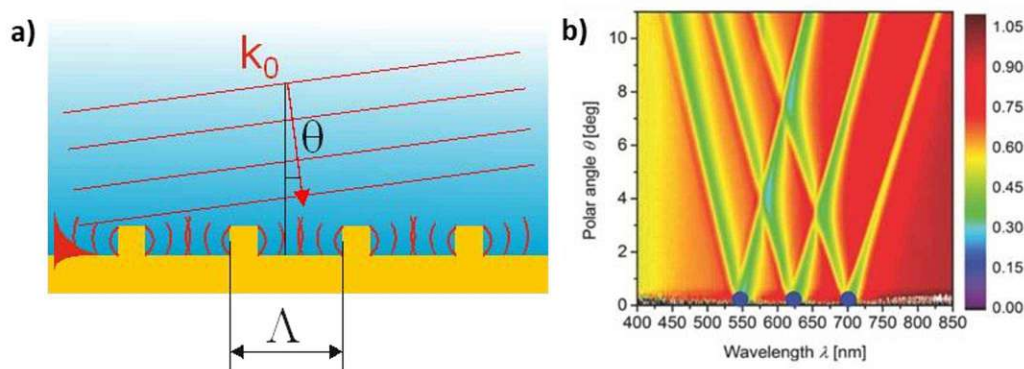


Figure 5 a) Schematic illustration of diffraction coupling by scattering on periodical surface features. b) Excitation of SPPs by multiple superimposed gratings on a metal-dielectric interface, observed as absorption lines in angular resolved reflectivity spectra, reproduced with permission from reference 92.

1.2.3. Localized Surface Plasmons

Localized surface plasmons (LSPs) originate from the interaction between the oscillating electromagnetic field and the conduction electrons in metallic particles smaller than the incident wavelength. The electron density is displaced by the electromagnetic force exerted by the external field, polarizing the particle, as illustrated in Figure 6a. The electrostatic

repulsion between the electrons acts as restoring force against the external field. With the inertia of the electrons, the system forms a resonator. The resulting polarization and resulting scattering properties can, for spherical particles, be analytically described by Mie theory⁹³ but needs to be determined numerically for more general shapes. The resonant oscillation leads to an increased field intensity at the particle surface along the polarization direction of the impinging optical field. It is also the cause of an increased extinction cross section σ_{ext} of metallic nanoparticles at the resonant wavelength, which greatly exceeds the geometric cross section.⁹⁴ Resonances associated with LSPs are typically much broader than SPPs in the same metal but confine the EM field intensity tighter to the surface. The spectrum of LSPs highly dependent on the size, shape, material properties of metal and the surrounding medium, and spacing between adjacent objects.^{95,96}

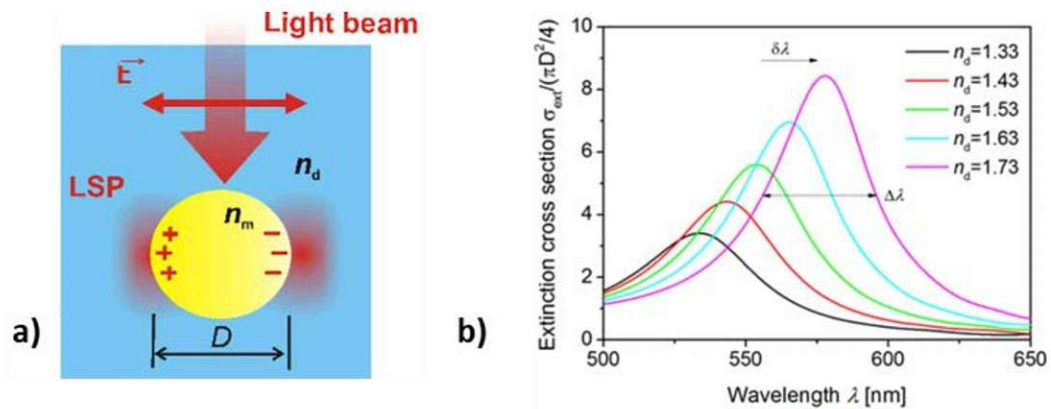


Figure 6 a) Polarization of an isolated metallic particle under illumination. b) Optical extinction cross section of Au nanoparticles embedded in dielectric media with different refractive index n_d . Image adapted from reference 97.

1.3. Plasmonic Nanostructures

Flat metal layer

The simplest plasmonic surface is a flat metal-dielectric interface. It supports propagating modes (SPPs), with optical properties purely defined by the material properties, as described in equation (3). It is, however, not possible to excite them directly with a propagating light beam, as discussed in section 1.2.2. Flat metallic surfaces are thus typically used in form of a thin film in connection with prism coupling. The preparation of a flat film system is typically straightforward, involving only the metal deposition steps. This is done by either chemical or physical methods, primarily by sputtering and evaporation

techniques. For films intended for use in optical applications, the surface smoothness is of great importance, as the roughness directly influences the dampening of the SPPs.⁹⁸ The specific parameters required to achieve the best surface properties depend on the used metal and have been subject to extensive studies.^{99,100}

Corrugated metallic surface

Periodically modulated surfaces and continuous metallization support plasmonic standing wave modes. The plasmon wave number is, for shallow modulations, given by the propagating plasmon dispersion relation (Equation (3)), and the surface plasmons can be excited by diffractive coupling by the periodic structure. Preparation of such structures is more complex than for flat films as the surface needs to be structured by lithography techniques, typically prior to the metal deposition process. For biosensor applications, corrugated surfaces are advantageous for the versatile coupling possibilities and the fact that only a single material, the metallic layer, is exposed to the sample, simplifying the chemical functionalization.

Nanoparticle arrays

Individual metallic nanoparticles with dimensions smaller than the plasmon wavelength support LSPs. Their optical absorption is manifested as a resonance in the wavelength spectrum of transmission or reflection. The shape and center wavelength of the resonance is determined by the geometrical and material properties of the particle and the surrounding medium. With randomly oriented or spherical particles, the observed spectrum does not change with the angle of incidence of the illuminating beam. The width of the observed absorption is typically also much broader compared to propagating SPPs.

For periodically arranged metallic nanoparticles, the scattered light on the individual particles acts as a coupling mechanism, giving rise to collective oscillations across the arrays. While the LSP mode of the individual particles is angular insensitive, the diffractive coupling generates comparably narrower and dispersive optical features. In these coupled systems, the resonant wavelength strongly depends on the particle size, shape, spacing, and material composition of the surrounding medium and the particles.^{96,101}

Nanohole arrays

Nanoholes, small perforations of thin metallic layers, support localized plasmons similar to nanoparticles. Like nanoparticles, the hole gets polarized by the rearrangement of electrical charge when exposed to an external electrical field. The localized modes of a nanohole can also be understood as whispering gallery modes. With increasing hole diameter, propagating plasmon modes on the hole walls form a standing wave pattern with an increasing number of hot spots. Periodically arranged nanoholes can exhibit collective oscillations. It is worth noting that coupling in such arrays is primarily mediated by propagating plasmons on the interfaces of the continuous metal film.¹⁰²

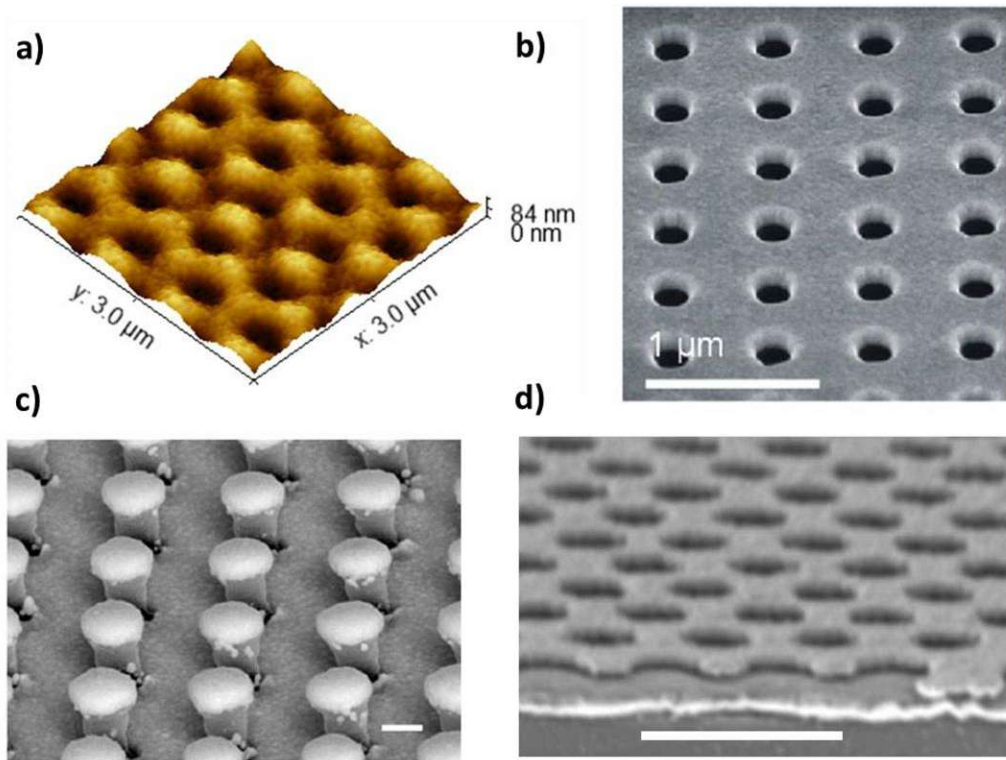


Figure 7: Advanced plasmonic 2D architectures: a) Multi-diffractive corrugated gold layer as published in reference 38, b) Nanohole array in Au layer reproduced from reference¹⁰³ under CC-BY^a license, c) Gold nano-mushroom architecture reproduced from reference¹⁰⁴ with permission from Springer Nature and d) Nanomesh-on-mirror architecture adapted from reference 102 with permission of the Royal Society of Chemistry. The scalebar length is 1 μm in b and d and 200 nm in c.

Coupled systems

^a <https://creativecommons.org/licenses/by/3.0/>

Recently, more complex architectures that combine the elements discussed above into three-dimensional plasmonic metamaterials, have gained attention. When plasmonic resonators with similar resonance frequencies are brought in close proximity, they start to influence each other via the overlapping electromagnetic field. These coupled systems exhibit different spectral features than the individual components, which have been described by a plasmon hybridization theory.¹⁰⁵ Among the architectures investigated are planar metal-insulator-metal structures, particle oligomers,^{106–108} core-shell particles, and metal-insulator-metal structures like nano-mushroom arrays,^{104,109} or nanomesh-on-metal approaches.¹¹⁰

Actively tunable plasmonic structures

Most plasmonic surface architectures are designed to be as static and as stable as possible in terms of geometry, chemistry, and optical properties. Recently, reversibly tunable plasmonic materials have been developed and found applications in miniaturized photonic circuits,¹¹¹ as well as sensors,^{112,113} forming the novel field of active plasmonics. The optical properties of the materials employed can be tuned by external parameters, including temperature, electromagnetic fields, and chemical reactions. The latest developments have been well summarized in a recent review by Jiang.¹¹⁴ In this work, plasmonic composite materials are pursued that integrate a thermoresponsive hydrogel as an active element.

In responsive hydrogels, a phase transition, associated with a substantial change in volume and density, can be induced in an aqueous environment by external factors like temperature¹¹⁵, pH,¹¹⁶ or ionic strength.¹¹⁷ The polymer networks can hold a large volume fraction of water in the swollen state, which is expelled upon the collapse of the polymer network during the phase transition. The volume change can be characterized by the swelling ratio $SR = V/V_{dry}$ given by the ratio of the hydrogel volume V over the volume in the dry state V_{dry} . Since the refractive index of water¹¹⁸ ($n_{H_2O} \approx 1.332$) is significantly smaller than the refractive index of typical hydrogel forming polymers ($n_p > 1.45$),¹¹⁹ the change in the swelling ratio can lead to a substantial change of optical properties. When such a material is integrated in a plasmonic surface architecture, as exemplary shown in Figure 8 for the hydrogel forming terpolymer poly(N-isopropylacrylamide) (pNIPAAm), strong modulation of the hydrogel refractive index occurs upon the phase transition from

the swollen state (with low refractive index) below the lower critical solution temperature (LCST) below 32°C to a collapsed state (with high refractive index) upon heating above the LCST.¹¹⁹

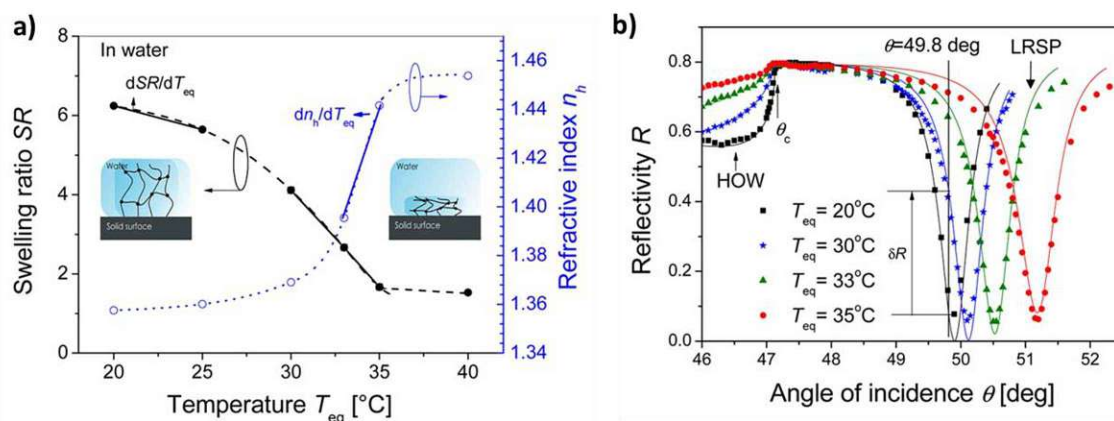


Figure 8 a) The phase transition of thermoresponsive pNIPAAm hydrogel from the hydrophilic state at low temperatures to the hydrophobic state at high temperatures is reflected as a sudden change in the swelling ratio (black line) and the refractive index (blue line). b) The change of material properties is observed as an SPR shift in angular spectroscopy. Adapted from reference 119 under a CC-BY license, Copyright © 2013 American Chemical Society

Moreover, the change of volume can be utilized to actively tune the distance between plasmonic resonators embedded in the gel and thus modulate the near-field coupling strength.¹¹³ It is also worth noting that the hydrophilic nature of hydrogels makes them an interesting candidate for antifouling surfaces³⁰ and the sparse 3D network can be functionalized with receptors, forming a high capacity binding matrix with good antifouling properties.^{34,119,120}

An interesting application of a responsive hydrogel in biosensors is as the binding matrix for fluorescence assays with plasmonic enhancement from LSPs at metallic nanoparticle arrays, as discussed in chapter 2.3. The sensitive area of the nanoparticles in such an array covers only a small fraction of the total surface area. To facilitate the effective analyte capture, the receptors can be immobilized in a hydrogel that covers a much larger volume in the swollen state and allows diffusion of the analyte and fluorescent labels. Upon collapse of the hydrogel cushion, the captured and labeled analyte is brought close to the particle surface to take advantage of the plasmonic enhancement of fluorescence during readout. The mechanisms behind the plasmon enhanced fluorescence are subject of the next chapter.

1.4. Fluorescence

Luminescence is an optical phenomenon associated with the emission of light from a substance in an electronically excited state and is divided into two categories, fluorescence, and phosphorescence, depending on the type of excited state. The term fluorescence is specifically used for the transition from the excited singlet S_1 state to the ground state S_0 .⁶¹ In the excited orbital, the electron carries the opposite spin of the electron in the ground orbital, the transition is thus allowed, and the lifetime of the excited state is thus in the order of nanoseconds. While fluorescence can be observed in a large variety of substances, from atoms to solids, specific biological^{121,122} and synthetic^{61,123} compounds have been discovered where fluorescence processes occur particularly efficiently. A comprehensive and well-written introduction to fluorescence for biomedical applications is given in the book of Lakowicz.⁶¹ Briefly, in fluorescent systems, electrons from the S_0 ground state are excited by photon absorption to the S_1 state. A schematic overview of the processes involved is shown in Figure 9. In most cases, the electron is not directly transferred to the S_1 ground state, but the molecule also experiences vibrational excitation. These vibrational excitations quickly decay by vibrational relaxation and internal conversion (IC) at timescales in the order of 10^{-14} s to 10^{-16} s.⁶¹ Similarly, the decay from the excited to the ground state is likely to end in a vibrationally excited state which rapidly decays to the ground state. These processes are observed as broadening of the absorption and emission lines and overall give rise to the Stokes shift observed between absorption and emission spectra. Competing with the radiative transition from the S_1 to the S_0 state are non-radiative decay processes and the inter system crossing (ISC) into an excited triplet state T_1 by spin inversion. The direct radiative transition from the T_1 to the S_0 state is forbidden and the lifetime thus is several orders of magnitude longer than the fluorescence lifetime. Molecules in the T_1 state thus don't participate in the fluorescence process anymore, reducing the number of active fluorophores. Furthermore, molecules in an excited state are more likely to undergo chemical reactions that can change the chemical structure and permanently disable fluorescence.¹²⁴ Together, these processes are observed as bleaching, the exponential decrease of fluorescence intensity under constant illumination. It is noteworthy, that the probability of undergoing a permanent transition to a nonfluorescent state is proportional to the time spent in the excited state and thus also proportional to the number of excitations a molecule experienced. Depending on the specific compound, an organic dye can yield 10^5 - 10^7 photons before bleaching.⁶¹

The fluorescence emission rate γ_r is proportional to the transition matrix element between the S_1 and S_0 state. Competing are, besides the intersystem crossing, also other nonradiative processes where the electron can lose energy. Common nonradiative processes include collisions with other molecules or the short-ranged metal-induced energy transfer.^{125,126} All nonradiative transitions to the ground state are subsumed under the term quenching.

The excitation from the S_0 to the S_1 state is characterized by the transition dipole moment.¹²⁵ While the excitation and emission probability are thus anisotropic and depending on the molecule orientation and polarization of the exciting light, the fluorescence lifetime is significantly larger than the rotational diffusion time of a molecule of this size, effectively decoupling the emission dipole orientation from the excitation. For free fluorophores in solution the emission is thus isotropic.¹²⁷ Modern linker chemistries for fluorescent labels are chosen such that the rotational diffusion is not restricted to prevent artifacts originating from the molecular orientation. For numerical simulation of fluorophores, this rotational diffusion must be considered.

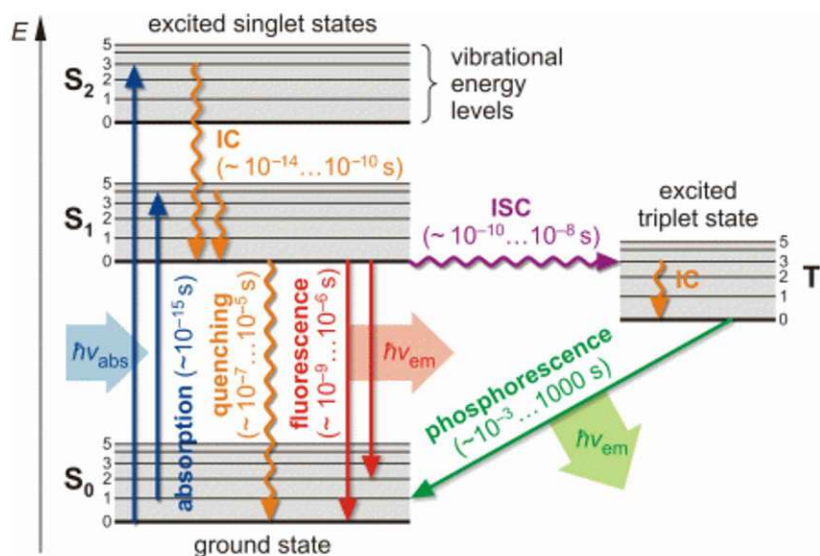


Figure 9 Jablonski diagram of excitation and decay processes in molecular fluorescence. (Figure by Steve Pawlizak, 2009.)

1.4.1. Fluorophores at Interfaces

Embedded in a homogeneous environment, the excitation and emission of fluorophores is characterized by the dipole character of the electronic transition. For most such molecules, this characteristic is smeared by the rapid Brownian rotation during the fluorescence lifetime, unless the motion of the molecule is restricted. In biosensor applications, however, the assays are frequently implemented on a solid substrate, placing fluorophores in the

proximity of an interface between two different media. In this case, the angular distribution of fluorescence emission can become highly anisotropic, as illustrated in Figure 10a. On the interface between two dielectric materials, for example, water ($n=1.33$) and BK7 glass ($n=1.5$), 72% of fluorescence is emitted towards the high refractive index material, particularly in the direction of the critical angle.¹²⁸

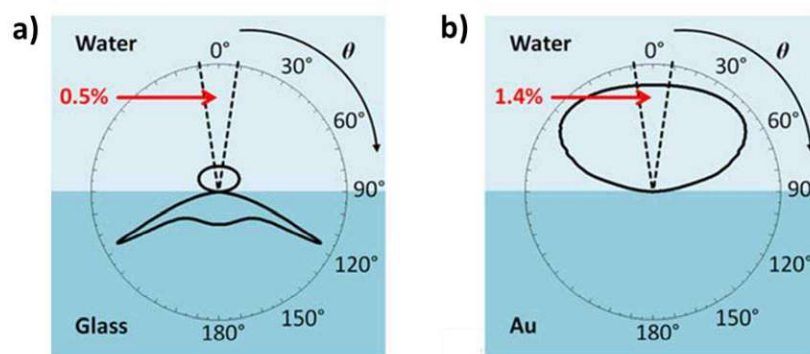


Figure 10 Cross section of averaged angular fluorescence intensity for a) a fluorophore on a water-glass interface and b) a water-gold interface. The collection cone for $NA=0.2$ is indicated as dashed line and the calculated collection efficiency is shown. Figure adapted from reference 129 with permission from Optica Publishing Group.

On a metal-dielectric interface, the fluorophore is affected by the surface in several ways: First, the metallic surface acts as a mirror, reflecting the emission from the interface, as indicated in Figure 10b. Furthermore, an excitation beam impinging from the dielectric half-space is also reflected at the surface, causing interference between the incident and the reflected beam above the surface. Depending on the distance to the surface, the emitter can thus be exposed to increased or decreased field intensity within the interference field. Fluorescence emission is also subject to interference and the brightness shows oscillating dependence on the surface distance.¹²⁵ These interference effects have typical length scales of a quarter wavelength; for optical frequencies this means distances to the surface of 100 nm – 200 nm. Closer to the surface, the fluorescence emission is quenched by a non-radiative electronic energy transfer to the metallic surface.¹³⁰ The efficiency of this metal-energy transfer drops with d^{-3} perpendicular distance d to the interface and has a characteristic length in the order of 10 nm - 50 nm.¹³¹ Part of the energy is transferred to oscillations in the electron density of the metal, plasmons, where it is dissipated to heat.

The interaction with plasmonic excitations is, however, not only detrimental but can rather lead to substantial gains in observed fluorescence intensity by orders of magnitude and improved photostability of the emitter.

1.4.2. Plasmon Enhanced Fluorescence - PEF

For sensor applications, the observed fluorescence intensity due to capturing of a target analyte at the detector of the sensor device is of utmost importance. Most devices use a form

of microscope optics to illuminate the sample and efficiently collect the emitted photons. The sensitivity of the sensor devices is limited by detector and electronics noise but also by the leakage of excitation light through the optical filters as well as fluorescence originating from other sources than the dye molecules, for example by autofluorescence of polymers used as substrates or cartridge materials. Plasmon enhanced fluorescence (PEF), an effect that occurs due to the interaction of a fluorophore with plasmonic modes on a metal-dielectric interface, can help to improve the limit of detection of a fluorescence assay by orders of magnitude by increasing the detected fluorescence emitter brightness while simultaneously reducing fluorescence background by selectively enhancing fluorescence only in the evanescent field of a SPP. The observed brightness of a fluorophore is determined by its excitation rate, the quantum yield, and the collection efficiency of the optical system for the emitted radiation. Surface plasmon modes on a metal-dielectric interface can improve all three of these parameters.¹³²

Excitation rate γ_{ex} : The excitation rate is proportional to the local field intensity $\gamma_{ex} \propto |\vec{E}|^2$. The resonant plasmonic modes strongly confine the field intensity in an exponentially decaying evanescent field, with characteristic penetration depth $d_p \approx 100 \text{ nm}$.¹³³ The achievable enhancement is determined by the dampening of the plasmon mode and is thus strongly material dependent.

Quantum yield η : The quantum yield η of a fluorophore is given by the ratio of the radiative decay rate γ_r over the total decay rate to the ground state $\eta = \frac{\gamma_r}{\gamma_r + \gamma_{nr}}$, including competing nonradiative processes γ_{nr} that reduce the quantum yield. Close to metallic structures, the radiative decay rate can be strongly increased by the increased local density of optical states.^{132,134} This short-range metal-energy transfer is also observed as a reduction in fluorescence lifetime.¹²⁶ The energy is partially transferred to plasmonic excitations, which in turn can be coupled out and observed, overall increasing observed brightness. It is worth noting that the reduced fluorescence lifetime also improves the ratio between radiative decays and intersystem crossing events or photochemical reactions that lead to photobleaching. The reduced lifetime is thus associated with reduced bleaching and hence offers an overall increased light budget.¹³⁵

Collection efficiency η_c : Due to geometric constraints, only a fraction of the emitted photons will be collected by the optical system and reach a detector. The geometric

collection efficiency for isotropic emission depends on the numerical aperture $NA = \sin \theta$, where θ is half the angular aperture and is given by $\gamma_c = 1 - \frac{1}{2} \cos \theta$. This means, that for an objective with $NA=0.2$, a common widefield optics, also used in some of the sensor systems presented in this work, only 1% of the photons isotropically emitted by a point source will reach the detector. Plasmon-mediated emission allows control of the angular distribution of the fluorescence light^{12,127} and consequently the improvement of the collection efficiency.

The overall improvement of PEF can be described by the enhancement factor EF:¹³²

$$EF = \frac{I}{I_0} \approx \frac{|E|^2}{|E_0|^2} \cdot \frac{\eta}{\eta_0} \cdot \frac{\eta_c}{\eta_{c,0}}. \quad (10)$$

The first factor, the increased electrical field intensity, is typically the most significant contribution. For a flat gold surface in contact with water, the field enhancement by SPP at a distance $d = 15 \text{ nm}$ above the surface depends on the wavelength and ranges from $\frac{|E^2|}{|E_0^2|} \sim 10$ at $\lambda = 550 \text{ nm}$ to $\frac{|E^2|}{|E_0^2|} \sim 85$ for $\lambda = 900 \text{ nm}$.⁶⁰ Much higher field intensity enhancement up to 1340x has been reported for hotspots formed in narrow gaps between nanoparticles,¹³⁶ or particles, and perforated metal layers.^{137,138} However, structures with such high field enhancement factors in narrow gaps usually don't provide equally enhanced fluorescence signal due to quenching. These coupled surface architectures are furthermore very sensitive to geometrical properties and usually prepared by slow and cost-demanding fabrication technologies like electron beam lithography, which limits practical applications.

1.5. Plasmonic Biosensors and Plasmon-Enhanced Spectroscopy

The strong electrical field enhancement generated by plasmonic surfaces has been used to enhance the performance of numerous optical spectroscopy applications, including surface enhanced infrared spectroscopy¹³⁹ (SEIRA), surface enhanced Raman spectroscopy¹⁴⁰ (SERS), plasmon enhanced fluorescence⁶⁰ and SPR biosensors.¹⁴¹

Refractometric SPR biosensors have been implemented using numerous modalities tailored for the specific needs of the application. Sensitive to the change of refractive index due to accumulation of mass on the surface, a plethora of established biorecognition elements^{142,143} can be used. Instruments based on propagating SPP, allow the direct and label-free observation of affinity binding kinetics on the sensor surface. Mostly using the traditional Kretschmann configuration, such systems have successfully been commercialized¹⁴⁴⁻¹⁴⁶ and offer a resolution of $\sim 10^{-7}$ RIU,⁵² corresponding to approximately 1 pg mm⁻² with limited multiplexing capabilities (up to 4 channels). Diffractive coupling to propagating SPP or arrays of nanoparticles supporting LSPs allows the use of simplified readers with similar sensitivity.^{147,148} Recent advances in substrate architectures and detector technologies allow to implement SPR imaging modalities with high spatial and refractometric resolution¹⁴⁹, that have been used to detect proteins,^{150,151} nucleic acids¹⁵² or whole bacteria¹⁵³ in a microarray format and even to study cell surface interaction.¹⁵⁴

For the detection of small analytes or very low concentrations of larger analytes, the sensitivity of refractometric sensors can be insufficient. By using a fluorescent assay, combined with the plasmonic enhancement of the fluorescence signal, direct detection assays can be implemented that allow omitting time-intensive amplification and purification steps. Numerous approaches to PEF-based assays have been presented, ranging from the introduction of a fluorescence label in assays probed by propagating SPP in Kretschmann configuration,^{155,156} fluorescence enhancement in the near-field of LSP supported by nanoparticles,^{157,158} and on nanostructured surfaces.^{134,137,159} Integration of fluorescence into actively tunable materials has been explored^{160,161} and the approach has recently been expanded for biosensor applications as a mechanical concentration step.³⁴

Despite all the promising results obtained, PEF has not found its way into commercial application yet. This can, in part, be attributed to the manufacturing technologies employed in substrate fabrication. In scientific research, precise but slow technologies like EBL are preferred for their versatility and high reproducibility. Recently, great efforts are being

made to develop surface architectures compatible with scalable manufacturing technology. Self-organizing bottom-up approaches, most notably colloidal lithography,^{162,163} are promising candidates to pattern large areas. Furthermore, top-down approaches are pursued, particularly the fast and reliable replication of a master structure by nanoimprint lithography (NIL)^{164,165} appears promising.

1.6. Research Aims

Research and development of tools for the sensitive and rapid analysis of chemical and biological species are gaining increasing momentum in order to establish a basis for the emerging field of information-driven and personalized medicine. Among others, we witnessed that rapid tests for harmful pathogens can tremendously impact the lives of billions of people. The current COVID19 pandemic made the dependence of modern society on reliable and highly sensitive sensors capable of detecting trace amounts of analytes very obvious. Recently, such performance characteristics are available only in part and the required sensitivity is dominantly achieved through biochemical amplification strategies, for example, polymerase chain and other enzymatic reactions. However, the use of these methods is associated with the need for extensive preparation steps, taking a considerable amount of time, and can only be performed in specialized laboratories. In contrast, alternative faster direct detection assays are pursued to overcome the need for enzymatic amplification. However, they often lack sensitivity due to weak output signals with respect to the background. The majority of both enzymatic and non-enzymatic sensor technologies take advantage of optical readout based on fluorescence. Fluorescence labeling has been established as an effective means for additional optical amplification, as a single fluorophore can emit $10^5 - 10^6$ photons before bleaching. Consequently, advanced optical methods are required to obtain the best results with the limited light budget. In the field of fluorescence-based detection of assays, that are implemented on the solid surface of sensor chips, various light management strategies are possible by using plasmonic nanostructures. In particular, they allow confining the electromagnetic field intensity to selectively probe captured target analyte species. In general, plasmonic nanostructures provide facile means for manipulating the fluorescence excitation and emission events and thus increasing output optical signal by several orders of magnitude while at the same time reducing background noise originating from the bulk liquid or other surfaces in the optical path.

This work aims at developing novel and practical optical materials that support multimodal optical biosensor concepts holding the potential to advance the analytical performance of optical sensor technologies. To take full advantage of the developed interface architectures, dedicated optical readers are developed to facilitate effective coupling with the tailored plasmonic resonances in the large field of view necessary for multiplexing and efficient capture of target species. In the area of fluorescence detection, there are pursued plasmonic

nanostructures providing high collection efficiency for emitted light that is selectively excited specifically at the biointerface. Going beyond fluorescence spectroscopy, the plasmonic resonances themselves can respond to optical changes due to affinity reactions on the sensor surface, opening door for label-free biosensors. While many nanophotonic surfaces have been developed during the last two decades, we witnessed that only few have found their way into practical applications. This can be largely attributed to the complex manufacturing technologies required to make the structures. Here, particular focus is put on the scalability of developed architectures with mass manufacturing technology. Low aspect ratio geometries are pursued that exhibit tolerance to minor defects introduced in the manufacturing process to facilitate compatibility with high volume manufacturing methods like roll-to-roll processes. The developed optical instruments are relying on configurations that are derived from standard instruments supporting optical microscopy and spectroscopy, assuring possible compatibility. Overall, the work aims to push forward the sensitivity of fluorescence assays and enable observation of affinity binding processes occurring for low concentrations of analytes. Furthermore, multimodal sensor approaches are pursued by combining different readout principles at the same interface to gain additional research insights and potentially expand the functionalities of currently used analytical tools.

The work is organized in three sections:

1. Exploration of nanophotonic 2D materials by numerical simulations, preparation at lab scale, and characterization. In particular, metallic nanostructures are combined with thermo-responsive polymers in actively tunable functional optical components. The temperature-dependent swelling of the used polymer networks allows for controlled structure geometry and affinity reactions occurring inside. Periodic arrays of nanoparticles, nanomeshes, holographic gratings and combinations of such systems are explored. Promising candidates are tailored for the readout of biochemical assays and biosensors derived from such structures are studied.
2. Development of new instruments that take advantage of the optical properties of the developed plasmonic surface architectures. An epifluorescence reader is devised that allows the simultaneous observation of affinity binding by monitoring the detuning of optical features of a nanophotonic surface upon analyte binding as well

as the observation of plasmon enhanced fluorescence. Furthermore, label-free surface plasmon resonance modality is integrated with a gate-modified, electrolyte-gated field-effect transistor. By employing these two different transducer modalities at the same surface, the instrument allows simultaneous, and time-resolved observation of mass change and reorganization of polymer assemblies at the sensor surface through parallel monitoring of optical and electronic signals.

3. The final section addresses the use of light management and plasmon-enhanced fluorescence, to push forward the sensitivity of fluorescence assays. Making use of the distance-dependent fluorophore quenching at metallic surfaces, the conformational change of a hairpin aptamer assay is translated to a change in fluorescence brightness through energy transfer, allowing sensitive, fast, reversible, and continuous monitoring of low molecular weight analytes. A multiresonant plasmonic substrate is developed that provides excellent fluorescence enhancement by taking advantage of plasmonic excitation and plasmon mediated emission of fluorescence, while maintaining compatibility with scaled-up industrial manufacturing processes. Together with a newly developed imaging reader system, this approach offers a route for highly multiplexed observation of binding kinetics on a large surface area with a limit of detection at femtomolar concentrations.

1.7. Methodology

The projects presented in this work are typically organized in three main tasks:

- Design and fabrication of a plasmonic substrate
- Design, implementation, or modification of an optical reader
- Design and optimization of the biochemical assay for the detection of an analyte.

The focus of this thesis lies on the first two steps, as the development of the biochemical assays was covered mainly by specialized partners within the collaborative projects.

The specific methods with detailed information and concrete values used within the different projects are discussed in the Methods sections of the respective publication in chapter 2. Here, a broad overview of the methods used and the considerations behind them will be given.

For the development of new nanophotonic surfaces, an iterative approach has been used. Initial numerical simulations are used to gain a fundamental understanding of the design parameters affecting the optical properties, and the idealized geometrical parameters are identified. Several iterations of numerical simulations, nanofabrication, and characterization have been carried out to prepare surfaces with the desired optical properties.

This is necessary, as the fabrication of plasmonic nanostructures requires a sequence of processing steps, that introduce small artifacts and deviations from the idealized structure. The obtained surface is then characterized by imaging and morphological methods, particularly atomic force microscopy (AFM) and scanning electron microscopy (SEM) after important process steps. In the end, the optical properties of the final structure are determined. The observed deviation of the morphological properties and the resulting optical spectra are then taken into consideration to iteratively improve the numerical simulations.

It is worth noting that for surfaces architectures with narrow plasmonic resonances like propagating SPPs, the chemical functionalization will change the optical properties and must be considered already in the design phase. Further dynamic effects, as swelling of polymers upon exposure to a liquid over extended periods of time, during the assay or functionalization can introduce artifacts that need to be identified and compensated for by

blank and reference measurements. Moreover, the mechanical stability, particularly the adhesion between layers of a surface architecture, is an important factor. The sensor surfaces are typically exposed to several chemical functionalization and washing steps during the assembly of the biointerface before being integrated into a microfluidic system. This process involves substantial mechanical stress on the surface and frequently also exposure to several different solvents that potentially degrade the interface before the measurement even starts.

1.7.1. Numerical Simulations

The preparation and characterization of nanoarchitectures in the laboratory is a time-consuming and expensive endeavor, with numerous process parameters influencing the final shape and homogeneity of the prepared structures and challenges in terms of reproducibility. To optimize the architectures, numerical simulations are an excellent tool to quickly study the dependence of observable optical properties on the geometrical properties of the nanostructure. The finite difference-time domain (FDTD) method¹⁶⁶ is particularly well suited for the numerical solving of the Maxwell equations, the classical formulation of the equations of the electromagnetic field. In this approach, the electric field \vec{E} and magnetic field \vec{H} are solved sequentially on interleaved rectangular grids, which allow the efficient calculation of the rotor operators in the Maxwell equations. In this work, the FDTD implementation of Lumerical Inc in the software package `fdtd-solutions` has been used. A good and detailed explanation of the method is given in the book “Computational Electrodynamics: The Finite-Difference Time-Domain Method” by A. Tavis and R. Loudon.¹⁶⁶

For the study of photonic materials, the spectral properties of the structures are of great interest, whereas the solver is operating in the time domain. This is addressed using a pulsed source, with the pulse comprised of the frequencies of interest. The frequency-dependent field distribution can then be obtained by the Fourier transform of the results in the time domain. A challenge for numerical methods is the frequency dependence of the properties of optical materials. While the dielectric materials used in this work show only a small variation of their refractive index over the wavelength range observed, metals show strong dispersion. To efficiently implement the frequency-dependent permittivity in the numeric solutions, experimental data is fit by analytical functions. This can lead to small deviations of the simulated behavior, particularly near resonant transitions in the material.

FDTD is a discrete numerical method that operates on regular square meshes. To ensure numerical stability, the computational mesh size must be chosen according to the field gradients occurring in the simulation. Particularly for LSP supported on small nanoparticles, fine mesh size down to 1 nm may be required to avoid computational artifacts. With strong gradients and particularly with strongly coupled systems, convergence of the simulation results becomes a major challenge.

For the study of nanostructured surfaces under external illumination, the simulation volume is chosen to reflect periodicity and symmetries of the studied geometry and enclosed with boundaries. In reflection and transmission direction, the simulation volume is constrained with perfectly matched layer (PML) boundary conditions. These boundary conditions comprise several layers with gradually changing optical properties and particularly absorption, designed to minimize reflections at the interface. The choice of in-plane boundary conditions is strongly dependent on the illumination and symmetries of the architecture. If a periodic unit cell can be identified, periodic boundary conditions may be applied for normal illumination, whereas Bloch boundary conditions take into consideration general angles of incidence, however at the expense of increased computing time.

For non-periodic architectures, the simulation volume is chosen sufficiently large to encompass at least one plasmon propagation length and is enclosed with PML boundary conditions on all sides. Such simulations require striking a balance between the simulation volume and the resolution, posing a challenge for strongly coupled structures with small geometric features. The convergence of the simulations is determined by monitoring the total energy contained within the simulation volume. A steady decrease of energy is observed when the pulse propagates through the simulation volume and resonances are dampened by the metallic absorption. However, numerical instabilities due to insufficient mesh resolution at strong gradients or not suitable boundary conditions can cause the simulation to diverge. Convergence tests, specifically the independence of the computation results from the specific mesh parameter, are most important.

To investigate the electromagnetic field, 2D monitors, essentially 2-dimensional slices, are placed in the simulation volume to monitor the transmitted and reflected field as well as cross sections of the near field within the architecture. After recording the field values over time, the near field distribution is obtained by a Fourier transform.

As a propagating wave is completely defined by its cross section, the angular distribution of light in any distance of the surface can be obtained by recording the electromagnetic field close to the surface and applying a far field projection.

The interaction of a fluorophore with a plasmonic surface is too complex to be investigated by a single simulation. The dye molecule can, for the simulation of the electromagnetic interaction, be well described by an electrical dipole. However, due to the fast thermally driven rotation of the molecule in a liquid environment, this dipole characteristic is smeared, and isotropic absorption and emission are observed. In numerical simulations, this is typically implemented by conducting separate simulations for linearly independent orientations of the dipole and averaging the obtained results, particularly for the dipole emission. The averaged relative excitation rate $\gamma_{ex} = \langle |\vec{E} \cdot \vec{\mu}| \rangle$, where \vec{E} denotes the electrical field strength and $\vec{\mu}$ is the dipole moment, can be obtained analytically by applying a geometric weighting factor to the calculated field magnitude.

$$\gamma_{ex} = \langle |\vec{E} \cdot \vec{\mu}| \rangle = \int_0^{\pi} |\vec{E}| |\vec{\mu}| \cos(\theta) d\theta = \frac{2}{\pi} |\vec{E}| |\vec{\mu}| \quad (11)$$

As previously discussed in section 1.4.1, the spontaneous emission rate of a fluorophore depends on the local density of states, which can be substantially increased when the fluorophore is placed within a resonator, known as the Purcell effect. In the used implementation of FDTD, this is already incorporated in the calculation of the radiated dipole power.

1.7.2. Nanostructure Preparation and Characterization

The fabrication of nanoscale structures with precision and reproducibility is a challenge that has been addressed by several methods with different advantages and disadvantages. For most architectures, multiple additive and erosive processes are sequentially employed to obtain the desired result. Among the most common additive techniques are the deposition of polymers by spin coating and the deposition of metal films by evaporation. Polymer layers are frequently used as resist materials for further processing steps, which are structured by a variety of lithography techniques like photolithography, electron beam lithography (EBL), or laser interference lithography (LIL). Using the masks, underlying layers can be structured with subtractive processes like wet & dry etching. It is further

possible to structure materials directly using a focused ion beam (FIB). While FIB and EBL provide excellent control over the written pattern, these processes require expensive machinery and suffer from slow writing speed. Lithography techniques allow the processing of larger areas at the same time. Not strictly fitting to these categories is colloidal lithography, where small spherical particles are used as shadow mask for the deposition of metallic films.¹⁶⁷ The density of particles can be controlled up to the formation of a dense monolayer with a high degree of short-distance ordering. The following techniques have been employed throughout the projects included in this work.

Thermal vapor deposition: The key to sensitive sensors and high Q-factor photonic surfaces is a metallic layer with low dampening. In a thermal evaporation process, a metal is heated in a vacuum chamber to the sublimation or boiling point. The substrates to be coated are mounted in a way that the metal vapor can condense on the substrate surface. Most metals tend to build isolated islands before complete surface coverage is achieved and continuous layers are formed. For gold, the material used in the projects presented here, continuous layers are formed when the gold film reaches a thickness of approximately 20 nm.¹⁶⁸ Adhesion-promoting layers, like a thin 2 nm layer of chromium or chemical functionalization, are used when the adhesion between metal and substrates is found not sufficient to prevent delamination.

Laser interference lithography (LIL): In LIL, photosensitive polymers are exposed to the interference pattern of two or more laser beams. By expanding the beams, large areas can be structured with a highly homogeneous grating pattern. In this work, a lithography setup in a Lloyd's mirror configuration, schematically shown in Figure 11a has been used. In this configuration, a high-quality mirror is placed at a 90° angle with respect to the photoresist-coated substrate. The expanded beam is then made impinging on both the substrate and the mirror, which reflects it onto the substrate as well to form a stable interference pattern. The grating period Λ is controlled by the angle of incidence θ relative to the sample surface normal: $2 \Lambda \sin\theta = \lambda$. The intensity profile exhibits a \sin^2 characteristic for two-beam lithography. Using multiple sequential exposures, a more complex pattern can be achieved. Higher contrast can be realized when multiple beams are used in the same exposure.¹⁶⁹

Nanoimprint lithography (NIL): NIL has proven to be an invaluable tool to quickly reproduce many identical copies of a nanostructured surface. It formed the basis of all grating-based projects discussed here and was successfully employed to reproduce highly

sensitive systems like the Bragg scattered plasmon architectures presented in chapter 2.4. In imprinting processes, a stamp is embossed in a soft polymer, which is subsequently cured to a solid state. One of the most commonly used processes involves UV curable polymers, that are spun on a carrier substrate, contacted with a pattern-carrying stamp, and cured,¹⁷⁰ as is illustrated in Figure 11b. On an industrial scale, thermal NIL or hot embossing is also widely used, where the imprint substrate is heated above the glass transition temperature and before the stamp is pressed on. Upon cooling, the pattern remains in the substrate. While highly reproducible, the processes involve substantial mechanical forces during demolding and thus impose some constraints on the achievable aspect ratio of the copied structure.

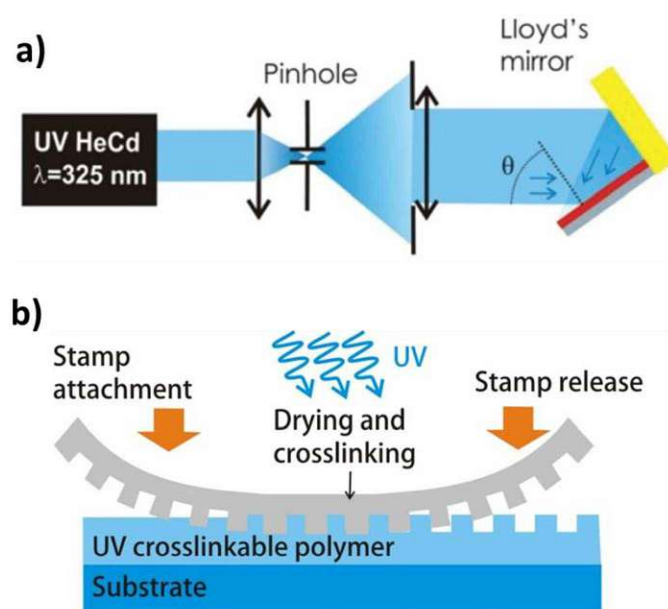


Figure 11 Schematic illustration of a) a laser interference lithography device in Lloyd's mirror configuration, reproduced from reference¹⁷¹ with permission from the Royal Society of Chemistry and b) a UV-NIL process. (Graphic by Jakub Dostalek)

Optical spectroscopy:

The optical properties of the nanophotonic surfaces were characterized using optical spectroscopy techniques in the visible and near-infrared range (400 nm to 1000 nm). Specifically, specular reflectivity and transmission were investigated using in-house developed optical instruments with commercial spectrometers (Andor Shamrock 303i and Ocean Optics HR4000) as detectors. To obtain the dispersion characteristics, an in-house developed angular resolved reflectivity setup was used, which was previously described by Bauch.¹⁷² Briefly, the system consists of a rotating sample holder stage and a coaxially

1.7. Methodology

rotating detector arm in a $\theta - 2\theta$ configuration with respect to the incident beam. The system allows to investigate the specular reflectivity with angles of incidence ranging from 0.6° to almost 90° . Furthermore, it allows to study transmission at angles ranging from 0° to 40° . The sample holder stage can be equipped with a temperature-controlled microfluidic flow cell.

The topological properties were investigated using atomic force microscopy (AFM) and scanning electron microscopy (SEM).

2. Results

Direct detection of pathogens and biomarkers requires high sensitivity, preferably without preamplification that requires time and considerable biochemical preparation efforts. In this work, several biosensor architectures for the direct detection and continuous monitoring of biomarkers at clinically relevant concentrations are presented. In particular, the focus lies on multimodal biosensors with surface plasmon based transducers. Plasmonic transducers allow the observation of biochemical reactions on a metallic surface by quantifying the accumulated surface mass. Furthermore, the confined electromagnetic field at the surface strongly enhances the observed intensity of fluorescent dye molecules by amplifying the excitation rate by plasmon enhanced fluorescence. Coupling with plasmon modes also allows to engineer the otherwise isotropic emission profile of a fluorophore and such improve the collection efficiency of the optical system, thus improving the LoD.

Optical biosensors are integrated devices with a functionalized biointerface, specific to the target analyte, an optical transducer and a read-out system. The development of such devices is a highly interdisciplinary process that in this work has been carried out as collaborative effort between biotechnologists, chemists and physicists. This work focusses on the development of novel transducer architectures and corresponding readout modalities. It is organized in three sections:

- The development of 2D nanophotonic surfaces suitable as plasmonic sensor interface
- The development of new instruments taking advantage of the optical properties of the plasmonic interfaces.
- Pushing forward the sensitivity of fluorescence assays by utilizing plasmonic light management and plasmon enhanced fluorescence.

The results are summarized in eight reports, focusing first on the development of plasmonic 2D materials as sensor interface. Starting from previously reported nanopillar arrays,^{137,173,174} several novel architectures were investigated: Chapter 2.1 discusses the optical properties of a nanomesh-on-mirror architecture, prepared by colloidal lithography. Chapter 2.2 studies a nanohole array coupled with a nanoparticle array

embedded in a responsive hydrogel cushion. This architecture holds the potential to serve as microfluidic valve that efficiently captures target analytes at sensitive plasmonic hot spots. A disadvantage of the architectures mentioned up to now are high requirements to the quality of the fabricated nanostructures. Particularly at industrial-scale roll-to-roll processes, the production of high aspect ratio geometries and vertical sidewalls were reported problematic by cooperation partners. Thus, holographic gratings were investigated as architecture with low aspect ratio, high flexibility and good optical coupling efficiency. Such gratings, structured with multiple gratings to generate plasmonic resonances at multiple wavelengths, have been employed successfully in chapter 2.7 for the detection of extracellular vesicles and in chapter 2.8 for the sensitive detection of fluorescent immunoassays. Chapter 2.4 reports on a novel concept that allows biosensing on metallic films structured with holographic gratings with backside excitation, allowing the use of such surfaces also for sensing in highly scattering media.

New instruments have been developed to take advantage of the optical properties of these 2D materials. An epifluorescence reader was adopted for the simultaneous observation of fluorescence and surface mass accumulation by grating plasmonics in chapter 2.7. Furthermore, chapter 2.5 reports on a new bimodal instrument, combining plasmonic sensing with a graphene field effect transistor, enabling the simultaneous observation of surface mass accumulation and change of electrical properties on the same interface, which has been used to gain further insight in polyelectrolyte layer assembly.

Finally, the interaction of fluorophores with a plasmonic surface has been investigated and utilized for the implementation of continuous monitoring of ATP using a hairpin aptamer, which is reported in 2.6. A multidiffractive holographic grating architecture, with resonances tailored to the excitation and emission of fluorescent dyes, and the plasmonic enhancement of their observed intensity, have been used in a custom-built fluorescence microscope with large field of view and collection efficiency, as reported in chapter 2.8 .

2.1. Surface Plasmon Modes of Nanomesh-on-Mirror Nanocavities prepared by Nanosphere Lithography

The following publication is reprinted with the permission of the Royal Society of Chemistry.

Christian Stelling, Stefan Fossati, Jakub Dostalek, and Markus Retsch Surface plasmon modes of nanomesh-on-mirror nanocavities prepared by nanosphere lithography. *Nanoscale* 10, 17983–17989 (2018). <https://doi.org/10.1039/c8nr05499a>

Copyright © The Royal Society of Chemistry 2018

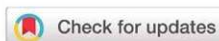
Advanced nanophotonic materials with complex optical properties have found numerous applications within sensors,⁸² photonic color filters,¹⁷⁵ nanooptics,⁷⁷ or photonic circuits.¹³³ For these applications, accurate design of optical properties via controlled characteristics of supported optical modes is required. Depending on the purpose, resonance wavelength, dispersive properties, and field localization need to be optimized. As optimization by manufacturing iterations is time-consuming, tedious, and expensive, numerical simulations are employed to study optical properties of nanophotonic materials before experimental implementation. The geometries studied numerically, are typically idealized versions of the experimental structures, constrained by computing power. With increasing volume and resolution, demands on the underlying computing system grow by the third power. This becomes especially challenging for structures with symmetries not reflected in the solver algorithm or periodic unit cells. This chapter reports on a metal-insulator-metal (MIM) architecture consisting of a hexagonal gold nanomesh, prepared by colloidal lithography that was transferred onto a PMMA spacer layer on top of a continuous metal layer. The resulting structure showed a complex spectrum of supported surface plasmon modes under tilted illumination, exhibiting dispersive and nondispersive character that degenerate under normal illumination. Using numerical simulations, the nature of the observed optical modes was identified. The observed dips in the far field reflectivity were attributed to two plasmonic modes, on the surface and in the gap. It was found that the

2.1. Surface Plasmon Modes of Nanomesh-on-Mirror Nanocavities prepared by Nanosphere Lithography

optical properties of the structure could be attributed to only diffraction coupling and Bragg-scattering of those two modes.

Christian Stelling carried out the experimental part of this study, prepared and characterized all the MIM structures under the supervision of Markus Retsch. Stefan Fossati performed the numerical simulations of the MIM structures and analysis of the optical properties and corresponding parts of the manuscript under the supervision of Jakub Dostalek.

Supporting information to this article is included in the appendix, section 5.1.



Surface plasmon modes of nanomesh-on-mirror nanocavities prepared by nanosphere lithography†

Cite this: *Nanoscale*, 2018, **10**, 17983

Christian Stelling,^a Stefan Fossati,^b Jakub Dostalek^b *^b and Markus Retsch^a *^a

Metal–insulator–metal (MIM) structures show great potential for numerous photonic applications due to their ability to confine light energy to volumes with deeply sub-wavelength dimensions. Here, MIM structures comprising hexagonal gold nanohole arrays were prepared by nanosphere lithography. Angle-resolved UV-vis-NIR spectroscopy revealed a series of narrow, dispersive and non-dispersive modes, which were attributed to the excitation of surface plasmon polariton (SPP) modes. Applying finite-difference time-domain (FDTD) simulations and analytical diffraction phase-matching theory all resonances can be ascribed to only two SPP modes traveling at the outer gold surface and in the gap layer sandwiched between two metal films. Metamaterial resonances, as reported in the literature for similar structures, are not needed to fully explain the reflectance spectra. Bragg scattering of the symmetric gap SPP mode results in a gap resonance, which is insensitive to the angle of incidence over a broad angular range. The spectral position of this flat band can be controlled by tuning the grating period of the nanohole array as well as the thickness and the refractive index of the dielectric gap.

Received 8th July 2018,
Accepted 11th September 2018

DOI: 10.1039/c8nr05499a

rsc.li/nanoscale

Introduction

Metallic nanohole arrays have been subject to extensive research after the seminal discovery of their extraordinary optical transmission.¹ They exhibit exceptional optical properties that are associated with the excitation of surface plasmon polariton (SPP) as well as localized surface plasmon (LSP) modes. As a consequence, metal nanohole arrays have been implemented into optical devices that serve as optical sensors,² color filters³ or transparent conducting electrodes.^{4–6}

When placed near an unperforated metal film, the arrays of nanoholes allow for the coupling of light to a metal–insulator–metal (MIM) structure. Such architecture exhibits rich characteristics including near perfect absorption^{7–9} and coupling to magnetic resonances, similar to that found for nanoparticle arrays.^{10,11} Near perfect absorbers were realized at visible frequencies^{7,8} and for the near-infrared part of the spectrum.⁹ The optical response of the perforated MIM structure is often

assigned to the excitation of Fabry–Pérot resonances in the tri-layer structures^{12,13} as well as to the resonant excitation of coupled SPP modes located at the opposite metal/dielectric interfaces.¹⁴

Due to their relatively simple structure, perforated MIM-type metasurfaces can be readily prepared *via* lithographic methods.^{8,10} Thereby, the optical properties are mainly defined by the precisely tuned structure of the material. Top-down lithographic processes such as e-beam lithography or focused-ion-beam milling give structural control on the nanometer range, thus being capable of fabricating metamaterials for wavelengths down to the visible spectrum.¹⁴ Nevertheless, for the sake of large-scale production, much effort is put into the development of solution-processed techniques, which capitalize on self-assembly methods.¹⁵ Nanohole arrays coupled with thin metal films were, therefore, prepared using nanosphere lithography (NSL).¹⁶ The wavelength of the primary resonance satisfied both the grating equation of the nanohole array and the Fabry–Pérot condition, thus showing a strong dependence on the distance between the nanohole array and the metal film.¹³ Closely connected are nanohole–dielectric–nanohole structures, which equally show the existence of gap modes.^{17–19}

Here we present a full and comprehensive understanding of a MIM structure, which is prepared by a facile and scalable implementation of NSL. The MIM architecture comprises a highly ordered nanohole array separated from a continuous gold film by a thin polymer layer. Using angle-resolved UV-vis-NIR spectroscopy, we were able to fully assign the rich plasmonic response of the resulting nanocavity arrays to diffraction

^aDepartment of Chemistry, University of Bayreuth, 95447 Bayreuth, Germany. E-mail: Retsch@uni-bayreuth.de

^bBiosensor Technologies, AIT-Austrian Institute of Technology GmbH, Konrad-Lorenz-Strasse 24, 3430 Tulln, Austria. E-mail: Jakub.Dostalek@ait.ac.at

† Electronic supplementary information (ESI) available: Optical microscopy images, UV-vis-NIR spectra of isolated metal nanohole array, UV-vis-NIR spectra of MIM structures with varying mirror thickness, angle-resolved UV-vis-NIR spectra of MIM structures with distinct insulator thickness and period, analytically derived dispersion curves of the SPP modes, AFM analysis of the plasma treated MIM structure, FDTD geometry, FDTD convergence test. See DOI: 10.1039/c8nr05499a

coupling to only two SPP modes. We explored the structure–property relationship concerning the gap size and period of the nanohole arrays in detail and identified rules to prepare structures with remarkably narrow resonances exhibiting high absorption efficiency.

Results and discussion

The preparation of the MIM structures starts with the fabrication of gold nanohole arrays on a sacrificial layer *via* NSL (Fig. 1a). Subsequently, the nanohole arrays were transferred onto the target substrate comprising the readily prepared gap layer [poly(methyl methacrylate) (PMMA)] on top of a continuous gold film, following the recently published, interface-mediated method.¹⁹ The process utilized in this paper allowed for a fast and modular production of metasurface areas at square centimeter scale with highly uniform and reproducible optical properties.²⁰ However, techniques that allow the preparation of wafer-scale and larger sample areas are readily available.^{21,22} The homogeneity of the samples is restricted by point defects and grain boundaries within the monolayer but is highly uniform regarding the particle–particle spacing and the defect density. In Fig. 1b the definition of the geometrical parameters of the assembled structures is illustrated. The lattice period p and the hole diameter d of the gold nanohole arrays are determined by the initial particle diameter and the particle diameter after plasma etching, respectively. The thickness of the bottom gold layer t_{gold} , the one of the PMMA gap layer t_{gap} and the thickness of gold film with nanohole arrays were controlled upon the deposition process. An SEM image of a typical sample is shown in Fig. 1c.

In order to characterize the optical properties of the prepared MIM nanostructures, a series of reflectance measurements were carried out for varied angles of incidence and wavelengths in the visible and near-infrared part of the optical spectrum. Firstly, the reflectance measurements were performed at an angle of incidence fixed at $\theta = 10^\circ$ for samples with different lattice period p . We chose periods of $p = 375$ nm, $p = 570$ nm, and $p = 1040$ nm while keeping the d/p ratio constant at 0.75. The thickness of the PMMA gap layer

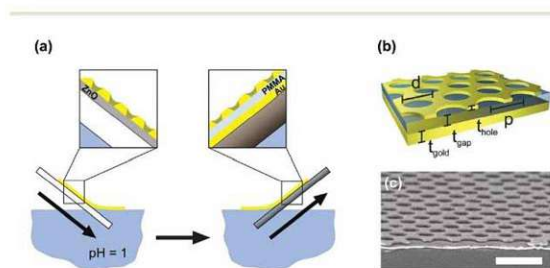


Fig. 1 Metal–insulator–metal structures. (a) Scheme of transfer of gold nanohole arrays *via* the water/air interface. (b) Schematic illustration of the MIM geometry. (c) Side-view scanning electron microscopy image of a prepared MIM structure. Scale bar is 1 μm .

and the perforated metallic film was adjusted to $t_{\text{gap}} = 40$ nm and $t_{\text{hole}} = 90$ nm, respectively. As the thickness of the bottom gold layer was set to $t_{\text{gold}} = 100$ nm, the transmittance through the structure is negligible. As seen in the photographs in the inset of Fig. 2 and the optical microscopy images (Fig. S1†), the samples with varied geometry exhibit distinct colors. The uniformity of these colors suggests an excellent spatial homogeneity over a sample area of >1 cm^2 that can be fabricated on very short timescales. As can be seen in Fig. 2, the perceived color of the gold MIM nanostructures is due to a series of narrow dips in the reflectivity spectrum, which occur in the visible and NIR part of the spectrum. In general, by increasing the lattice period p the spectral position of the reflectance dips shifts to longer wavelengths. For example, the MIM nanostructure with $p = 375$ nm exhibits the most prominent reflectivity dip at a wavelength of 665 nm, while it is strongly redshifted to 926 nm for $p = 570$ nm and further to 1363 nm for $p = 1040$ nm. These resonances exhibit extraordinarily high Q -factors compared to other self-assembled materials.²³ The corresponding Q -factors (calculated by dividing the resonance wavelength by the full width at half minimum of the resonance) are equal to 14, 8 and 6 for the samples with periods of 375 nm, 570 nm, and 1040 nm, respectively. These high values are surprising considering the defects that are inevitable when using a bottom-up approach and support the robustness of our method. The dependence of the determined Q factors on the wavelength can be attributed to varied coupling strength for the chosen d/p ratio (which may cause over-coupling of the longer wavelength resonances) and higher sensitivity to defects of the lattice that is attributed to the increasing propagation length of SPPs with the wavelength.

Additionally, a broad absorption band is visible below 500 nm which does not change with the period p and which originate from the decreased reflectivity from gold above its plasma frequency. The narrow dips occurring in the red and

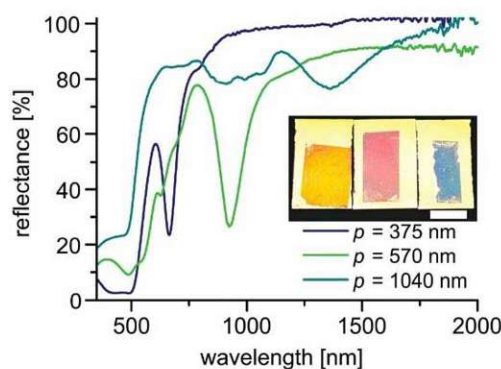


Fig. 2 Influence of the lattice period. Total reflectance of MIM structures with distinct lattice periods of the nanohole arrays measured at an angle of incidence of $\theta = 10^\circ$ with unpolarized light. The inset shows a photograph of the macroscopic samples with $p = 375$ nm, $p = 570$ nm and $p = 1040$ nm (from left to right). Scale bar is 10 mm.

2.1. Surface Plasmon Modes of Nanomesh-on-Mirror Nanocavities prepared by Nanosphere Lithography

NIR part of the spectrum are attributed to the resonant excitation of SPP modes supported by the MIM structure with a dielectric gap layer sandwiched between the flat bottom gold layer and the gold film with the nanohole arrays. These resonances are not visible for nanohole arrays without the bottom gold layer (Fig. S2†) and rapidly vanish when reducing the thickness of the bottom gold layer to a thickness comparable to the skin depth of gold (~20–45 nm) (Fig. S3†). As soon as the bottom gold film exceeds the skin depth of gold, however, the optical properties are hardly affected by the film thickness.²⁴

To clarify the nature of the observed resonances, we performed reflectance measurements with incident angles between $\theta = 6^\circ$ and $\theta = 60^\circ$. Fig. 3a shows an example of the measured spectra for a structure with $p = 570$ nm and $t_{\text{gap}} = 50$ nm. These results show a rich set of spectral features that shift with the angle of incidence, particularly at around 700 nm, and which appear non-dispersive for the resonance close to 900 nm. Additional reflectance dips are observed at longer wavelengths of around 1160 nm for non-normal angles of incidence, and split into three branches for increasing angles of incidence. All these resonances depend on the grating period p of the nanohole array (Fig. S5 and S6†).

Interestingly, the observed optical properties of MIM nanostructures are in stark contrast to that of nanohole arrays without the bottom gold film, which represents a well-characterized system (Fig. S4†). In order to elucidate the nature of the observed resonances at perforated MIM structures, finite-difference time-domain (FDTD) simulations were employed, and these results were complemented by an analytical theory based on diffraction phase-matching to surface plasmon waves. The modal analysis was performed for non-perforated top gold films, and it revealed that only two surface plasmon modes with transverse magnetic (p) polarization are supported by the MIM structure. The first surface plasmon mode, SP_{air} , propagates at the top Au/air interface. The second gap surface plasmon, SP_{gap} , confines its energy in the PMMA layer sandwiched between two metallic films. This mode exhibits a symmetric profile of the electric field. Moreover, an additional

anti-symmetric gap surface plasmon can occur but the investigated thicknesses of the PMMA gap $t_{\text{gap}} < 100$ nm are below its cutoff, and therefore this mode is not present.²⁵

The light incident at the periodically perforated MIM structure can couple to SP_{air} and SP_{gap} by diffraction. The resonant excitation of these modes occurs when the phase-matching condition is fulfilled, and the real part of the mode propagation constant $\text{Re}\{\beta\}$ is matched to that of the parallel component of incident light $k_0 \sin(\theta)$ by the grating momentum $2\pi/p$. In general, the diffraction coupling to surface plasmon modes on a grating with hexagonal symmetry depends on the orientation of the lattice with respect to the incident plane and can occur *via* different diffraction orders (Fig. S7†). It is worth noting that the measurements were performed on areas of several mm^2 , which is much larger than the single crystalline domain size of the prepared MIM 2D crystal structures. Therefore, the measured resonances due to the diffraction coupling become averaged over different orientations of the lattice.

Fig. 3b compares the simulated reflectance spectra with those experimentally measured, which are presented in Fig. 3a. Due to the angular dispersion of the plane wave source, the angular range for which the simulation can be carried out is limited. For the smallest angle of incidence $\theta = 6^\circ$, two resonances are observed in the measured data at a wavelength of about 690 nm, and 910 nm and simulations predict almost identical results with two resonance dips located at 700 and 900 nm (field distributions are discussed in Fig. 4). According to the analytical theory, these two modes are associated with the first and second order diffraction coupling to SP_{gap} and first diffraction order coupling to SP_{air} on a hexagonal grating with $p = 570$ nm. As can be seen in Fig. S7a,† the analytical phase matching-based model predicts the appearance of these modes at longer wavelengths of 770 nm and 1200 nm. This discrepancy can be attributed to changes in the propagation constant β due to the perforation, which is not taken into account by the analytical model. When increasing the angle of incidence θ , the experimentally observed short wavelength resonance splits into two branches, which indicates diffraction coupling. Also, one can see a spectrally broad decrease in the reflectivity in between these two measured branches. However, the simulations indicate a richer spectrum of modes appearing in the same spectral window when increasing the angle of incidence θ , which can be attributed to the mixing of the second order excitation of SP_{gap} with the first order excitation of SP_{air} . This discrepancy can be attributed to the potential smearing of these features in the measured reflectivity spectrum that can be ascribed to the averaging over differently oriented lattices occurring in the colloidal crystal. In contrast to shorter wavelength resonances, the first order SP_{gap} resonance located at about 900 nm does not shift with the angle of incidence θ as observed experimentally as well as captured by simulations. Instead, a series of dispersive bands appear at longer wavelengths around 1200 nm and 1400 nm when increasing the angle of incidence θ . The fact that these modes disappear at normal incidence

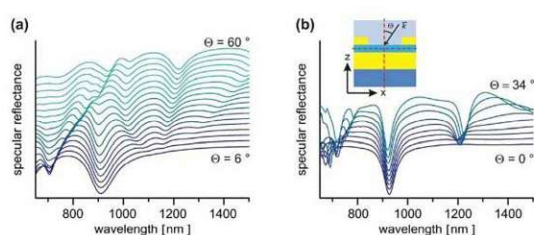


Fig. 3 Influence of angle of incidence. Angle-resolved reflectance measurements (a) and FDTD simulations (b) for a sample with $p = 570$ nm and $t_{\text{gap}} = 50$ nm and p -polarized light. The measurements in (a) were conducted in 3° steps. Spectra in (b) were calculated at $\theta = 0^\circ, 4^\circ, 8^\circ, 14^\circ, 18^\circ, 22^\circ, 26^\circ, 30^\circ, 34^\circ$. The angle of incidence is defined in the inset of (b).

2.1. Surface Plasmon Modes of Nanomesh-on-Mirror Nanocavities prepared by Nanosphere Lithography

Paper

Nanoscale

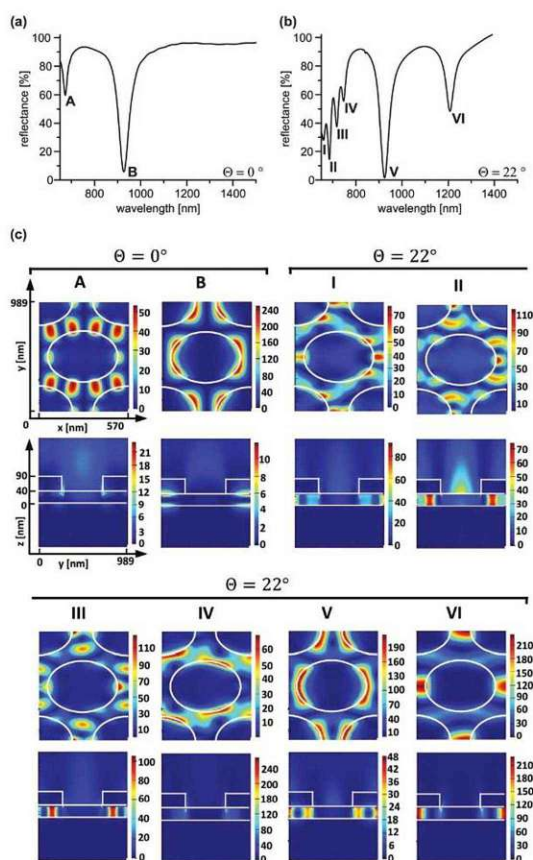


Fig. 4 Simulation of the electric near-field distribution. (a) Simulated reflectance spectrum at normal incidence. (b) Simulated reflectance spectrum at $\theta = 22^\circ$. (c) Electric field intensity $|E|^2$ distributions normalized to the incident electric field intensity $|E_0|^2$ for the resonance wavelengths assigned in (a) and (b). The electric field enhancement was evaluated along the horizontal and vertical cross-sections shown in the inset of Fig. 3b.

and that the SP_{gap} mode at 900 nm is non-dispersive qualitatively agrees with the simulations and can be explained by strong Bragg-scattering of the SP_{gap} modes, which is known to flatten the dispersion relation of propagating surface plasmons.²⁶

Following this, we simulated the near-field distribution of the electromagnetic field for specific reflectivity dips at normal ($\theta = 0^\circ$) and tilted ($\theta = 22^\circ$) illumination of the structure with the period of $p = 570$ nm (Fig. 4a). The spatial distribution of the electric field intensity $|E|^2$ was normalized with that of the incident light beam $|E_0|^2$ and showed as a cross-section parallel and perpendicular to the structure (indicated as a dashed line in the inset of Fig. 3b). At normal incidence, only two resonances are distinctively visible in the simulated spectra at 923 nm and 670 nm. The corresponding near-field distri-

butions predict an extreme electric field intensity confinement within the gap between the two metal films, indicating a gap-like nature of the resonances (Fig. 4c). A dipolar characteristic is clearly apparent for the longer wavelength resonance (B) reaching an enhancement factor $|E|^2/|E_0|^2$ of approximately 25. The resonance at 670 nm (A) shows a higher order field distribution and the field is partially confined outside the structure at the air interface. Thus, these observations agree with the hypothesis of 1st and 2nd order diffraction coupling to SP_{gap} and partial mixing with the excitation of SP_{air} at the outer interface.

Tilting the angle of incidence θ leads to the splitting of the resonances for different diffraction orders, which are otherwise degenerated and excited simultaneously at normal incidence.^{27,28} Therefore, new resonances are observed in the numerically simulated data between 650 nm and 780 nm and at 1194 nm (Fig. 4b). The near-field distribution of the series of resonances noted as I–VI (as indicated in Fig. 4b) is presented in Fig. 4c. Interestingly, the field distribution of the strongest non-dispersive resonance (V) is not altered by changing the angle of incidence θ . The electric field maps of the short wavelength modes I–IV show a mixed nature due to the overlap of the SP_{gap} , and the SP_{air} and particularly resonance II exhibits substantial field confinement at the outer interface. When compared with the experiments, probably only mode IV is visible, and the other resonances are smeared by averaging over lattice orientations. The longer wavelength resonances such as VI exhibit solely the SP_{gap} nature as seen in the respective near-field plots. Thus, all resonances, including the non-dispersive modes, can be attributed to either SP_{air} or SP_{gap} . This highlights the simplicity of the given description which provides an alternative view to previous interpretations using magnetic, localized hole plasmons or Fabry–Pérot resonances.^{9,10,13}

The influence of the gap layer thickness was examined experimentally as well as theoretically (Fig. 5). In the experiments, the gap PMMA film thickness t_{gap} was controlled between 25 nm and 77 nm by adjusting the spin-coating parameters, and layers with a smaller thickness between 1 nm and 15 nm were prepared using a layer-by-layer approach. When decreasing the thickness t_{gap} from 77 nm to 1 nm, the strongest SP_{gap} resonance drastically shifts from 826 nm to 1417 nm. This observation is confirmed by numerical simulations (see Fig. 5c), and the same trend is predicted by the phase-matching model due to the increased propagation constant of SP_{gap} when decreasing the gap thickness t_{gap} (see Fig. S7c†). Concomitantly, the higher order SP_{gap} resonances become strongly apparent at shorter wavelength, and they shift towards longer wavelengths when decreasing t_{gap} . In contrast, the resonance below 600 nm that is ascribed to the excitation of SP_{air} is weakly affected by changing the gap thickness t_{gap} as only a small portion of its electric field intensity is confined in the gap. For narrow gaps, gap resonances can be observed even for high angles of incidence (Fig. S8 and S9†). In contrast, for thick gap layers, all resonances appear in a narrow wavelength range leading to strong coupling between SP_{gap} and

2.1. Surface Plasmon Modes of Nanomesh-on-Mirror Nanocavities prepared by Nanosphere Lithography

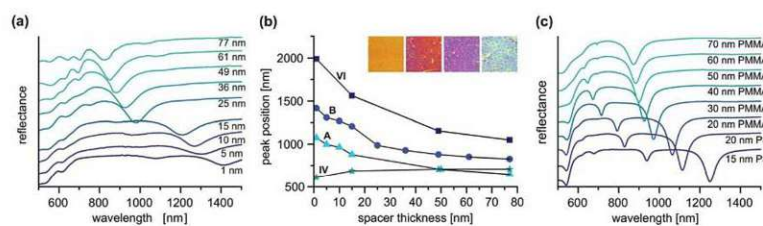


Fig. 5 Influence of gap thickness. (a) Reflectance of MIM structures with distinct gap thickness measured at $\theta = 10^\circ$ with unpolarized light. Gap layers with a thickness of $t_{\text{gap}} < 20$ nm were prepared using a layer-by-layer approach. Layer thicknesses with $t_{\text{gap}} > 20$ nm were prepared by spin-coating of PMMA. (b) Peak positions in dependence on the gap thickness obtained from reflectance measurements. Modes IV and VI were extracted from angle-resolved measurements. The inset shows macroscopic photographs of 7×7 mm² MIM structures with gap thickness $t_{\text{gap}} = 32$ nm, 40 nm, 61 nm, and 77 nm. (c) Simulated reflectance of MIM structures with distinct gap thickness for normal incident light.

SP_{air} modes at larger angles of incidence (Fig. S10 and S11[†]). This results in a mixed nature of the resonance at large angles of incidence showing a dispersive behavior.

A complementary approach to shed light on the observed resonances was performed based on examining the influence of the refractive index environment. For this purpose, the samples were immersed in glycerine–water mixtures with different compositions. Thereby, the refractive index above the structure can be tuned between 1.33 (pure water) and 1.47 (pure glycerine). At first, the effect of the surrounding medium was analyzed using the as-prepared MIM structure ($p = 570$ and $t_{\text{gap}} = 50$ nm). When increasing the surrounding refractive index from 1.33 to 1.47, the SPP confined to the outer Au interface (SP_{air}) shifts to longer wavelengths by approximately 53 nm (Fig. 6a). In accordance with the field profiles predicted by numerical simulations, the resonances occurring at longer wavelengths (SP_{gap}) are not sensitive to changes in the refractive index as their electric field is mainly confined inside the structure.

Next, capitalizing on the organic gap layer, we varied the refractive index of the dielectric gap layer with an initial thickness of $t_{\text{gap}} = 51$ nm by plasma etching (Fig. 6b). In consecutive etching steps, the PMMA within the holes of the nanohole array is gradually removed until the bottom gold layer is reached after 120 s. This can be inferred from the increasing depth of the holes measured by atomic force microscopy (see

Fig. S12[†]). Nevertheless, the distance between the metal films and the homogeneity of the sample are not affected. Due to the strongly decreasing refractive index environment in the gap, all resonances (including SP_{gap}) are shifting to shorter wavelengths. Further etching results in an ongoing shift of the resonance wavelength as now the gold-covered PMMA between the holes is removed (underetching). Thus, a quasi-free-standing nanohole array is produced. The smallest shift of 54 nm after 150 s is observed for the mode confined to the Au/air interface (SP_{air}). A higher sensitivity to a change in the refractive index was expected for the gap modes because of the high electric field intensities within the dielectric gap. Indeed, a strong spectral shift from 824 nm to 714 nm is seen for SP_{gap} resonance. We then immersed the MIM sample with a quasi-free-standing nanohole array into glycerine–water mixtures (Fig. 6c). Thus, the liquid medium can penetrate the nanohole arrays and change the refractive index between the two gold films. As expected, with a spectral shift of 60 nm, the sensitivity of the SP_{air} resonance in the etched sample is comparable to the non-etched sample. At the same time, the resonance wavelength of the SP_{gap} mode is now influenced. A shift of 39 nm can be observed when increasing the surrounding refractive index from 1.33 to 1.47. Altogether, the sensitivity of the MIM-stack results in 379 nm per RIU and 429 nm per RIU for the SP_{air} mode in the unetched and etched sample and 279 nm per RIU for the SP_{gap} mode.

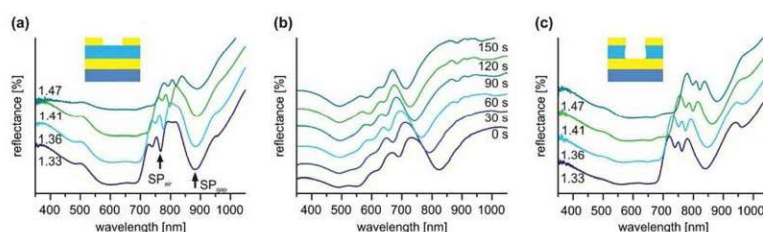


Fig. 6 Refractive index sensitivity. (a) Reflectance of the as-prepared MIM structure immersed in glycerine–water mixtures with distinct refractive indices. (b) Reflectance of the MIM structures in air after different times of plasma etching. (c) Reflectance of the MIM structure etched for 150 s, immersed in glycerine–water mixtures with distinct refractive indices.

Conclusions

In summary, we demonstrated the production of trilayer MIM cavities *via* a simple bottom-up approach. By using an interface-mediated transfer of gold nanohole arrays prepared *via* nanosphere lithography, high-quality metamaterials were fabricated on a substrate with square centimeter area. We thoroughly characterized the optical properties of the resulting MIM stacks composed of an opaque gold film, a polymer gap layer and a second gold film comprising the nanohole array. The rich plasmonic response can be assigned to the coupling to only two propagating surface plasmon modes, which is strongly dependent on the grating period of the nanohole array and the thickness of the dielectric gap. The resonant excitation of the symmetric SP_{gap} mode is insensitive to the angle of incidence and shows an unusually high Q -factor for self-assembled materials comparable to those prepared by top-down lithography techniques. The detailed understanding of the presented phenomena in combination with absorbing layers is of great importance for light harvesting devices.^{4,29,30}

Materials and methods

Materials

Polystyrene particles were purchased at Microparticles GmbH (Berlin).

Fabrication of ZnO coated substrates

The ZnO layers were prepared using a sol-gel method. For this, glass slides were cleaned for 10 min by ultrasonication in 2% aqueous Hellmanex (Hellma GmbH, Mühlheim, Germany) solution in MilliQ water. After rinsing off the surfactant with MilliQ water, the substrates were further sonicated for 10 minutes in ethanol and finally dried with compressed air. Subsequently, the ZnO films were formed by spin coating a zinc acetate solution (110 mg zinc acetate in 30 μ l 2-aminoethanol and 1 ml 2-methoxyethanol) at 2000 rpm for 50 s and subsequent baking at 150 °C for 5 min.

Fabrication of Au nanomeshes

Monolayers of polystyrene particles were prepared according to the procedure of Retsch *et al.*²⁰ Cationically functionalized glass slides were spin-coated with a 3 wt% particle dispersion at 4000 rpm. Subsequently, the coated glass substrates were immersed into a 0.1 mM SDS solution in MilliQ. The aqueous phase was adjusted to pH 12 by adding a few drops of NH_3 . A monolayer was formed at the liquid/air interface by self-assembly of the detaching particles. The monolayer was transferred to the ZnO coated glass substrates and dried in air. The monolayers were etched in a plasma reactor MiniFlecto (Plasma Technology GmbH, Herrenberg, Germany) with 75% argon and 25% oxygen at 80 W at a pressure of 0.14 mbar to obtain non-close packed monolayers. A 3 nm chromium layer and 50 nm gold were deposited using a Balzers BA360 thermal evaporation chamber. The layer thickness was monitored *via*

an SQM 160 microbalance (Sigma Instruments, Schaefer Technologie GmbH). Afterward, the particles were removed using Scotch® tape (3 M) giving the nanohole arrays. The gold-coated substrates were cleaned by ultrasonication for 10 min in THF and dried with compressed air. All samples were stored under inert gas.

Fabrication of MIM structures

100 nm thick gold film was deposited on cleaned microscopy slides. Subsequently, the gap layer was prepared by spin-coating commercially available poly(methyl methacrylate) (PMMA). Thin gap layers (1 nm–15 nm) were made *via* a layer-by-layer approach. For this, one layer of polyethyleneimine followed by alternating layers of poly(styrene sulfonate) and poly(allylamine hydrochloride) were applied by spray-coating. The Au nanohole arrays were detached from their parental substrate by immersion into an aqueous hydrochloric acid solution (pH 1) with a speed of 1 mm min^{-1} and an immersion angle of 45° using a home built dip-coater system. After complete detachment of the gold film, the nanohole array is transferred when lifting the receiving substrate out of the water phase.

Characterization

UV-vis-NIR spectra were measured using the Diffuse Reflectance Accessory of a Cary 5000 UV-vis-NIR Spectrophotometer (Agilent Technologies) at 10° angle of incidence with unpolarized light. Angle-resolved UV-vis-NIR spectroscopy was conducted with the Universal Measurement Accessory of the same spectrometer with 3° increment with p- and s-polarized light. To examine the effect of the refractive index environment the samples were immersed in glycerine/water mixtures with refractive indices of 1.33 (pure water), 1.36 (20% glycerine), 1.41 (60% glycerine) and 1.47 (pure glycerine).

SEM images were taken on a LEO 1530 Gemini Field Emission SEM (Carl Zeiss AG, Oberkochen, Germany). The images were evaluated with the software ImageJ.³¹

Atomic force microscopy was performed in tapping mode on a Dimension 3100 microscope (Veeco, USA) with a Nanoscope IV controller and OTESPA-R3 (Bruker) cantilevers. The AFM images were analyzed with the software Nanoscope Analysis.

FDTD simulations

A commercial package by Lumerical that relies on the finite-difference time-domain method was used to simulate optical properties of gold nanomeshes.³² As shown in Fig. S13,† a rectangular unit cell with the hexagonal arrays of holes was used. Bloch boundary conditions were applied at the interfaces of the unit cell that are perpendicular to the structure surface while perfectly matched layers were used on its top and bottom. The investigated structure was approximated by a stack of a perforated gold layer with the thickness of $t_{\text{hole}} = 50$ nm, an intermediate layer of PMMA with a thickness of t_{gap} and a flat gold layer with a thickness of $t_{\text{gold}} = 100$ nm. Refractive index of PMMA of $n_{\text{PMMA}} = 1.4848$ was used in the whole spectral range, and the refractive index of gold was determined by fitting to CRC data.³³ The BK7 glass substrate

2.1. Surface Plasmon Modes of Nanomesh-on-Mirror Nanocavities prepared by Nanosphere Lithography

with $n_{\text{substrate}} = 1.52$ was assumed below the plasmonic stack of layers. The excitation light beam was generated with a plane wave source in the air above the structure, and it was made incident on the perforated gold film. In the used version of FDTD solutions, planar sources exhibit angular dispersion if the beam does not propagate normal to the source. To minimize the angular dispersion, simulations were carried out for wavelength range 550 nm to 900 nm and 900 nm to 1500 nm separately, and the spectra were subsequently stitched. Field intensity and power monitors were placed above or below the unit cell in order to obtain reflectivity and transmission spectra. Electric near-field intensity profiles were calculated by using monitors placed inside the structure. Convergence of the simulation results was confirmed by variation of the mesh size and comparison of the reflectance results (Fig. S14†).

Conflicts of interest

There are no conflicts to declare.

Acknowledgements

The work in Bayreuth was funded by the German Research Foundation (DFG) by the SFB840. C. S. acknowledges support from the Elite Network of Bavaria (ENB). The authors thank Dr Beate Förster and Martina Heider from the Bavarian Polymer Institute (BPI) for their support using the scanning electron microscopy facilities. J. D. and S. F. was supported by European Union's Horizon 2020 research and innovation programme under grant agreement no 633937, project ULTRAPLACAD.

References

- 1 T. W. Ebbesen, H. J. Lezec, H. F. Ghaemi, T. Thio and P. A. Wolff, *Nature*, 1998, **391**, 667–669.
- 2 N. Sharma, H. Keshmiri, X. Zhou, T. I. Wong, C. Petri, U. Jonas, B. Liedberg and J. Dostalek, *J. Phys. Chem. C*, 2016, **120**, 561–568.
- 3 D. Inoue, A. Miura, T. Nomura, H. Fujikawa, K. Sato, N. Ikeda, D. Tsuya, Y. Sugimoto and Y. Koide, *Appl. Phys. Lett.*, 2011, **98**, 093113.
- 4 C. Stelling, C. R. Singh, M. Karg, T. A. F. König, M. Thelakkat and M. Retsch, *Sci. Rep.*, 2017, **7**, 42530.
- 5 J. Zhu, X. Zhu, R. Hoekstra, L. Li, F. Xiu, M. Xue, B. Zeng and K. L. Wang, *Appl. Phys. Lett.*, 2012, **100**, 143109.
- 6 A. J. Morfa, E. M. Akinoglu, J. Subbiah, M. Giersig and P. Mulvaney, *J. Appl. Phys.*, 2013, **114**, 054502.
- 7 C. Hu, Z. Zhao, X. Chen and X. Luo, *Opt. Express*, 2009, **17**, 11039.
- 8 F. Cheng, X. Yang, D. Rosenmann, L. Stan, D. Czaplowski and J. Gao, *Opt. Express*, 2015, **23**, 25329–25339.
- 9 P. Pitchappa, C. P. Ho, P. Kropelnicki, N. Singh, D.-L. Kwong and C. Lee, *J. Appl. Phys.*, 2014, **115**, 193109.
- 10 G. Behera and S. A. Ramakrishna, *J. Phys. D: Appl. Phys.*, 2016, **49**, 075103.
- 11 T. Maurer, P.-M. Adam and G. Lévêque, *Nanophotonics*, 2015, **4**, 363–382.
- 12 S. Shu and Y. Y. Li, *Opt. Lett.*, 2015, **40**, 934–937.
- 13 G. Tagliabue, C. Höller, H. Eghlidi and D. Poulidakos, *Nanoscale*, 2014, **6**, 10274–10280.
- 14 Z. Fang, Y.-R. Zhen, L. Fan, X. Zhu and P. Nordlander, *Phys. Rev. B: Condens. Matter*, 2012, **85**, 245401.
- 15 M. Mayer, M. Tebbe, C. Kuttner, M. J. Schnepf, T. A. König and A. Fery, *Faraday Discuss.*, 2016, **191**, 159–176.
- 16 N. Vogel, C. K. Weiss and K. Landfester, *Soft Matter*, 2012, **8**, 4044–4061.
- 17 Z. Wu, X. Chen, M. Wang, J. Dong and Y. Zheng, *ACS Nano*, 2018, **12**, 5030–5041.
- 18 R. Ortuño, C. García-Meca, F. J. Rodríguez-Fortuño, J. Martí and A. Martínez, *Phys. Rev. B: Condens. Matter Mater. Phys.*, 2009, **79**, 075425.
- 19 C. Stelling and M. Retsch, *Adv. Mater. Interfaces*, 2018, **5**, 1800154.
- 20 M. Retsch, Z. Zhou, S. Rivera, M. Kappl, X. S. Zhao, U. Jonas and Q. Li, *Macromol. Chem. Phys.*, 2009, **210**, 230–241.
- 21 N. Vogel, S. Goerres, K. Landfester and C. K. Weiss, *Macromol. Chem. Phys.*, 2011, **212**, 1719–1734.
- 22 M. Parchine, J. McGrath, M. Bardosova and M. E. Pemble, *Langmuir*, 2016, **32**, 5862–5869.
- 23 K. Volk, J. P. S. Fitzgerald, P. Ruckdeschel, M. Retsch, T. A. F. König and M. Karg, *Adv. Opt. Mater.*, 2017, **5**, 1600971.
- 24 A. Christ, G. Leveque, O. J. Martin, T. Zentgraf, J. Kuhl, C. Bauer, H. Giessen and S. G. Tikhodeev, *J. Microsc.*, 2008, **229**, 344–353.
- 25 J. A. Dionne, L. A. Sweatlock, H. A. Atwater and A. Polman, *Phys. Rev. B: Condens. Matter*, 2006, **73**, 035407.
- 26 W. L. Barnes, T. W. Preist, S. C. Kitson and J. R. Sambles, *Phys. Rev. B: Condens. Matter*, 1996, **54**, 6227–6244.
- 27 H. Ghaemi, T. Thio, D. Grupp, T. Ebbesen and H. Lezec, *Phys. Rev. B: Condens. Matter*, 1998, **58**, 6779–6782.
- 28 M. Couture, Y. Liang, H. P. Poirier Richard, R. Faid, W. Peng and J. F. Masson, *Nanoscale*, 2013, **5**, 12399–12408.
- 29 I. Diukman, L. Tzabari, N. Berkovitch, N. Tessler and M. Orenstein, *Opt. Express*, 2011, **19**(Suppl 1), A64–A71.
- 30 C. Fei Guo, T. Sun, F. Cao, Q. Liu and Z. Ren, *Light: Sci. Appl.*, 2014, **3**, e161.
- 31 W. S. Rasband, *ImageJ*, U. S. National Institutes of Health, Bethesda, Maryland, USA, <http://imagej.nih.gov/ij>, 2016.
- 32 Lumerical Inc., <http://www.lumerical.com/tcad-products/fdtd/>.
- 33 J. H. Weaver and H. P. R. Frederikse, in *CRC Handbook of Chemistry and Physics*, ed. D. R. Lide, CRC Press, Boca Raton, 2005, ch. 12, pp. 33–156.

2.1. Surface Plasmon Modes of Nanomesh-on-Mirror Nanocavities prepared by Nanosphere Lithography

2.2. Actuated Plasmonic Nanohole Arrays for Sensing and Optical Spectroscopy Applications

The following publication is reprinted under the Creative Commons Attribution 3.0 Unported Licence 3.0^b from The Royal Society of Chemistry.

Daria Kotlarek, Stefan Fossati, Priyamvada Venugopalan, Nestor Gisbert Quilis, Jiří Slabý, Jiří Homola, Médéric Lequeux, Frédéric Amiard, Marc Lamy de la Chapelle, Ulrich Jonas, and Jakub Dostálek Actuated plasmonic nanohole arrays for sensing and optical spectroscopy applications. *Nanoscale* 12, 9756–9768 (2020). <https://doi.org/10.1039/d0nr00761g>

Copyright © The Royal Society of Chemistry 2020

In this chapter, a hybrid plasmonic structure consisting of a metal nanomesh array, forming pores in contact with gold nanoparticles embedded in a thermo-responsive hydrogel, is presented. Prepared by nanoimprint lithography and subsequent template stripping, the structure supports several optical modes, which allow the probing of different regions on the structure. A coupled mode between the nanoholes and the nanoparticles is of particular interest, as it is tightly confining the electromagnetic field at the pore. One of the main challenges in optical sensor techniques, that employ tightly confined electromagnetic hot spots for signal amplification, is the efficient transport of the analyzed species to the sensitive areas. In this structure, the analyte-carrying solution passes through the pores, and the first point of contact with receptor elements is within the volume probed by a hybridized gap mode. This flow-through architecture provides efficient delivery to the plasmonic hot spot. The capture of analytes is observed as a shift in wavelength of the resonant features in a label-free manner. Furthermore, the enhanced field intensity within the gap mode is suitable for surface enhanced Raman spectroscopy.

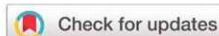
In this work, Daria Kotlarek acted as the main author, developing the sensor concept, the assay, preparing the substrates, and conducting the bio experiments. Stefan Fossati was

^b <https://creativecommons.org/licenses/by/3.0/>

2.2. Actuated Plasmonic Nanohole Arrays for Sensing and Optical Spectroscopy Applications

involved in the development of the nanoimprint procedure and the optical characterization of the substrates. Specifically, optical spectroscopy methods including transmission and angular resolved specular reflection spectroscopy, AFM, and SEM have been employed to characterize the prepared nanostructures and optimize the production process. Furthermore, Stefan Fossati developed the instrument for the time-resolved tracking of optical features and, together with Priyamvada Venugopalan, contributed to the numerical simulations of the optical properties of the responsive hydrogel-based structure under the supervision of Jakub Dostalek.

Supporting information to this article is included in the appendix, section 5.2.



Cite this: DOI: 10.1039/d0nr00761g

Actuated plasmonic nanohole arrays for sensing and optical spectroscopy applications†

Daria Kotlarek,[‡] Stefan Fossati,^a Priyamvada Venugopalan,^{§a,b} Nestor Gisbert Quilis,^a Jiří Slabý,^c Jiří Homola,^{id c} Médéric Lequeux,^d Frédéric Amiard,^e Marc Lamy de la Chapelle,^e Ulrich Jonas^f and Jakub Dostálek^{id *a}

Herein, we report a new approach to rapidly actuate the plasmonic characteristics of thin gold films perforated with nanohole arrays that are coupled with arrays of gold nanoparticles. The near-field interaction between the localized and propagating surface plasmon modes supported by the structure was actively modulated by changing the distance between the nanoholes and nanoparticles and varying the refractive index symmetry of the structure. This approach was applied by using a thin responsive hydrogel cushion, which swelled and collapsed by a temperature stimulus. The detailed experimental study of the changes and interplay of localized and propagating surface plasmons was complemented by numerical simulations. We demonstrate that the interrogation and excitation of the optical resonance to these modes allow the label-free SPR observation of the binding of biomolecules, and is applicable for *in situ* SERS studies of low molecular weight molecules attached in the gap between the nanoholes and nanoparticles.

Received 28th January 2020,
Accepted 30th March 2020
DOI: 10.1039/d0nr00761g
rsc.li/nanoscale

Metallic nanohole arrays (NHAs) have attracted increasing attention after Ebbesen's observation of the extraordinary optical transmission¹ assigned to surface plasmon-mediated light tunneling through periodically arranged subwavelength pores. Subsequently, NHA structures have been employed in diverse application areas including optical filters,^{2,3} amplification of weak spectroscopy signals such as fluorescence^{4,5} and Raman scattering,^{6–9} second-harmonic generation,¹⁰ and particularly sensing. To date, NHA-based sensors have been utilized for the direct optical probing of proteins,^{11,12–14} exosomes,¹⁵ viruses,^{16,17} bacteria,¹⁸ and even cancer cells^{19,20} and

organelles.²¹ Moreover, NHA have enabled studies on lipid membranes that span over the holes²² and allowed the facile incorporation of membrane proteins for interaction studies with drug candidates.^{16,23}

NHA structures enable the electromagnetic field to be strongly confined inside subwavelength nanoholes²⁴ due to the excitation of two types of surface plasmon modes, propagating surface plasmons (PSPs, also referred to as surface plasmon polaritons) traveling along the metal surface and localized surface plasmons (LSPs), which occur at the sharp edges of the holes. The coupling to these modes can be tailored for specific purposes by controlling the structure geometry, including hole shape, diameter, and lateral periodic or quasi-periodic spacing.²⁵ In addition, a more complex spectrum of supported plasmonic modes can be utilized by combining complementary geometries that support LSP modes at similar wavelengths based on Babinet's principle.²⁶ When the NHA geometry approaches that of complementary metallic nanoparticle (NP) arrays, additional LSP resonance is introduced, which can near-field couple with the NHA.²⁷ Moreover, NHA structures that comprise stacks of periodically perforated metallic films²⁸ and NHA + NP structure with a defined lateral offset of NPs with respect to the nanohole center²⁹ have been investigated. Herein, we report a new approach to rapidly actuate the plasmonic characteristics of thin gold films perforated with nanohole arrays by thermo-responsive hydrogel and demonstrate its utilization to sensing with flow-through format SPR and SERS readout.³⁰ It is worth noting that arran-

^aBiosensor Technologies, AIT-Austrian Institute of Technology GmbH, Konrad-Lorenz-Straße 24, 3430 Tulln an der Donau, Austria. E-mail: jakub.dostalek@ait.ac.at

^bCEST Kompetenzzentrum für elektrochemische Oberflächentechnologie GmbH, TTF, Wiener Neustadt, Viktor-Kaplan-Strasse 2, 2700 Wiener Neustadt, Austria

^cInstitute of Photonics and Electronics of the Czech Academy of Sciences, Chaberská 57, 18251 Praha 8, Czech Republic

^dUniversité Paris 13, Sorbonne Paris Cité, Laboratoire CSPBAT, CNRS, (UMR 7244), 74 rue Marcel Cachin, 93017 Bobigny, France

^eInstitut des Molécules et Matériaux du Mans (IMMM – UMR CNRS 6283), Avenue Olivier Messiaen, 72085 Le Mans cedex 9, France

^fMacromolecular Chemistry, Department Chemistry-Biology, University of Siegen, Adolf Reichwein-Strasse 2, Siegen 57076, Germany

† Electronic supplementary information (ESI) available. See DOI: 10.1039/d0nr00761g

‡ Current address: Captor Therapeutics Inc., ul. Duńska 11, 54-427 Wrocław, Poland.

§ Current address: NYU Abu Dhabi, Saadiyat Campus, P.O. Box 129188, Abu Dhabi, United Arab Emirates.

2.2. Actuated Plasmonic Nanohole Arrays for Sensing and Optical Spectroscopy Applications

Paper

Nanoscale

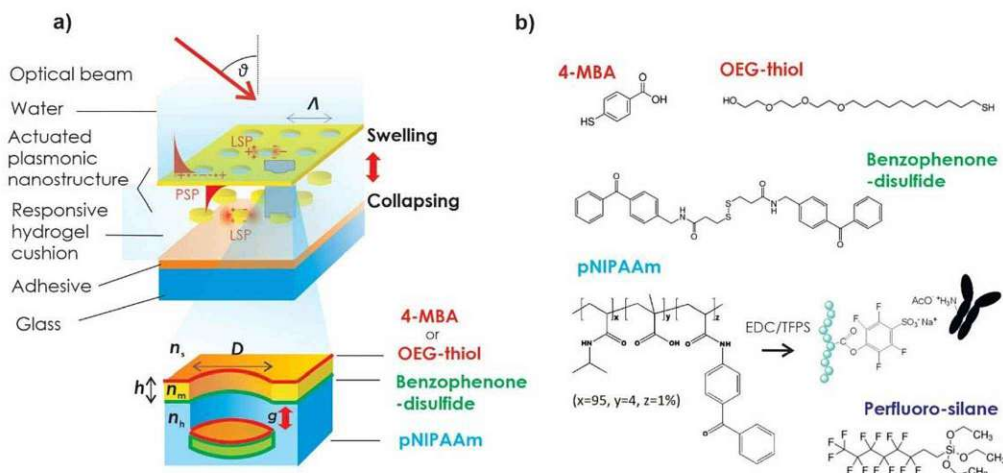


Fig. 1 (a) Schematics of plasmonic nanostructure composed of periodic nanohole arrays (NHA) coupled with arrays of nanoparticles (NP) by the use of responsive hydrogel cushion implemented by materials with the chemical structure shown in (b).

ging the metallic nanoholes and nanoparticles in periodic arrays also decreases the damping of plasmonic modes by their diffraction coupling through the formation of the so-called surface lattice resonances.³¹

Perforated metal layer structures with NHA have been recently prepared using a range of lithography processes. In top-down approaches, a variety of geometries become accessible using focused ion beam milling (FIB) and electron beam lithography (EBL).^{32,33} Nanoimprint lithography and template stripping³⁴ are used to partially alleviate the limited throughput of EBL and FIB by the replication of the NHA structure from pre-fabricated templates. Alternatively, NHAs were also prepared using bottom-up approaches, mostly relying on the self-organization of colloid particles.³⁵ Using sub-monolayer surface coverage of colloids, the colloid particles are used as a mask for the preparation of sparse and disordered nanoholes, while dense monolayers of colloids are employed to create well-ordered nanohole geometries.^{28,29,36} This approach allows the pattern period, Λ , to be controlled by the size of the colloid particles and the hole diameter, D , can be independently adjusted *via* isotropic etching of the assembled particles before metal deposition. This technique was further extended for the preparation of nanoholes on cavities,³⁷ and a lift-off approach of the NHA membrane was also adopted for its subsequent transfer to more complex structures with multiple stacked patterned metallic layers.²⁸

Typically, NHAs used for sensing applications are prepared *via* stripping-based techniques or lithographic methods directly on a non-permeable solid support, which is loaded to a microfluidic device.^{38,39} However, the liquid sample to be analyzed is flowed over the perforated NHA surface with closed-ended pores, where the liquid flow velocity is equal to zero, and consequently, the transport of molecules to and inside the pores is dominantly driven by slow diffusion.^{40,41}

Thus, to overcome this limitation, there a flow-through assay format has been developed, in which the analyte solution is transported internally across the nanoporous film.^{8,16,41,42} However, these experiments typically rely on the structure of the NHA prepared on thin nitride membranes, which requires multiple lithography steps and complicates their application in sensing experiments.

The present study demonstrates a new type of NHA + NP structure, which is supported by a thermo-responsive hydrogel cushion. It is made from an *N*-isopropylacrylamide hydrogel material that can expand and contract in an aqueous environment, thereby actuating the plasmonic properties of metallic nanostructures.^{43–45} In this architecture, the hydrogel cushion accommodates arrays of gold NPs, which are located below the NHA and their mutual distance, g , can be on demand actuated (Fig. 1). Herein, we investigate the spectra of supported PSP and LSP modes and their spectral detuning by temperature-induced reversible swelling and collapsing of a hydrogel cushion. In addition, the hydrogel can serve as a three-dimensional binding matrix for the immobilization of bio-functional molecules and the applicability of the structure for SPR (surface plasmon resonance) and SERS (surface-enhanced Raman scattering) detection is demonstrated with the use of plasmonic modes that probe the open pores, through which aqueous samples can be actively flowed.

Results and discussion

We developed a method to prepare a nanostructure geometry that combines thin gold films perforated with NHA and arrays of gold NP, which are suspended in a thin layer of a poly(*N*-isopropyl acrylamide) (pNIPAAm)-based hydrogel. It serves as a responsive cushion, which responds to temperature changes

since pNIPAAm exhibits a lower critical solution temperature (LCST) of 32 °C. Below its LCST, it is hydrophilic, and it contains large amounts of water in its polymer network structure. When the temperature increases above its LCST, it abruptly collapses by expelling water. In the nanostructure geometry (Fig. 1a), the pNIPAAm-based hydrogel cushion was allowed to swell and collapse *via* the diffusion of water through the NHA pores and its volume changes were utilized for active control of the distance, g , between NHA and NP. In addition, the hydrogel was made from a terpolymer that carries pendant groups attached to its backbone, enabling its post-modification with bio-functional molecules (Fig. 1b) for application in optical spectroscopy and biosensors.⁴⁶ It is worth noting that this thermo-responsive hydrogel cushion allowed the controlled opening and closing of the nanohole arrays of pores, and switching to the open state was accompanied by the rapid diffusion of water, which drags contained biomolecules through the pores, where a plasmonic hotspot occurs. The spectrum of plasmonic modes probing the pores of the structure and their near field coupling was investigated in detail, as follows.

Preparation of NHA + NP structure with hydrogel cushion

The NHA + NP structure featuring actively tunable plasmonic properties was prepared by a combination of UV nanoimprint lithography (UV-NIL) and template-stripping (Fig. 2a). Arrays of nanopillars cast to the transparent OrmoStamp material were used as a template. AFM observation of the structure topography showed that the arrays of nanopillars exhibited a diameter of $D = 100$ nm, height of 100 nm, and they were arranged in rectangular arrays with a set period of $\Lambda = 460$ nm (Fig. 2b). The arrays of OrmoStamp nanopillars were then activated by UV-ozone treatment and modified with perfluoro-silane using vapor deposition to reduce their surface energy. Subsequently, the nanopillars with a perfluoro-silane anti-adhesive layer were coated by a gold layer with a thickness of $h = 50$ nm. SEM observation (Fig. 2c) revealed that the gold deposition led to the formation of a continuous layer, which is protruded by the nanopillars and their top is capped by gold that is not connected to the bottom continuous gold layer. Afterward, the outer gold surface was modified by a self-assembled monolayer of photo-active benzophenone-disulfide, and subsequently coated with a pNIPAAm-based terpolymer layer. This terpolymer contains the same photo-reactive benzophenone groups in its backbone (see Fig. 1b) and upon irradiation with UV light these chains were simultaneously covalently crosslinked and attached to the gold *via* the benzophenone-disulfide linker. Then, the outer surface of the crosslinked pNIPAAm-based polymer was pressed against a glass substrate with a soft adhesive layer (Ostemer resin pre-cured with UV light), which was subsequently thermally cured overnight at a temperature of 50 °C. Finally, the assembly was stripped at the OrmoStamp-gold interface (treated with anti-adhesive layer) to yield a structure with a thin gold film perforated by NHA, which were attached to the pNIPAAm-based crosslinked polymer networks and underneath comprised of embedded

gold NPs spatially separated from the perforated continuous gold film. The AFM topography image in Fig. 2d shows that the pores exhibit the same diameter, D , as the nanopillars and the SEM image of an edge of the structure in Fig. 2e confirms that under the NHA, arrays of gold NPs are present (which were stripped from the top of the OrmoStamp pillars). It is worth noting that the distortions of the surface that are visible in Fig. 2e are a result of breaking the sample to obtain the cross-section image.

Optical observation of plasmonic modes

The spectra of the LSP and PSP modes supported by the prepared nanostructure were investigated *via* optical transmission measurements. To distinguish between the diffraction coupling to the dispersive PSP modes (traveling along the gold film) and non-dispersive LSP resonances (supported by the pores in the NHA + NP nanostructure), transmission spectra were measured *via* collimated beam impinging on the NHA + NP structure at angles in the range of $\theta = 0^\circ$ to 25° . The transmitted beam emitted from a halogen light bulb was then analyzed with a spectrometer in the wavelength range of $\lambda = 500$ – 850 nm. Firstly, the wavelength-angular dependence of the transmission was measured for a structure that was dry and in contact with air (with a refractive index of $n_s = 1$). As presented in Fig. 3a, the acquired spectrum shows that the excitation of non-dispersive resonance is manifested as a dip centered at a wavelength of $\lambda_A = 600$ nm. Moreover, an additional dispersive mode occurs, and its excitation is associated with the dip in the transmission spectrum at $\lambda_C^d = 750$ nm, which splits when the angle of incidence, θ , deviates from zero. Secondly, the structure was clamped to a flow-cell and water (with a refractive index of $n_s = 1.33$) was flowed over its surface, which was kept at a temperature of $T = 40$ °C. This temperature is above the LCST of pNIPAAm, and thus this material exhibits hydrophobic properties, preventing the diffusion of water into the polymer networks through the NHA pores. Since the refractive index of the dielectric above the structure n_s increased, a new dispersive dip resonance centered at a wavelength of $\lambda_B^d = 650$ nm appeared, while the resonance features λ_A and λ_C^d changed negligibly (Fig. 3b). Thirdly, the structure in contact with water was cooled to $T = 22$ °C, which is below the LCST of pNIPAAm. Then, a strong blueshift in the λ_A and λ_C^d resonances occurred in the transmission spectrum, and also much weaker spectral shift of λ_B^d accompanied by a decrease in coupling efficiency at this wavelength (Fig. 3c). These observations indicate that the resonances at λ_A and λ_C^d are associated with the coupling to the surface plasmon modes that confine the electromagnetic field in the inner side of the structure in contact with the pNIPAAm-based hydrogel (with a refractive index of $n_h = 1.47$ at $T = 22$ °C and $n_h = 1.37$ at $T = 40$ °C, see ESI, Fig. S1†). The resonance λ_B^d probes the upper part of the structure in contact with water ($n_s = 1.33$), which changes its refractive index with temperature much less than pNIPAAm. Since the resonances at λ_B^d and λ_C^d are dispersive, they can be attributed to the PSP modes traveling at the upper or bottom interface of the gold film, respect-

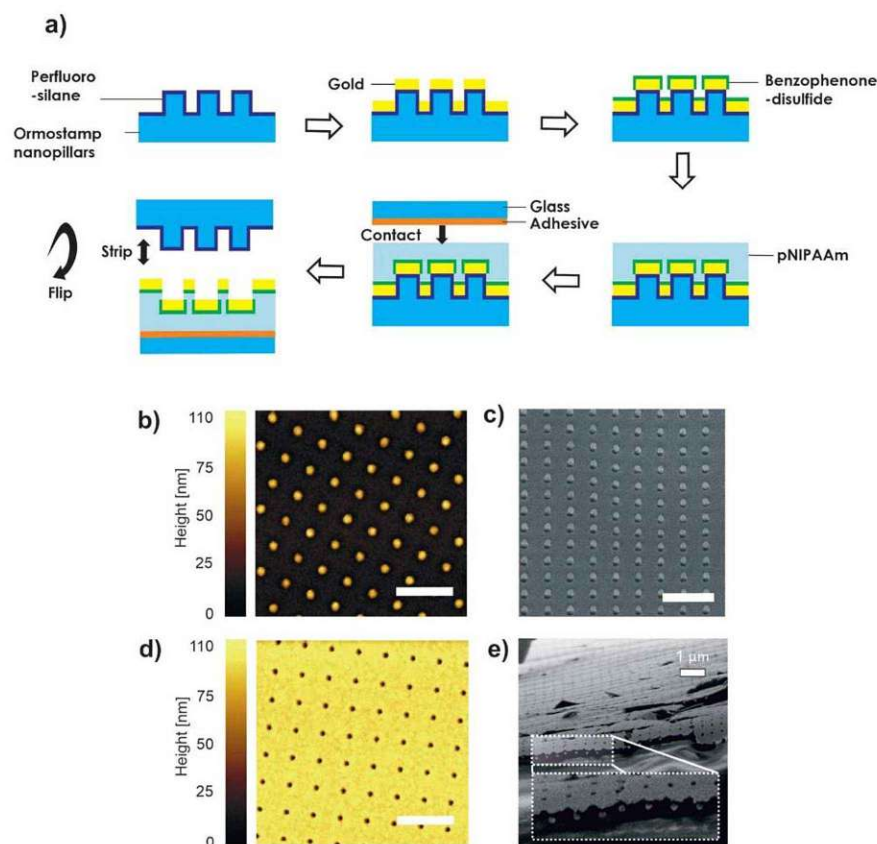


Fig. 2 (a) Schematic of the preparation steps of the investigated NHA + NP nanostructure, (b) AFM image of the template with arrays of nanopillars cast to OrmoStamp, (c) SEM image after coating of the template with a 50 nm thick gold layer, (d) AFM image of the topography of the stripped surface with gold NHA, and (e) SEM image of a broken edge of the NHA + NP structure tethered to a solid surface via the responsive pNIPAAm-based polymer. All scale bars are 1 μm in length.

ively. The non-dispersive nature of the λ_A resonance indicates it can be ascribed to the LSP mode.

A more detailed dependence of the transmission spectra on temperature T was investigated for the normal angle of incidence $\theta = 0$ (Fig. 3d). The spectra were measured using a different light source (supercontinuum laser) in order to extend the wavelength range to 900 nm, which allowed us to observe an additional feature manifested as a transmission peak at $\lambda_C^p = 810$ nm. Moreover, this showed more clearly that close to λ_B^d , a peak appeared at a wavelength λ_B^p . It is worth noting that the measured transmission spectra were normalized with that obtained for a flat 50 nm thick gold film, which exhibited a rapidly decreasing transmission with wavelength in the red and near infrared region of the spectrum. Therefore, the measurement of absolute transmission values was not possible, and thus only relative values are presented. In addition, the spectral positions of the resonances in Fig. 3a, b and d slightly differ since they were measured with different

(although fabricated under identical conditions) NHA + NP nanostructures.

Identification of plasmonic modes aided by simulations

The five observed resonant features in the measured transmission spectra were identified using numerical finite difference time domain (FDTD) simulations. This model was employed to calculate the absorption wavelength spectra and near-field distribution of the electromagnetic field occurring in the structure upon a plane wave normally impinging at its surface. The simulations of the absorption spectra allowed us to distinguish the resonant excitation of the LSP and PSP modes (which is accompanied with damping) from other features occurring in the transmission spectrum, which are related to the interference between multiple specular and non-specular diffracted beams and their falling after the horizon in the superstrate or substrate. As shown in Fig. 4a (blue curve), we initially analyzed a structure composed of only arrays of

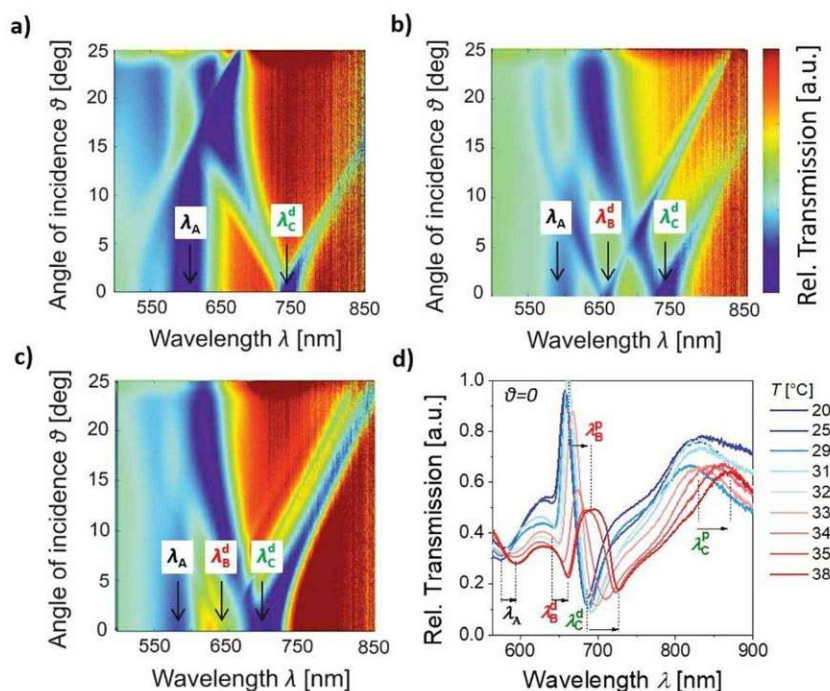


Fig. 3 Measured dependence of wavelength transmission spectra on angle of incidence, θ , for the NHA + NP structure in contact with (a) air ($n_s = 1$ and $n_h = 1.48$), (b) for the collapsed state of the pNIPAAm-based cushion that is in contact with water at $T = 40$ °C ($n_s = 1.33$ and $n_h = 1.48$), and (c) for the swollen state of pNIPAAm cushion in water at $T = 22$ °C ($n_s = 1.33$ and $n_h = 1.37$). (d) Comparison of the wavelength transmission spectra for θ and NHA + NP structure in contact with water at varying temperature, T . The transmission spectra were normalized with that measured for the flat structure without the perforated Au film.

cylindrically shaped nanoparticles (NPs with a height of $h = 50$ nm, average diameter of $D = 100$ – 120 nm, and period of $\Lambda = 460$ nm) embedded between dielectrics with the refractive indices of $n_h = 1.47$ and $n_s = 1.33$. The simulated spectrum reveals that the resonance associated with the coupling to LSP on the arrays of NPs is manifested as a strong absorption peak at a wavelength of about 707 nm. The complementary NHA structure was composed of a 50 nm thick gold film that was perforated with arrays of cylindrical nanoholes exhibiting the same diameter D and sandwiched between the same dielectrics with refractive indices of $n_h = 1.47$ and $n_s = 1.33$. The absorption spectrum in Fig. 4a (red curve) shows three resonances located at the wavelengths of $\lambda_A = 630$ nm, $\lambda_B = 676$ nm, and $\lambda_C = 774$ nm. At these wavelengths, the near-field distribution of the electric field amplitude $|E|$ (normalized with that of the incidence plane wave $|E_0|$) was simulated, as can be observed in the right part of Fig. 4a. These plots reveal that the resonance at wavelength λ_A exhibits the characteristics of the dipolar LSP mode, which confines the field inside the nanohole. The resonance at the longer wavelength λ_B shows a more delocalized field profile on the top interface of the gold film with the superstrate $n_s = 1.33$, which confirms it is due to first-order diffraction coupling to the traveling PSP mode at this

surface. The resonance at the NIR wavelength λ_C is accompanied with the confinement of the electric field at the bottom gold layer interface with the dielectric $n_h = 1.47$, which peaks at the mouth of the pore and its distribution suggests the main origin corresponds to the first-order diffraction coupling to the PSPs traveling along the bottom gold film surface. It should be noted that these simulations were carried out for the mouth of the nanopores filled by a dielectric with a refractive index n_s since the fabrication procedure involving stripping from arrays of nanopillars suggests this geometry (see Fig. 2a).

The simulations in Fig. 4b (brown curve) reveal that the short wavelength resonance was blue-shifted to $\lambda_A = 621$ nm, the middle resonance blue-shifted to $\lambda_B = 672$ nm, and the long-wavelength resonance red-shifted to $\lambda_C = 813$ nm after the coupling of the nanohole arrays with the cylindrical nanoparticle arrays (NHA + NP). In these simulations, the gap distance between the bottom edge of the nanopore and the upper surface of the cylindrical shaped nanoparticle was set to $g = 50$ nm, which corresponds to the difference between the nanopillar height of 100 nm and the thickness of the gold layer of $h = 50$ nm (see Fig. 1 and 2). When the refractive index of the superstrate decreased from $n_s = 1.33$ (representing

2.2. Actuated Plasmonic Nanohole Arrays for Sensing and Optical Spectroscopy Applications

Paper

Nanoscale

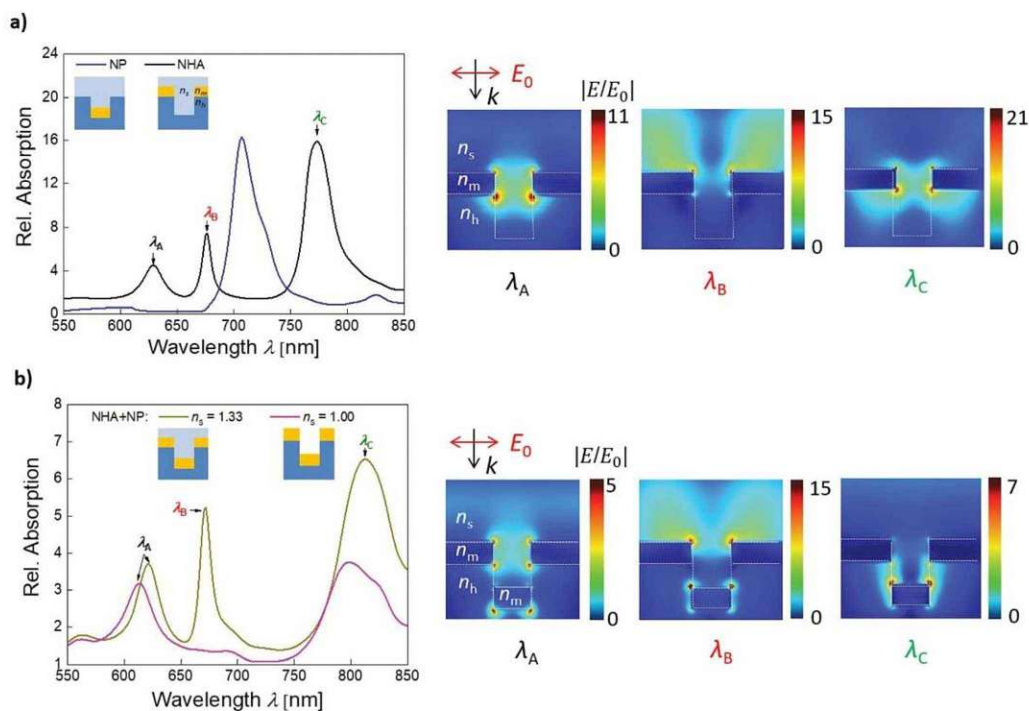


Fig. 4 Simulation-based investigation of the spectrum of supported plasmonic modes: absorption spectra obtained for normally incident beam at (a) structure with a thin gold film perforated with arrays of nanoholes (NHA), with arrays of cylindrical nanoparticles (NP), and for the combined geometry (NHA + NP) with superstrate refractive indices $n_s = 1$ and 1.33 and substrate refractive index $n_h = 1.47$. (b) Absorption spectrum simulated for the NHA + NP geometry for superstrate refractive indices $n_s = 1$ and 1.33. The substrate refractive index was of $n_h = 1.47$, gap distance between NP and NHA was of $g = 50$ nm, period of $\Lambda = 460$ nm, diameter averaged between $D = 100$ – 120 nm, and height of $h = 50$ nm. The cross-section of spatial distribution of the electric field amplitude was simulated for the plasmonic modes as indicated in the inset.

water) to $n_s = 1$ (representing air), the middle-wavelength resonance disappeared, as shown in Fig. 4b (green curve). This observation agrees with the measurements presented in Fig. 3 and confirms that the middle resonance occurs due to the first-order diffractive coupling to the PSP mode at the outer gold layer surface, which is the most sensitive to variations in refractive index on the upper interface (superstrate n_s). In addition, this refractive index decrease led to a slight blue shift in λ_A and λ_C since the field distribution corresponding to these resonances also partially probe the dielectric n_s . The spatial profile of the near field-enhanced electric field amplitude in the right part of Fig. 4b shows that the presence of gold disk nanoparticles slightly perturbed the nanohole LSP resonance at λ_A as the field is dragged to the bottom part of the disk nanoparticle. The resonance at λ_B due to the PSPs traveling on the top interface only weakly couples with the disk nanoparticles, contrary to the bottom PSP mode λ_C , which exhibits a field distribution with a more pronounced confinement in the gap.

Interestingly, the simulations predicted that only three plasmonic modes are supported in the investigated wavelength

range (Fig. 4b, brown curve) when the geometry of NHA (with three plasmonic modes, black curve Fig. 4a) and NP arrays (with one mode, blue curve in Fig. 4a) are combined to yield the experimentally investigated structure NHA + NP. However, five features were identified in the experimental transmission data presented Fig. 3, which is greater than the number of predicted plasmonic modes. The discrepancy between the simulated absorption spectra and experimentally measured specular transmission can be explained by the Fano shape of the two measured transmission resonances. The middle wavelength peak at λ_B^p and dip at λ_B^d can be attributed to the excitation of a single PSP mode at the interface of the structure with superstrate n_s and its asymmetric shape can be ascribed to the interference with additional waves generated by the structure in a broader wavelength range (previously observed for related plasmonic nanostructure by simulations³). Similarly, the long wavelength peak at λ_C^p and dip at λ_C^d can be attributed to the excitation of the PSP mode at the opposite interface of the structure with superstrate n_h .

In the next step, we performed more detailed simulations to reveal the spectral detuning of the resonances by the refrac-

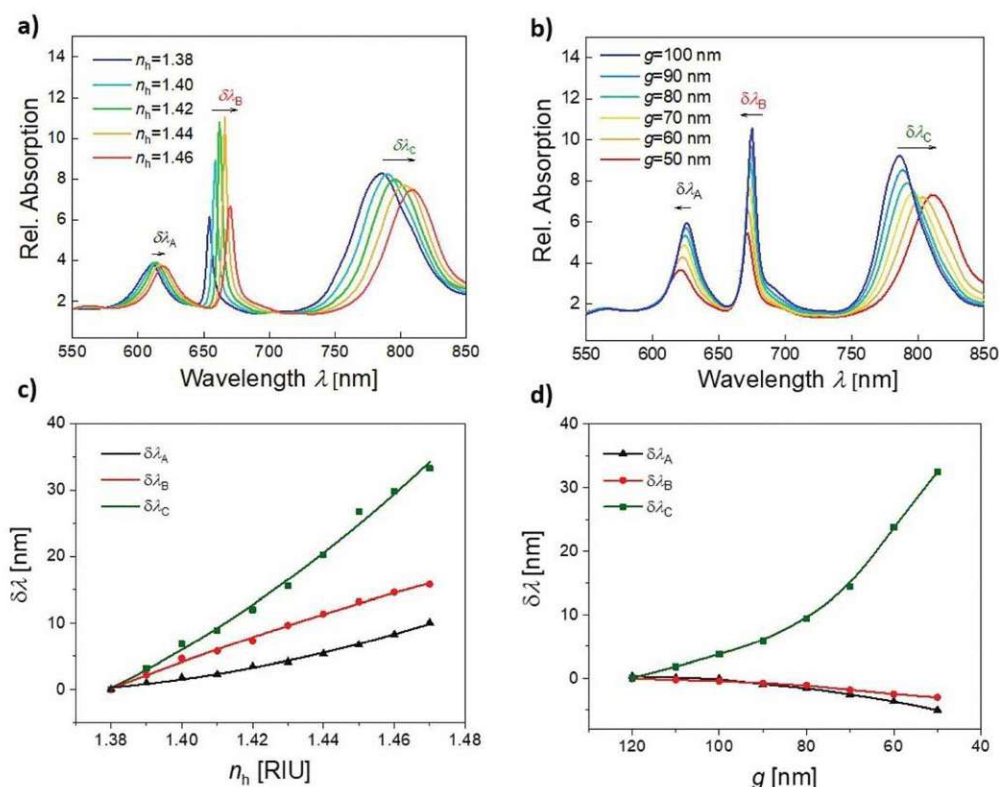


Fig. 5 Simulated absorption spectra for the structure NHA + NP for varying: (a) refractive index of substrate n_h , and (b) distance g between NHA and NP. From these spectra, the spectral shift of three resonant features were determined for changes in (c) n_h and (d) g . The superstrate refractive index was set to $n_s = 1.33$, the substrate refractive index for (b) and (d) was $n_h = 1.47$, gap distance between NP and NHA for (a) and (c) was set as $g = 50$ nm, period was $\Lambda = 460$ nm, average diameter between $D = 100$ – 120 nm, and height $h = 50$ nm.

index changes of the bottom dielectric n_h and distance g between the gold NPs and NHA. These simulations represent the expected effect of the swelling and collapsing of the pNIPAAm-based hydrogel cushion. In general, an increase in swelling is assumed to be accompanied with a prolongation of distance g , a decrease in polymer volume content, and consequently a decrease in the refractive index n_h . Fig. 5a and b show that the refractive index n_h gradually increased from 1.38 to 1.46 and distance g varied between 50 and 100 nm, respectively. The increase in the substrate refractive index n_h led to a redshift for all three resonances (Fig. 5a), which is consistent with the experimental data presented in Fig. 3d. For small changes in the refractive index, the variations in the resonant wavelengths can be assumed to be linear, and accordingly, the determined refractive index sensitivity of $\delta\lambda_B/\delta n_h = 190$ nm RIU $^{-1}$ and $\delta\lambda_C/\delta n_h = 390$ nm RIU $^{-1}$ were obtained from the simulated data. These values are in the range reported for another SPR sensor configuration, which utilizes grating coupling to PSP modes.⁴⁷ The lower sensitivity of $\delta\lambda_A/\delta n_h = 90$ nm RIU $^{-1}$ for the LSP mode is also in accordance with the previous

observations on LSPR.⁴⁴ Similarly, the refractive index sensitivity of the three plasmon modes to a change in the refractive index of the superstrate n_s was determined to be $\delta\lambda_A/\delta n_s = 137$ nm RIU $^{-1}$, $\delta\lambda_B/\delta n_s = 260$ nm RIU $^{-1}$ and $\delta\lambda_C/\delta n_s = 83$ nm RIU $^{-1}$ according to the data presented in Fig. S2.† Apparently, the highest sensitivity is observed for the mode at λ_B , which is ascribed to the PSP at the outer interface, where the field is dominantly confined.

The simulated spectra for varying gap distances g are presented in Fig. 5b. They show more complex behavior and the resonances λ_A and λ_B are weakly blue-shifted with a decrease in distance g , while λ_C is strongly red-shifted. These changes exhibit non-linear behavior, and for the shorter distances of g , they are more pronounced than for the longer distances of g . Therefore, this observation can be attributed to the near-field coupling between the gold NPs and NHA, which is particularly pronounced for the resonance λ_C with its field tightly confined in the gap (see right part of Fig. 4b). Interestingly, for the long distance g , an increase in the absorption close to the wavelength of 700 nm occurred, which may be due to the re-occur-

rence of the LSP resonance supported by gold NP arrays not coupled with NHA, as presented in Fig. 4a.

Actuating of plasmonic modes

The swelling and collapsing of the pNIPAAm-based hydrogel cushion by varying the temperature around its LCST were further exploited for actuating the plasmonic modes supported by the prepared structure NHA + NP. In this experiment, we varied temperature in the range of $T = 20\text{--}38\text{ }^\circ\text{C}$ and tracked the resonant positions of all the identified spectral features, including the transmission dip at $\lambda_A = 577\text{ nm}$ due to the LSP in the nanoholes, spectral dip at $\lambda_B^d = 641\text{ nm}$ and peak at $\lambda_B^p = 658\text{ nm}$, which are ascribed to the Fano resonance of the PSPs on the top NHA surface, and spectral dip at $\lambda_C^d = 684\text{ nm}$ and peak at a wavelength of $\lambda_C^p = 825\text{ nm}$ attributed to the Fano resonance of PSP at the bottom NHA surface coupled with arrays of NPs (measured at temperature $T = 20\text{ }^\circ\text{C}$). The obtained response was measured with time upon a step-wise increase and decrease in temperature T according to the analysis of the spectra presented in Fig. 3d. The obtained time kinetics in Fig. 6 show that the changes are reversible. The features presented in Fig. 6a show a gradual increase in spectral position with an increase in temperature T . The Fano resonance features λ_B^d and λ_B^p exhibit similar shifts and the maximum change of about 20 nm occurred when the temperature increased from $T = 22\text{ }^\circ\text{C}$ to $38\text{ }^\circ\text{C}$. The highest slope in the shift occurred close to the LCST of pNIPAAm of $32\text{ }^\circ\text{C}$. At a higher temperature, it was not possible to track the spectral shift in the peak due to the fact that it became weakly pronounced. The spectral dip λ_C^d showed the same trend and exhibited a stronger maximum shift of 40 nm for the temperature increase from $T = 22\text{ }^\circ\text{C}$ to $38\text{ }^\circ\text{C}$.

Interestingly, the dependence of λ_A and λ_C^p shows different behavior. When the temperature increased above $T = 22\text{ }^\circ\text{C}$, an initial decrease in the resonance λ_A occurred followed by an increase with a local maximum at $T = 29\text{ }^\circ\text{C}$, then it decreased again, and above the LCST of pNIPAAm, it rapidly increased and shifted by about 20 nm. The peak position λ_C^p showed a complementary trend and it strongly decreased by 15 nm when the temperature increased from $22\text{ }^\circ\text{C}$ to $27\text{ }^\circ\text{C}$, and then it increased with the local maximum at $30\text{ }^\circ\text{C}$, and when passing the LCST it rapidly redshifted by 38 nm. These anomalous dependencies can be explained by the competing effect of the near-field coupling (which is dominantly controlled by distance g and exhibit non-linear dependence, as shown in Fig. 5d) and refractive index change, which shifts the resonance linearly (see Fig. 5c). The anomalous changes occurred below the LCST of pNIPAAm, which indicates that distance g is not directly proportional to the swelling degree of the hydrogel cushion layer, and other effects such as filling the pores with the swelling polymer networks can occur.

Local probing of molecular binding events

To explore the potential of the developed hybrid nanostructure for applications in sensing, we employed the plasmonic resonances for local probing of molecular binding events at specific parts. In the first experiment, we directly monitored the binding of biomolecules in the pNIPAAm-based hydrogel cushion from the associated refractive index changes. These changes detuned the SPR wavelengths, where the excitation of the modes probing different the sub-parts of the structure occurred. After the stripping of the structure, the outer gold surface and the mouth of the pores were passivated by the thiol SAM with oligoethylene glycol (OEG) groups. Then, the pNIPAAm-based hydrogel cushion was post-modified *in situ* by covalent coupling of mouse immunoglobulin G, mIgG. The

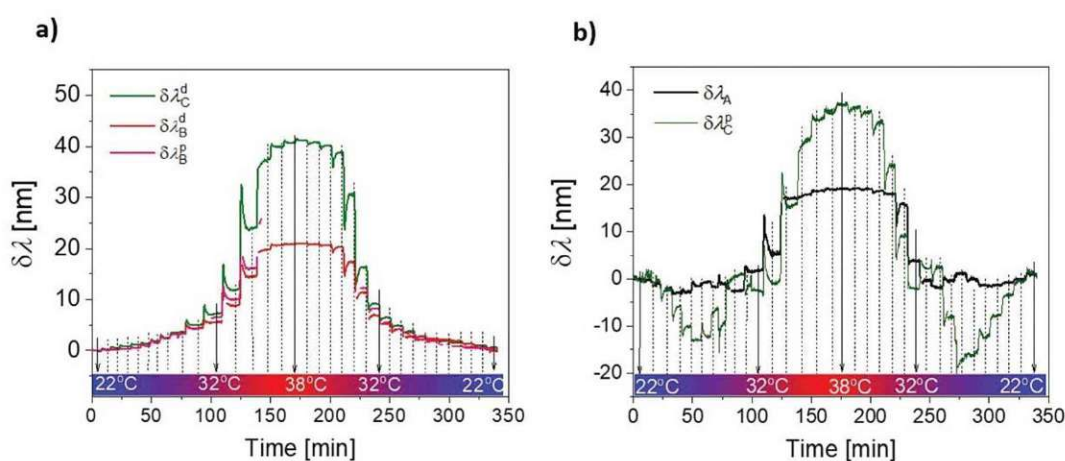


Fig. 6 Dependence of spectral position of plasmonic features plotted as function of time for different temperatures in the range of $T = 22\text{ }^\circ\text{C}$ to $T = 38\text{ }^\circ\text{C}$: (a) gradual variation in the spectral positions of dips λ_B^d and λ_C^d and peak at λ_B^p and (b) anomalous variations in the spectral positions of dip λ_A and peak λ_C^p .

spectral positions of the resonances at λ_A and λ_C^d were monitored by tracking their spectral detuning upon the surface reactions, as can be seen in Fig. 7a. These two resonances were

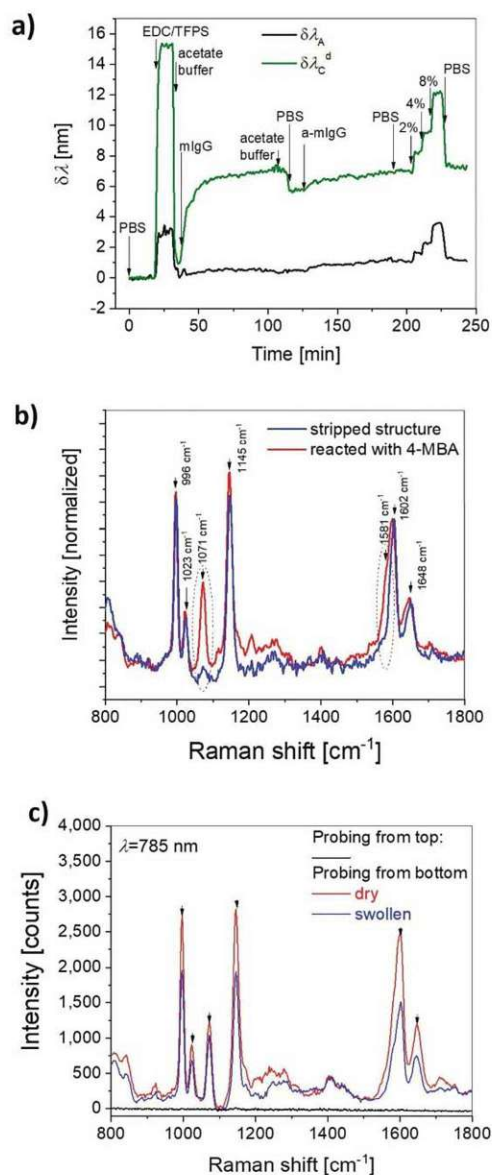


Fig. 7 (a) Probing of covalent coupling of immunoglobulin G molecules (IgG) to pNIPAAm hydrogel polymer networks with the plasmonic modes centred at λ_A and λ_C^d . (b) SERS spectra measured before and after post-modification of the stripped area of gold with 4-MBA, as measured with a laser wavelength of 785 nm. The structure NHA + NP was swollen in water. (c) Comparison of the acquired Raman spectra from the top (dry NHA + NP structure) and bottom (swollen and dry NHA + NP structure).

selected since they probe different parts of the structure and are well pronounced in the transmission spectrum. To activate the carboxylic groups within the hydrogel cushion, they were reacted with EDC/TFPS and then a solution with mIgG was flowed over the surface in the time range of 45 to 120 min. After rinsing with a buffer at time 120 min, resonance λ_C^d shifted by 6 nm due to the covalent coupling of mIgG, while resonance λ_A showed a much weaker shift of about 0.5 nm. This observation proves that the mIgG molecules could diffuse through the pores and bind to the bottom swollen hydrogel (probed at λ_C^d), while they do not attach to the pores (probed at λ_A). Then, a series of PBS solutions with sucrose dissolved at a concentration of 2%, 4% and 8% was flowed over the surface to change the bulk refractive index by $2.8, 5.6$ and 11.2×10^{-3} RIU, respectively. These low molecular weight molecules did not interact with the structure but freely diffused into the pNIPAAm-based hydrogel, and thus changed the refractive index on both sides of superstrate n_s and substrate hydrogel cushion n_h . From the measured shifts in λ_A and λ_C^d , the sensitivity of these resonances was determined to be $d\lambda_A/dn = 218$ nm RIU $^{-1}$ and $d\lambda_C^d/dn = 454$ nm RIU $^{-1}$, respectively. These values are close to the predicted sum of the sensitivities $d\lambda/dn_s$ and $d\lambda/dn_h$, and support the fact that the refractive index changes at both interfaces of the permeable thin gold film.

In the second experiment, we tested the structure as a substrate for SERS detection. Accordingly, we probed the upper and bottom interfaces by a laser beam focused from the superstrate or substrate side by a lens with a numerical aperture of 0.5. The laser beam had a wavelength of $\lambda = 785$ nm, which is close to the resonance observed at λ_C^p associated with the confinement of the incident field in the gap between the NHA and NP (see Fig. 4b). In this experiment, we directly used a structure that was stripped and compared the acquired Raman (Stokes shifted) spectra with that acquired for the same structure in which the upper gold surface and the pore mouth were modified with a Raman-active 4-MBA monolayer (see schematic in Fig. 1b). The results presented in Fig. 7b show a series of Raman peaks in the spectral range of 800–1800 cm^{-1} for the pristine stripped structure that was probed from the bottom substrate through the pNIPAAm-based cushion. These peaks can be ascribed to the benzophenone molecules at the inner gold interface since their spectral positions are close to that reported in previous works.⁴⁸ After modifying the pore mouth and the upper gold interface with 4-MBA, two additional peaks appeared at 1071 cm^{-1} (aromatic ring breathing, symmetric C–H in-plane bending, and C–S stretching) and 1581 cm^{-1} (aromatic ring C–C stretching, asymmetric C–H in-plane bending). These spectral positions are close to that observed previously for this molecule.^{48,49}

Finally, a comparison of the Raman peak intensity was carried out for probing from the top (through the superstrate) and from the bottom (through the pNIPAAm cushion substrate). As can be seen in Fig. 7c, the Raman peaks were observed only for the probing from the bottom, where the mode at λ_C^p could be efficiently excited with the laser beam at the wavelength of 785 nm. In addition, the spectral tuning of

this mode by collapsing and swelling the structure led to variations in the Raman peak intensity. An increase in the Raman peak intensity by about 45% occurred by collapsing the structure (by drying) with respect to the geometry when the hydrogel cushion was swollen in water. This can be attributed to the potentially stronger field intensity enhancement in the gap between the nanopores in the NHA and the bottom metallic nanoparticles as well as the shift in the resonance at λ_C^p to its optimized spectral position with respect to the excitation wavelength and Raman scattered peaks, which was observed to provide most efficient SERS.^{50–55}

Conclusions

We developed a new approach for the preparation of a hybrid plasmonic nanostructure that can be actuated and consists of arrays of nanoholes in a thin gold film, which is connected to arrays of gold nanoparticles by a responsive hydrogel cushion attached to a solid substrate. We explored the spectrum of the plasmonic modes supported by the structure and identified their origin due to the resonant excitation of three localized surface plasmons (confined in the nanopores and at the surface of the nanoparticles) and diffractive coupling to propagating surface plasmons (traveling along the top and bottom interfaces of the thin gold film). By swelling and collapsing the hydrogel cushion, the characteristics of these modes could be changed on-demand and the field confinement as well as resonant wavelength (up to 50 nm shifts) could be actively actuated. Among the modes, the near-field coupling between the nanoparticles and nanoholes was observed, and the simulations predicted that it leads to strong confinement of the electromagnetic field in the respective gap in the near-infrared part of the spectrum. This is particularly attractive for biosensing applications, as demonstrated by SPR observation of the attachment of 160 kDa IgG molecules inside the structure and SERS measurement of low molecular weight Raman active 4-MBA molecules immobilized in the pore mouth. In addition, this structure offers a unique opportunity to open and close the pores by swelling and collapsing the hydrogel cushion. Accordingly, the pores can be switched between the dead-end geometry and open state when water molecules are actively driven through the pores, dragging dissolved biomolecules across the plasmonic hotspot by diffusion.

Experimental

Materials

OrmoStamp® resin was purchased from Micro Resist Technology GmbH (Germany). Ostemer 322 Crystal Clear was purchased from Mercene Labs AB (Sweden). Polydimethylsiloxane Sylgard 184 (PDMS) was obtained from Dow Corning (USA). Trichloro(1*H*,1*H*,2*H*,2*H*-perfluorooctyl)silane (perfluoro-silane), dimethyl sulfoxide (DMSO) and 1-ethyl-3-(3-dimethylaminopropyl)carbodiimide (EDC) were obtained from Sigma Aldrich (Germany).

(11-Mercaptoundecyl)triethylene glycol (PEG-thiol, SPT-0011) was purchased from SensoPath Technologies Inc. (USA). The pNIPAAm-based terpolymer composed of *N*-isopropylacrylamide, methacrylic acid, and 4-methacryloyloxybenzophenone (in a ratio of 94 : 5 : 1), benzophenone-disulfide and 4-sulfotetrafluorophenol (TFPS) were synthesized in our laboratory, as previously reported.^{56,57} IgG from mouse serum (mIgG, I 5381) and Tween 20 (P9416) were purchased from Sigma Aldrich (Austria), and phosphate-buffered saline (PBS) and sodium acetate were obtained from VWR Chemicals (Austria). Goat anti-mouse IgG (a-mIgG, A11375) was acquired from Life Technologies, (Eugene OR, US).

UV-nanoimprint lithography

A template structure bearing arrays of nanopillars was fabricated from a silicon master that carried 1 cm² rectangular arrays of nanoholes with a diameter of $D = 90$ nm, depth 260 nm, and period $\Lambda = 460$ nm, fabricated by Temicon GmbH (Germany). 200 μ L of OrmoPrime was spun on a clean BK7 glass substrate at 4000 rpm for 60 s and hard-baked at 150 °C for 5 min. The BK7 substrate coated with OrmoPrime was contacted with the silicon master using a drop of OrmoStamp and kept still for 10 min to spread over the structure and fill the pores. The OrmoStamp was cured using UV light at $\lambda = 365$ nm with the irradiation dose of 1 J cm⁻² (UV lamp Bio-Link 365, Vilber Lourmat). Then, the silicon master was carefully detached, leaving the BK7 substrate with an imprinted pattern of nanopillars in the OrmoStamp resin. The fabricated arrays of nanopillars were treated with UV-ozone for 5 min to remove the excess OrmoStamp and activate the surface for silanization. An anti-adhesive layer was deposited on the OrmoStamp structure under an argon atmosphere using 13 μ L of trichloro(1*H*,1*H*,2*H*,2*H*-perfluorooctyl)silane in a desiccator (volume 5.8 L) heated to $T = 250$ °C for 20 min. A 50 nm thin layer of gold was deposited on the arrays of nanopillars, serving as a template, by vacuum thermal evaporation (HHVAUTO 306 from HHV Ltd) at a deposition rate of 2 Å s⁻¹ in a vacuum greater than 10⁻⁶ mbar. Each sample consisted of a nanostructured region and a flat region for reference in the optical measurements.

Deposition of the responsive polymer

The OrmoStamp arrays of nanopillars coated with 50 nm of gold were incubated overnight in a 1 mM solution of benzophenone-disulfide in DMSO to form a self-assembled monolayer serving as a linker. Then, this structure was coated with a uniform layer of pNIPAAm-based terpolymer by spin-coating 3 wt% ethanolic solution of the polymer at a spin rate of 2000 rpm for 1 min. The layer of the pNIPAAm-based terpolymer was dried overnight under vacuum at 50 °C yielding, a thickness of 230 nm. The resulting polymer film was crosslinked *via* the benzophenone moieties by UV light at $\lambda = 365$ nm with an irradiation dose of 10 J cm⁻².

Template stripping

A drop of Ostemer epoxy was spread on clean BK7 glass by contacting it with a flat piece of PDMS and irradiating it with UV-

light at $\lambda = 365 \text{ nm}$ (2 J cm^{-2}). The PDMS block was peeled-off leaving a glass substrate with a flat layer of pre-cured Ostemer epoxy on its top. Then, the Ostemer surface was pressed against the template coated with the crosslinked pNIPAAm-based film and incubated overnight at $50 \text{ }^\circ\text{C}$ to allow its attachment to the pNIPAAm-based surface *via* its epoxy groups. Due to the pre-curing step, the Ostemer did not penetrate the pNIPAAm polymer network layer. Finally, the BK7 substrate with a layer of Ostemer was used to strip off the pNIPAAm-based film with the layer of gold from the template modified with the thin anti-adhesive layer.

Morphological characterization

Atomic force microscopy (AFM) measurements of the patterned structures in air were performed in tapping mode using PPP-NCHR-50 tips (Nanosensors, Switzerland) and a PicoPlus instrument (Molecular Imaging, Agilent Technologies, USA). In addition, a scanning electron microscope (Zeiss Supra 40 VP (Carl Zeiss Microscopy GmbH, Germany) was used for imaging of the longitudinal and cross-section interfaces of the nanostructures at an electron high tension of $\text{EHT} = 5 \text{ kV}$. The height, diameter and lateral spacing of the nanoscale features were determined using the Gwyddion free software (version 2.47 from gwyddion.net).

Optical configuration for angular-wavelength transmission measurement

Transmission optical spectra were acquired using a polychromatic light beam emitted from a halogen lamp (LSH102 LOT-Oriel, Germany), which was coupled to a multimode optical fiber and collimated with a lens. It was made incident at the structure and the transmitted beam was collected by a lens to another multimode optical fiber and delivered to a spectrometer (HR4000, Ocean Optics, USA). The obtained transmission spectra were normalized with that obtained on a reference flat 50 nm thick gold film. A flow-cell with a Peltier element⁵⁸ connected to a controller from Wavelength Electronics Inc. (USA) was clamped against the investigated structure to control the temperature of the liquid flowed over its surface. Deionized water was flowed by employing a peristaltic pump from Ismatec (Switzerland). The investigated structure with a flow cell was mounted on a rotation stage driven by a stepper motor from Huber GmbH (Germany) to control the angle of incident light, θ . Transmission spectra were recorded using the in-house developed Labview software and processed using a dedicated Python script.

Tracking of resonant wavelengths

Polychromatic light emitted from a supercontinuum laser source (WhiteLaser Micro, Fianium, UK) was collimated and the beam was expanded and spectrally filtered by a long-pass filter. The beam was made incident at a normal angle on the structure mounted in the temperature-stabilized flow cell. The transmitted beam was collected by a GRIN lens to a multimode fiber and delivered to the input of a spectrometer (S2000, Ocean Optics, USA). The acquired transmission spectra were

normalized to that measured for a reference flat gold film (thickness of 50 nm) and analyzed using the SPR UP software developed at the Institute of Photonics and Electronics, Czech Academy of Sciences.

Finite-difference time-domain simulations

FDTD simulations were performed using the Lumerical FDTD Solutions software. The geometry of the nanoparticle arrays was described using Cartesian coordinates with the x - and y -axis in the plane and the z -axis perpendicular to the plane of the arrays. Infinite arrays were considered in the simulations by choosing periodic boundary conditions (symmetric or anti-symmetric) along the x - and y -axis and using perfectly matched layers (PML) above and below the structure. For the field profile simulations, the simulation mesh was set to 2 nm over the volume of the unit cell. A transmission monitor was placed $0.4 \text{ }\mu\text{m}$ below the nanoparticle arrays and a 2D monitor in the xz -plane was employed for simulating the near field distribution of the electric field intensity. The structure was illuminated by a normally incident plane wave with its polarization set along the x -direction. The optical constants for Au were taken from the CRC Optical Data Tables ($450\text{--}950 \text{ nm}$). To consider the deviations in the experimental geometry from the (idealized) simulated geometry, the diameter D was varied in the range of $100\text{--}120 \text{ nm}$ and the respective optical response was averaged.

Immunoassay experiment

The substrate carrying the NHA + NP structure was clamped against a transparent flow-cell and loaded in an optical system for tracking of the SPR dips or peaks in the transmission spectrum. A polychromatic optical beam was made incident at a normal angle of incidence of $\theta = 0^\circ$ at the structure, and by analysis of the transmitted light spectrum, the variations in the resonant wavelengths were monitored with time. These variations were determined by fitting the acquired spectrum with a polynomial function, as reported previously,⁴⁷ and which allowed the spectral shifts of the dip or peak features to be measured with the accuracy of $0.1\text{--}0.01 \text{ nm}$, depending on the coupling strength and noise in the transmission spectrum. Firstly, the baseline in the resonant wavelength kinetics was established upon a flow of PBS for 20 min . Then, a mixture of EDC/TFPS dissolved in water at concentrations 75 and 21 mg mL^{-1} , respectively, was flowed over the structure for 10 min to activate the carboxylic moieties of the pNIPAAm hydrogel. The surface was quickly rinsed with $\text{pH } 5$ acetate buffer and reacted with a solution of $50 \text{ }\mu\text{g mL}^{-1}$ mouse IgG in the same buffer for 60 min to covalently attach the mIgG molecules to the polymer chains. Finally, the structure was rinsed with PBS, followed by the flow of PBS spiked with 2% , 4% and 8% sucrose ($\Delta n = 2.8 \times 10^{-3}$, 5.6×10^{-3} and $11.2 \times 10^{-3} \text{ RIU}$, respectively).

SERS experiments

The NHA + NP structure was incubated overnight in 1 mM ethanolic solution of 4-mercaptobenzoic acid to form a self-

2.2. Actuated Plasmonic Nanohole Arrays for Sensing and Optical Spectroscopy Applications

Paper

Nanoscale

assembled monolayer of SERS-active molecules. Prior to the experiment, the structure was rinsed with ethanol and dried. The SERS experiments were performed using an Xplora Raman microspectrometer (Horiba Scientific, France) with a $\times 50$ long working distance objective (numerical aperture of 0.5). The laser beam at $\lambda = 785$ nm was focused at the investigated NHA + NP structure. The spectrum was accumulated for 20 s.

Conflicts of interest

There are no conflicts to declare.

Acknowledgements

DK acknowledges funding from the European Union's Horizon 2020 research and innovation programme under grant agreement no. 642787, Marie Skłodowska-Curie Innovative Training Network BIOGEL. SF, JS, JD, JH and UJ were supported by European Union's Horizon 2020 research and innovation programme under grant agreement no. 633937, project ULTRAPLACAD. PV, ML, and MDLC are grateful for the financing from the project jointly funded by Agence Nationale de la Recherche (ANR) and Austrian Science Fund (FWF) under the grant agreements ANR-15-CE29-0026 and I 2647, respectively. SF and JD received support by the Austrian Research Promotion Agency (FFG) with grant agreement no. 861578 (ERANET project PLABAN). JS and JH acknowledge financial support from the Czech Science Foundation, grant agreement #19-02739S. The Raman analysis was performed at the Vibrational Spectroscopy platform of the IMMM, Université du le Mans.

Notes and references

- 1 T. W. Ebbesen, H. J. Lezec, H. F. Ghaemi, T. Thio and P. A. Wolff, *Nature*, 1998, **391**, 667–669.
- 2 M. Najiminaini, F. Vasefi, B. Kaminska and J. J. L. Carson, *Sci. Rep.*, 2013, **3**, 1–7.
- 3 M. S. Ahn, T. Chung and K. H. Jeong, *Nanoscale*, 2018, **10**, 6313–6317.
- 4 A. G. Brolo, S. C. Kwok, M. G. Moffitt, R. Gordon, J. Riordon and K. L. Kavanagh, *J. Am. Chem. Soc.*, 2005, **127**, 14936–14941.
- 5 Q. Zhang, L. Wu, T. I. Wong, J. Zhang, X. Liu, X. Zhou, P. Bai, B. Liedberg and Y. Wang, *Int. J. Nanomed.*, 2017, **12**, 2307–2314.
- 6 A. G. Brolo, E. Arctander, R. Gordon, B. Leathem and K. L. Kavanagh, *Nano Lett.*, 2004, **4**, 2015–2018.
- 7 P. Zheng, S. K. Cushing, S. Suri and N. Wu, *Phys. Chem. Chem. Phys.*, 2015, **17**, 21211–21219.
- 8 S. Kumar, S. Cherukulappurath, T. W. Johnson and S. Oh, *Chem. Mater.*, 2014, **26**, 6523–6530.
- 9 T. Wu and Y. W. Lin, *Appl. Surf. Sci.*, 2018, **435**, 1143–1149.

- 10 S. P. Sahu, A. Mahigir, B. Chidester, G. Veronis and M. R. Gartia, *Nano Lett.*, 2019, **19**, 6192–6202.
- 11 M. E. Stewart, N. H. Mack, V. Malyarchuk, J. A. N. T. Soares, T.-W. Lee, S. K. Gray, R. G. Nuzzo and J. A. Rogers, *Proc. Natl. Acad. Sci. U. S. A.*, 2006, **103**, 17143–17148.
- 12 A. A. Yanik, A. E. Cetin, M. Huang, A. Artar, S. H. Mousavi and A. Khanikaev, *Proc. Natl. Acad. Sci. U. S. A.*, 2011, **108**, 11784–11789.
- 13 K. Nakamoto, R. Kurita, O. Niwa, T. Fujii and M. Nishida, *Nanoscale*, 2011, **3**, 5067–5075.
- 14 X. Li, M. Soler, C. I. Özdemir, A. Belushkin, F. Yesilköy and H. Altug, *Lab Chip*, 2017, **17**, 2208–2217.
- 15 H. Im, H. Shao, Y. I. Park, V. M. Peterson, C. M. Castro, R. Weissleder and H. Lee, *Nat. Biotechnol.*, 2014, **32**, 490–495.
- 16 A. A. Yanik, M. Huang, O. Kamohara, A. Artar, T. W. Geisbert, J. H. Connor and H. Altug, *Nano Lett.*, 2010, **10**, 4962–4969.
- 17 J. A. Jackman, E. Linaryd, D. Yoo, J. Seo, W. B. Ng, D. J. Klemme, N. J. Wittenberg, S. H. Oh and N. J. Cho, *Small*, 2016, **12**, 1159–1166.
- 18 J. Gomez-Cruz, S. Nair, A. Manjarrez-Hernandez, S. Gavilanes-Parra, G. Ascanio and C. Escobedo, *Biosens. Bioelectron.*, 2018, **106**, 105–110.
- 19 L. Tu, X. Li, S. Bian, Y. Yu, J. Li, L. Huang, P. Liu, Q. Wu and W. Wang, *Sci. Rep.*, 2017, **7**, 11020.
- 20 J. T. Lim, Y. S. Yoon, W. Y. Lee, J. T. Jeong, G. S. Kim, T. G. Kim and S. K. Lee, *Nanoscale*, 2017, **9**, 17224–17232.
- 21 S. Kumar, G. G. Wolken, N. J. Wittenberg, E. A. Arriaga and S. H. Oh, *Anal. Chem.*, 2015, **87**, 1973–1977.
- 22 M. P. Jonsson, P. Jönsson, A. B. Dahlin and F. Höök, *Nano Lett.*, 2007, **7**, 3462–3468.
- 23 L. Plucinski, M. Ranjan, W. R. Arnold, A. Ameen, T. Chang, A. Hsiao, G. Logan and A. Das, *Biosens. Bioelectron.*, 2016, **75**, 337–346.
- 24 W.-C. Liu and T. D. Ping, *Phys. Rev. B: Condens. Matter Mater. Phys.*, 2002, **65**, 155423.
- 25 F. J. Garcia-Vidal, L. Martin-Moreno, T. W. Ebbesen and L. Kuipers, *Rev. Mod. Phys.*, 2010, **82**, 729–787.
- 26 M. Horak, V. Krapek, M. Hrton, A. Konecna, F. Ligmajer, M. Stoeger-Pollach, T. Samoril, A. Patak, Z. Edes, O. Metelka, J. Babocký and T. Sikola, *Sci. Rep.*, 2019, **9**, 4004.
- 27 L. Wang, B. Xu, W. Bai, J. Zhang, L. Cai, H. Hu and G. Song, *Plasmonics*, 2012, **7**, 659–663.
- 28 C. Stelling and M. Retsch, *Adv. Mater. Interfaces*, 2018, **5**, 1–7.
- 29 R. Mohammadi, M. Ochs, A. Andrieu-Brunsen and N. Vogel, *J. Phys. Chem. C*, 2020, **124**, 2609–2618.
- 30 M. Hentschel, T. Weiss, S. Bagheri and H. Giessen, *Nano Lett.*, 2013, **13**, 4428–4433.
- 31 V. G. Kravets, A. V. Kabashin, W. L. Barnes and A. N. Grigorenko, *Chem. Rev.*, 2018, **118**, 5912–5951.
- 32 J. F. Masson, M. P. Murray-Méthot and L. S. Live, *Analyst*, 2010, **135**, 1483–1489.

Nanoscale

This journal is © The Royal Society of Chemistry 2020

2.2. Actuated Plasmonic Nanohole Arrays for Sensing and Optical Spectroscopy Applications

Nanoscale

Paper

- 33 C. Escobedo, *Lab Chip*, 2013, **13**, 2445–2463.
- 34 H. Im, S. H. Lee, N. J. Wittenberg, T. W. Johnson, N. C. Lindquist, P. Nagpal, D. J. Norris and S. H. Oh, *ACS Nano*, 2011, **5**, 6244–6253.
- 35 S. H. Lee, K. C. Bantz, N. C. Lindquist, S.-H. Oh and C. L. Haynes, *Langmuir*, 2009, **25**, 13685–13693.
- 36 B. Ai, Y. Yu, H. Möhwald, G. Zhang and B. Yang, *Adv. Colloid Interface Sci.*, 2014, **206**, 5–16.
- 37 J. Junesch, T. Sannomiya and A. B. Dahlin, *ACS Nano*, 2012, **6**, 10405–10415.
- 38 H. Im, J. N. Sutherland, J. A. Maynard and S.-H. Oh, *Anal. Chem.*, 2012, **84**, 1941–1947.
- 39 A. Barik, L. M. Otto, D. Yoo, J. Jose, T. W. Johnson and S. H. Oh, *Nano Lett.*, 2014, **14**, 2006–2012.
- 40 J. Dostálek and W. Knoll, *Plasmonics*, 2012, vol. 2.
- 41 Y. Zhao, G. Gaur, S. T. Retterer, P. E. Laibinis and S. M. Weiss, *Anal. Chem.*, 2016, **88**, 10940–10948.
- 42 C. Escobedo, A. G. Brolo, R. Gordon and D. Sinton, *Anal. Chem.*, 2010, **82**, 10015–10020.
- 43 N. Sharma, C. Petri, U. Jonas and J. Dostalek, *Opt. Express*, 2016, **24**, 2457.
- 44 N. Gisbert Quilis, M. van Dongen, P. Venugopalan, D. Kotlarek, C. Petri, A. Moreno Cencerrado, S. Stanesco, J. L. Toca Herrera, U. Jonas, M. Möller, A. Mourran and J. Dostalek, *Adv. Opt. Mater.*, 2019, **7**, 1–11.
- 45 N. Sharma, H. Keshmiri, X. Zhou, T. I. Wong, C. Petri, U. Jonas, B. Liedberg and J. Dostalek, *J. Phys. Chem. C*, 2016, **120**, 561–568.
- 46 A. Aulasevich, R. F. Roskamp, U. Jonas, B. Menges, J. Dostálek and W. Knoll, *Macromol. Rapid Commun.*, 2009, **30**, 872–877.
- 47 A. T. Reiner, N. G. Ferrer, P. Venugopalan, R. C. Lai, S. K. Lim and J. Dostálek, *Analyst*, 2017, **142**, 3913–3921.
- 48 Y. Fleger, Y. Mastai, M. Rosenbluh and D. H. Dressler, *Surf. Sci.*, 2009, **603**, 788–793.
- 49 N. G. Quilis, M. Lequeux, P. Venugopalan, I. Khan, W. Knoll, S. Boujday, M. L. de la Chapelle and J. Dostalek, *Nanoscale*, 2018, **10**, 10268–10276.
- 50 S. J. Lee, Z. Guan, H. Xu and M. Moskovits, *J. Phys. Chem. C*, 2007, **111**, 17985–17988.
- 51 M. Chirumamilla, A. Gopalakrishnan, A. Toma, R. P. Zaccaria and R. Krahn, *Nanotechnology*, 2014, **25**, 235303.
- 52 N. Guillot and M. L. de la Chapelle, *J. Quant. Spectrosc. Radiat. Transfer*, 2012, **113**, 2321–2333.
- 53 N. Guillot, B. Fremaux, H. Shen, O. Péron, E. Rinnert, T. Toury and M. Lamy De La Chapelle, *Appl. Phys. Lett.*, 2010, **97**, 023113.
- 54 S. Kessentini, D. Barchiesi, C. D'Andrea, A. Toma, N. Guillot, E. Di Fabrizio, B. Fazio, O. M. Maragó, P. G. Gucciardi and M. Lamy De La Chapelle, *J. Phys. Chem. C*, 2014, **118**, 3209–3219.
- 55 F. J. Colas, M. Cottat, R. Gillibert, N. Guillot, N. Djaker, N. Lidgi-Guigui, T. Toury, D. Barchiesi, A. Toma, E. Di Fabrizio, P. G. Gucciardi and M. L. De La Chapelle, *J. Phys. Chem. C*, 2016, **120**, 13675–13683.
- 56 P. W. Beines, I. Klosterkamp, B. Menges, U. Jonas and W. Knoll, *Langmuir*, 2007, **23**, 2231–2238.
- 57 K. Sergelen, C. Petri, U. Jonas and J. Dostalek, *Biointerphases*, 2017, **12**, 051002.
- 58 M. Toma, U. Jonas, A. Mateescu, W. Knoll and J. Dostalek, *J. Phys. Chem. C*, 2013, **117**, 11705–11712.

2.3. UV-Laser Interference Lithography for Local Functionalization of Plasmonic Nanostructures with Responsive Hydrogel

The following publication is reprinted under the terms of the Creative Commons CC-BY^c license.

Nestor Gisbert Quilis, Simone Hageneder, Stefan Fossati, Simone K. Auer, Priyamvada Venugopalan, Anil Bozdogan, Christian Petri, Alberto Moreno-Cencerrado, Jose Luis Toca-Herrera, Ulrich Jonas, and Jakub Dostalek UV-Laser Interference Lithography for Local Functionalization of Plasmonic Nanostructures with Responsive Hydrogel. *J. Phys. Chem. C* **124**, 3297–3305 (2020). <https://doi.org/10.1021/acs.jpcc.9b11059>

Copyright © 2020 American Chemical Society

Gold nanoparticle arrays provide a versatile platform for optical sensing applications based on localized surface plasmons. Depending on the pattern period, however, only a small fraction of the surface is covered by the nanoparticles while the area in between the substrate is left exposed. This leads to challenges with surface functionalization as surface passivation needs to be established for two different materials. Local attachment of a thermoresponsive polymer network provides a high-capacity binding matrix that can be collapsed to bring the captured analyte into proximity of the particle surface by a temperature change. The gold film was patterned by 4-beam laser interference lithography (LIL), as was the subsequently deposited hydrogel film. Phase-matching between the gold nanoparticle array and the hydrogel nanoparticle array was achieved using slightly different periods, creating a Moiré pattern of aligned and misaligned areas. Remarkably, the hydrogel tends to collapse preferably towards and enclose the metallic particles even for slightly misaligned areas. The increased binding capacity and plasmonic fluorescence enhancement of such structures were demonstrated by the affinity capture of fluorescently labeled antibodies.

^c <http://creativecommons.org/licenses/by/4.0/>, Appendix 5.7.2

2.3. UV-Laser Interference Lithography for Local Functionalization of Plasmonic Nanostructures with Responsive Hydrogel

This research was driven by Nestor Gisbert Quilis, who developed the processes to create superimposed hydrogel and nanoparticle arrays. Stefan Fossati was involved in the development of the LIL process, optical and topographical characterization of the samples, and developed the optical instrument employed for the biochemical affinity binding studies. Simone Auer and Priyamvada Venugopalan helped to carry out the LIL process. Simone Hageneder and Anil Bozdogan established the hydrogel functionalization and carried out affinity assays. The hydrogel was synthesized by Christian Petri under the supervision of Ulrich Jonas and the *in-situ* observation of the actuating hydrogel architecture by liquid AFM was carried out by Alberto Moreno-Cencerrado under the supervision of Jose Luis Toca-Herrera.

Supporting information to this article is included in the appendix, section 5.3.

UV-Laser Interference Lithography for Local Functionalization of Plasmonic Nanostructures with Responsive Hydrogel

Nestor Gisbert Quilis, Simone Hageneder, Stefan Fossati, Simone K. Auer, Priyamvada Venugopalan, Anil Bozdogan, Christian Petri, Alberto Moreno-Cencerrado, Jose Luis Toca-Herrera, Ulrich Jonas, and Jakub Dostalek*

Cite This: *J. Phys. Chem. C* 2020, 124, 3297–3305

Read Online

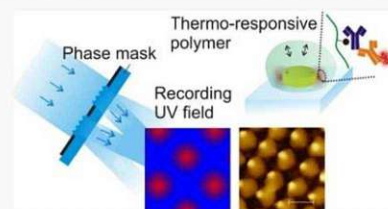
ACCESS |

Metrics & More

Article Recommendations

Supporting Information

ABSTRACT: A novel approach to local functionalization of plasmonic hotspots at gold nanoparticles with biofunctional moieties is reported. It relies on photocrosslinking and attachment of a responsive hydrogel binding matrix by the use of a UV interference field. A thermoresponsive poly(*N*-isopropylacrylamide)-based (pNIPAAm) hydrogel with photocrosslinkable benzophenone groups and carboxylic groups for its postmodification was employed. UV-laser interference lithography with a phase mask configuration allowed for the generation of a high-contrast interference field that was used for the recording of periodic arrays of pNIPAAm-based hydrogel features with the size as small as 170 nm. These hydrogel arrays were overlaid and attached on the top of periodic arrays of gold nanoparticles, exhibiting a diameter of 130 nm and employed as a three-dimensional binding matrix in a plasmonic biosensor. Such a hybrid material was postmodified with ligand biomolecules and utilized for plasmon-enhanced fluorescence readout of an immunoassay. Additional enhancement of the fluorescence sensor signal by the collapse of the responsive hydrogel binding matrix that compacts the target analyte at the plasmonic hotspot is demonstrated.



INTRODUCTION

A variety of naturally occurring or synthetic biopolymers has been tailored for specific biomedical¹ and analytical² applications, and among these, stimuli-responsive polymers represent particularly attractive “smart” materials capitalizing on their ability to undergo physical or chemical changes triggered by an external stimulus.^{3–5} Such materials can be incorporated into architectures that are on-demand actuated by stimuli, including temperature, pH, or electric current.^{6–8} A prominent example of a responsive polymer is the poly(*N*-isopropylacrylamide) (pNIPAAm), which is well-known for its thermoresponsive behavior. pNIPAAm exhibits a lower critical solution temperature (LCST) with pronounced and fully reversible hydrophobic-to-hydrophilic transition close to the body temperature.⁹ pNIPAAm has been utilized in drug delivery micro/nanogels,¹⁰ for modulating cellular interactions,^{5,11} biosensors,¹² and in opto-responsive coatings.¹³

The nanoscale patterning of responsive polymer materials is important to let them serve in diverse areas ranging from sensing,¹⁴ optical components,¹⁵ and catalysis¹⁶ to tissue engineering¹⁷ and cell biology.¹⁸ Self-assembly represents a widely used method for the preparation of nano- and microstructures based on, for instance, block-copolymer that combines hydrophobic and hydrophilic segments.^{19,20} In addition, casting of microstructures by polymerization in template cavities has been utilized for the fabrication of miniature responsive polymer objects actuated in aqueous solution.²¹ To prepare structures that are attached to a solid

surface, photolithography has been extensively used for various types of responsive polymer structures.²² Shadow mask photolithography-based methods typically enable facile means for the patterning of microstructures over macroscopic areas. To gain finer nanoscale control of the morphology of responsive polymer structures, electron beam lithography was employed for the structuring on a small footprint.^{23,24} In addition, UV nanoimprint lithography has been introduced to harness both nanoscale precision and compatibility with scaled-up production.²⁵ This method is based on a transfer of a target motif carried by a stamp to a polymer layer by the subsequent polymerization²⁶ or photocrosslinking.²⁷

Metallic nanostructures can be incorporated into responsive polymer architectures to provide means for their optical actuating^{28,29} or to be employed for the optical readout in bioanalytical applications.³⁰ Metallic nanostructures support localized surface plasmons (LSPs) that tightly confine the electromagnetic field in their vicinity through its coupling with collective charge density oscillations. The resonant excitation of LSPs is accompanied by a strongly enhanced electromagnetic field intensity,³¹ locally increased temperature³² or, for instance, an emission of hot electrons.³³ In bioanalytical

Received: November 26, 2019

Revised: January 9, 2020

Published: January 10, 2020

2.3. UV-Laser Interference Lithography for Local Functionalization of Plasmonic Nanostructures with Responsive Hydrogel

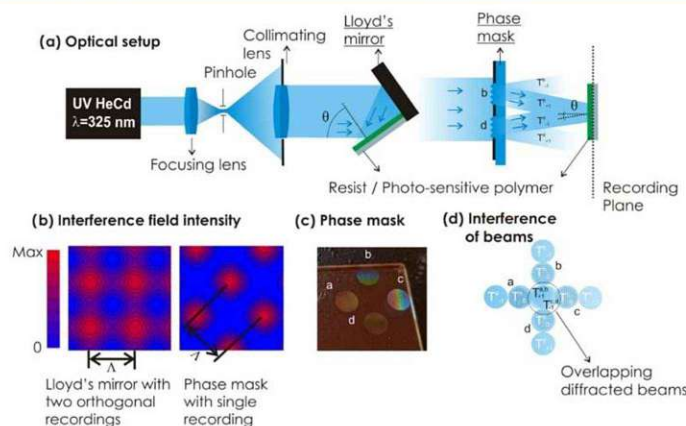


Figure 1. (a) Optical configuration of the UV-laser interference lithography with Lloyd's mirror configuration (left) and the phase mask configuration (right). (b) Simulations of the interference field generated by Lloyd's mirror configuration (left) and developed phase mask (right). (c) Schematics of the phase mask carrying four circular transmission gratings marked as a, b, c, and d. (d) Schematics of the overlapping of collimated waves at the recording plane with zero-order T_0 and first-order diffracted $T_{\pm 1}$ beams.

sensing applications, the LSPs are utilized for the probing of target molecules that are brought in contact with the metallic nanoparticles. In affinity-based plasmonic biosensors, mostly thiol self-assembled monolayers are deployed at the two-dimensional (2D) surface of plasmonic nanoparticles for attaching of ligand molecules that specifically capture target molecules from the analyzed liquid sample.³⁴ In general, the sensitivity of LSP-based biosensors can be advanced by strategies that allow for selective capture of target analytes only at the regions where the electromagnetic field is confined (e.g., edges and walls of cylindrical gold nanoparticles), commonly referred as to "plasmonic hotspots". To deploy ligand molecules that specifically capture target species at the plasmonic hotspot, 2D surface architectures were combined with lithography-based strategies generating masks.^{35,36} In addition, other strategies, including material-orthogonal chemistries,³⁷ surface plasmon-triggered polymerization,³⁸ and surface plasmon-enhanced two-photon cleavage of photo-sensitive organic moieties,³⁹ have been reported to attain local functionalization of metallic nanostructures.

The LSPs typically probe rather small subareas of the metallic nanoparticles, and their field reaches only a short distance of several tens of nanometers away from their surface.⁴⁰ Therefore, the performance of various LSP-based biosensor modalities is hindered by the reduced probability of analyte capture in these narrow spatial zones, where the electromagnetic field is confined. The use of biointerfaces composed of 3D polymer brushes or networks provides means to increase the surface area and respective binding capacity,^{41,42} offering higher capture probability of the target analyte in the hotspot zones probed by LSPs. The present paper reports on the local attachment of a 3D hydrogel binding matrix in the vicinity of well-ordered gold nanoparticles, which can be postmodified for specific affinity capture of target analytes and actuated for their compacting at the plasmonic hotspot.

METHODS

Materials. OrmoPrime08, S1805 and SU-8 photoresist, SU-8 2000 thinner, and an AZ303 developer were purchased

from Micro Resist Technology (Germany). Dimethyl sulfoxide (DMSO), acetic acid, propylene glycol monomethyl ether acetate, and 1-ethyl-3-(3-dimethylaminopropyl)carbodiimide (EDC) were obtained from Sigma Aldrich (Germany). pNIPAAm-based terpolymer composed of *N*-isopropylacrylamide, methacrylic acid, and 4-methacryloyloxybenzophenone (in a ratio of 94:5:1), benzophenone disulfide, and 4-sulfotetrafluorophenol (TFPS) were synthesized in our laboratory as previously reported.^{43–45}

IgG from mouse serum (mIgG, I 5381), Tween 20 (P9416), and bovine serum albumin (A2153) were purchased from Sigma Aldrich (Austria). Phosphate-buffered saline (PBS) and sodium acetate were obtained from VWR Chemicals (Austria). Alexa Fluor 790 goat anti-mouse IgG (a-mIgG, A11375) was acquired from Life Technologies (Eugene, OR).

Optical Configuration of Laser Interference Lithography. A He-Cd laser (IK 3031 R-C) from Kimmon (Japan) emitting at $\lambda = 325$ nm with 4 mW was employed. The coherent beam was expanded with a spatial filter consisting of a pinhole (10 μm) and $\times 40$ microscope lens. For Lloyd's mirror configuration, the expanded beam was collimated and impinged at a substrate carrying a photosensitive polymer and a UV-reflecting mirror with the area of several cm^2 . The measured intensity of the beam in the recording plane was around $30 \mu\text{W cm}^{-2}$. For recording with the phase mask configuration, the power of the recording field in the recording plane was increased to $400 \mu\text{W cm}^{-2}$.

Preparation of a Phase Mask. OrmoPrime08 was employed as an adhesion promoter to prevent delamination of the resist. A Quartz substrate (20 \times 20 \times 1 mm) was dehydrated on a hot plate for 5 min at 200 $^\circ\text{C}$, and the OrmoPrime solution composed of organofunctional silanes was subsequently spun on the top at 4000 rpm for 60 s. Then, the substrate was placed on the hot plate for 5 min at 150 $^\circ\text{C}$. Afterward, undiluted S1805 positive photoresist was deposited at a spin rate of 4500 rpm applied for 45 s followed by a hard-bake treatment at 100 $^\circ\text{C}$ for 2 min. The substrate with a photoresist was placed in Lloyd's mirror setup for recording by laser interference lithography as previously reported.⁴⁶ An interference pattern, originating from two interfering beams,

2.3. UV-Laser Interference Lithography for Local Functionalization of Plasmonic Nanostructures with Responsive Hydrogel

was recorded in the photoresist layer, and a stencil mask with two symmetric circular apertures was utilized to define the area to be exposed. Custom-made stainless stencil masks were fabricated from PIU-PRINTEX (Austria) and carefully placed on top of the photoresist-coated glass substrates. The irradiation dose of 18 mJ cm^{-2} was used for the recording of two circular gratings, and subsequently, the substrate was rotated 90° and exposed once more to the same interference field with the same dose. Finally, the phase mask carrying 4 transmission gratings with two perpendicular orientations was obtained by immersing the substrate in the AZ303 developer solution diluted with deionized water (1:15 ratio) for 40 s. The angle of the collimated interfering beams was set to $\theta = 13.6^\circ$, yielding a period of the four gratings of $\Lambda_{\text{PM}} = 690 \text{ nm}$. The circular patterned area of each of the four gratings exhibited a diameter of 4 mm (see Figure 1). The measured depth of the resist gratings was about 250 nm (see Figure S1). This depth was achieved by optimizing the developing time after the recording step, and it corresponds to that providing the maximum efficiency of the first-order diffraction in transmission mode (of about 30%, data not shown).

Preparation of Gold Nanoparticles. Gold nanoparticle arrays were prepared as previously reported by the use of two-beam laser interference lithography with Lloyd's configuration.⁴⁶ Briefly, 2 nm Cr and 50 nm Au were evaporated (HHV AUTO 306 from HHV Ltd) on top of BK7 glass slides with the size of $20 \times 20 \text{ mm}$. Subsequently, a 100 nm thick layer of S1805 positive photoresist (diluted 1:2 with propylene glycol monomethyl ether acetate) was deposited at a spin rate of 4500 rpm applied for 45 s. Hard-baking of the resist was conducted at 100°C for 2 min. The angle between the interfering beams was set to $\theta = 20.69^\circ$ yielding a period of $\Lambda_{\text{G}} = 460 \text{ nm}$, and the dose was set to 6.75 mJ cm^{-2} . The parameters were adjusted to obtain arrays of cylindrical resist features with a diameter of $D = 132 \pm 5 \text{ nm}$ after the development step using the AZ303 developer (1:15 ratio deionized water). The arrays of resist features were transferred to the underlying gold layer using a dry etching process consisting of the bombardment of the surface with argon ions (Roth & Rau IonSys 500). Resist-free gold nanoparticles were finally obtained by exposing the substrate to an oxygen plasma process.

Preparation of Hydrogel Nanostructures. Covalent attachment of the pNIPAAm-based polymer to a BK7 glass substrate was achieved using a thin SU-8 linker layer. SU-8 was dissolved with its thinner (2% solution) and spun onto the surface of the BK7 glass substrate at the spin rate of 5000 rpm for 60 s. Afterward, the coated substrate was thermally cured in an oven at 50°C for 2 h. To attach the pNIPAAm-based polymer to gold nanoparticles, their gold surface was modified with UV-reactive benzophenone moieties by reacting overnight with 1 mM benzophenone disulfide dissolved in DMSO. Subsequently, a 2% pNIPAAm-based polymer dissolved in ethanol was spun (2000 rpm for 2 min) over the flat substrate (with SU-8 or with gold nanoparticle arrays carrying benzophenone disulfide), followed by its overnight drying in a vacuum oven ($T = 50^\circ \text{C}$). The pNIPAAm-coated substrate was placed in the laser interference lithography setup. The 4-beam phase mask with $\Lambda_{\text{PM}} = 690 \text{ nm}$ and the pNIPAAm-based polymer-coated substrate were made parallel to each other and separated by a distance of 5.6 mm by in-house made dedicated holders. The recording was carried out by four interfering beams transmitted through the phase mask (T_{-1}

and T_{+1} transmission diffraction orders) with the middle part blocked to prevent the interference with a normally propagating beam (T_0). The irradiation dose was set between 84 and 240 mJ cm^{-2} for the SU-8 substrates by adjusting the irradiation time and by keeping the intensity of the UV beam fixed ($400 \mu\text{W cm}^{-2}$). Local crosslinking of the pNIPAAm-based polymer on top of gold nanoparticle arrays was attained by exposure to the UV interference field with a dose of 108 mJ cm^{-2} and the same UV beam intensity ($400 \mu\text{W cm}^{-2}$). The irradiation dose was obtained as a product of the power of the collimated UV beam and the irradiation time that was set between 210 and 600 s. The pNIPAAm-based polymer in the nonexposed regions was washed away with deionized water, and the obtained structure was dried on the hot plate at a temperature above the LCST of pNIPAAm. For the control experiment, a 30 nm thick pNIPAAm hydrogel layer was attached and crosslinked on a flat 100 nm Au film that was reacted with benzophenone disulfide using a UV lamp (365 nm) and an irradiation dose of 2 J cm^{-2} .

Morphological Characterization. Atomic force microscopy (AFM) measurements of the patterned structures in contact with air were performed in tapping mode with the PicoPlus instrument (Molecular Imaging, Agilent Technologies). The topography in contact with water was observed in situ with the Nanowizard III (JPK Instruments, Germany) using a temperature-controlled module consisting of a flow cell with a Peltier element. Silicon nitride cantilevers DNP-S10 (Bruker) with a nominal spring constant of 0.24 N m^{-1} were utilized. Height, diameter, and lateral spacing of the nanoscale features were determined by employing Gwyddion free software.

LSPR Transmission Measurements. The polychromatic light beam emitted from a halogen lamp (LSH102 LOT-Oriel, Germany) was coupled to a multimode optical fiber. This beam was out-coupled from the fiber, collimated with a lens, and made normally incident at a substrate carrying arrays of gold nanoparticles. The transmitted beam was collected by a lens to another multimode optical fiber and delivered to a Shamrock SR-303I-B spectrometer from Andor Technology (Ireland). The obtained transmission spectra were normalized with that obtained without the investigated substrate. A flow cell with a Peltier element¹² was clamped against the substrate with the gold nanoparticles to control the temperature of the liquid flowed over its surface. Deionized water was flowed through using a peristaltic pump from Ismatec (Switzerland).

Plasmon-Enhanced Fluorescence Instrument. Fluorescence experiments were conducted with an in-house-developed fluorescence reader utilizing epifluorescence geometry.⁴⁷ The biochip carrying arrays of gold nanoparticles wrapped by the pNIPAAm-based hydrogel was placed in a microfluidic module with a flow cell and illuminated with a collimated beam at a wavelength of 785 nm and an intensity of 1.2 mW cm^{-2} . The spatial distribution of intensity of fluorescence light emitted at a wavelength of 810 nm at the biochip surface was collected and then detected with a cooled CCD camera. The optical system can be seen in Figure S2. It consisted of a diode laser (IBeam Smart 785 nm, TOptica, DE) that emitted a collimated monochromatic beam, which passed through a narrow bandwidth laser clean-up filter (LL01-785, Semrock) and a spatial filter built from a 60 \times microscope objective, a 40 μm pinhole, and a collimating lens (AC-254-40-B, Thorlabs) to reduce the speckles. The excitation beam traveled through a lens (AC-254-35-B, Thorlabs) and was

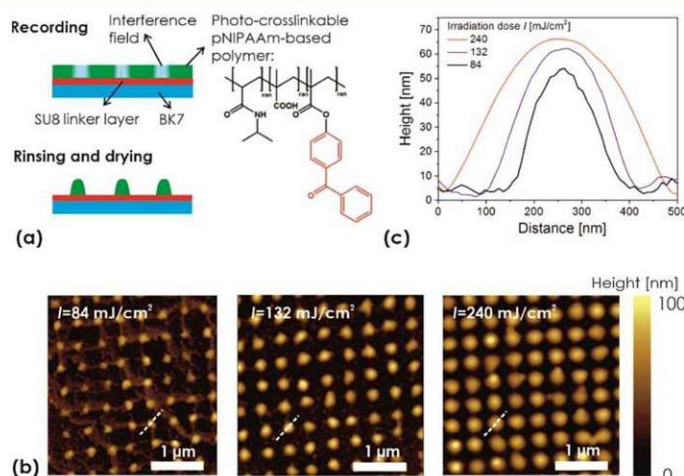


Figure 2. (a) Schematics of the local crosslinking of a responsive pNIPAAm-based polymer layer with arrays of interference maxima. The effect of the irradiation dose on (b) overall topography as observed with AFM and (c) the polymer feature cross-section.

reflected at a dichroic mirror (Di02-R785, Semrock) toward the biochip with arrays of gold nanoparticles. The incident excitation beam was then passed through another lens (AC-254-35-B, Thorlabs) to become recollimated before impinging on the biochip. The biochip was placed in the focal plane of the last lens in an in-house built microfluidic device. It was clamped against a flow cell that was temperature-controlled by the use of a Peltier device. Fluorescence light emitted at the biochip surface at a wavelength of 810 nm was collected by the same lens and passed through the dichroic mirror toward the detector. After passing an imaging lens (AC-254-80-B, Thorlabs), the remaining light at the excitation wavelength of 785 nm was blocked with a notch filter (NF03-785E-25, Semrock) and a fluorescence bandpass filter (FF01-810/10-25, Semrock) before hitting a scientific EM-CCD camera (Ixon 885K, Andor, UK). The camera was operated at a stable temperature of $-70\text{ }^{\circ}\text{C}$, and 10 images for 1 s exposure time were accumulated for an increased dynamic range. The whole device was controlled, and the data were collected by the in-house developed dedicated LabView-based software. It was used for the acquisition of fluorescence intensity from arrays of circular spots (each spot exhibited a diameter of $220\text{ }\mu\text{m}$). The acquired fluorescence intensity from each spot was averaged over its area from the raw image acquired by the optical system with an optical resolution limited to about $4\text{ }\mu\text{m}$ owing to the size of the CCD camera pixel of $8\text{ }\mu\text{m}$ and optical magnification of 2.

Immunoassay Experiment. COOH groups carried by the pNIPAAm-based polymer chains on the biochip surface were activated by reacting for 15 min with EDC and TFPS dissolved in water at a concentration of 75 and 21 mg/mL, respectively. A substrate with pNIPAAm-based polymer networks forming a hydrogel nanostructure overlaid with gold nanoparticle arrays or a thin hydrogel layer on the top of a flat gold film was then rinsed with deionized water, dried, and reacted with mIgG dissolved at a concentration of $50\text{ }\mu\text{g/mL}$ in acetate buffer (pH 4) for 90 min under shaking. Afterward, the surface was washed two times for 15 min with PBS working buffer, which contained 0.05% Tween 20 and 1 mg/mL BSA. Then, the substrate was rinsed, dried, and clamped into a flow cell to

perform plasmon-enhanced fluorescence observation of affinity binding inside the pNIPAAm-based hydrogel matrix. The flow cell was connected to a peristaltic pump through a microfluidic tubing system with a total volume of $\approx 1\text{ mL}$. After establishing a stable baseline in the fluorescence signal upon a flow of working buffer (PBS with Tween and BSA), changes in the fluorescence signal emitted from different spots on the biochip due to the affinity binding were measured using dedicated LabView-based software. A dilution series of a-mIgG (conjugated with Alexa Fluor 790) at concentrations of 1, 5, 10, 50, and 100 pM and a volume of 1 mL were flowed over the biochip surface for 15 min, followed by a 5 min rinsing with the working buffer in between.

RESULTS AND DISCUSSION

At first, the patterning of pNIPAAm-based nanostructures by UV-laser interference lithography (UV-LIL) with a phase mask configuration is described. This approach allows for generating a high-contrast UV interference field pattern that is used for nanoscale control of the attachment and crosslinking of a responsive pNIPAAm-based polymer. This strategy is then employed to overlay at the nanoscale pNIPAAm structure with periodic arrays of gold nanoparticles supporting LSPs. The LSPs supported by these nanoparticles are employed to observe swelling and collapsing of the pNIPAAm hydrogel, which caps the gold nanoparticle surface, by means of detuning the resonant wavelength at which the LSPs are optically excited. In addition, this wavelength is closely tuned to the absorption and emission wavelengths of a fluorophore that serves as a label in fluorescence immunoassays. Consequently, the pNIPAAm-based hydrogel is employed as a binding matrix that is postmodified with a protein ligand and utilized for surface plasmon-amplified fluorescence readout of the assay. Additional signal enhancement by the collapse of the gel is demonstrated using the developed hybrid plasmonic material.

UV-Laser Interference Lithography with a Phase Mask. As illustrated in Figure 1a, laser interference lithography relies on the recording of an interference pattern formed by overlapping coherent optical beams to a photosensitive polymer layer. In the UV-LIL configuration with Lloyd's

2.3. UV-Laser Interference Lithography for Local Functionalization of Plasmonic Nanostructures with Responsive Hydrogel

mirror shown in Figure 1b, a periodic sinusoidal pattern is recorded by two plane waves impinging on a layer of the photosensitive polymer at an angle θ . The recorded structure typically exhibits smoothly varying features⁴⁸ arranged in an array with a period equal to $\Lambda = \lambda/2 \sin(\theta)$, where λ is the wavelength of the recording interference beam. To record a periodic pattern with higher contrast, we employed four interfering waves with a setup shown in Figure 1a, featuring a phase mask. This phase mask consists of four transmission gratings a, b, c, and d on a UV-transparent glass slide, as depicted in Figure 1c. The area between the gratings is made reflective; thus, only the coherent plane wave impinging on the grating regions of the mask is transmitted. Each grating diffracts the coherent incident beam to a series of transmission orders marked as T_{-1} , T_0 , and T_{+1} , as shown in Figure 1d. These orders propagate to different directions, and the mask was designed so that four coherent diffractive beams T_{-1} and T_{+1} overlap in the central zone at a distance of 5.6 mm, forming an interference field as indicated in Figure 1c. This pattern exhibits arrays of more confined peaks in the harmonic spatial distribution of the interference field intensity when compared to that achieved by the conventional Lloyd's mirror configuration with two interfering beams, see Figure 1b. The intensity of the pattern generated by four interfering beams (phase mask configuration) drops to zero between the peaks, while that for the sequential orthogonal recording of two interfering beams (Lloyd's mirror configuration) does not. The period of the pattern generated by the four coherent interfering beams is $\Lambda = \Lambda_{PM}/\sqrt{2}$, where Λ_{PM} is the period of the transmission gratings on the phase mask. The full width of the half maximum (FWHM) of the peaks in this pattern is of $\Lambda/2$. To observe the interference pattern formed by the phase mask with a grating period of $\Lambda_{PM} = 690$ nm at a wavelength of $\lambda = 325$ nm, it was recorded to a layer of S1805 positive-tone photoresist with a thickness of 100 nm. After developing the recorded field distribution (an irradiation dose of 27 mJ cm^{-2}), atomic force microscopy (AFM) was employed for the observation of the structured resist topography. The obtained results presented in Figure S1 show a series of circular holes in the resist layer with a periodicity of $\Lambda = 490 \pm 4$ nm, which is in agreement with the simulated profile of the interference field distribution, as shown in Figure 1b.

Recording of pNIPAAm-Based Hydrogel Arrays. To prepare arrays of responsive pNIPAAm-based hydrogel features, the terpolymer shown in Figure 2a was used. This terpolymer carries pendant benzophenone groups for photocrosslinking and covalent attachment to a solid surface upon irradiation with UV light.⁴³ In addition, methacrylic acid was copolymerized, as the incorporated carboxyl groups promote swelling in water and provide a chemical postmodification site for the incorporation of biomolecules via amine coupling.⁴⁹

The pNIPAAm-based polymer layer with a thickness of 70 nm was spun onto a glass substrate carrying a thin adhesion-promoting SU-8 film. After complete drying of the pNIPAAm polymer layer, the substrate was placed in the 4-beam UV-LIL optical system and exposed to the interference pattern generated by a phase mask to record a crosslinked structure with a period of $\Lambda_H = 488$ nm. Upon irradiation, the pNIPAAm-based polymer in the area of high UV intensities is crosslinked and attached to the substrate, while the unexposed areas remain unchanged. Therefore, after subsequent rinsing of the layer with ethanol and water, the crosslinked pNIPAAm network remains in the exposed zones and only noncrosslinked

polymer is washed away in the area in between. After drying on a hot plate at temperature $T = 100$ °C, AFM images of the pNIPAAm surface topography were acquired. In Figure 2b, a periodic pattern of nonconnected domains of crosslinked pNIPAAm with a height similar to the initial thickness of the original polymer layer can be seen. When increasing the irradiation dose of the UV light from $I = 84$ to 132 and 240 mJ cm^{-2} , the pNIPAAm domains exhibit an increasing diameter (FWHM) of $D = 168 \pm 9$, 208 ± 8 , and 293 ± 9 nm, respectively, which were determined from the cross-sections presented in Figure 2c. These values are around FWHM of the peaks in the interference field pattern of $\Lambda_H/2 = 244$ nm, and the changes in D reflect the nonlinear dependence of the crosslinking on the irradiation dose. In addition, the height of the structure between 50 and 65 nm determined from the cross-sections in Figure 2c are lower than the thickness of the original (noncrosslinked) pNIPAAm film, which can be ascribed to the effect of smearing of the recorded features after their swelling and drying before the AFM observation.

Interestingly, the topography of the pNIPAAm-based domains changes depending on the conditions in which they are dried prior to the AFM observation in air. As Figure 3

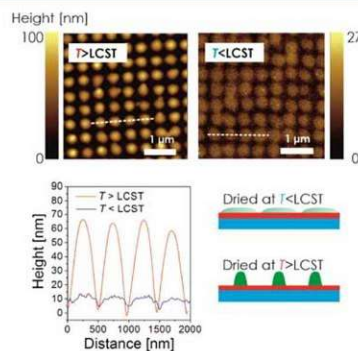


Figure 3. AFM observation of nanostructured pNIPAAm hydrogel topography dried at a temperature below and above the LCST. The structure was prepared with an irradiation dose of 240 mJ cm^{-2} .

illustrates, the height of the features strongly decreases, and the diameter increases when the surface is rinsed with water and dried at room temperature. This observation relates to what is already reported for sinusoidal corrugation of similar pNIPAAm crosslinked layers⁴⁸ and nanoimprinted nanopillars.²⁷ It can be attributed to the strong deformation of the elastic polymer network by the surface tension of the aqueous medium upon evaporation. The elasticity of the wet pNIPAAm network is strongly temperature-dependent due to its thermoresponsive solvation properties: below the LCST of 32 °C, the network swells in water and forms a soft structure that is planarized in the drying process (the height decreases by a factor of about 10). However, above the LCST in water, the polymer network collapses and forms more compact, rigid domains that are resistant to mechanical deformation upon drying. This swelling behavior was also investigated by acquiring AFM images of the prepared thermoresponsive nanostructures in water at varying temperatures around the LCST. As shown in Figure 4, at $T = 30$ °C, the topography of the swollen soft pNIPAAm structure is barely captured by the AFM tip. However, when the temperature is increased above

2.3. UV-Laser Interference Lithography for Local Functionalization of Plasmonic Nanostructures with Responsive Hydrogel

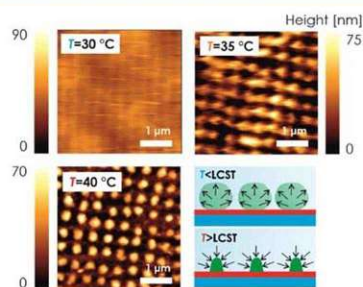


Figure 4. AFM observation of nanostructured pNIPAAm hydrogel topology in water for the temperature $T = 30, 35,$ and $40\text{ }^{\circ}\text{C}$. The structure was prepared with an irradiation dose of $240\text{ mJ}/\text{cm}^2$.

the LCST to $T = 35\text{ }^{\circ}\text{C}$, the inscribed pattern becomes apparent for the collapsed and more rigid hydrogel network. Interestingly, upon further temperature increase to $T = 40\text{ }^{\circ}\text{C}$, the observed geometry in water fully resembles the morphology that was recorded in air, as presented in Figure 2b.

Hybrid Au-pNIPAAm Nanostructures. The developed approach for the preparation of arrays with thermoresponsive pNIPAAm-based features was further applied to gold nanoparticle arrays to yield a hybrid plasmonic nanomaterial. First, gold nanoparticle arrays were prepared on a glass surface using UV-LIL with Lloyd's mirror configuration and a dry etching protocol, as previously reported.⁴⁶ The obtained cylindrical gold nanoparticle exhibited a diameter of $D = 132 \pm 5\text{ nm}$, a height of about 50 nm , and an array periodicity of $\Lambda_G = 463 \pm 2\text{ nm}$, as revealed by the AFM image in Figure 5a. Afterward, the gold surface of the nanoparticles was modified with a self-assembled monolayer (SAM) of benzophenone disulfide, on top of which a pNIPAAm polymer film was deposited (the benzophenone disulfide serves here as a linker for the covalent photoattachment of the polymer chains to gold⁴⁴).

Then, the same phase mask-based procedure (for recording the four-beam UV interference field with the period of $\Lambda_H = 488 \pm 2\text{ nm}$) was applied to generate arrays of pNIPAAm-based polymer structures, followed by rinsing with water and drying.

To circumvent the difficulty to precisely align both arrays of the hydrogel features and the gold nanoparticles, a slight mismatch of the array periodicities by 5% was intentionally

applied to yield a Moiré effect between both features. As a result, it is expected that the topography will vary periodically across the surface, resulting in a repeating pattern of areas with aligned and with misaligned geometry. The characteristic size of these domains can be estimated as $\Lambda_H \cdot \Lambda_G / (\Lambda_H - \Lambda_G)$ in the range of about $8\text{ }\mu\text{m}$. Figure 5b shows an AFM image for the topography of a $2 \times 2\text{ }\mu\text{m}$ subarea of the structure that exhibits hydrogel features aligned with the gold nanoparticle arrays after drying below the LCST. Apparently, the gold nanoparticles are visible as areas with an increased height of about 85 nm surrounded by partially planarized pNIPAAm zones of lower height that spread to a diameter of about 400 nm (see also the representative cross-section in Figure S3). When the structure is exposed to water and dried again above the LCST, the morphology changes, as shown in Figure 5c. The metallic nanoparticle topography is not protruding through the pNIPAAm hydrogel, which appears more compact and spreading to a smaller diameter of about 300 nm . The maximum height of the pNIPAAm features (with metallic nanoparticle inside) of 90 nm is slightly higher than for the structure dried below LCST. The morphology variations due to drying in the swollen and collapsed state of pNIPAAm networks attached to gold nanoparticles are less pronounced than on the flat SU-8 film. It can be attributed to different means of the attachment (swelling and collapsing on the curved surface of Au nanoparticle walls) and to the potential difference in the interaction of pNIPAAm chains with SU-8 and BK7 glass (surrounding the hydrogel structure). For comparison, an area where the gold nanoparticles and hydrogel features are misaligned is presented in Figure 5d. The patterned hydrogel features around the metallic structures exhibit more irregular morphology compared to those measured without the gold nanoparticles in Figures 2–4. This observation can be attributed to gradually changing alignment between the center of the hydrogel feature and the gold nanoparticle along the surface and the fact that the collapse tends to pull pNIPAAm-based polymer toward gold where the attachment is utilized via the benzophenone disulfide linker.

Actuating of LSP. The collapse of the pNIPAAm hydrogel is associated with an increase of the polymer volume fraction and the refractive index on the surface of gold nanoparticles. Therefore, the pNIPAAm collapse around these metallic objects detunes the localized surface plasmon resonance

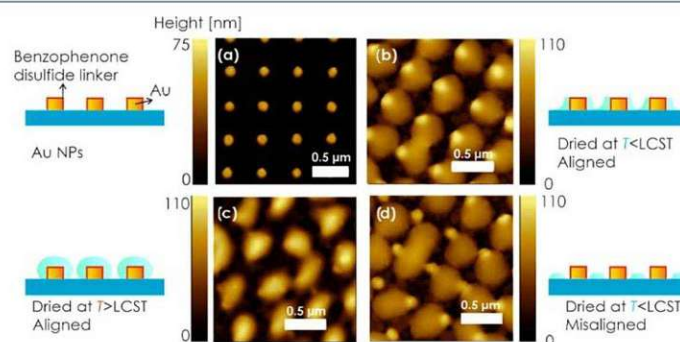


Figure 5. AFM topography of (a) gold nanoparticle arrays subsequently covered with covalently attached pNIPAAm-based nanostructures that are aligned with the gold nanoparticles and dried (b) below and (c) above the LCST. (d) Example of misaligned arrays of gold nanoparticles with pNIPAAm-based nanostructures dried below the LCST.

2.3. UV-Laser Interference Lithography for Local Functionalization of Plasmonic Nanostructures with Responsive Hydrogel

(LSPR) and manifests itself as a redshift of the resonant wavelength. Figure 6a shows the transmission spectra

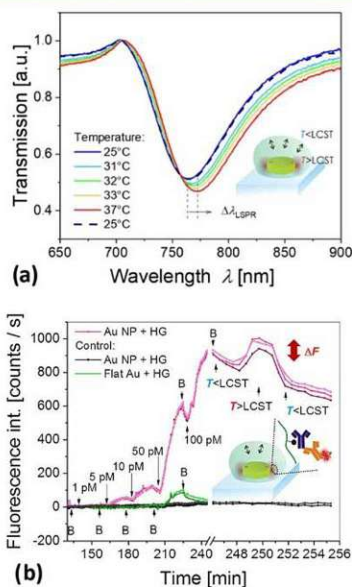


Figure 6. (a) Measured reversible shift in LSPR spectra upon temperature-induced swelling and collapse of the pNIPAAm-based hydrogel wrapped over metallic nanoparticles. (b) Employment of the hybrid material for plasmonic amplification of a fluorescence immunoassay with the pNIPAAm-based hydrogel serving as an affinity binding matrix that can be swollen and collapsed by an external temperature stimulus. The red-colored lines show the fluorescence signal acquired from spots with a diameter of 220 μm at different locations on the same biochip carrying the pNIPAAm-based hydrogel that was functionalized with ligands. The black curves correspond to control spots on the same biochip that were not functionalized with the ligand molecules, and the green curves show the control experiment on a planar-functionalized hydrogel binding matrix attached to the flat gold film. The analyte concentration is clearly indicated in the graph, and B corresponds to the rinsing step with working buffer.

measured over the area of about 1 mm^2 , which averages the variations in the alignment between gold nanoparticles and hydrogel features with a domain size $<10 \mu\text{m}$. LSPR for the structure at the temperature $T = 25 \text{ }^\circ\text{C}$ manifests itself as a dip in the transmission spectrum centered at a wavelength of $\lambda_{\text{LSPR}} = 763.9 \text{ nm}$. The gradual collapse of the hydrogel induces a red-shift of the LSPR wavelength upon an increase in the temperature. At a temperature of $T = 37 \text{ }^\circ\text{C}$, far above the LCST, the LSPR wavelength shifts to 771.9 nm. These changes are fully reversible, as after cooling to $T = 25 \text{ }^\circ\text{C}$, the LSPR spectrum shifts back to the original shape. It is worth noting that the observed shift of about 6 nm is half of that measured for a structure covered with a compact pNIPAAm hydrogel film (data not shown), which can be ascribed to the fact that about half of the nanoparticles is not in contact with the polymer due to the periodic regions of misalignment in the Moiré pattern.

LSP-Enhanced Fluorescence Assay. Finally, the developed structure was tested to serve as a biochip interface for the fluorescence readout of an immunoassay. First, the responsive

pNIPAAm-based hydrogel features wrapping (about half) of the gold nanoparticles that were postmodified with mouse IgG antibodies (mIgG). The polymer carboxylic groups were employed for establishing covalent bonds between the lysine groups of the protein and the polymer chain based on the established amine coupling scheme.⁴⁹ Then, the substrate was clamped against a flow cell, and a series of liquid samples with an increasing concentration of goat antibodies specific to mIgG (a-mIgG) were pumped over its surface. To detect the affinity binding, the goat antibody a-mIgG was labeled with an organic dye (Alexa Fluor 790). This label exhibits its absorption and emission wavelengths ($\lambda_{\text{ex}} = 785 \text{ nm}$, $\lambda_{\text{em}} = 810 \text{ nm}$) in the vicinity of the LSPR wavelength ($\lambda_{\text{LSPR}} = 764 \text{ nm}$). Therefore, the kinetics of the affinity binding of a-mIgG from the liquid sample was measured using plasmon-enhanced fluorescence.⁵⁰

The surface of the sample was irradiated by a laser beam at a wavelength of 785 nm that resonantly couples to LSPs and locally excites the bound fluorophores with its enhanced field intensity. The emitted light at a wavelength of 810 nm was collected with a home built instrument⁴⁷ separated from the excitation beam using a dichroic mirror, bandpass filter, and notch filter and detected with a cooled CCD camera. The fluorescence signal was acquired with dedicated software from a series of spots carrying the gold nanoparticle arrays in reference to an area without nanoparticles, and the data were tracked in time upon sequential flow of analyte samples. The fluorescence intensity was averaged over the surface of each circular spot with a diameter of 220 μm that was much larger than the size of domains with aligned and misaligned arrays of gold nanoparticles and hydrogel features. The liquid samples were prepared from phosphate-buffered saline that was spiked with a-mIgG at concentrations of 1, 5, 10, 50, and 100 pM. Each sample was flushed over the surface for 15 min, followed by 5 min rinsing. As Figure 6b shows, the binding of a-mIgG manifests itself as a gradual increase in the fluorescence signal, and upon rinsing, a fluorescence intensity decrease occurs due to bleaching of the emitters. The fluorescence signal on gold nanoparticle arrays capped with the pNIPAAm hydrogel matrix (red curves in Figure 6a) is about 6 times higher compared to a control experiment (green curves in 6a). The control experiment was carried out on the hydrogel biointerface prepared in the form of a layer attached to a flat nonstructured gold film. It is worth noting that the plasmonic enhancement on the structured surface is probably higher than the factor of 6 due to the fact that the control flat architecture exhibits a larger area for the capture of the target analyte and that at least half of the metallic nanoparticles are not capped with the hydrogel binding matrix due to the miss-alignment. The measured data for a structured hydrogel biointerface overlaid with gold nanoparticles indicate that the limit of detection of the prepared biochip is 0.7 pM (determined for the standard deviation fluorescence signal baseline of 2 counts/s and the slope of the fluorescence signal of 9 counts/s/pM). After this titration experiment, the temperature of the biochip surface was increased from 25 to 40 $^\circ\text{C}$, above the LCST of the hydrogel. As seen in Figure 6b, the induced collapse of the responsive hydrogel with the affinity-captured and fluorophore-labeled a-mIgG leads to an increase of the fluorescence signal by about 20%. This is due to the collapse and compacting of the hydrogel, which increases the polymer volume fraction and affinity-bound analyte molecules closer to the gold surface, where the plasmonic hotspot is located. This observation corroborates that affinity binding occurs in the

2.3. UV-Laser Interference Lithography for Local Functionalization of Plasmonic Nanostructures with Responsive Hydrogel

vicinity of the metallic nanoparticles within the matrix of the responsive pNIPAAm-based polymer network and indicates that the triggered collapse can provide an additional enhancement mechanism for high sensitivity fluorescence assays.

CONCLUSIONS

A technique based on four-beam laser interference lithography utilizing a phase mask-based configuration allows for the preparation of well-defined responsive hydrogel nanostructures with the tailored spacing and diameter. Periodic arrays of pNIPAAm-based hydrogel nanostructures exhibiting a disk shape with a tunable diameter, as low as 170 nm, were prepared with a submicron period. The temperature-induced swelling and collapse of the inscribed polymer features were investigated, and their local attachment on top of the periodic gold nanoparticle arrays was achieved based on the Moiré effect. The fully reversible actuation by temperature changes was demonstrated by measuring the variations in LSPR of the gold nanoparticle arrays. In addition, the pNIPAAm-based hydrogel was postmodified with biorecognition elements to serve as a 3D high binding capacity matrix, and a model bioassay based on fluorescence readout was conducted. The limit of detection was proven to be in the sub-picomolar range owing to the plasmonic amplification of the fluorescence signal by the plasmonic nanoparticles. Finally, the capability of the pNIPAAm network to compact the affinity-captured analyte at the plasmonic hotspots by a temperature-induced polymer collapse was tested. The presented hybrid architecture provides a novel approach for the local attachment of chemical and biological species in the vicinity of metallic nanostructures to fully exploit the probing with the LSP field at the so-called plasmonic hotspots, where the optical field intensity is the strongest.

ASSOCIATED CONTENT

Supporting Information

The Supporting Information is available free of charge at <https://pubs.acs.org/doi/10.1021/acs.jpcc.9b11059>.

Schematic and atomic force spectroscopy images of the phase mask and recorded interference pattern employing a positive photoresist; schematic of the optical setup used for the plasmon-enhanced spectroscopy assay; cross-sections of AFM topography of hydrogel nanostructures (PDF)

AUTHOR INFORMATION

Authors

- Nestor Gisbert Quilis** – BioSensor Technologies, AIT-Austrian Institute of Technology GmbH, 3430 Tulln, Austria
Simone Hageneder – BioSensor Technologies, AIT-Austrian Institute of Technology GmbH, 3430 Tulln, Austria
Stefan Fossati – BioSensor Technologies, AIT-Austrian Institute of Technology GmbH, 3430 Tulln, Austria
Simone K. Auer – BioSensor Technologies, AIT-Austrian Institute of Technology GmbH, 3430 Tulln, Austria
Priyamvada Venugopalan – BioSensor Technologies, AIT-Austrian Institute of Technology GmbH, 3430 Tulln, Austria; CEST Kompetenzzentrum für elektrochemische Oberflächentechnologie GmbH, TFZ, Wiener Neustadt, 2700 Wiener Neustadt, Austria

Anil Bozdogan – CEST Kompetenzzentrum für elektrochemische Oberflächentechnologie GmbH, TFZ, Wiener Neustadt, 2700 Wiener Neustadt, Austria

Christian Petri – Macromolecular Chemistry, Department Chemistry-Biology, University of Siegen, Siegen 57076, Germany

Alberto Moreno-Cencerrado – Institute for Biophysics, Department of Nanobiotechnology, University of Natural Resources and Life Sciences Vienna (BOKU), Vienna 1190, Austria

Jose Luis Toca-Herrera – Institute for Biophysics, Department of Nanobiotechnology, University of Natural Resources and Life Sciences Vienna (BOKU), Vienna 1190, Austria

Ulrich Jonas – Macromolecular Chemistry, Department Chemistry-Biology, University of Siegen, Siegen 57076, Germany; orcid.org/0000-0002-2161-4541

Jakub Dostalek – BioSensor Technologies, AIT-Austrian Institute of Technology GmbH, 3430 Tulln, Austria; orcid.org/0000-0002-0431-2170

Complete contact information is available at: <https://pubs.acs.org/10.1021/acs.jpcc.9b11059>

Notes

The authors declare no competing financial interest.

ACKNOWLEDGMENTS

N.G.Q. acknowledges funding from the European Union's Horizon 2020 research and innovation program under Grant agreement no. 642787, Marie Skłodowska-Curie Innovative Training Network BIOGEL. P.V. was supported by the project jointly funded by Agence Nationale de la Recherche (ANR) and the Austrian Science Fund (FWF) under the grant agreements ANR-15-CE29-0026 and I 2647, respectively. S.H., S.F., C.P., and J.D. received support from the European Union's Horizon 2020 research and the innovation program under Grant Agreement no. 633937, project ULTRAPLACAD. S.A. is grateful for the support from FEMTEC and S.H., S.F., and J.D. were supported by the Austrian Research Promotion Agency (FFG) with Grant agreement no. 861578 (ERANET project PLABAN).

REFERENCES

- (1) Green, J. J.; Elisseff, J. H. Mimicking Biological Functionality with Polymers for Biomedical Applications. *Nature* **2016**, *540*, 386.
- (2) Mateescu, A.; Wang, Y.; Dostalek, J.; Jonas, U. Thin Hydrogel Films for Optical Biosensor Applications. *Membranes* **2012**, *2*, 40–69.
- (3) Liu, F.; Urban, M. W. Recent Advances and Challenges in Designing Stimuli-Responsive Polymers. *Prog. Polym. Sci.* **2010**, *35*, 3–23.
- (4) Wei, M.; Gao, Y.; Li, X.; Serpe, M. J. Stimuli-Responsive Polymers and Their Applications. *Polym. Chem.* **2017**, *8*, 127–143.
- (5) De las Heras Alarcón, C.; Pennadam, S.; Alexander, C. Stimuli Responsive Polymers for Biomedical Applications. *Chem. Soc. Rev.* **2005**, *34*, 276–285.
- (6) Jiang, N.; Zhuo, X.; Wang, J. Active Plasmonics: Principles, Structures, and Applications. *Chem. Rev.* **2017**, *118*, 3054–3099.
- (7) Huck, W. T. Responsive Polymers for Nanoscale Actuation. *Mater. Today* **2008**, *11*, 24–32.
- (8) Sidorenko, A.; Krupenkin, T.; Taylor, A.; Fratzl, P.; Aizenberg, J. Reversible Switching of Hydrogel-Actuated Nanostructures into Complex Micropatterns. *Science* **2007**, *315*, 487–490.
- (9) Haq, M. A.; Su, Y.; Wang, D. Mechanical Properties of Pnipam Based Hydrogels: A Review. *Mater. Sci. Eng., C* **2017**, *70*, 842–855.

2.3. UV-Laser Interference Lithography for Local Functionalization of Plasmonic Nanostructures with Responsive Hydrogel

- (10) Guan, Y.; Zhang, Y. Pnippam Microgels for Biomedical Applications: From Dispersed Particles to 3d Assemblies. *Soft Matter* **2011**, *7*, 6375–6384.
- (11) Nash, M. E.; Healy, D.; Carroll, W. M.; Elvira, C.; Rochev, Y. A. Cell and Cell Sheet Recovery from Pnippam Coatings; Motivation and History to Present Day Approaches. *J. Mater. Chem.* **2012**, *22*, 19376–19389.
- (12) Toma, M.; Jonas, U.; Mateescu, A.; Knoll, W.; Dostalek, J. Active Control of Spr by Thermoresponsive Hydrogels for Biosensor Applications. *J. Phys. Chem. C* **2013**, *117*, 11705–11712.
- (13) Kawano, T.; Niidome, Y.; Mori, T.; Katayama, Y.; Niidome, T. Pnippam Gel-Coated Gold Nanorods for Targeted Delivery Responding to a near-Infrared Laser. *Bioconjugate Chem.* **2009**, *20*, 209–212.
- (14) Erickson, D.; Mandal, S.; Yang, A. H.; Cordovez, B. Nanobiosensors: Optofluidic, Electrical and Mechanical Approaches to Biomolecular Detection at the Nanoscale. *Microfluid. Nanofluid.* **2008**, *4*, 33–52.
- (15) Paquet, C.; Kumacheva, E. Nanostructured Polymers for Photonics. *Mater. Today* **2008**, *11*, 48–56.
- (16) Ghosh, S.; Kouamé, N. A.; Ramos, L.; Remita, S.; Dazzi, A.; Deniset-Besseau, A.; Beauvier, P.; Goubard, F.; Aubert, P.-H.; Remita, H. Conducting Polymer Nanostructures for Photocatalysis under Visible Light. *Nat. Mater.* **2015**, *14*, 505.
- (17) Slepicka, P.; Kasalkova, N. S.; Siegel, J.; Kolska, Z.; Bacakova, L.; Svorcik, V. Nano-Structured and Functionalized Surfaces for Cytocompatibility Improvement and Bactericidal Action. *Biotechnol. Adv.* **2015**, *33*, 1120–1129.
- (18) Nie, Z.; Kumacheva, E. Patterning Surfaces with Functional Polymers. *Nat. Mater.* **2008**, *7*, 277.
- (19) Cheng, J. Y.; Mayes, A. M.; Ross, C. A. Nanostructure Engineering by Templated Self-Assembly of Block Copolymers. *Nat. Mater.* **2004**, *3*, 823.
- (20) Hu, H.; Gopinadhan, M.; Osuji, C. O. Directed Self-Assembly of Block Copolymers: A Tutorial Review of Strategies for Enabling Nanotechnology with Soft Matter. *Soft Matter* **2014**, *10*, 3867–3889.
- (21) Zhang, H.; Mourran, A.; Möller, M. Dynamic Switching of Helical Microgel Ribbons. *Nano Lett.* **2017**, *17*, 2010–2014.
- (22) Chen, J.-K.; Chang, C.-J. Fabrications and Applications of Stimulus-Responsive Polymer Films and Patterns on Surfaces: A Review. *Materials* **2014**, *7*, 805–875.
- (23) Yu, Q.; Ista, L. K.; Gu, R.; Zauscher, S.; López, G. P. Nanopatterned Polymer Brushes: Conformation, Fabrication and Applications. *Nanoscale* **2016**, *8*, 680–700.
- (24) Idota, N.; Tsukahara, T.; Sato, K.; Okano, T.; Kitamori, T. The Use of Electron Beam Lithographic Graft-Polymerization on Thermoresponsive Polymers for Regulating the Directionality of Cell Attachment and Detachment. *Biomaterials* **2009**, *30*, 2095–2101.
- (25) Traub, M. C.; Longsine, W.; Truskett, V. N. Advances in Nanoimprint Lithography. *Annu. Rev. Chem. Biomol. Eng.* **2016**, *7*, 583–604.
- (26) Guo, L. J. Nanoimprint Lithography: Methods and Material Requirements. *Adv. Mater.* **2007**, *19*, 495–513.
- (27) Pirani, F.; Sharma, N.; Moreno-Cencerrado, A.; Fossati, S.; Petri, C.; Descrovi, E.; Toca-Herrera, J. L.; Jonas, U.; Dostalek, J. Optical Waveguide-Enhanced Diffraction for Observation of Responsive Hydrogel Nanostructures. *Macromol. Chem. Phys.* **2017**, *218*, No. 1600400.
- (28) Mourran, A.; Zhang, H.; Vinokur, R.; Möller, M. Soft Microrobots Employing Nonequilibrium Actuation Via Plasmonic Heating. *Adv. Mater.* **2017**, *29*, No. 1604825.
- (29) Volk, K.; Fitzgerald, J. P. S.; Retsch, M.; Karg, M. Time-Controlled Colloidal Superstructures: Long-Range Plasmon Resonance Coupling in Particle Monolayers. *Adv. Mater.* **2015**, *27*, 7332.
- (30) Valsecchi, C.; Brolo, A. G. Periodic Metallic Nanostructures as Plasmonic Chemical Sensors. *Langmuir* **2013**, *29*, 5638–5649.
- (31) Halas, N. J.; Lal, S.; Chang, W.-S.; Link, S.; Nordlander, P. Plasmons in Strongly Coupled Metallic Nanostructures. *Chem. Rev.* **2011**, *111*, 3913–3961.
- (32) Baffou, G.; Quidant, R. Thermo-Plasmonics: Using Metallic Nanostructures as Nano-Sources of Heat. *Laser Photonics Rev.* **2013**, *7*, 171–187.
- (33) Brongersma, M. L.; Halas, N. J.; Nordlander, P. Plasmon-Induced Hot Carrier Science and Technology. *Nat. Nanotechnol.* **2015**, *10*, 25.
- (34) Mayer, K. M.; Hafner, J. H. Localized Surface Plasmon Resonance Sensors. *Chem. Rev.* **2011**, *111*, 3828–3857.
- (35) Goerlitzer, E. S. A.; Speichermann, L. E.; Mirzaa, T. A.; Mohammadia, R.; Vogel, N. Addressing the Plasmonic Hotspot Region by Site-Specific Functionalization of Nanostructures. *Nanoscale Adv.* **2020**, *2*, 136.
- (36) Piliarik, M.; Kvasnicka, P.; Galler, N.; Krenn, J. R.; Homola, J. Local Refractive Index Sensitivity of Plasmonic Nanoparticles. *Opt. Express* **2011**, *19*, 9213–9220.
- (37) Jonsson, M. P.; Dahlin, A. B.; Feuz, L.; Petronis, S.; Hook, F. Locally Functionalized Short-Range Ordered Nanoplasmonic Pores for Bioanalytical Sensing. *Anal. Chem.* **2010**, *82*, 2087–2094.
- (38) Herzog, N.; Kind, J.; Hess, C.; Andrieu-Brunsen, A. Surface Plasmon & Visible Light for Polymer Functionalization of Mesopores and Manipulation of Ionic Permselectivity. *Chem. Commun.* **2015**, *51*, 11697–11700.
- (39) Dostert, K.-H.; Álvarez, M.; Koynov, K.; del Campo, A.; Butt, H.-J. r.; Kreiter, M. Near Field Guided Chemical Nanopatterning. *Langmuir* **2012**, *28*, 3699–3703.
- (40) Mazzotta, F.; Johnson, T. W.; Dahlin, A. B.; Shaver, J.; Oh, S. H.; Hook, F. Influence of the Evanescent Field Decay Length on the Sensitivity of Plasmonic Nanodisks and Nanoholes. *ACS Photonics* **2015**, *2*, 256–262.
- (41) Wang, Y.; Brunsen, A.; Jonas, U.; Dostalek, J.; Knoll, W. Prostate Specific Antigen Biosensor Based on Long Range Surface Plasmon-Enhanced Fluorescence Spectroscopy and Dextran Hydrogel Binding Matrix. *Anal. Chem.* **2009**, *81*, 9625–9632.
- (42) Huang, C. J.; Dostalek, J.; Knoll, W. Long Range Surface Plasmon and Hydrogel Optical Waveguide Field-Enhanced Fluorescence Biosensor with 3d Hydrogel Binding Matrix: On the Role of Diffusion Mass Transfer. *Biosens. Bioelectron.* **2010**, *26*, 1425–1431.
- (43) Beines, P. W.; Klosterkamp, I.; Menges, B.; Jonas, U.; Knoll, W. Responsive Thin Hydrogel Layers from Photo-Cross-Linkable Poly (N-Isopropylacrylamide) Terpolymers. *Langmuir* **2007**, *23*, 2231–2238.
- (44) Sergelen, K.; Petri, C.; Jonas, U.; Dostalek, J. Free-Standing Hydrogel-Particle Composite Membrane with Dynamically Controlled Permeability. *Biointerphases* **2017**, *12*, No. 051002.
- (45) Gee, K. R.; Archer, E. A.; Kang, H. C. 4-Sulfotetrafluorophenyl (Stp) Esters: New Water-Soluble Amine-Reactive Reagents for Labeling Biomolecules. *Tetrahedron Lett.* **1999**, *40*, 1471–1474.
- (46) Quilis, N. G.; Lequeux, M.; Venugopalan, P.; Khan, I.; Knoll, W.; Boujday, S.; de la Chapelle, M. L.; Dostalek, J. Tunable Laser Interference Lithography Preparation of Plasmonic Nanoparticle Arrays Tailored for Sers. *Nanoscale* **2018**, *10*, 10268.
- (47) Dostalek, J.; Knoll, W.; Fossati, S.; Hageneder, S.; Jungbluth, V. Plasmon-Enhanced Fluorescence Spectroscopy Imaging by Multi-Resonant Nanostructures. European Patent Application No. 19164960.72019.
- (48) Sharma, N.; Petri, C.; Jonas, U.; Dostalek, J. Reversibly Tunable Plasmonic Bandgap by Responsive Hydrogel Grating. *Opt. Express* **2016**, *24*, 2457–2465.
- (49) Aulasevich, A.; Roskamp, R. F.; Jonas, U.; Menges, B.; Dostalek, J.; Knoll, W. Optical Waveguide Spectroscopy for the Investigation of Protein-Functionalized Hydrogel Films. *Macromol. Rapid Commun.* **2009**, *30*, 872–877.
- (50) Bauch, M.; Toma, K.; Toma, M.; Zhang, Q.; Dostalek, J. Plasmon-Enhanced Fluorescence Biosensors: A Review. *Plasmonics* **2014**, *9*, 781–799.

2.4. Multi-diffractive Grating for Surface Plasmon Biosensors with Direct Back-side Excitation

The following publication is reprinted under the OSA Open Access Publishing Agreement.

Simone Hageneder, **Stefan Fossati**, Nicolas-Guillermo Ferrer, Batuhan Güngörmez, Simone K. Auer, and Jakub Dostalek Multi-diffractive grating for surface plasmon biosensors with direct back-side excitation. *Opt. Express* **28**, 39770 (2020). <https://doi.org/10.1364/oe.410416>

Copyright © 2020 Optical Society of America. Users may use, reuse, and build upon the article or use the article for text or data mining, as long as such uses are for non-commercial purposes and appropriate attribution is maintained. All other rights are reserved.

Surface plasmon resonance spectroscopy is a sensitive means for label-free biosensing and is mostly implemented using sensor chips coated with a thin metallic layer that supports propagating surface plasmons. Since plasmons cannot be excited from within the medium the surface is contacting, as discussed in section 1.2.2, two main coupling strategies have been established: Prism coupling in the Kretschmann configuration allows backside excitation of surface plasmons utilizing a high refractive index prism. The required optical configuration with the bulky prism, refractive index matching between sample and prism, and illumination under about 50° has limited the use to dedicated devices. The second coupling strategy, diffraction coupling by a grating, allows the excitation of SPPs on the illuminated surface. These modes, however, are dispersive and depend on the angle of illumination. Commercially used optical readers use either focused beams for illumination or, in the case of microwell plate readers, illuminate through a curved, refracting water-air interface. In both cases, the observed broadening of the resonance is associated with a loss of sensitivity. In this section, a diffractive structure consisting of two superimposed gratings is presented that allows cross-coupling through the thin metal film. The additional grating has a period of about half the excitation grating and opens an optical bandgap in the SPP supported by the two interfaces. For a sufficiently large bandgap, cross-coupling is achieved, allowing the excitation of plasmons on the opposite surface even under normal

2.4. Multi-diffractive Grating for Surface Plasmon Biosensors with Direct Back-side Excitation

incidence. The observed optical features allow refractive index sensing with sensitivity comparable with the other coupling strategies.

In this work, Simone Hageneder was responsible for the assay development, chip functionalization and carried out the bioassays. Stefan Fossati was responsible for the development and fabrication of the nanostructures by numerical simulations and NIL and LIL with the help of Nicolas-Guillermo Ferrer and Batuhan Güngörmez. SF and NGF furthermore developed the optical instrument and measurement software. Simone K. Auer contributed to the topological investigation by AFM. The project was based on an idea of Jakub Dostalek and was carried out under his supervision.

Multi-diffractive grating for surface plasmon biosensors with direct back-side excitation

SIMONE HAGENEDER,¹ STEFAN FOSSATI,¹ NICOLAS-GUILLEMO FERRER,^{1,2} BATUHAN GÜNGÖRMEZ,^{1,3} SIMONE K. AUER,^{1,4} AND JAKUB DOSTALEK^{1,5,*} 

¹AIT-Austrian Institute of Technology GmbH, Konrad-Lorenz-Strasse 24, Tulln 3430, Austria

²University of Tokyo, Department of Advanced Materials Science, Kashiwanoha 5-1-5, Kashiwa, Chiba 277-8561, Japan

³Department of Materials Science and Engineering, Gebze Technical University, Gebze, Kocaeli, Turkey

⁴CEST Kompetenzzentrum für elektrochemische Oberflächentechnologie GmbH, TFZ, Wiener Neustadt 2700, Austria

⁵FZU-Institute of Physics, Czech Academy of Sciences, Na Slovance 2, Prague 182 21, Czech Republic
*jakub.dostalek@ait.ac.at

Abstract: A multi-diffractive nanostructure is reported for the resonant excitation of surface plasmons that are cross-coupled through a thin metallic film. It consists of two superimposed periodic corrugations that allow diffraction excitation of surface plasmons on the inner side of a thin metal film and their subsequent phase matching with counterpropagating surface plasmons travelling to the opposite direction on its other side. This interaction leads to establishing of a set of cross-coupled Bragg-scattered surface plasmon modes that exhibit an electromagnetic field localized on both metal film interfaces. The reported structure is attractive for surface plasmon resonance biosensor applications, where direct optical probing can be done through the substrate without the need of optical matching to a high refractive index prism. In addition, it can be prepared by mass production – compatible means with UV-nanoimprint lithography and its biosensing performance characteristics are demonstrated by refractometric and biomolecular affinity binding studies.

© 2020 Optical Society of America under the terms of the OSA Open Access Publishing Agreement

1. Introduction

Metallic nanostructures increasingly serve for optical probing of biomolecules and their interactions in important fields of analytical technologies and life science research. They allow for the resonant coupling of light to surface plasmon modes originating from collective oscillations of electron density and associated electromagnetic field that is tightly confined on the metallic surface. Such confinement of electromagnetic field leads to the enhancement of its intensity and local density of optical states, and it has been exploited in surface plasmon resonance (SPR) biosensors [1] as well as for the amplification of weak optical spectroscopy signal including Raman scattering [2], fluorescence [3] and near-infrared absorption [4].

The majority of SPR biosensors utilize sensor chips with a thin metallic film supporting propagating surface plasmons (PSPs). In Kretschmann configuration of attenuated total internal reflection (ATR) method, these sensor chips are optically matched to an optical prism for the coupling of PSPs at the outer side of the metallic film with an optical beam travelling through the sensor chip substrate [5]. The outer sensor surface is brought in contact with an analyzed liquid sample, and the molecular binding events are observed by interrogating resonant excitation of PSPs in the wavelength [6] or angular [5] reflectivity spectrum. Alternative approaches based on diffraction grating-based excitation of PSPs [7] were pursued, and also metallic nanostructures supporting localized surface plasmons (LSPs) [8] were used to avoid the optical matching of sensor chips to bulky ATR prism. The wavelength interrogation of LSPs can be utilized from both

sample and sensor chip sides in transmission [9] or reflection mode [10]. This measurement can be performed by dedicated instruments [11] and also by using already established optical readers deployed in standard molecular biology laboratories. These particularly include microtiter plates where the bottom wells carry adsorbed gold nanoparticles prepared by chemical synthesis [12] and thin metallic films perforated with arrays of nanoholes by lithography [13,14].

In general, the measurement in reflection mode from the substrate side of a sensor chip carrying plasmonic nanostructures offers the advantage of avoiding passing the probing optical beam through the analyzed liquid sample. This back-side coupling allows for rapid direct analysis of complex matrices (such as minimally processed blood) that absorb or scatter light. Also, it offers improved stability for the *in situ* SPR measurements, which otherwise require using of transparent flow-cells and make the measurements prone to respond to the sample flow fluctuations. The separation of the fluidic and the optical parts of the plasmonic sensor chip was reported by cross-coupled PSP modes on thin gold films that are perforated with arrays of nanoholes and attached to a low refractive index dielectric film [15]. This configuration takes advantage of refractive index symmetrical geometry that enables cross-coupling of PSP at opposite interfaces leading to the establishment of long-range surface plasmon modes [16]. Another possible approach to diffraction-based excitation of PSPs on non-conformal diffraction gratings was demonstrated on metallic films that were corrugated only on inner side [17]. However, the preparation of such nanostructures for back-side excitation of coupled PSPs or LSPs can be only prepared by using methods involving multiple lithography steps. Typically, periodic arrays of plasmonic nanoholes and discs are prepared by electron beam lithography, which offers precise control of the nanostructure geometry. However, it represents an approach relying on complex infrastructure that is suitable only for research as the fabrication over larger areas $> 100 \mu\text{m}$ is slow. Among others, UV-laser interference lithography [18] and UV-nanoimprint lithography combined with lift-off [19], dry etching steps [20], or template stripping [21,22] have been proposed, but they elevate this limitation only partially.

In this paper, we report on a new approach for back-side excitation of PSPs based on multi-periodic gratings (MPG) coated with a thin metallic film. The structure is based on a corrugation profile with multiple superimposed relief periodic modulations that have been explored before for the broadband plasmonic absorbers [23], multi-resonant plasmonic nanostructures for the amplification of weak fluorescence signal [24], and SPR biosensors with Bragg-scattered surface plasmons [25]. We report for the first time on tailoring this geometry for the cross-coupling of PSPs across a thin metallic film and implement it for real-time *in situ* observation of molecular binding-induced refractive index changes based on detuning of the tailored plasmonic resonance that is measured with the back-side excitation geometry.

2. Materials and methods

2.1. Preparation of multi-diffractive grating structures

The MPG structure was recorded by UV laser interference lithography (UV-LIL) with Lloyd's mirror configuration. Positive photoresist Microposit S1805 from Microchem (USA) was spun on a BK7 glass substrate at 4500 rpm for 45 seconds (yielding a thickness of 500 nm) and dried on a hot plate at 98 °C for 120 sec. Afterwards, the substrate was mounted to the UV-LIL setup and exposed to the field of two interfering collimated beams (with an intensity of $32 \mu\text{W cm}^{-2}$) emitted from a HeCd laser IK 3031 R-C from Kimmon (Japan) at wavelength $\lambda=325 \text{ nm}$. The angle of the interfering beams was set to $69^{\circ}05'$ and $47^{\circ}10'$ deg, which corresponds to periods of $\Lambda_1=455$ and $\Lambda_2=239 \text{ nm}$, respectively. To record the MPG structure, the photoresist layer was sequentially exposed to the interference field at each respective angle. For the preparation of crossed gratings, the sequential exposure to interference field was carried out twice for two orientations of the sample rotated by 90 degrees. The relief corrugation was etched into the photoresist by a developer AZ 303 from MicroChemicals (Germany) diluted by distilled water at

a ratio of 1:15. For the measurements discussed below, we used a grating C2.2.ABPO with a recording time of the period Λ_1 of 10 min, recording time of the period Λ_2 of 25 min, and the development time 90 s.

Prepared photoresist grating was cast to polydimethylsiloxane (PDMS) Sylgard 184 from Dow Corning (USA). Multiple generation copies were prepared, and PDMS was cured at elevated temperature to fine-tune the periods and the modulation depth of the recorded structure and to serve as a working stamp after the detachment of the cured polymer. Cleaned BK7 glass substrates were coated with the UV-curable polymer Amonil MMS 10 from AMO GmbH (Germany) by spin-coating at 3000 rpm for 120 s. Then, the PDMS working stamp was placed on the top of the fluid Amonil layer and, after 5 min rest time, irradiated by UV light with a dose of 2 J cm^{-2} (UV lamp Bio-Link 365, Vilber Lourmat). Finally, the PDMS working stamp was detached from the UV-cured Amonil MMS 10, leaving a copy of the master structure on the glass substrate. The copied MPG structure was placed on a hot plate at $120 \text{ }^\circ\text{C}$ for 4 min, then coated with 50 nm of gold by vacuum thermal evaporation by using an instrument HHV AUTO 306 from HHV Ltd (UK) in vacuum better than 10^{-6} mBar.

2.2. Optical setup

A polychromatic light beam emitted from a halogen light source LSH102 from LOT-Oriel (Germany) was coupled to a multimode optical fiber M25L02 from Thorlabs (UK). The beam emitted from the optical fiber end was collimated by using a lens with $f=30$ mm and made normally incident at the gold MPG surface through the glass substrate. The reflected beam was collected from a multimode optical fiber M26L02 from Thorlabs (UK) by using a collimator F810SMA-635 from Thorlabs (UK) and delivered to a spectrometer HR4000 from Ocean Optics (USA) or Shamrock 303i from Andor (USA). Raw wavelength spectra of the light beam reflected from the MPG surface were normalized with a spectrum acquired for a reference flat gold surface. A flow-cell was clamped against the grating sensor chip, and it consisted of a polished plastic substrate with drilled input and output ports and a thin PDMS gasket. The volume of the flow-cell was $10 \text{ }\mu\text{L}$, and analyzed liquid samples were flowed through by using the peristaltic pump REGLO Digital MS-4/8 from Ismatec (Switzerland) and tubing with a 0.64 mm inner diameter from Ismatec Wertheim (Germany) at a flow rate of $80 \text{ }\mu\text{L}/\text{min}$. The sensing spot in the flow-cell was illuminated by a polychromatic beam with a diameter of about 5 mm. The normalized reflectivity spectra were evaluated by a dedicated software developed in-house by using LabView from National Instruments (USA). The sequentially acquired specular reflectivity spectra $R_0(\lambda)$ were processed by a routine centroid [26] in the selected wavelength range $\lambda_{n1} - \lambda_{n2}$ in order to track the refractive index changes in realtime. The reflectivity spectra $R_0(\lambda)$ were acquired with an integration time of 5 ms and the accumulation of 300 was used to reduce noise. The centroid wavelength was determined from discrete reflectivity values $R_0(\lambda_i)$ as:

$$\lambda_{\text{cen}} = \frac{\sum_{i=N_1}^{N_2} \lambda_i [R_t - R_0(\lambda_i)]}{\sum_{i=N_1}^{N_2} [R_t - R_0(\lambda_i)]}, \quad (1)$$

where N_1 and N_2 are indexes that define pixels over which the centroid routine was applied, λ_i is the wavelength corresponding to the i^{th} detector pixel, and R_t is a threshold.

2.3. Optical simulations

Finite element method was employed as implemented in a diffraction grating solver DiPoG (Weierstrass Institute, Germany). A grating in a computation cell with a length of up to $\Lambda=4.6 \text{ }\mu\text{m}$ and height $1 \text{ }\mu\text{m}$ was approximated by a mesh of triangles (convergence check was performed by increasing the number of triangles). Cartesian coordinates with the x and z axes in the plane of the MPG structure and y -axis perpendicular to the MPG structure were used as seen in Fig. 1(a).

The corrugation profile with two superimposed relief gratings (period $\Lambda_1=0.46 \mu\text{m}$ and $\Lambda_2=0.242 \mu\text{m}$) and were defined as higher harmonics: $y = a_1 \sin(2\pi/\Lambda_1 \cdot x) + a_2 \sin(2\pi/\Lambda_2 \cdot x)$, where a_1 and a_2 states for amplitudes and $n_1=10$ and $n_2=19$. In the used numerical model, the set of Maxwell equations was solved by using the PARDISO solver of sparse linear systems developed at University of Basel (Switzerland).

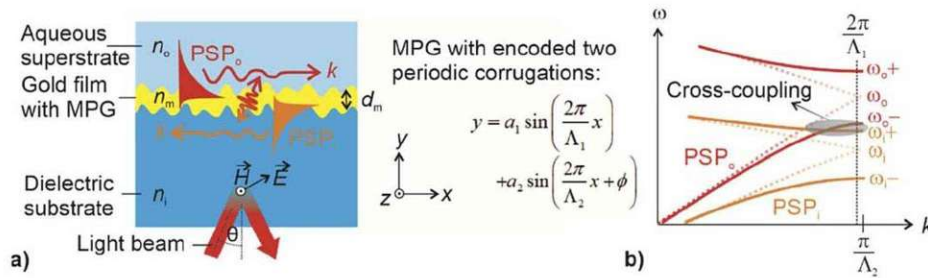


Fig. 1. Schematics of a) the cross-coupling of PSPs across a thin metallic film on an MPG with encoded longer period Λ_1 and shorter period Λ_2 . b) Schematics of the dispersion relation of PSPs at the outer and inner interfaces that is folded into first Brillouin zone.

2.4. Biomolecular binding study

After the deposition of 50 nm thick gold layer to the MPG surface, its surface was modified with a self-assembled thiol monolayer (SAM) by immersion in ethanolic solution with dissolved thiols carrying functional biotin (0.2 mM HS-C11-EG6-Biotin) and passivating oligoethylene glycol groups (0.8 mM HS-C11-EG6-OH) from Prochimia Surfaces in Gdynia (Poland). After overnight incubation, the substrates with MPG were rinsed with ethanol, dried in a stream of nitrogen and stored in argon atmosphere until further use. For the affinity binding measurements, a flow cell was clamped onto the surface of the MPG, and phosphate-buffered saline (137 mM NaCl, 2.7 mM KCl, 12 mM phosphate buffer, pH 7.4, no. E504) from VWR (USA) spiked with 0.05% Tween 20 BioXtra, from SigmaAldrich, (USA) (PBST) was flowed until a stable baseline of the sensor response λ_{cen} is reached. Then, the calibration was done using PBST spiked with sucrose at concentrations of 1, 2 and 4%. Afterwards, the surface was reacted with neutravidin (NA) from Thermo Scientific (Austria) and biotinylated monoclonal capture antibody cAB #13-7349-81 from eBioscience (Austria). This antibody is specific to human tumor necrosis alpha (TNF- α) BMS301 from eBioscience (Austria), and a sandwich immunoassay format was implemented by using a secondary monoclonal antibody sAB against another part of TNF- α #14-7348-81 from eBioscience (Austria).

3. Results and discussion

In order to resonantly excite PSP modes that are cross-coupled through a thin gold film, a relief profile of MPG with two superimposed periodic corrugations is investigated. As illustrated in Fig. 1(a), there is assumed the geometry where a collimated optical beam is travelling through a dielectric substrate (refractive index of glass n_i) and impinges on a corrugated thin gold film (refractive index n_m , thickness of d_m). A normally incident beam ($\theta=0$) is coupled to the PSPs at the inner interface between the substrate n_i and gold n_m by the first-order diffraction on grating corrugation component with a period Λ_1 . In general, this corrugation component also allows to couple the incident beam to PSP modes travelling along the outer interface between the gold film n_m and a lower refractive index dielectric (water with refractive index n_o). However, the coupling efficiency is negligible as the majority of the incident beam intensity is reflected at an

inner interface with the substrate n_i and does not reach the opposite interface in contact with the superstrate n_o .

To solve this problem, additional corrugation component with a shorter period Λ_2 was superimposed over the corrugation with the period Λ_1 . As schematically indicated in the PSP dispersion relation folded to the first Brillouin zone in Fig. 1(b), the introduction of shorter Λ_2 can be utilized for its splitting at the outer and inner interfaces so new Bragg-scattered PSPs occur at distinct wavelengths (represented by frequencies ω_i and ω_o) with an optical bandgap in between. These Bragg-scattered modes are further noted as ω_+ and ω_- and they are associated with diffraction coupling of counter-propagating PSP modes on the corrugation component Λ_2 at individual interfaces generating standing wave-like modes [27]. In general, the spectral width of the optical bandgap in the dispersion relation of PSP modes at ω_i and ω_o can be tuned, so the short-wavelength Bragg-scattered PSP on the inner interface ω_i^+ overlaps with the long-wavelength Bragg-scattered PSP on the outer interface ω_o^- . Then, these modes become phase-matched along the surface and allow to transfer the electromagnetic field intensity through the metallic film via their penetrating evanescent field tails.

This concept was firstly analyzed by using numerical simulations. In this study, a thickness of the gold film of $d_m=50$ nm was assumed with conformally corrugated interfaces between the substrate with refractive index $n_i=1.5$ (BK7 glass) and superstrate with lower refractive index $n_o=1$ (air) and $n_o \sim 1.33$ (water). There was used relief profile composed of sinusoidal corrugation with a longer period $\Lambda_1=460$ nm superimposed over additional sinusoidal corrugation exhibiting a shorter period $\Lambda_2=242$ nm. Firstly, we simulated zero-order reflectivity spectrum R_0 for the corrugation profile, in which the amplitude for the long period Λ_1 component was set to $a_1=10$ nm and the shorter period component Λ_2 was not present by assuming $a_2=0$ nm. Then, the first order excitation of the PSP mode at the inner interface occurs and manifests itself as a dip in the wavelength spectrum of R_0 centered at a wavelength $\lambda_i=745$ nm, Fig. 2(a). When increasing the refractive index of the dielectric at the outer interface from $n_o=1.33$ to 1.35, a negligible shift in the resonance wavelength $\delta\lambda_i=0.7$ nm occurs as the majority of the field intensity associated with this resonance is confined at the opposite inner interface with the glass substrate [see the profile of magnetic field amplitude in Fig. 2(c)].

When introducing the shorter period component Λ_2 forming the complete MPG structure with the amplitudes $a_1=10$ and $a_2=10$ nm, the resonance at λ_i splits and two overlapping dips occur at wavelengths of $\lambda_{i1}=724$ and $\lambda_{i2}=744$ nm. Interestingly, when increasing the refractive index at the outer interface from $n_o=1.33$ to 1.35, both resonances shift by about 6.5 nm and the coupling strength to shorter wavelength resonance λ_{i1} increases while that to λ_{i2} decreases, Fig. 2(b). The reason that the split resonance can be efficiently detuned by the refractive index change at the outer interface n_o is due to the fact that the associated field profile is confined at both interfaces as cross-coupling of PSPs through the metallic film occurs, Fig. 2(c). Notably, the coupling strength to the cross-coupled PSPs is decreased compared to the geometry when PSPs travelling on the individual interface are excited with the selected corrugation amplitude a_1 . The coupling strength can be optimized by tuning this parameter as indicated by the following experimental study.

Experimentally, the MPG structure was prepared by sequential recording of the periodic interference field with periods Λ_1 and Λ_2 into a photoresist layer by using UV-LIL. The corrugation profile was then etched to the layer by a developer, and the tuning of modulation depths a_1 and a_2 was facilitated by controlling the irradiation time of each step and by the adjusting development time. Afterwards, the structure was cast to PDMS in order to serve as a working stamp, and multiple copies were prepared by transferring the corrugation to a UV-curable polymer Amonil followed by the coating with a gold film with a thickness of $d_m=50$ nm. The corrugation profile was observed by atomic force microscopy (AFM), as presented in Fig. 3(a). It shows a crossed structure where the MPG corrugation profile was recorded in both x and z directions and the fast Fourier transform analysis presented in Fig. 3(b) revealed the parameters of $\Lambda_1=462.0$ nm,

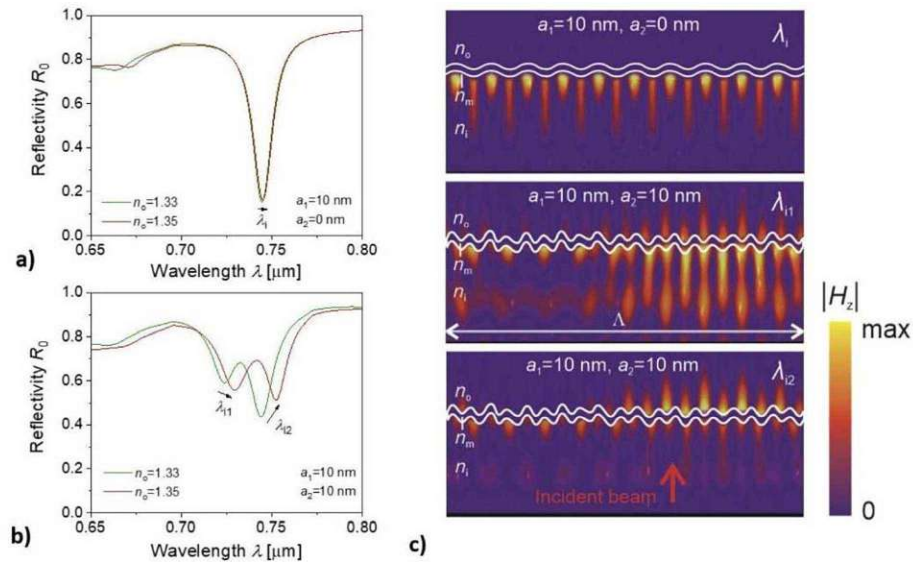


Fig. 2. Simulated reflectivity R_0 for transverse magnetically polarized normally impinging beam from a substrate at the structure with a) encoded single period ($a_1=10$ nm, $a_2=0$ nm) and b) two periods ($a_1=10$ nm, $a_2=10$ nm). c) Near field distribution of magnetic field intensity $|H_z|$ in the xy plane at wavelength λ_i , λ_{i1} and λ_{i2} . The simulations were carried out for a super-period $\Lambda=4.6$ μm , longer period $\Lambda_1=460$ nm, shorter period $\Lambda_2=242$ nm, and $n_0=1.33$.

$\Lambda_2=236.4$ nm, $a_1=13$ nm and $a_2=4$ nm. It is worth of noting that the period Λ_1 was selected to slightly deviate from the $2\Lambda_2$ (as was originally studied on gratings with photonic bandgap [28]) in order to lift out the sensitivity on the mutual phase between these corrugations ϕ . The reason is that the used UV-LIL recording of the MPG structure does not allow for controlling this parameter and by introducing a small offset the phase dependence is averaged when irradiating surface with area at mm^2 scale.

The MPG structure on a glass substrate was used as a sensor chip, and its top outer surface was clamped against a flow-cell, see Fig. 3(c). Then, a polychromatic light beam was made reflected from the inner surface of the gold film on the sensor chip and its spectrum was analyzed by a spectrometer. As described further, there were observed changes in the specular reflectivity spectrum $R_0(\lambda)$ due to the variations of the refractive index of a liquid n_0 flowed through the flow-cell as well as upon refractive index changes induced by molecular binding events. Reflectivity spectra $R_0(\lambda)$ were firstly measured for refractive index $n_0=1$ (air was present in the flow-cell) and $n_0=1.33$ (water was flowed through the flow-cell), Fig. 4(a). In contact with air, reflectivity spectra measured from the inner substrate side (BK7 glass) and the outer superstrate side (flow-cell) show resonances manifested as a dip in $R_0(\lambda)$. For the inner substrate side, the dip is centered at a wavelength close to 720 nm (red curve, ω_{i+}) which is spectrally separated from that observed from the superstrate outer side at 575 nm (blue curve, ω_{o-}). When increasing the outer refractive index to $n_0=1.33$, the reflectivity spectrum $R_0(\lambda)$ measured from the inner superstrate side (green curve) changes and exhibits two spectrally separated dips. These two dips are located at wavelengths of 650 nm (ω_{o+}) and 720 nm (ω_{o-}), and they can be interpreted as first-order diffraction coupling by the corrugation component Λ_1 to PSP modes that are Bragg-scattered on the outer interface by the corrugation component Λ_2 . Importantly, the spectral position of the resonance ω_{o-} is coincident with ω_{o+} that is observed when probing from the inner substrate

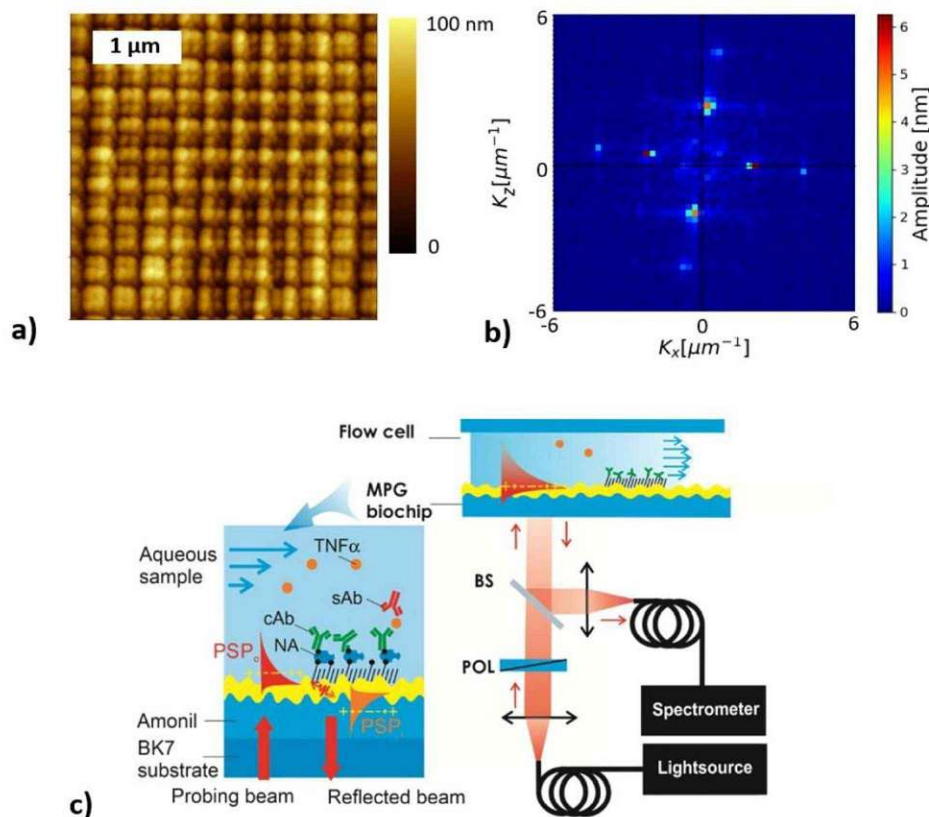


Fig. 3. a) AFM observation of the topography of the prepared MPG corrugation carrying the recorded corrugation with longer period $\Lambda_1=462$ nm, $a_1=13$ nm and shorter period $\Lambda_2=236.4$ nm, $a_2=10.5$ nm as determined by b) Fourier transform analysis. c) Schematics of the sensor chip with the MPG corrugation and the optical setup for the measurement of spectral reflectivity R_0 with beam splitter (BS) and polarizer (POL).

side. Therefore, the overlaid resonance shows a character of two superimposed Lorentzian dips. A similar profile is observed when the reflectivity $R_0(\lambda)$ is measured from the inner substrate side (black curve), which further confirms that a cross-coupling of PSP modes through the metallic film occurs as predicted by the simulations in Fig. 2(b). The small deviations in the measured resonance spectral position and the stronger coupling can be attributed to the effect of roughness of the gold film that was not taken into account in the mode, increased modulation amplitude a_1 , and possible differences in the optical constants of used thin films.

In order to investigate this phenomenon in more detail, the bulk refractive index of the aqueous solution on the outer surface of the sensor chip was changed from $n_0=1.33$ to 1.38, and the reflectivity $R_0(\lambda)$ was measured from the inner substrate side. As Fig. 4(b) shows, the spectral shape of the resonance dip changes and the lower wavelength component (centered at λ_{i1}) red shifts and become more pronounced. The longer wavelength part (centered at λ_{i2}) also red shifts, but its coupling strength decreases when increasing n_0 . This observation is in qualitative agreement with the simulations presented in Fig. 2(b) and confirms that the proposed concept allows for the cross-coupling of PSP modes through the metallic film and to optically monitor changes in the refractive index from the opposite side.

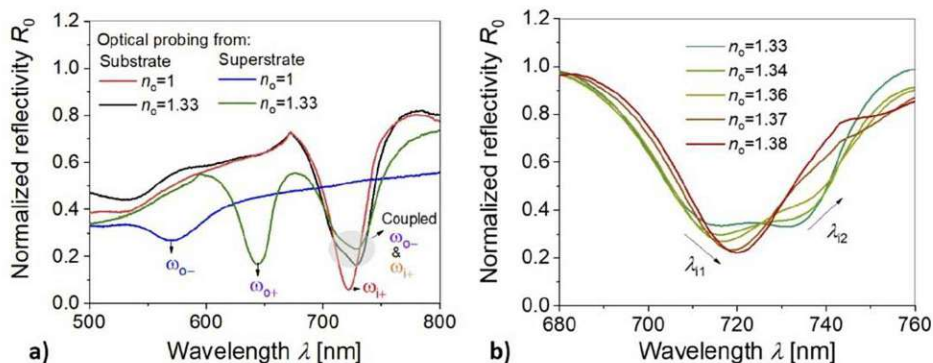


Fig. 4. a) Measured reflectivity R_0 with a beam normally incident at the sensor chip carrying MPG from its substrate (n_i) and superstrate (n_o) sides and air ($n_o=1$) and water ($n_o=1$) on the top. b) A detail of the reflectivity spectrum in the spectral region with cross-coupled surface plasmon resonance and refractive index on the top of the structure varied between $n_o=1.33$ and 1.38.

To implement the developed MPG structure for *in situ* realtime SPR measurements, the reflectivity spectra R_0 were acquired in time, and a centroid method was applied in the spectral region where the cross-coupled SPR dip occurs. This approach was chosen as the variation in the coupling strength to the two overlapped resonances λ_{i1} and λ_{i2} appears to be more pronounced than the spectral shifts $\delta\lambda_{i1}$ and $\delta\lambda_{i2}$. In general, the centroid wavelength λ_{cen} is blue-shifted when increasing the refractive index of the outer dielectric medium n_o , as illustrated in Fig. 5(a). This trend is opposite to classical SPR (where a red shift occurs) due to the observed coupling strength changes of respective dips at λ_{i1} and λ_{i2} . To test the performance of the approach, we tracked the centroid wavelength λ_{cen} in real-time upon changing the bulk refractive index n_o and upon the affinity binding of biomolecules on the gold MPG surface. Before this experiment, the MPG sensor chip was modified by a mixed thiol SAM with biotin head groups. Then the chip was loaded to the optical reader, and a baseline in the sensor signal λ_{cen} was established upon a flow of working buffer PBST, see Fig. 5(b). The centroid threshold parameter was optimized and the best signal-to-noise-ratio was obtained close to $R_t=0.5$, similar to the previous works where a shift in the SPR resonance dip was measured in reflectivity spectra [26]. Afterwards, the PBST solution was spiked with sucrose (1%, 2%, and 4%) and sequentially flowed over the surface to increase the bulk refractive index ($\delta n_o=1.4 \times 10^{-3}$, 2.8×10^{-3} , 5.6×10^{-3} RIU, respectively). As can be seen in Fig. 5(b), the increase in refractive index n_o is accompanied by a stepwise decrease in the sensor signal λ_{cen} , from which a sensitivity of $S_b=\delta\lambda_{cen}/\delta n_o=-252$ nm/RIU was determined. For the baseline noise quantified with a standard deviation of $\sigma(\lambda_{cen})=3.75 \times 10^{-3}$ nm, this sensitivity corresponds to the refractive index resolution of 1.5×10^{-5} . It is worthy of noting that such resolution is comparable to similar sensors with regular grating-coupled SPR (resolution of 6×10^{-6} RIU was reported [29]). The accuracy of the proposed approach is apparently hampered by the fact that the cross-coupled PSP modes travel on both interfaces, while the regular grating-coupled SPR allows for better field confinement by the excitation of PSPs only at individual (active) surface. This can be estimated to reduce the sensitivity (and respectively the refractive index resolution) by a factor of two. Additional parameter that can be used to further optimize the performance of the proposed concept is the thickness of the metal film d_m . In general, decreasing this parameter leads to increasing the coupling strength between the surface plasmon modes travelling along the outer (PSP_o) and inner (PSP_i) by stronger overlapping their field profiles. However, there will also occur an increase in radiative damping of PSP_o that is in general leaky mode into the substrate with higher index of refraction n_i . We assume that then the

spectral width of the coupled resonance will be broadened and the performance characteristics impeded. The chosen thickness of $d_m=50$ nm was selected as the radiative damping is still weak and it already allows to achieve the cross-coupling with the prepared MPG topography.

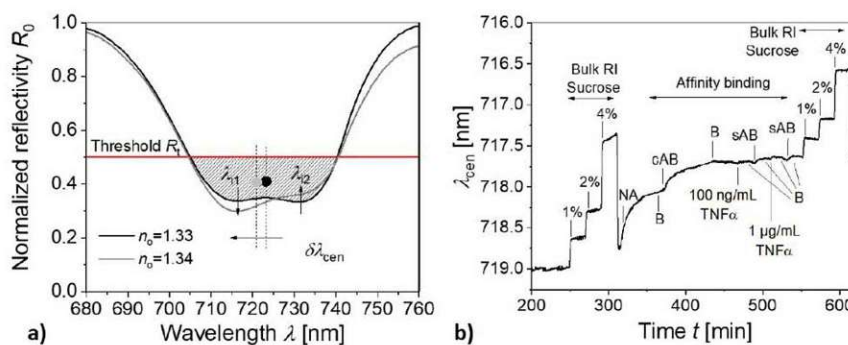


Fig. 5. a) Evaluation of the resonance variations due to refractive index changes by using the centroid method and b) example of the measured kinetics data for bulk refractive index changes δn_0 induced by a flow of buffer solution spiked with sucrose at 1%, 2% and 4% and for the affinity binding on the sensor surface. B indicates the rinsing with PBST.

Finally, the MPG sensor chip was used for the probing of affinity binding of biomolecules that constitute an assay for the detection of a protein biomarker TNF- α – human tumor necrosis factor alpha. Firstly, a solution with neutravidin – NA – dissolved in PBST at a concentration of 125 μ g/mL was flowed through the sensor for 45 min. The respective SPR sensor signal presented in Fig. 5(b) shows a gradual decrease of λ_{cen} by 0.75 nm due to the affinity binding of NA to biotin groups carried by the thiol SAM on the gold MPG surface. Then, biotinylated capture antibody – cAB – that is specific to TNF- α was immobilized from PBST solution spiked at a concentration of 2 μ g/mL that was flowed over the sensor surface for 45 min. Similar to the previous step, the affinity binding of cAB is manifested as a gradual decrease in λ_{cen} , which levels as a change of 0.30 nm. Afterwards, the sensor surface is used for the detection of TNF- α that was amplified by using a secondary antibody cAB that is also specific to TNF- α . The detection consisted of 15 min flow of TNF- α , 5 min rinsing with PBST, and additional 15 min binding of the sAB dissolved at 500 ng/mL in PBST. As seen in Fig. 5(b), a shift in λ_{cen} (0.028 nm) was measured for direct binding of the TNF- α at a concentration of 100 ng/mL, and an additional drop (0.04 nm) was observed after the sAB amplification. In the second step, the same assay was repeated for the TNF- α concentration increased to 1 μ g/mL and the affinity binding resulted in a stronger response (0.036 nm and 0.059 nm, respectively). Let us note that these values are not directly proportional to the TNF- α concentration in a liquid sample as the sensor surface binding capacity probably reached its saturation. At the end of the experiment, the calibration was repeated by changing the bulk refractive index n_0 with sucrose spiking of PBST, leading to similar shifts as at the start of the experiment.

4. Conclusions

The proposed concept of multi-period grating – MPG – was theoretically investigated and experimentally demonstrated to provide efficient means for the direct back-side excitation of propagating surface plasmons. Compared to alternative approaches based on long-range surface plasmons relying on low refractive index polymers and localized surface plasmons supported by arrays of metallic nanoparticles, the developed structures can be prepared without complex lithography steps and do not rely on expensive polymer materials. In conjunction with

advancements in the nanoimprint lithography that can be scaled up using roll-to-roll configuration, large areas carrying MPG structure can be prepared and exploited in various sensor modalities. The refractometric experiment and a model assay experiment confirm that the accuracy of the sensor configuration probed from the back-side sensor chip is similar to that measured for regular grating coupled SPR when the probing is performed through the analyzed liquid sample.

Funding

ESIF and MEYS (CZ.02.2.69/0.0/0.0/18_053/0016627); Lower Austria (WST3-F-5030820/010-2019); Österreichische Forschungsförderungsgesellschaft (861578).

Disclosures

The authors declare no conflicts of interest to this article.

References

1. J. Homola, "Surface plasmon resonance sensors for detection of chemical and biological species," *Chem. Rev.* **108**(2), 462–493 (2008).
2. M. F. Cardinal, E. V. Ende, R. A. Hackler, M. O. McAnally, P. C. Stair, G. C. Schatz, and R. P. Van Duyne, "Expanding applications of SERS through versatile nanomaterials engineering," *Chem. Soc. Rev.* **46**(13), 3886–3903 (2017).
3. M. Bauch, K. Toma, M. Toma, Q. Zhang, and J. Dostalek, "Plasmon-enhanced fluorescence biosensors: a review," *Plasmonics* **9**(4), 781–799 (2014).
4. D. Rodrigo, A. Tittl, N. Ait-Bouziad, A. John-Herpin, O. Limaj, C. Kelly, D. Yoo, N. J. Wittenberg, S. H. Oh, H. A. Lashuel, and H. Altug, "Resolving molecule-specific information in dynamic lipid membrane processes with multi-resonant infrared metasurfaces," *Nat. Commun.* **9**(1), 2160 (2018).
5. B. Liedberg, C. Nylander, and I. Lunström, "Surface plasmon resonance for gas detection and biosensing," *Sens. Actuators* **4**, 299–304 (1983).
6. J. Homola, J. Dostalek, S. F. Chen, A. Rasooly, S. Y. Jiang, and S. S. Yee, "Spectral surface plasmon resonance biosensor for detection of staphylococcal enterotoxin B in milk," *Int. J. Food Microbiol.* **75**(1-2), 61–69 (2002).
7. J. Dostalek, J. Homola, and M. Miler, "Rich information format surface plasmon resonance biosensor based on array of diffraction gratings," *Sens. Actuators, B* **107**(1), 154–161 (2005).
8. B. Spackova, P. Wrobel, M. Bockova, and J. Homola, "Optical Biosensors Based on Plasmonic Nanostructures: A Review," *Proc. IEEE* **104**(12), 2380–2408 (2016).
9. A. J. Haes and R. P. Van Duyne, "A nanoscale optical biosensor: Sensitivity and selectivity of an approach based on the localized surface plasmon resonance spectroscopy of triangular silver nanoparticles," *J. Am. Chem. Soc.* **124**(35), 10596–10604 (2002).
10. O. Kedem, A. Vaskevich, and I. Rubinstein, "Improved Sensitivity of Localized Surface Plasmon Resonance Transducers Using Reflection Measurements," *J. Phys. Chem. Lett.* **2**(10), 1223–1226 (2011).
11. J. A. Jackman, V. P. Zhdanov, and N. J. Cho, "Nanoplasmonic Biosensing for Soft Matter Adsorption: Kinetics of Lipid Vesicle Attachment and Shape Deformation," *Langmuir* **30**(31), 9494–9503 (2014).
12. J. Yamamichi, T. Ojima, M. Iida, K. Yurugi, T. Imamura, E. Ashihara, S. Kimura, and T. Maekawa, "Surface chemical approach to single-step measurement of antibody in human serum using localized surface plasmon resonance biosensor on microtiter plate system," *Anal. Bioanal. Chem.* **406**(18), 4527–4533 (2014).
13. M. Couture, K. K. Ray, H. P. Poirier-Richard, A. Crofton, and J. F. Masson, "96-Well Plasmonic Sensing with Nanohole Arrays," *ACS Sens.* **1**(3), 287–294 (2016).
14. D. M. Zhang, Y. L. Lu, Q. Zhang, Y. Yao, S. Li, H. L. Li, S. L. Zhuang, J. Jiang, G. L. Liu, and Q. J. Liu, "Nanoplasmonic monitoring of odorants binding to olfactory proteins from honeybee as biosensor for chemical detection," *Sens. Actuators, B* **221**, 341–349 (2015).
15. M. Vala, C. T. Ertsgaard, N. J. Wittenberg, and S. H. Oh, "Plasmonic Sensing on Symmetric Nanohole Arrays Supporting High-Q Hybrid Modes and Reflection Geometry," *ACS Sens.* **4**(12), 3265–3274 (2019).
16. D. Sarid, "Long range surface plasma waves on very thin metal films," *Phys. Rev. Lett.* **47**(26), 1927–1930 (1981).
17. N. C. Lindquist, T. W. Johnson, J. Jose, L. M. Otto, and S. H. Oh, "Ultrasoother metallic films with buried nanostructures for backside reflection-mode plasmonic biosensing," *Ann. Phys.* **524**(11), 687–696 (2012).
18. M. Vala and J. Homola, "Multiple beam interference lithography: A tool for rapid fabrication of plasmonic arrays of arbitrary shaped nanomotifs," *Opt. Express* **24**(14), 15656–15665 (2016).
19. G. Barbillon, "Plasmonic Nanostructures Prepared by Soft UV Nanoimprint Lithography and Their Application in Biological Sensing," *Micromachines* **3**(1), 21–27 (2012).
20. N. G. Quilis, M. Leveque, I. Khan, W. Knoll, S. Boujday, M. Lamy de la Chapelle, and J. Dostalek, "Tunable laser interference lithography preparation of plasmonic nanoparticle arrays tailored for SERS," *Nanoscale* **10**(21), 10268–10276 (2018).

2.4. Multi-diffractive Grating for Surface Plasmon Biosensors with Direct Back-side Excitation

Research Article

Vol. 28, No. 26 / 21 December 2020 / *Optics Express* 39780

Optics EXPRESS

21. H. Im, S. H. Lee, N. J. Wittenberg, T. W. Johnson, N. C. Lindquist, P. Nagpal, D. J. Norris, and S. H. Oh, "Template-Stripped Smooth Ag Nanohole Arrays with Silica Shells for Surface Plasmon Resonance Biosensing," *ACS Nano* **5**(8), 6244–6253 (2011).
22. N. Q. Quilis, M. van Dongen, P. Venugopalan, D. Kotlarek, C. Petri, A. M. Cencerrado, S. Stanescu, J. L. Toca Herrera, U. Jonas, M. Möller, A. Mourran, and J. Dostalek, "Actively tunable collective localized surface plasmons by responsive hydrogel membrane," *Adv. Opt. Mater.* **7**(15), 1900342 (2019).
23. I. Khan, H. Keshmiri, F. Kolb, T. Dimopoulos, and E. List-Kratochvil, "Plasmonic absorber based on multi-diffractive grating," *Adv. Opt. Mater.* **4**(3), 435–443 (2016).
24. S. Fossati, S. Hageneder, S. Menad, E. Mailart, and J. Dostalek, "Multiresonant plasmonic nanostructures for ultrasensitive fluorescence biosensing," *Nanophotonics* **9**(11), 3673–3685 (2020).
25. P. Adam, J. Dostalek, and J. Homola, "Multiple surface plasmon spectroscopy for study of biomolecular systems," *Sens. Actuators, B* **113**(2), 774–781 (2006).
26. G. G. Nenninger, M. Piliarik, and J. Homola, "Data analysis for optical sensors based on spectroscopy of surface plasmons," *Meas. Sci. Technol.* **13**(12), 2038–2046 (2002).
27. W. L. Barnes, T. W. Preist, S. C. Kitson, J. R. Sambles, N. K. Cotter, and D. J. Nash, "Photonic gaps in the dispersion of surface plasmons on gratings," *Phys. Rev. B* **51**(16), 11164–11167 (1995).
28. W. L. Barnes, T. W. Preist, S. C. Kitson, and J. R. Sambles, "Physical origin of photonic energy gaps in the propagation of surface plasmons on gratings," *Phys. Rev. B* **54**(9), 6227–6244 (1996).
29. D. Kotlarek, M. Vorobii, W. Ogieglo, W. Knoll, C. Rodriguez-Emmenegger, and J. Dostalek, "Compact Grating-Coupled Biosensor for the Analysis of Thrombin," *ACS Sens.* **4**(8), 2109–2116 (2019).

2.5. Dual Monitoring of Surface Reactions in Real Time by Combined Surface Plasmon Resonance and Field-Effect Transistor Interrogation

The following publication is reprinted under the ACS AuthorChoice^d publishing agreement.

Patrik Aspermaier, Ulrich Ramach, Ciril Reiner-Rozman, Stefan Fossati, Bernadette Lechner, Sergio E. Moya, Omar Azzaroni, Jakub Dostalek, Sabine Szunerits, Wolfgang Knoll, and Johannes Binterger Dual Monitoring of Surface Reactions in Real Time by Combined Surface-Plasmon Resonance and Field-Effect Transistor Interrogation. *J. Am. Chem. Soc.* **142**, 11709–11716 (2020). <https://doi.org/10.1021/jacs.9b11835>

Copyright © 2020 American Chemical Society

Biosensors detect analytes based on the change of some physical quantity of the sensor interface in response to one or more physical or chemical properties of the analyte. The transducers rely on properties like mass, electrical charge, and electrical or hydrodynamic permittivity. The signals derived are sometimes ambiguous, for example, a thin layer of densely packed molecules can create a signal very similar to the signal caused by a less densely packed thicker layer in mass sensitive sensor modalities. By probing the same interface with two different modalities at the same time, complementary properties of the surface can be probed to mitigate some of the ambiguities.

In this chapter, an instrument is presented that is capable of simultaneous observation of mass deposition to a metallic interface that also serves as the gate electrode of an electrolyte-gated graphene-oxide field effect transistor. SPR is used to monitor the adsorption of material onto the surface while simultaneously observing the changes of the electrical properties of the interface using the transistor. With this bimodal instrument, the layer-by-layer formation of a polyelectrolyte film is observed. The deposition of the material onto the interface is observed by the SPR modality while the strongest influence on the transistor signal is exerted by the net surface charge. Remarkably, the two modalities reveal different

^d Appendix 5.7.2

2.5. Dual Monitoring of Surface Reactions in Real Time by Combined Surface Plasmon Resonance and Field-Effect Transistor Interrogation

time constants for their corresponding processes, which allow new insights into the layer formation process that would not be conceivable with separate observations.

This work was initiated by Johannes Bintinger and Stefan Fossati, who developed the concept and built the first working device for the integrated SPR and gFET measurements. The instrument was then further developed by Patrik Aspermaier for routine measurements, carried out by Ulrich Ramach and Bernadette Lechner. During further development, Stefan Fossati was responsible for the SPR part of the experimental setup and contributed to the corresponding parts of the manuscript. The development of the theory for the data analysis of the combined gFET/SPR system was a joint effort of the authors under the lead of Ciril Reiner-Rozman.

Supporting information to this article is included in the appendix, section 5.4.

2.5. Dual Monitoring of Surface Reactions in Real Time by Combined Surface Plasmon Resonance and Field-Effect Transistor Interrogation

This is an open access article published under an ACS AuthorChoice License, which permits copying and redistribution of the article or any adaptations for non-commercial purposes.



J | A | C | S
JOURNAL OF THE AMERICAN CHEMICAL SOCIETY

pubs.acs.org/JACS

Article

Dual Monitoring of Surface Reactions in Real Time by Combined Surface-Plasmon Resonance and Field-Effect Transistor Interrogation

Patrik Aspermaier,¹ Ulrich Ramach,¹ Ciril Reiner-Rozman, Stefan Fossati, Bernadette Lechner, Sergio E. Moya, Omar Azzaroni, Jakub Dostalek, Sabine Szunerits, Wolfgang Knoll, and Johannes Bintinger*

Cite This: *J. Am. Chem. Soc.* 2020, 142, 11709–11716

Read Online

ACCESS |

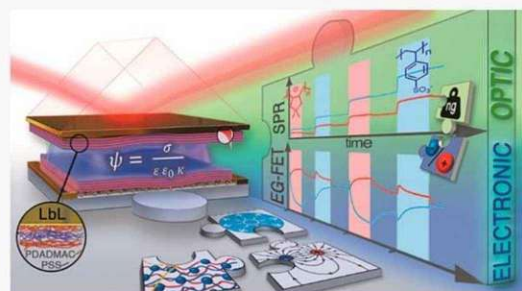
Metrics & More

Article Recommendations

Supporting Information

ABSTRACT: By combining surface plasmon resonance (SPR) and electrolyte gated field-effect transistor (EG-FET) methods in a single analytical device we introduce a novel tool for surface investigations, enabling simultaneous measurements of the surface mass and charge density changes in real time. This is realized using a gold sensor surface that simultaneously serves as a gate electrode of the EG-FET and as the SPR active interface. This novel platform has the potential to provide new insights into (bio)adsorption processes on planar solid surfaces by directly relating complementary measurement principles based on (i) detuning of SPR as a result of the modification of the interfacial refractive index profile by surface adsorption processes and (ii) change of output current as a result of the emanating effective gate voltage modulations.

Furthermore, combination of the two complementary sensing concepts allows for the comparison and respective validation of both analytical techniques. A theoretical model is derived describing the mass uptake and evolution of surface charge density during polyelectrolyte multilayer formation. We demonstrate the potential of this combined platform through the observation of layer-by-layer assembly of PDADMAC and PSS. These simultaneous label-free and real-time measurements allow new insights into complex processes at the solid–liquid interface (like non-Fickian ion diffusion), which are beyond the scope of each individual tool.



INTRODUCTION

Electronic sensing devices including those based on electrolyte gated field-effect transistors (EG-FETs) have attracted increasing attention in recent years due to their potential for the use in compact and cost-efficient analytical devices.^{1–7} Despite the progress in understanding the underlying principles and even demonstrating label-free single-molecule detection,⁸ no commercial EG-FET biosensor has yet entered the market. Specifically, low reproducibility, unspecific binding, sensor drift, and batch to batch variations have hindered large-scale deployment of this emerging class of biosensors.⁹ In the early 1980s and 1990s, comparable challenges were addressed in the field of surface plasmon resonance (SPR) biosensor systems.^{10,11} Research carried out over the last decades has paved the way for establishing this method in the market of biomolecular interaction analysis,¹² and we have witnessed the gradual advancement of this technology for rapid detection of chemical and biological species.^{10,13} SPR biosensors allow direct label-free monitoring of molecular affinity binding events on the sensor surface associated with changes in surface mass density.^{14,15} They are probed by the confined optical field of

surface plasmons and monitored through variations in the local refractive index. Over the last years, progress in the instrumentation of SPR biosensor technology has allowed for detection of minute changes in surface mass density, enabling analysis of molecules with low molecular weight and species that are present in trace amounts in analyzed liquid samples. However, they typically rely on complex optical systems that are deployed in specialized laboratories, particularly when combined with other techniques for measurement of additional parameters beyond the affinity binding rates. These parameters include identification of biomolecular interactions by coupling SPR biosensors with mass spectrometry,¹⁶ surface-enhanced Raman spectrometry,¹⁷ fluorescence spectroscopy,¹⁸ or monitoring of conformational changes of biomolecules with

Received: November 11, 2019

Published: May 14, 2020



ACS Publications

© 2020 American Chemical Society

11709

<https://dx.doi.org/10.1021/jacs.9b11835>
J. Am. Chem. Soc. 2020, 142, 11709–11716

2.5. Dual Monitoring of Surface Reactions in Real Time by Combined Surface Plasmon Resonance and Field-Effect Transistor Interrogation

plasmonically enhanced IR spectroscopy.¹⁹ In comparison with these methods, EG-FET systems offer the advantage of simpler device architecture combined with an electronic readout principle, scalable cost-efficient production, low power consumption, and facile integration into point-of-care platforms that do not require specialists for operation.⁷ The measurement principle is based on sensing of complementary changes caused by electric field effects,^{2,20–25} associated with changes in charge distribution upon capture of a target species. This approach allows probing at closer proximity to the sensor surface²⁶ than SPR and has the potential to monitor effects that are beyond the scope of the optical SPR technique, for instance, conformational changes of biomolecule surface reactions.²⁷ As many biologically relevant processes are inherently linked to mass and charge variations, fusing different sensing techniques into one multifunctional instrument could offer intriguing possibilities to investigate phenomena from different perspectives. Only a few reports in this context attempt to separate mass and charge effects,^{28–30} and neither offered temporal resolution, performed proper spatial coupling of the system, nor provided a satisfying theoretical framework.

Here, we report an approach to combine SPR (optical) and EG-FET (electronic) readouts for simultaneous and real-time observation of optical and electronic aspects of molecular interactions. It is realized that using a gold sensor surface simultaneously serves as the gate electrode of the EG-FET and as the SPR-active interface (Figure 1). We demonstrate the

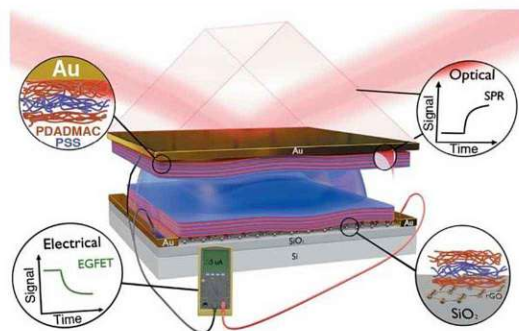


Figure 1. Schematic illustration of the combined SPR/EG-FET setup. Top Au electrode plays the dual role of SPR sensing surface and EG-FET gate electrode.

capabilities of the developed SPR/EG-FET platform through the real-time observation of layer-by-layer (LbL) assembly of charged polyelectrolytes. We elucidate surface effects including intralayer ion diffusion processes from complementary techniques. This surface architecture represents a well-established system that offers a simple bottom-up modification strategy on different substrates.^{31–35} LbL multilayers are sequentially assembled using the attractive forces between oppositely charged polyelectrolytes and typically characterized after each layer deposition step. Moreover, this technology shows great potential in multiple, diverse fields such as fuel cells,³⁶ batteries,³⁷ drug delivery,³⁸ and water desalination,³⁹ but a better understanding of the intrinsic processes and the resulting film properties is essential for guiding the development of new films and specific applications.^{40,41}

Real-time measurement using the SPR/EG-FET approach offer a means to observe typically inaccessible effects associated

with the kinetics of binding and redistribution of mass and charge density during the growth of individual layers. In addition, the reported approach of the bifunctional sensor can be extended in a straightforward manner for measurement of other (bio)molecular interactions and serve to further develop these platforms and to elucidate surface effects that neither SPR nor EG-FET can address individually. Due to their relatively large mass and high charge density, LbL architectures are well-suited model systems to demonstrate the capability of the novel platform for monitoring mass deposition and charge distribution.

RESULTS

SPR chemo-optical signal transduction relies on the detuning of the resonant optical excitation of surface plasmons on a metallic surface. It occurs due to the increase of refractive index upon growth of a (bio)molecular assembly on the sensor surface.¹¹ The observed detuning of SPR can be converted into changes in the surface mass density Γ of the (bio)molecular layer using effective medium theory.^{42,43} In contrast, the chemo-electrical signal transduction in EG-FETs is based on the locally induced electric field variations induced by surface charge density changes on the sensor modulating the Fermi level,⁴⁴ observed as a shift of the Dirac point V_D , the voltage of lowest conductance (Figure 2). We observed LbL assembly of polyelectrolyte multilayers (PEM) using SPR with Kretschmann configuration of the attenuated total internal reflection method.

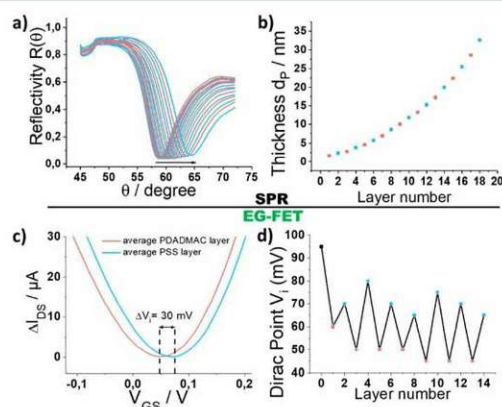


Figure 2. (Top) Sequential LbL assembly monitored by a SPR system using a planar gold surface. (a) Shift of the resonance angle as result of layer deposition, and (b) total thickness of the adsorbed films as a function of deposited layers. (Bottom) LbL assembly monitored in situ by an EG-FET system based on rGO. (c) Transfer curves of EG-FET for PDADMAC/PSS assemblies, and (d) change of the Dirac points V_D as a function of the number of adsorbed layers and their respective charges.

The resonant excitation of surface plasmons manifests itself as a dip in the angular reflectivity $R(\theta)$ (Figure 2a). At the resonant angle, the excited surface plasmons probe the gold sensor surface with a PEM that was sequentially grown from positively charged poly(diallyldimethylammonium chloride) (PDADMAC; average molecular weight < 100 kDa) and negatively charged poly(sodium 4-styrenesulfonate) (PSS; average molecular weight approximately 70 kDa) during

2.5. Dual Monitoring of Surface Reactions in Real Time by Combined Surface Plasmon Resonance and Field-Effect Transistor Interrogation

continuous flow (100 $\mu\text{L}/\text{min}$). Polymer solutions (1 mg/mL in 0.1 M KCl aqueous solution) with refractive index $n_s = 1.333$ were sequentially pumped over the UV–ozone activated gold sensor surface with intermediate rinsing steps (see Supporting Information for details). After growth of each layer, angular reflectivity scans $R(\theta)$ were recorded and the thickness d_p and refractive index n_p of the assembled PEM were obtained by fitting the spectra using the Fresnel reflectivity model. Analysis was described in detail in previous work,³⁵ and the refractive index of PDADMAC/PSS layers was measured as $n_p = 1.577$ when dried in contact with air. After swelling of the PEM in 0.1 M aqueous KCl solution, its refractive decreases to $n_p = 1.476$. Fitting $R(\theta)$ for swollen PEMs allows determining the dependence of layer thickness d_p on the number of growth steps, which can be seen in Figure 2b (corresponding kinetic measurements as well as angular scans are shown in Figure S1). In accordance with previous reports,⁴⁵ this dependence exhibits a parabolic trend, and the average increase of $\Delta d_p = 0.95$ nm was determined for the first eight layers. The average surface mass density increase $\Delta\Gamma$ per layer associated with LbL deposition of the PEM was determined by^{46,47}

$$\Delta\Gamma = \Delta d_p \cdot (n_p - n_s) \cdot \left(\frac{\partial n}{\partial c}\right)^{-1} \quad (1)$$

resulting in $\Delta\Gamma = 69$ ng/cm². In this equation the coefficient $\partial n/\partial c = 0.2$ mm³ mg⁻¹ relates the changes in refractive index with the concentration of (bio)polymers bound to the surface.⁴⁸

We further investigated the PEM assembly using reduced-graphene oxide-based field-effect transistors (rGO-FET) by monitoring the resulting Dirac point shifts ΔV_i (Figure 2c and 2d).^{34,35} rGO-FETs were fabricated by previously reported procedures (see Supporting Information).³⁵ All measurements were performed in a dedicated flow cell (Figures S19 and S20). Electrical measurements were performed by applying a 50 mV source–drain bias and sweeping the gate potential V_{GS} while monitoring the current between the drain and the source I_{DS} using a Keysight U2722A instrument with custom-made LabVIEW software (Figure S21). An Ag/AgCl reference electrode was used as a gate electrode. As shown in Figure 2c, positively charged PDADMAC layers shift the transfer curve ($I_{DS}V_{GS}$) to more negative voltage values compared to a positive Dirac shift ΔV_i introduced by negatively charged PSS layers, which is in agreement with previous publications.⁴⁹ The observed ΔV_i between alternating layers are on the order of 25–40 mV. Furthermore, the dependence on the ionic strength of the KCl solutions was also evaluated (Figure S11).

Interestingly, these shifts obtained from dynamic LbL-processes are smaller than values obtained from static assembly processes, as recently shown by our group,³⁵ and can be explained by the absent drying step after each layer deposition. The drying step causes a collapse of the polymer layer and thus increases the surface charge density σ .

After determining the viability of in situ monitoring LbL assembly using individual SPR and EG-FET measurements, each in a separate flow cell configuration, the concept of the dual-electro/plasmonic signal transduction was demonstrated with the combined SPR/EG-FET tool. A 50 nm thin gold layer used in SPR measurements with Kretschmann configuration was simultaneously employed as the gate electrode of the EG-

FET. A custom-made polydimethylsiloxane gasket defining the flow cell volume (5 μL , 400 μm flow channel thickness) attached the EG-FET to the SPR substrate. The flow cell was sealed using a 3D-printed holder with a commercially available interdigitated electrode chip (Micrux IDE1) using rGO as channel material (Figures 1, S17, and S19).

Sequential LbL growth of PEM, composed of PDADMAC and PSS, was monitored in parallel using the optical (SPR) and electronic (EG-FET) readout channels. The acquired sensor response kinetics are presented in Figure 3 for the growth of layers 3–8, revealing a stepwise increase in the SPR response and an alternating, more complex, electrical EG-FET signal.

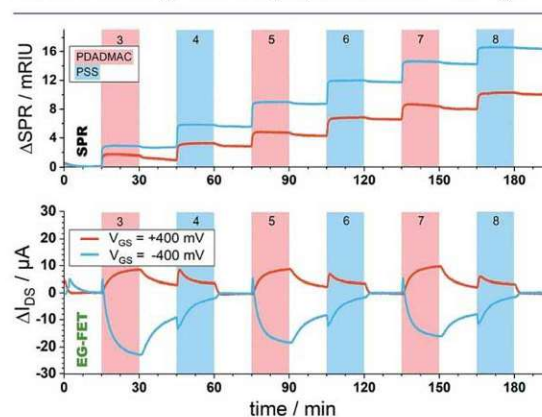


Figure 3. In situ readout of the sequential growth of alternating PDADMAC (red bars, $N = 3, 5, 7$) and PSS (blue bars, $N = 4, 6, 8$) layers by the use of SPR (upper graph) and EG-FET (bottom graph). Device was operated with applied negative (blue curve) and positive (red curve) V_{GS} voltages. Baseline correction was applied to level post-PSS I_{DS} current values to zero. See Figures S1 and S13 for raw data and gate leakage current values.

The first two layers (see Figure S1 for raw data) act as precursor and ensure sufficient PEM coverage for the subsequent layers.⁵⁰ The SPR sensor response was measured in refractive index unit (RIU) by calibrating the sensor to bulk refractive index changes n_s (Figure S1). Prior to growth of the second pair of PDADMAC/PSS layers (layers 3 and 4), a baseline was established (KCl, 100 mM, 0–15 min). Then the solution with positively charged PDADMAC was injected (15 min), and a rapid increase in SPR response was observed as a result of surface mass deposition. The system was rinsed with KCl for 15 min, and a rapid small decrease in the SPR signal was observed due to the bulk refractive index change n_s and the desorption of loosely bound polymer chains.⁵¹ Next, the solution with negatively charged PSS was injected for 15 min followed again by a 15 min rinsing step, leading to a similar increase in SPR signal. The growth of the first 8 layers was linearly approximated (Figure S12) and shows a gate-voltage dependency.

The equilibrium ΔSPR signal of 10–16 mRIU (and respective surface mass density $\Delta\Gamma$ and PEM thickness d_p) are in accordance with those measured in static mode and presented in Figure 2. Interestingly, the overall surface mass density Γ of the grown PEM was about 60% higher for the negative V_{GS} applied to the gold surface compared to the positive one due to the respective changes in the surface mass density of the initial positively charged PDADMAC layer. Due

to the polarizability of charged polymers, the polymer chains exhibit instantaneous response to the electrostatic attraction by V_{GS} .⁵² Hence, electrophoretic deposition occurs and the electrostatic compensation process between cationic and anionic polyelectrolytes is stronger, resulting in thicker films as seen by the SPR signals (Figure S12). This corresponds to a mean layer growth of $d_p = 2.82 \pm 0.06$ nm with $\Delta\Gamma = 202 \pm 4$ ng/cm² for $V_{GS} = -400$ mV and $d_p = 1.69 \pm 0.06$ nm with $\Delta\Gamma = 121 \pm 4$ ng/cm² for $V_{GS} = +400$ mV, as extracted from the coupled SPR/EG-FET system according to eq 1. As the same PEM is formed on both interfaces of the flow cell, we further assume that both SPR and EG-FET channels respond to the same supramolecular architecture. While the SPR is sensitive to the binding of higher molecular weight PDADMAC and PSS polymers, it will not respond to the presence of low molecular weight K^+ and Cl^- ions. In contrast, the EG-FET responds to charge density variations independent of the molecular weight.

In comparison to the SPR, the response observed with the EG-FET channel (ΔI_{DS}), shown in Figure 3, shows different behavior. In this experiment changes in ΔI_{DS} were measured in time for a fixed applied gate-potential (V_{GS}), which defines the working point of the EG-FET system. The measured current changes are proportional to the slope of the $I_{DS}V_{GS}$ curve, which is opposite for the set $V_{GS} = \pm 400$ mV (Figure S14). The binding of positively charged PDADMAC polymer and negatively charged PSS polymer is accompanied by opposite changes in I_{DS} current as the binding of these polymers shifts the Dirac point V_i to more negative or positive voltages, respectively (Figure 2c). Only the ambipolar properties of certain semiconducting materials (such as rGO) allow for using both positive and negative gate voltages (V_{GS}) and thus investigating the electric field dependence of the LbL adsorption.

Strikingly, trends in the EG-FET signal due to growth of PEMs are inherently different from those observed with SPR, in terms of both magnitude and kinetics. For example, deposition of positively charged PDADMAC gradually increases the I_{DS} current (in the case of $V_{GS} = +400$ mV) until equilibrium is reached in about 15 min, thus taking 30 times longer than the SPR signal. At the beginning of PSS injection, a rapid increase in I_{DS} (in the case of $V_{GS} = +400$ mV) occurs in about 1 min and overlays with a slow competing decrease that reaches equilibrium in about 15 min. As expected, the current output sign is reversed when applying a negative gate potential ($V_{GS} = -400$ mV).

A detailed investigation of the EG-FET signal reveals two contributions, both exhibiting exponential behavior with different time constants (Figure S2). The two processes can be attributed to the accumulated charge density σ (EG-FET), which is composed of (i) σ_a , originating from adsorbed charged mass density (SPR), and (ii) σ_i , induced by capacitive effects, according to $\sigma = \sigma_a + \sigma_i$.

Changes of the surface charge density correspond to variations of the surface potential ψ (Debye–Hückel, eq 2), thus modifying I_{DS}

$$\psi = \frac{\sigma}{\epsilon\epsilon_0\kappa} \quad (2)$$

where $\kappa = 1/\lambda_D = [(2 z^2 e^2 n_0)/(\epsilon k_B T)]^{-1/2}$, with Debye length λ_D , ion valency z , electron charge e , ion concentration of the bulk n_0 , Boltzmann constant k_B , temperature T , permittivity constant ϵ_0 , and relative permittivity ϵ of the solution.

Experimental confirmation was obtained by eliminating any capacitive contributions ($\sigma_i = 0$), which was realized by replacing the gate electrode with a nonconductive substrate (Figure S4), thus leading to $\sigma = \sigma_a$. Such two-terminal devices have been demonstrated for sensing applications.⁵³ As shown in Figure 4, the time constants t_0 for noncapacitive experiments

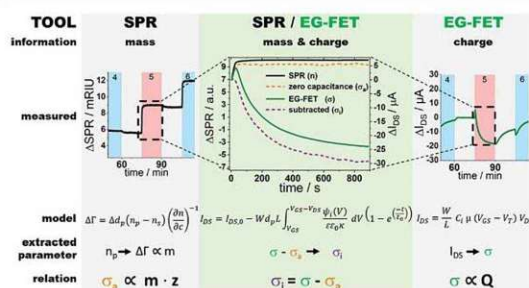


Figure 4. (Left and right) Detailed signal response of layer 5 from Figure 3. (Middle) Obtained capacitance contribution by subtracting the zero-capacitance measurement from the EG-FET response upon layer formation.

(orange dashed line) are nearly identical to the SPR response (black solid line), which is attributed to the adsorbed surface charge density σ_a . Hence, we demonstrated that the SPR mass uptake is proportional to σ_a , which is deduced from the adsorbed mass using the molar weight and valency of the monomers (Figure S12). Calculating the surface charge density for formation of the PDADMAC/PSS multilayers, we obtain $\sigma_a = 120.2 \pm 2.5$ $\mu\text{C}/\text{cm}^2$ for PDADMAC for $V_{GS} = -400$ mV and $\sigma_a = 72.0 \pm 2.6$ $\mu\text{C}/\text{cm}^2$ for $V_{GS} = +400$ mV and for PSS $\sigma_a = 104.9 \pm 2.5$ $\mu\text{C}/\text{cm}^2$ for $V_{GS} = -400$ mV and $\sigma_a = 62.9 \pm 2.6$ $\mu\text{C}/\text{cm}^2$ for $V_{GS} = +400$ mV. Subtracting the zero-capacitance data from the EG-FET response (green solid line) reveals the contribution of the induced surface charge density σ_i (purple dashed line).

DISCUSSION

The different nature of the SPR and EG-FET originates from the capacitive contributions (σ_i), yielding additional information about the charge distribution processes in PEMs. The SPR signal corresponds to mass uptake, attesting to the adsorption of long polymer chains in a fast process. Counterions surrounding the charged polymer backbone in the bulk solution are introduced into the PEM structure during surface adsorption. Oppositely charged PEMs achieve their electro-neutrality by intrinsic charge compensation, resulting in expulsion of previously trapped counterions. This Donnan exclusion originates from the electroosmotic pressure of trapped counterions⁵⁴ and from screening between charge-like polymers due to layer to layer charge neutralization.^{55,56} The resulting intralayer K^+ or Cl^- flux can be described as slow non-Fickian diffusion^{50,57} to the solid–liquid interface, modifying the surface charge density σ_i .⁵⁴ Hence, the potential in the PEM layer changes over time, and a corresponding electrical double layer forms at the polyelectrolyte interface, extending approximately 100 nm into the ion solution (Figure S16),^{55,58} leading to a modulation in the local electric field. The changes in charge distribution and ion concentration can also be described by the chemical potential by a thermodynamic approach (eq S19, Chapter S1C). Since our

2.5. Dual Monitoring of Surface Reactions in Real Time by Combined Surface Plasmon Resonance and Field-Effect Transistor Interrogation

setup allows a direct measurement of mass and charge, we describe the equivalent by the more direct approach using a theoretical model for determination of the surface charge density utilizing a diffusion model⁵⁸

$$\sigma_i(t) = \sigma_{\text{EDL}}(1 - e^{-(t/t_0)}) + I_f t \quad (3)$$

where I_f is the Faraday current density at the gate. We measured a constant gate current I_{GS} (leakage current, 21 nA) during all experiments and deposition steps, thus indicating a negligible redox potential at the electrode (Figure S13). Therefore, we assume I_f to be close to zero. The standard FET equation for I_{DS} is

$$I_{\text{DS}} = \frac{W}{L} C_i \mu (V_{\text{GS}} - V_T) V_{\text{DS}} \quad (4)$$

where W is the channel width, L the channel length, C_i the insulating layer capacitance, μ the charge mobility in the rGO, and V_T the threshold voltage. Rewriting eq 4 as a function of the surface charge density⁵⁹ and expressing the surface potential ψ via the Debye–Hückel model (see eq 2), we obtain eq 5, which describes the modulation of the observed I_{DS} as a consequence of ψ from σ_i due to ion diffusion and the depletion layer in the EDL

$$I_{\text{DS}} = I_{\text{DS},0} - W d_p L \int_{V_{\text{GS}}}^{V_{\text{GS}} - V_{\text{DS}}} \frac{\psi_i(V)}{\epsilon \epsilon_0 \kappa} dV \cdot (1 - e^{-(t/t_0)}) \quad (5)$$

where d_p is the polyelectrolyte layer thickness. Equation 5 describes the modulation of the observed I_{DS} resulting from changes in the Fermi level of the rGO from the surface potential $\psi(V_{\text{GS}})$, which is determined by the voltage drop in the PEMs and the potential drop at the solid–electrolyte interface in proximity of the depletion layer (Figure 5). From eqs 2 and 5 it becomes clear that the corresponding potential drop ψ_i results in a change of the observed EG-FET signal.

The EG-FET signal after PDADMAC deposition gradually decreased throughout rinsing with KCl solution and equilibrated over about 15 min, while ΔSPR stabilized rapidly. This observation hints at the loss of approximately 5% of the loosely bound surface layer⁶⁰ into which the majority of the ions previously diffused. The desorption results in a surface charge density alteration and triggers the corresponding EDL formation, leading to a minute SPR response but a distinct EG-FET response. Our observations originate from inherent material properties and corresponding ion interactions, leading to different charge densities at the surface. Therefore, rinsing with KCl after PSS deposition exhibits a less prominent but faster change to a stable current.

The applied electric field (from V_{GS}) effects the diffusion, depending on the charge polarity of ions by either slowing or accelerating the diffusion flux. To evaluate the characteristics of the observed behavior, kinetics obtained from the EG-FET regarding σ_i were used for assessment of an arbitrary time ratio ξ , which is obtained from the time constant ratio of layer deposition and rinsing ($\xi = t_{\text{on}}/t_{\text{off}}$) (Chapter S1c). Therefore, we assume that the obtained time ratio ξ reflects a measure for ion affinity during diffusion, similar to diffusion-influenced transport in transmembrane channels.⁶¹ $\xi = 1.7 \pm 0.2$ for PDADMAC at $V_{\text{GS}} = -400$ mV and 1.3 ± 0.1 for +400 mV, while obtained ξ values for PSS are 0.22 ± 0.02 at -400 mV and 0.32 ± 0.04 at +400 mV. This is intuitive because negatively charged PEMs layers have stronger affinities toward

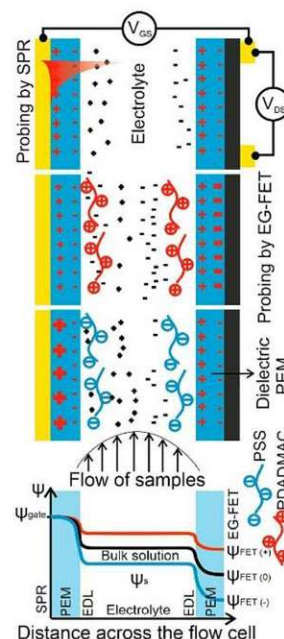


Figure 5. Schematics of the simultaneous readout of surface mass and charge density at the two interfaces of the combined SPR/EG-FET platform. Upper graph demonstrates initial conditions, followed by subsequent PDADMAC and PSS depositions under constant flow of polyelectrolyte solutions. Left side illustrates the SPR-Au-PEM surface, and right side represents the PEM-rGO-EG-FET. Surface charge density variations upon layer formation lead to the gate potential (ψ) drop across the fluidic channel that is shown below.

positively charged ions in the Helmholtz layer at positive applied V_{GS} . The values of ξ for PDADMAC and PSS PEMs are different as measured with the EG-FET. Most likely the differences of ξ are related to the polarity of V_{GS} , the corresponding Helmholtz double layer ion type, and the intrinsic charge of the PEMs. Furthermore, we speculate that the trapping of counterions is more pronounced in PSS layers due to ionic π -interactions,⁶² leading to slower ion diffusion in comparison to PDADMAC. Additionally, the π - π interactions of the PSS layer itself could lead to a difference in interlayer ion diffusion flux.

SUMMARY

In summary, we herein present a powerful novel combinatorial sensing platform which provides new insights into real-time surface processes and enables direct measurement of surface charge density and mass obtained from electro/plasmonic signal transductions. We applied this platform to investigate PEM formation using a PDADMAC/PSS system. Due to the complementary sensing principles, the solid–liquid interface can be investigated from different perspectives, which is crucial as certain processes are beyond the scope of each individual tool. For instance, sole observation of the layer formation via SPR would suggest a completed material deposition within 60 s, whereas the subsequent slower charge diffusion takes more than 15 min as observed by EG-FET. To the best of our knowledge, this is the first report of a SPR/EG-FET platform for simultaneous real-time monitoring under dynamic flow

conditions, deconvoluting mass and charge contributions. On the basis of experimental observations, we derived a theoretical model to account for the evolution of surface charge density due to PEM adsorption and intralayer ion diffusion. The theory describes the time dependence of both mass uptake and charge distribution, elucidated from changes of the refractive index and surface potential at the solid–liquid interface. To this end, we combined the Debye–Hückel model and non-Fickian diffusion theory to unravel intrinsic material processes. Correlation of optical and electronic read-outs allows for the discrimination of superimposed signals which originate from charged mass uptake and subsequent surface charge redistribution. We attribute each contribution to adsorbed and induced components by deconvoluting the superimposed yet time-correlated, EG-FET signal from the SPR data. By doing so, we can interpret an optical signal such that a direct comparison to an electronic signal is possible. Thus, our bifunctional sensor platform is a new tool to monitor surface events by simultaneously analyzing both the adsorbed mass and the intrinsic molecular charges at the same surface and under dynamic conditions. We hope these new insights can lead to a better understanding of intrinsic processes, aid in predicting material properties, and thus guide material and application development.

■ ASSOCIATED CONTENT

SI Supporting Information

The Supporting Information is available free of charge at <https://pubs.acs.org/doi/10.1021/jacs.9b11835>.

Experimental details and fabrication procedures, additional EG-FET and SPR measurements, detailed theoretical framework, SPR/EG-FET setup, software, materials (PDF)

■ AUTHOR INFORMATION

Corresponding Author

Johannes Bintinger – Biosensor Technologies, Austrian Institute of Technology, 3430 Tulln, Austria; orcid.org/0000-0002-6397-4254; Email: johannes.bintinger@ait.ac.at

Authors

Patrik Aspermaier – Biosensor Technologies, Austrian Institute of Technology, 3430 Tulln, Austria; CEST Competence Center for Electrochemical Surface Technologies, 3430 Tulln, Austria; CNRS, Centrale Lille, ISEN, Université Valenciennes, UMR 8520-IEMN, Université de Lille, 59000 Lille, France; orcid.org/0000-0003-1671-1328

Ulrich Ramach – CEST Competence Center for Electrochemical Surface Technologies, 3430 Tulln, Austria; orcid.org/0000-0002-1111-2994

Ciril Reiner-Rozman – Biosensor Technologies, Austrian Institute of Technology, 3430 Tulln, Austria; orcid.org/0000-0002-6476-2413

Stefan Fossati – Biosensor Technologies, Austrian Institute of Technology, 3430 Tulln, Austria; orcid.org/0000-0002-1109-0035

Bernadette Lechner – Biosensor Technologies, Austrian Institute of Technology, 3430 Tulln, Austria; orcid.org/0000-0002-4949-5118

Sergio E. Moya – CIC biomaGUNE, 20014 San Sebastian, Spain; orcid.org/0000-0002-7174-1960

Omar Azzaroni – Instituto de Investigaciones Físicoquímicas Teóricas y Aplicadas (INIFTA), Departamento de Química, Facultad de Ciencias Exactas, Universidad Nacional de La Plata–CONICET, 1900 La Plata, Argentina; orcid.org/0000-0002-5098-0612

Jakub Dostalek – Biosensor Technologies, Austrian Institute of Technology, 3430 Tulln, Austria; orcid.org/0000-0002-0431-2170

Sabine Szunerits – CNRS, Centrale Lille, ISEN, Université Valenciennes, UMR 8520-IEMN, Université de Lille, 59000 Lille, France; orcid.org/0000-0002-1567-4943

Wolfgang Knoll – Biosensor Technologies, Austrian Institute of Technology, 3430 Tulln, Austria; CEST Competence Center for Electrochemical Surface Technologies, 3430 Tulln, Austria; orcid.org/0000-0003-1543-4090

Complete contact information is available at: <https://pubs.acs.org/10.1021/jacs.9b11835>

Author Contributions

[†]P.A. and U.R. contributed equally.

Author Contributions

This manuscript was written through contributions of all authors. All authors have given approval to the final version of the manuscript.

Funding

We gratefully acknowledge the financial support from the Austrian Research Promotion Agency (FFG; 870025) for this research. SF and JD are grateful for the support from the Austrian Research Promotion Agency (FFG; 861578, ERANET project PLABAN). This work was financially supported by the European Union's Horizon 2020 research and innovation program under grant agreement No 690836. General financial supports from the Centre National de la Recherche Scientifique (CNRS), the University of Lille, and the Hauts-de-France region are acknowledged.

Notes

The authors declare no competing financial interest.

■ ACKNOWLEDGMENTS

We thank Esteban Piccinini for valuable input and discussions and David Ebner for initial design input. Cover art by Ella Maru Studio.

■ REFERENCES

- (1) Das, A.; Pisana, S.; Chakraborty, B.; Piscanec, S.; Saha, S. K.; Waghmare, U. V.; Novoselov, K. S.; Krishnamurthy, H. R.; Geim, A. K.; Ferrari, A. C.; Sood, A. K. Monitoring Dopants by Raman Scattering in an Electrochemically Top-Gated Graphene Transistor. *Nat. Nanotechnol.* **2008**, *3* (4), 210–215.
- (2) Kergoat, L.; Herlogsson, L.; Braga, D.; Piro, B.; Pham, M.-C.; Crispin, X.; Berggren, M.; Horowitz, G. A Water-Gate Organic Field-Effect Transistor. *Adv. Mater.* **2010**, *22* (23), 2565–2569.
- (3) Palazzo, G.; De Tullio, D.; Magliulo, M.; Mallardi, A.; Intraruovo, F.; Mulla, M. Y.; Favia, P.; Vikholm-Lundin, I.; Torsi, L. Detection Beyond Debye's Length with an Electrolyte-Gated Organic Field-Effect Transistor. *Adv. Mater.* **2015**, *27* (5), 911–916.
- (4) Casalini, S.; Leonardi, F.; Cramer, T.; Biscarini, F. Organic Field-Effect Transistor for Label-Free Dopamine Sensing. *Org. Electron.* **2013**, *14* (1), 156–163.
- (5) Ang, P. K.; Chen, W.; Wee, A. T. S.; Loh, K. P. Solution-Gated Epitaxial Graphene as PH Sensor. *J. Am. Chem. Soc.* **2008**, *130* (44), 14392–14393.

2.5. Dual Monitoring of Surface Reactions in Real Time by Combined Surface Plasmon Resonance and Field-Effect Transistor Interrogation

- (6) Sailapu, S. K.; Macchia, E.; Merino-Jimenez, I.; Esquivel, J. P.; Sarcina, L.; Scamarcio, G.; Minter, S. D.; Torsi, L.; Sabaté, N. Standalone Operation of an EGO-FET for Ultra-Sensitive Detection of HIV. *Biosens. Bioelectron.* **2020**, *156*, 112103.
- (7) Berto, M.; Diacci, C.; D'Agata, R.; Pinti, M.; Bianchini, E.; Lauro, M. D.; Casalini, S.; Cossarizza, A.; Berggren, M.; Simon, D.; Spoto, G.; Biscarini, F.; Bortolotti, C. A. EGO-FET Peptide Aptasensor for Label-Free Detection of Inflammatory Cytokines in Complex Fluids. *Adv. Biosyst.* **2018**, *2* (2), 1700072.
- (8) Macchia, E.; Manoli, K.; Holzer, B.; Di Franco, C.; Ghittorelli, M.; Torricelli, F.; Alberga, D.; Mangiatordi, G. F.; Palazzo, G.; Scamarcio, G.; Torsi, L. Single-Molecule Detection with a Millimetre-Sized Transistor. *Nat. Commun.* **2018**, *9* (1), 3223.
- (9) Pappa, A.-M.; Parlak, O.; Scheiblin, G.; Mailley, P.; Salleo, A.; Owens, R. M. Organic Electronics for Point-of-Care Metabolite Monitoring. *Trends Biotechnol.* **2018**, *36* (1), 45–59.
- (10) Homola, J. Surface Plasmon Resonance Sensors for Detection of Chemical and Biological Species. *Chem. Rev.* **2008**, *108* (2), 462–493.
- (11) Liedberg, B.; Nylander, C.; Lunström, I. Surface Plasmon Resonance for Gas Detection and Biosensing. *Sens. Actuators* **1983**, *4*, 299–304.
- (12) Olaru, A.; Bala, C.; Jaffrezic-Renault, N.; Aboul-Enein, H. Y. Surface Plasmon Resonance (SPR) Biosensors in Pharmaceutical Analysis. *Crit. Rev. Anal. Chem.* **2015**, *45* (2), 97–105.
- (13) Homola, J. Present and Future of Surface Plasmon Resonance Biosensors. *Anal. Bioanal. Chem.* **2003**, *377* (3), 528–539.
- (14) Englebienne, P.; Hoonacker, A. V.; Verhas, M. Surface Plasmon Resonance: Principles, Methods and Applications in Biomedical Sciences. *Spectroscopy* **2003**, *17* (2–3), 255–273.
- (15) Piliarik, M.; Vaisocherová, H.; Homola, J. Surface Plasmon Resonance Biosensing. In *Biosensors and Biodection*; Rasooly, A., Herold, K. E., Eds.; Methods in Molecular Biology™; Humana Press: Totowa, NJ, 2009; pp 65–88. DOI: 10.1007/978-1-60327-567-5_5.
- (16) Bouffartigues, E.; Leh, H.; Anger-Leroy, M.; Rimsky, S.; Buckle, M. Rapid Coupling of Surface Plasmon Resonance (SPR and SPRi) and ProteinChip™ Based Mass Spectrometry for the Identification of Proteins in Nucleoprotein Interactions. *Nucleic Acids Res.* **2007**, *35* (6), e39–e39.
- (17) Zhang, X.; Young, M. A.; Lyandres, O.; Van Duyne, R. P. Rapid Detection of an Anthrax Biomarker by Surface-Enhanced Raman Spectroscopy. *J. Am. Chem. Soc.* **2005**, *127* (12), 4484–4489.
- (18) Sergelen, K.; Fossati, S.; Turupcu, A.; Oostenbrink, C.; Liedberg, B.; Knoll, W.; Dostálek, J. Plasmon Field-Enhanced Fluorescence Energy Transfer for Hairpin Aptamer Assay Readout. *ACS Sens.* **2017**, *2* (7), 916–923.
- (19) Rodrigo, D.; Tittel, A.; Ait-Bouziad, N.; John-Herpin, A.; Limaj, O.; Kelly, C.; Yoo, D.; Wittenberg, N. J.; Oh, S.-H.; Lashuel, H. A.; Altug, H. Resolving Molecule-Specific Information in Dynamic Lipid Membrane Processes with Multi-Resonant Infrared Metasurfaces. *Nat. Commun.* **2018**, *9* (1), 1–9.
- (20) Mulla, M. Y.; Tuccori, E.; Magliulo, M.; Lattanzi, G.; Palazzo, G.; Persaud, K.; Torsi, L. Capacitance-Modulated Transistor Detects Odorant Binding Protein Chiral Interactions. *Nat. Commun.* **2015**, *6*, 6010.
- (21) Panzer, M. J.; Frisbie, C. D. Exploiting Ionic Coupling in Electronic Devices: Electrolyte-Gated Organic Field-Effect Transistors. *Adv. Mater.* **2008**, *20* (16), 3177–3180.
- (22) Barbaro, M.; Bonfiglio, A.; Raffo, L. A Charge-Modulated FET for Detection of Biomolecular Processes: Conception, Modeling, and Simulation. *IEEE Trans. Electron Devices* **2006**, *53* (1), 158–166.
- (23) Cramer, T.; Kyndiah, A.; Murgia, M.; Leonardi, F.; Casalini, S.; Biscarini, F. Double Layer Capacitance Measured by Organic Field Effect Transistor Operated in Water. *Appl. Phys. Lett.* **2012**, *100* (14), 143302.
- (24) Ohno, Y.; Maehashi, K.; Yamashiro, Y.; Matsumoto, K. Electrolyte-Gated Graphene Field-Effect Transistors for Detecting PH and Protein Adsorption. *Nano Lett.* **2009**, *9* (9), 3318–3322.
- (25) Torsi, L.; Magliulo, M.; Manoli, K.; Palazzo, G. Organic Field-Effect Transistor Sensors: A Tutorial Review. *Chem. Soc. Rev.* **2013**, *42* (22), 8612–8628.
- (26) Tibaldi, A.; Fillaud, L.; Anquetin, G.; Woytasik, M.; Zrig, S.; Piro, B.; Mattana, G.; Noël, V. Electrolyte-Gated Organic Field-Effect Transistors (EGOFETs) as Complementary Tools to Electrochemistry for the Study of Surface Processes. *Electrochem. Commun.* **2019**, *98*, 43–46.
- (27) Nakatsuka, N.; Yang, K.-A.; Abendroth, J. M.; Cheung, K. M.; Xu, X.; Yang, H.; Zhao, C.; Zhu, B.; Rim, Y. S.; Yang, Y.; Weiss, P. S.; Stojanović, M. N.; Andrews, A. M. Aptamer-Field-Effect Transistors Overcome Debye Length Limitations for Small-Molecule Sensing. *Science* **2018**, *362* (6412), 319–324.
- (28) Goda, T.; Maeda, Y.; Miyahara, Y. Simultaneous Monitoring of Protein Adsorption Kinetics Using a Quartz Crystal Microbalance and Field-Effect Transistor Integrated Device. *Anal. Chem.* **2012**, *84* (17), 7308–7314.
- (29) Okuda, S.; Ono, T.; Kanai, Y.; Ikuta, T.; Shimatani, M.; Ogawa, S.; Maehashi, K.; Inoue, K.; Matsumoto, K. Graphene Surface Acoustic Wave Sensor for Simultaneous Detection of Charge and Mass. *ACS Sens.* **2018**, *3* (1), 200–204.
- (30) Kojori, H. S.; Ji, Y.; Paik, Y.; Braunschweig, A. B.; Kim, S. J. Monitoring Interfacial Lectin Binding with Nanomolar Sensitivity Using a Plasmon Field Effect Transistor. *Nanoscale* **2016**, *8* (39), 17357–17364.
- (31) Decher, G.; Eckle, M.; Schmitt, J.; Struth, B. Layer-by-Layer Assembled Multicomposite Films. *Curr. Opin. Colloid Interface Sci.* **1998**, *3* (1), 32–39.
- (32) Dubas, S. T.; Schlenoff, J. B. Factors Controlling the Growth of Polyelectrolyte Multilayers. *Macromolecules* **1999**, *32* (24), 8153–8160.
- (33) Ai, H.; Jones, S. A.; Lvov, Y. M. Biomedical Applications of Electrostatic Layer-by-Layer Nano-Assembly of Polymers, Enzymes, and Nanoparticles. *Cell Biochem. Biophys.* **2003**, *39* (1), 23.
- (34) Piccinini, E.; Blum, C.; Reiner-Rozman, C.; Battaglini, F.; Azzaroni, O.; Knoll, W. Enzyme-Polyelectrolyte Multilayer Assemblies on Reduced Graphene Oxide Field-Effect Transistors for Biosensing Applications. *Biosens. Bioelectron.* **2017**, *92*, 661–667.
- (35) Piccinini, E.; Alberti, S.; Longo, G. S.; Berninger, T.; Breu, J.; Dostálek, J.; Azzaroni, O.; Knoll, W. Pushing the Boundaries of Interfacial Sensitivity in Graphene FET Sensors: Polyelectrolyte Multilayers Strongly Increase the Debye Screening Length. *J. Phys. Chem. C* **2018**, *122* (18), 10181–10188.
- (36) Michel, M.; Taylor, A.; Sekol, R.; Podsiadlo, P.; Ho, P.; Kotov, N.; Thompson, L. High-Performance Nanostructured Membrane Electrode Assemblies for Fuel Cells Made by Layer-By-Layer Assembly of Carbon Nanocolloids. *Adv. Mater.* **2007**, *19* (22), 3859–3864.
- (37) Wu, F.; Li, J.; Su, Y.; Wang, J.; Yang, W.; Li, N.; Chen, L.; Chen, S.; Chen, R.; Bao, L. Layer-by-Layer Assembled Architecture of Polyelectrolyte Multilayers and Graphene Sheets on Hollow Carbon Spheres/Sulfur Composite for High-Performance Lithium–Sulfur Batteries. *Nano Lett.* **2016**, *16* (9), 5488–5494.
- (38) Ariga, K.; Lvov, Y. M.; Kawakami, K.; Ji, Q.; Hill, J. P. Layer-by-Layer Self-Assembled Shells for Drug Delivery. *Adv. Drug Delivery Rev.* **2011**, *63* (9), 762–771.
- (39) Gu, J.-E.; Lee, S.; Stafford, C. M.; Lee, J. S.; Choi, W.; Kim, B.-Y.; Baek, K.-Y.; Chan, E. P.; Chung, J. Y.; Bang, J.; Lee, J.-H. Molecular Layer-by-Layer Assembled Thin-Film Composite Membranes for Water Desalination. *Adv. Mater.* **2013**, *25* (34), 4778–4782.
- (40) Richardson, J. J.; Cui, J.; Björnalm, M.; Braunger, J. A.; Ejima, H.; Caruso, F. Innovation in Layer-by-Layer Assembly. *Chem. Rev.* **2016**, *116* (23), 14828–14867.
- (41) Richardson, J. J.; Björnalm, M.; Caruso, F. Technology-Driven Layer-by-Layer Assembly of Nanofilms. *Science* **2015**, *348* (6233), aaa2491–aaa2491.
- (42) Aspnes, D. E. Local-field Effects and Effective-medium Theory: A Microscopic Perspective. *Am. J. Phys.* **1982**, *50* (8), 704–709.

2.5. Dual Monitoring of Surface Reactions in Real Time by Combined Surface Plasmon Resonance and Field-Effect Transistor Interrogation

- (43) Ogieglo, W.; Wormeester, H.; Eichhorn, K.-J.; Wessling, M.; Benes, N. E. In Situ Ellipsometry Studies on Swelling of Thin Polymer Films: A Review. *Prog. Polym. Sci.* **2015**, *42*, 42–78.
- (44) Piccinini, E.; Bliem, C.; Giussi, J. M.; Knoll, W.; Azzaroni, O. Reversible Switching of the Dirac Point in Graphene Field-Effect Transistors Functionalized with Responsive Polymer Brushes. *Langmuir* **2019**, *35*, 8038.
- (45) Tang, K.; Besseling, N. A. M. Formation of Polyelectrolyte Multilayers: Ionic Strengths and Growth Regimes. *Soft Matter* **2016**, *12* (4), 1032–1040.
- (46) De Feijter, J. A.; Benjamins, J.; Veer, F. A. Ellipsometry as a Tool to Study the Adsorption Behavior of Synthetic and Biopolymers at the Air–Water Interface. *Biopolymers* **1978**, *17* (7), 1759–1772.
- (47) Stenberg, E.; Persson, B.; Roos, H.; Urbaniczky, C. Quantitative Determination of Surface Concentration of Protein with Surface Plasmon Resonance Using Radiolabeled Proteins. *J. Colloid Interface Sci.* **1991**, *143* (2), 513–526.
- (48) Perlmann, G. E.; Longworth, L. G. The Specific Refractive Increment of Some Purified Proteins. *J. Am. Chem. Soc.* **1948**, *70* (8), 2719–2724.
- (49) Wang, Y. Y.; Burke, P. J. Polyelectrolyte Multilayer Electrostatic Gating of Graphene Field-Effect Transistors. *Nano Res.* **2014**, *7* (11), 1650–1658.
- (50) Donath, E.; Vardanyan, I.; Meyer, S.; Murray, R. A.; Moya, S. E.; Navoyan, Z.; Arakelyan, V. A Typical Diffusion Monitored by Flow Cytometry: Slow Diffusion of Small Molecules in Polyelectrolyte Multilayers. *Nanoscale* **2018**, *10* (2), 765–772.
- (51) Wong, J. E.; Zastrow, H.; Jaeger, W.; von Klitzing, R. Specific Ion versus Electrostatic Effects on the Construction of Polyelectrolyte Multilayers †. *Langmuir* **2009**, *25* (24), 14061–14070.
- (52) Ko, Y. H.; Kim, Y. H.; Park, J.; Nam, K. T.; Park, J. H.; Yoo, P. J. Electric-Field-Assisted Layer-by-Layer Assembly of Weakly Charged Polyelectrolyte Multilayers. *Macromolecules* **2011**, *44* (8), 2866–2872.
- (53) Kim, Y.-T.; Lee, S.; Park, S.; Lee, C. Y. Graphene Chemiresistors Modified with Functionalized Triphenylene for Highly Sensitive and Selective Detection of Dimethyl Methylphosphonate. *RSC Adv.* **2019**, *9* (58), 33976–33980.
- (54) Sui, Z.; Schlenoff, J. B. Phase Separations in PH-Responsive Polyelectrolyte Multilayers: Charge Extrusion versus Charge Expulsion. *Langmuir* **2004**, *20* (14), 6026–6031.
- (55) Klos, J. S. Dendritic Polyelectrolytes Revisited through the Poisson–Boltzmann–Flory Theory and the Debye–Hückel Approximation. *Phys. Chem. Chem. Phys.* **2018**, *20* (4), 2693–2703.
- (56) Dai, J.; Balachandra, A. M.; Lee, J. I.; Bruening, M. L. Controlling Ion Transport through Multilayer Polyelectrolyte Membranes by Derivatization with Photolabile Functional Groups. *Macromolecules* **2002**, *35* (8), 3164–3170.
- (57) Song, L.; Sun, W.; Gao, J. Time Dependent Chloride Diffusion Coefficient in Concrete. *J. Wuhan Univ. Technol., Mater. Sci. Ed.* **2013**, *28* (2), 314–319.
- (58) Tybrandt, K.; Zozoulenko, I. V.; Berggren, M. Chemical Potential–Electric Double Layer Coupling in Conjugated Polymer–Polyelectrolyte Blends. *Sci. Adv.* **2017**, *3* (12), eaao3659.
- (59) Shirinskaya, A.; Horowitz, G.; Rivnay, J.; Malliaras, G.; Bonnassieux, Y. Numerical Modeling of an Organic Electrochemical Transistor. *Biosensors* **2018**, *8* (4), 103.
- (60) Iturri Ramos, J. J.; Stahl, S.; Richter, R. P.; Moya, S. E. Water Content and Buildup of Poly(Diallyldimethylammonium Chloride)/Poly(Sodium 4-Styrenesulfonate) and Poly(Allylamine Hydrochloride)/Poly(Sodium 4-Styrenesulfonate) Polyelectrolyte Multilayers Studied by an in Situ Combination of a Quartz Crystal Microbalance with Dissipation Monitoring and Spectroscopic Ellipsometry. *Macromolecules* **2010**, *43* (21), 9063–9070.
- (61) Zhou, H.-X. Diffusion-Influenced Transport of Ions across a Transmembrane Channel with an Internal Binding Site. *J. Phys. Chem. Lett.* **2010**, *1* (13), 1973–1976.
- (62) Schottel, B. L.; Chifotides, H. T.; Dunbar, K. R. Anion- π Interactions. *Chem. Soc. Rev.* **2008**, *37* (1), 68–83.

2.6. Plasmon Field-Enhanced Fluorescence Energy Transfer for Hairpin Aptamer Assay Readout

The following publication is reprinted under the Creative Commons CC-BY^e license.

Khulan Sergelen, **Stefan Fossati**, Aysegül Turupcu, Chris Oostenbrink, Bo Liedberg, Wolfgang Knoll, and Jakub Dostálek Plasmon field-enhanced fluorescence energy transfer for hairpin aptamer assay readout. *ACS Sensors* 2, 916–923 (2017). <https://doi.org/10.1021/acssensors.7b00131>

Copyright © 2017 American Chemical Society

The continuous monitoring of the presence of a specific chemical compound in a medium is essential in a wide range of applications. To facilitate continuous monitoring of the reversible binding between a surface-immobilized receptor and the ligand can be utilized. In contrast to high sensitivity assays, the affinity between the compounds is required to be lower, as the dissociation rate defines the response time of the sensor system. This means, that also the occupation density of binding sites, and with that the observed signal, is reduced. Enhancement strategies are thus required to improve the sensitivity of such assays to match the practical requirements.

Aptamers, short single-stranded RNA or DNA strands, that can fold into simple geometric forms, are promising candidates for receptors for their highly adaptable properties by the exchange of oligonucleotides in their sequence. The variability combined with high throughput screening methods allows tailoring of sequences acting as an indicator in a biosensor.^{176,177}

In this study, a DNA aptamer folded to a hairpin shape is employed for the detection of adenosine and adenosine triphosphate, important indicators in medical diagnostics. The aptamer is immobilized on a gold surface with complementary sequences at the ends of the strand that facilitate the folding and an open-loop region exposing a sequence known to bind the selected analyte. The free terminal is decorated with a fluorescent dye, which in

^e <http://creativecommons.org/licenses/by/4.0/>

2.6. Plasmon Field-Enhanced Fluorescence Energy Transfer for Hairpin Aptamer Assay Readout

the folded state is within the metal-energy transfer range of the surface and consequently quenched. Upon the capture of the analyte in the open loop, the hairpin structure unfolds, and the distance of the fluorescent label from the surface is increased, exponentially decreasing quenching and increasing the observed brightness. Upon dissociation of the analyte, the hairpin conformation is eventually restored, and the fluorescence emission is quenched.

In this study, Khulan Sergelen was responsible for the aptamer design, assay development, and biosensor experiments. Stefan Fossati studied the optical properties of the fluorescent dye in proximity to a metal surface using FDTD simulations and contributed to the corresponding parts of the manuscript. The experimental work was carried out under the supervision of Jakub Dostalek and Wolfgang Knoll. Conformation studies using a random coil model were conducted by Aysegül Turupcu under the supervision of Chris Oostenbrink.

Supporting information to this article is included in the appendix, section 5.5.

Plasmon Field-Enhanced Fluorescence Energy Transfer for Hairpin Aptamer Assay Readout

Khulan Sergelen,^{†,‡,§} Stefan Fossati,[†] Aysegül Turupcu,^{||} Chris Oostenbrink,^{||} Bo Liedberg,^{‡,●} Wolfgang Knoll,[†] and Jakub Dostálek^{*,†,●}

[†]BioSensor Technologies, AIT-Austrian Institute of Technology, Muthgasse 11, 1190 Vienna, Austria

[‡]Nanyang Technological University, Centre for Biomimetic Sensor Science, School of Materials Science and Engineering, 50 Nanyang Drive, Singapore 637553

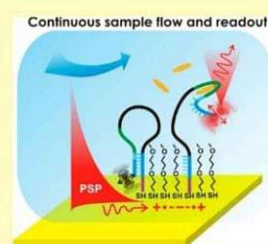
[§]International Graduate School on Bionanotechnology, University of Natural Resources and Life Sciences, Austrian Institute of Technology, and Nanyang Technological University, 1190 Vienna, Austria

^{||}University of Natural Resources and Life Sciences, Institute of Molecular Modeling and Simulation, Muthgasse 18, 1190 Vienna, Austria

Supporting Information

ABSTRACT: Surface plasmon field-enhanced fluorescence energy transfer is employed for sensitive optical readout of a reversible hairpin aptamer assay that is suitable for continuous monitoring of low-molecular-weight chemical analytes. A hairpin aptamer specific to adenosine and adenosine triphosphate with Alexa Fluor 647 fluorophore attached to its 5' end was anchored via 3' end thiol to a gold thin film. Molecular spacers were used to control the distance of the fluorophore from the surface in the aptamer "off" and "on" states. The specific binding of the target analyte changes the aptamer conformation, which alters the distance of the fluorophore from the gold surface and translates to variations in the detected fluorescence intensity. The plasmonically mediated fluorescence signal increases the measured signal-to-noise ratio and allows for real-time observation of the analyte binding. Theoretical as well as experimental study of the optical signal dependence on fluorophore orientation, design of spacers, and angular distribution of collected light is presented for rational design of the assay. The detected sensor signal increased by a factor as large as 23 upon switching the aptamer from the "off" to "on" state due to the hairpin opening associated with the specific capture of target analyte.

KEYWORDS: aptamer, surface plasmon field-enhanced fluorescence, plasmonic amplification, quenching, adenosine triphosphate, fluorescence energy transfer



The coupling of fluorophores with the confined field of surface plasmons originating from collective oscillations of the electron density at metallic surfaces offers powerful means for the amplification of emitted fluorescence light intensity.^{1,2} The plasmonic confinement is associated with the enhanced intensity of the electromagnetic field and the local density of optical states which has been exploited in fluorescence studies of single molecules³ as well as in the measurement on ensembles of fluorophore-labeled biomolecules.^{4,5} The interaction of fluorophore labels with the plasmonically enhanced electromagnetic field allows an increase of excitation rate and improvement of the collection yield of emitted fluorescence photons. The combined coupling of fluorophores at their absorption and emission wavelengths with propagating surface plasmons (PSPs) on metallic films or localized surface plasmons (LSPs) at metallic nanoparticles can be engineered to enhance detected fluorescence intensity by a factor exceeding 3 orders of magnitude.⁶

In plasmonically amplified fluorescence assays, biomolecules that are labeled with fluorophores are affinity captured on a metallic sensor surface at distances in the range of 15–20 nm at

which the plasmonic fluorescence enhancement typically reaches its maximum.^{7–9} At shorter distances the quenching becomes dominant and the emitted fluorescence signal is attenuated rather than enhanced while at longer distances the binding events occur outside the evanescent surface plasmon field. Aptamers become increasingly popular in analytical technologies for specific capture and sensitive detection of low-molecular-weight analytes^{10,11} for which more commonly used antibody immunoassays are not possible. These versatile building blocks can be employed in numerous detection formats that take advantage of the measurement of fluorescence quenching,¹² plasmonic fluorescence enhancement,¹³ or plasmonic near-field coupling between metallic nanoparticles.¹⁴ Such variety of readout modality is possible through the flexibility in aptamer design that can be tailored for assays relying on conformation changes,¹⁴ displacement,¹⁵ or formation of sandwich¹⁶ which are architectures not possible

Received: March 3, 2017

Accepted: June 21, 2017

Published: June 21, 2017

to realize with conventionally used antibodies against low-molecular-weight analytes. A particularly interesting aspect of the aptamer flexibility in design is the possibility of their implementation to molecular beacon-based biosensors. In short, single-stranded nucleic acids are modified at their opposite ends with a fluorophore and a quencher and specific analyte binding is detected by changes in the fluorescence intensity. Fluorescence intensity is mediated by the aptamer analyte complex formation that leads to structural changes or most commonly displacement of complementary stem region of a hairpin aptamer, rendering the quencher and fluorophore pair to separate to a distance farther than energy transfer or quenching to occur.¹⁷

The majority of plasmon field-enhanced fluorescence assays that has been pursued with aptamers carrying a fluorophore attached to their DNA or RNA strand relied on chemically synthesized metallic nanoparticles that support LSPs. These modes typically confine electromagnetic energy at distances of few tens of nanometers and they have been used in fluorescence displacement assays that employ the distance-modulated plasmonic enhancement¹⁸ of fluorescence signal or quenching.¹⁹ In these works, the difference in the fluorescence signal from the aptamer with and without analyte captured was typically <6-fold. An aptamer fluorescence assay that is mediated by PSPs on metallic films has been reported to offer higher, 18-fold change, of fluorescence intensity upon analyte binding²⁰ when probed with less confined PSP field reaching about 100 nm from the metal surface.

This paper reports on the reversible direct detection of a small molecule analyte by conformational changes of a hairpin aptamer which is labeled with a fluorophore and attached to a metallic film supporting PSP modes. Plasmonic amplification of the fluorescence signal enabled in situ continuous monitoring of variations in concentration of low-molecular-weight analytes—adenosine and adenosine triphosphate. By using simulations and experiments, the rational design of the aptamer molecular spacers and optical readout is investigated based on the emitted fluorescence intensity dependence on distance, orientation of the emitter, and angular range used for the collection of the fluorescence light.

EXPERIMENTAL SECTION

Materials. Sodium chloride, tris hydrochloride, 4-(2-hydroxyethyl)-piperazine-1-ethanesulfonic acid (HEPES), polyethylene glycol sorbitan monolaurate (Tween 20), magnesium chloride hexahydrate, adenosine, guanosine, adenosine 5'-triphosphate (ATP) disodium salt hydrate, and tris(2-carboxyethyl)phosphine hydrochloride solution (TCEP) were purchased from Sigma-Aldrich (Austria). (11-Mercaptoundecyl)triethylene glycol (PEG-thiol, SPT-0011) was obtained from SensoPath Technologies (USA). Two DNA aptamers were synthesized by Integrated DNA Technologies (IDT-DNA, Leuven, Belgium). The ATP hairpin aptamer with the short loop sequence (SLA) consisted of Alexa Fluor 647N 5'-CA CCT GGG GGA GTA TTG CGG AGG AAG GTT PEG6 CCA GGT G-SH 3' and the long loop ATP hairpin aptamer (LLA) sequence was Alexa Fluor 647N 5'-CA CCT GGG GGA GTA TTG CGG AGG AAG GTT TTT TTT TTT TTT TTT TTT TTT TTT TTT TTT CCA GGT G TT PEG6 -SH 3'. All reagents were used as received and buffer solutions were prepared using ultrapure water (Arium Pro, Sartorius Stedim).

Preparation of the Sensor Chips. A BK7 glass substrate was coated with 2 nm Cr and 50 nm Au films by thermal vacuum evaporation (Model HHV FL400, HHV Ltd., UK). The Au surface was rinsed with ethanol, dried under a stream of air, and stored under argon atmosphere until use. LLA or SLA aptamer was dissolved at

concentration of 1 μM in 200 μL of 10 mM Tris buffer (pH= 7.4) containing 6 mM MgCl_2 . Afterward, the aptamer was reacted with 100-fold excess TCEP (100 μM). After 4 h of incubation, the reduced ATP hairpin aptamer solution was spiked with PEG-thiol at concentration of 10 μM and the mixture was flowed over the Au surface in a closed loop system for 2 h in order to form a self-assembled monolayer (SAM).

Optical Setup. A schematic of the optical setup can be seen in Figure 1. The sensor chip with the aptamer biointerface on top was

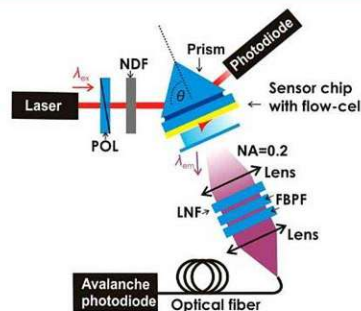


Figure 1. Schematics of the optical configuration used in the surface plasmon field-enhanced fluorescence measurements.

optically matched to an LASFN9 glass prism by using refractive index matching oil (from Cargille Inc., USA). The HeNe laser ($\lambda_{\text{ex}} = 632.8$ nm, ~ 2 mW) beam was transverse magnetically (TM) polarized by passing through a polarizer (POL) and was coupled to the prism to resonantly excite the PSPs by the Kretschmann configuration of the attenuated total reflection (ATR) method. The prism and sensor chip assembly was mounted on a rotation stage to control the angle of incidence θ and the angular reflectivity spectra $R(\theta)$ were measured by a photodiode detector connected to a lock-in amplifier (EG&G, USA). The enhanced field intensity occurring upon the coupling to PSPs at a resonant angle θ_{SPR} were used to excite Alexa Fluor-647 molecules at the sensor surface. The fluorescence light emitted at a wavelength around $\lambda_{\text{em}} = 670$ nm to the direction normal to the surface was collected by a lens (focal length 30 mm, numerical aperture of NA = 0.2), passed through two bandpass filters (FBF, transmission wavelength $\lambda = 670$ nm, 670FS10-25, Andover Corporation Optical Filter, USA) and a notch filter (LNF, central stop-band wavelength $\lambda = 632.8$ nm, XNF-632.8-25.0M, CVI Melles Griot, USA). Then the fluorescence light was coupled to a multimode optical fiber (FT400EMT, Thorlabs, UK) that was connected to an avalanche photodiode photon counter (Count-200-FC, Laser Components, Germany). Its intensity (F) was measured by a counter (53131A, Agilent, USA) in counts per second (cps) and recorded by the software Wasplas (Max Planck Institute for Polymer Research, Mainz, Germany). During the fluorescence measurements, the intensity of the laser beam illuminating an area of about 1 mm^2 was decreased by using a neutral-density filter (NDF, optical density OD = 2, Linos Plano Optics) in order to reduce the effect of fluorophore bleaching. The measurement of reflectivity R and fluorescence intensity F as a function of time t was performed at an incidence angle θ that was fixed close to the resonance.

Aptamer Assay. A flow-cell with a volume of 10 μL was clamped to the sensor surface to contain liquid samples transported via fluidic tubing (Tygon LMT-55) with 0.25 mm inner diameter at a flow rate of 15 $\mu\text{L}/\text{min}$. The flow-cell consisted of a PDMS gasket (thickness of ~ 130 μm) and a transparent glass substrate with drilled inlet and outlet ports. Throughout the assay measurements, 10 mM Tris buffer (pH = 7.4) containing 6 mM MgCl_2 was used (further referred to as hairpin aptamer assay buffer—HAB), which was similar to the buffer condition used during the aptamer selection process with minor modifications.²¹ Following the aptamer immobilization, the sensor surface was washed for 15 min with HAB to establish a stable baseline

2.6. Plasmon Field-Enhanced Fluorescence Energy Transfer for Hairpin Aptamer Assay Readout

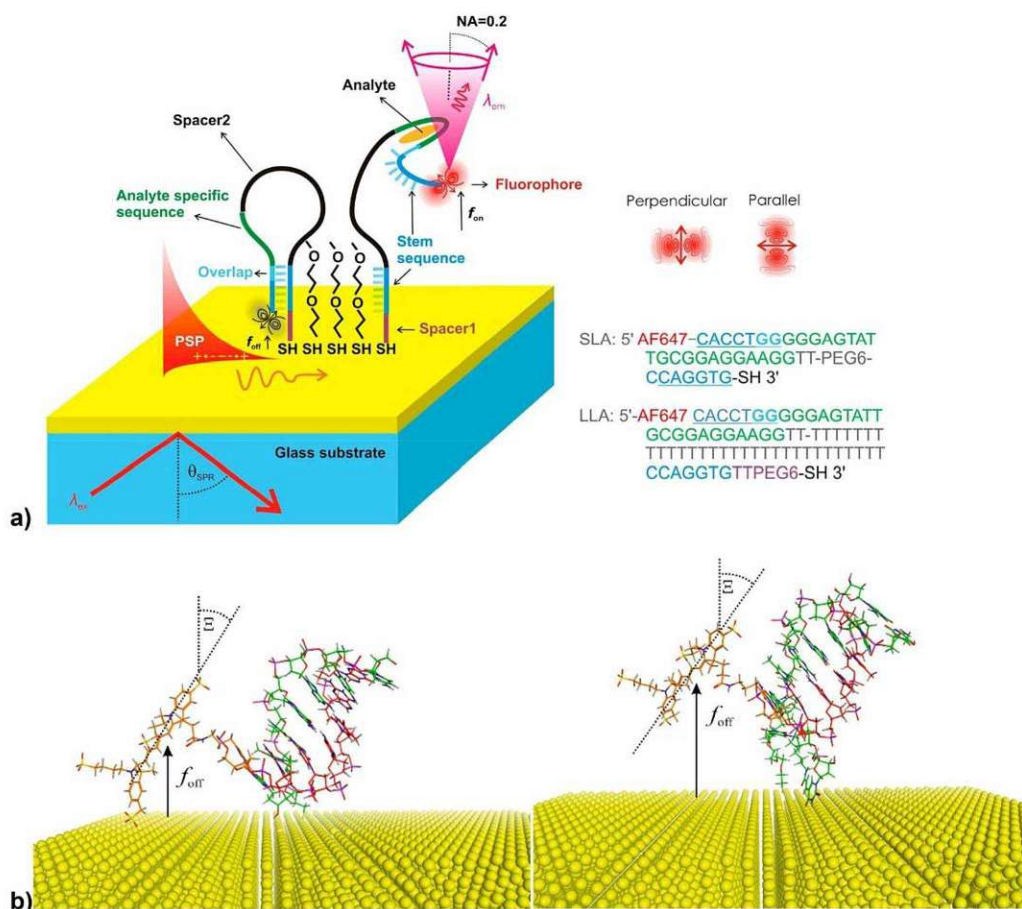


Figure 2. (a) Schematics of the aptamer-based assay on the gold sensor surface that utilizes a fluorophore coupled to surface plasmons (PSP). Short loop hairpin aptamer (SLA) or long loop hairpin aptamer (LLA) were anchored to the gold surface via a thiol group at the 3' end and their surface density was diluted by using polyethylene glycol-thiol (PEG). (b) Examples of possible closed hairpin conformations of SLA (left) and LLA (right) in the absence of analyte and with Alexa Fluor 647 fluorophore attached to the 5' DNA strand end.

of the fluorescence signal F_0 . Then, a series of samples spiked with target and reference analytes were sequentially injected. Each sample was flowed for 3 min during which the sensor signal $F(t)$ reached saturation. For comparison, a high ionic strength HEPES buffer was used (10 mM HEPES pH = 7.4 containing 150 mM NaCl, 5 mM $MgCl_2$, and 0.005% Tween 20) for the affinity binding studies besides HAB.

Optical Simulations. Numerical simulations were carried out in order to determine the light intensity emitted to the far field by fluorophores that are exposed to the evanescent field of PSPs in close proximity to a metallic surface. The simulations were performed by using the finite difference time domain (FDTD) method that was implemented in the package FDTD Solutions (Lumerical Solutions Inc., Canada). Fluorophores were represented by an infinitely small dipole source placed above a plane gold surface at a distance f with the orientation parallel (\parallel) or perpendicular (\perp) to the surface. The angular distribution of emitted light intensity to the far field was determined by using a monitor placed above the structure. Perfectly matched layer boundary conditions were applied at all interfaces of a $1 \mu m \times 1 \mu m \times 3.5 \mu m$ simulation volume. A region of $120 \text{ nm} \times 120 \text{ nm} \times 300 \text{ nm}$ around the emitter was studied with a 1 nm mesh, while the remaining volume was partitioned with a nonuniform conformal mesh. Water, as background medium surrounding the emitter, was

described by a constant refractive index medium with $n = 1.332$ and the wavelength-dependent refractive index of gold was obtained by fitting CRC data.²³ In order to determine the emission probability to the defined numerical aperture NA, the emitted intensity at $\lambda_{em} = 670 \text{ nm}$ was integrated over the angles falling in the defined range and normalized with the total emitted power at the same wavelength. The emission rate to a chosen NA was obtained as a product of emission probability and excitation rate. The excitation rate of a fluorophore was assumed proportional to the electric field intensity $|E|^2$ at $\lambda_{ex} = 633 \text{ nm}$ which was simulated for the resonant coupling to PSPs.

Analysis of Aptamer Conformations. A random-coil approach²³ was used based on a model in which the end-to-end distance of polymer chain with N elements is determined as $\alpha a N^{1/2}$, where a is the length between the monomers and α is a coefficient. An average distance of $a = 0.63 \text{ nm}$ was assumed for nucleic acid monomers²⁴ and $a = 0.15 \text{ nm}$ for the bonds within PEG segments. The segments of oligonucleotide strands were assumed to rotate completely freely and thus α was set to $\alpha = 1$. For the PEG spacers, α was set to $2^{1/2}$ to take into account their stiffer chain. It is important to note that this model neglects a wide range of effects including repulsive Coulombic interactions (e.g., between negatively charged bases in the DNA strand and with the negatively charged Alexa Fluor 647N), steric hindrance, or defined DNA strand conformations as a result of the affinity bound

target analyte. Visualizations of possible conformations of the studied aptamers were created in the Molecular Operating Environment (MOE, 2013.08, Chemical Computing Group Inc., Canada).

RESULTS AND DISCUSSION

As seen in Figure 2a, the gold sensor surface carried a DNA hairpin aptamer anchored via a thiol group at its 3' end. The thiol-PEG SAM was used to dilute the surface density of the aptamer to reduce steric hindrance during analyte binding and aptamer unfolding, as well as to serve as an antifouling carpet. The aptamers specific to adenosine and adenosine triphosphate (ATP) were derived from the structure which was reported to exhibit dissociation constant in the bulk solution of $K_d \sim 6 \mu\text{M}$ for adenosine.²¹ In order to utilize a readout strategy based on surface plasmon field-enhanced fluorescence energy transfer, the 5' end of the aptamer strand was labeled with Alexa Fluor 647N dye. Seven bases of the aptamer at two locations close to the 5' and 3' ends were designed to be complementary (marked blue in Figure 2a) to form the stem. By using these sequences, the aptamer forms a hairpin structure with the fluorophore present close to the metal surface at a distance of f_{off} . The sequence of the stem region close to the 5' end partially overlaps with the sequence of 22 bases that is specific to the target analytes adenosine and ATP (analyte specific segment marked green in Figure 2a). Therefore, the affinity binding of ATP disrupts the hairpin structure and switches the aptamer to its open conformation state with a fluorophore present at longer distance f_{on} from the gold surface. By using molecular spacers between the thiol anchor and the stem sequence (spacer 1) and between the stem sequence and the analyte specific sequence (spacer 2), the distance between Au and Alexa Fluor 647 dyes in the "off" state f_{off} and in the "on" state f_{on} can be tuned in order to achieve a maximum difference in the detected optical signals.

Distance of the Fluorophore from the Surface. Two designs of ATP aptamers with different molecular spacers 1 and 2 were used. The long loop aptamer—LLA—carried spacer 1 with 6 PEG groups and two T bases between the anchor group and the 3' stem sequence. In addition, spacer 2 composed of 32 T bases was inserted between the ATP specific sequence and the stem sequence. The second hairpin aptamer with short loop sequence—SLA—had no spacer 1 and a shorter spacer 2 (two T bases and 6 PEG groups). To estimate the distance between the fluorophore and gold surface in the "off" and "on" states, possible conformations of the SLA and LLA were analyzed. Two examples of conformations of the stem region with the fluorophore in the closed hairpin SLA and LLA can be seen in Figure 2b. The distances of the fluorophore from the metal surface in the absence f_{off} and the presence f_{on} of the analyte were estimated based on random-coil model for polymers. For LLA with longer molecular spacers, the average distance in the closed hairpin conformation was estimated as $f_{\text{off}} \sim 1.6$ nm and in the open hairpin conformation as $f_{\text{on}} \sim 6.6$ nm. In the closed hairpin conformation, the spacer 1 (6 PEG groups and two T bases) and linker between the fluorophore and the aptamer were assumed to be flexible. Similarly, for the SLA the average distances were estimated as $f_{\text{off}} \sim 0.9$ nm and $f_{\text{on}} \sim 5.2$ nm (see summary in Table S1). The range of rotational freedom of the fluorophore dye attached to SLA and LLA in the f_{off} state is visualized in Figure S1. The Alexa Fluor 647N dye in SLA appears less flexible as compared to LLA where it possesses a broader range of possible conformational states (rotational freedom). As in the readout of the assay, the fluorescence signal

$F(t)$ is collected with about 1 s integration time, the orientation of the fluorophore is expected to be averaged and the mean polar angle is $\Xi \sim 60^\circ$ for both "off" and "on" states when the fluorophore is free to rotate. For SLA in the closed hairpin, the fluorophore is in close proximity to the gold surface which may sterically hinder its rotation and thus a parallel orientation is likely preferred, $\Xi > 60^\circ$ (note that a parallel orientation of the dipole corresponds to $\Xi = 90^\circ$ and the perpendicular orientation to $\Xi = 0^\circ$).

Simulations of Competing Plasmonic Enhancement and Quenching. The optical response of Alexa Fluor 647N to conformation changes of the investigated SLA and LLA aptamers between the closed and open hairpin states were numerically simulated by FDTD. As Figure 3a shows, PSPs

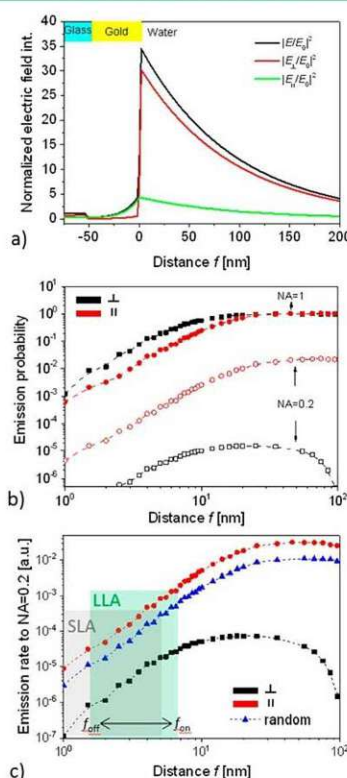


Figure 3. (a) Simulated parallel and perpendicular component of electric field intensity upon the resonant excitation of PSP at $\lambda_{\text{ex}} = 633$ nm depending on distance from the surface f . (b) Emission probability for a dipole representing the fluorophore emitting at $\lambda_{\text{em}} = 670$ nm to a cone above the gold surface with NA = 0.2 and NA = 1 as a function of distance f and dipole orientation. (c) Emission rate of a fluorophore emitting to NA = 0.2 at $\lambda_{\text{em}} = 670$ nm that is excited via PSPs at $\lambda_{\text{ex}} = 633$ nm for its parallel and perpendicular orientation and varied distance f .

probe the gold–water interface with a characteristic profile of the electromagnetic field that evanescently decays away from the gold surface with a penetration depth of about $L_p = 190$ nm (defined as the distance from the surface at which the field amplitude $|E|$ decreases by a factor of e). In addition, it shows that the field component $|E_{\perp}|^2$ that is perpendicular to the

surface is enhanced by a factor of about 35 with respect to that of the incident field component. The intensity of the parallel component $|E_{\parallel}|^2$ is approximately 5 times lower than that of the perpendicular one $|E_{\perp}|^2$.

In general, the radiation of fluorescence emitter placed above the plane interface between gold and water can be quenched, coupled via the near field to PSPs traveling along the gold surface, or it can be emitted to the far field. The total emission probability to the far field (represented by numerical aperture $NA = 1$) from a radiating dipole above the gold surface is close to 1 at long distances and it rapidly drops when decreasing the distance f below 15 nm, see Figure 3b. These data also reveal that the emitter oriented parallel (\parallel) to the gold emits to the far field with smaller probability than that with perpendicular orientation (\perp). Interestingly, this behavior is opposite if light is only collected to a narrow cone of angles close to the normal direction. The reason for the stronger emission probability from the parallel dipole (that is more quenched) into the normal direction is that emission occurs dominantly in the direction normal to dipole oscillation. Let us note that for the in situ measurement of fluorescence signal through a flow-cell, the numerical aperture NA of lens used for the collecting of fluorescence light is limited as it cannot approach close to the sensor surface. The value used herein of $NA = 0.2$ holds for typically used configurations in diffraction as well as ATR-based plasmon field-enhanced fluorescence biosensors.^{2,5}

Figure 3c presents the emission rate of fluorophore that is coupled by the resonantly excited PSPs waves at wavelength λ_{ex} which occurs in a narrow angular range within $NA = 0.2$. It shows that the difference between the emission probability from parallel (\parallel) and perpendicularly (\perp) oriented emitter is partially compensated by the stronger excitation of perpendicular dipoles (see $|E_{\perp}|^2$ in Figure 3a) than parallel dipoles (see $|E_{\parallel}|^2$ in Figure 3a). For short distances ($1 < f < 15$ nm), the emission rate rapidly increases with increasing distance similar to the emission probability as the PSP field decays slowly. However, when increasing the distance f toward the PSP penetration depth, the emission rate decreases with the distance as the excitation field gets substantially weaker. In summary, simulations predict that fluorescence intensity detected from a fluorophore that is placed at the distance $f < 15$ nm and excited with enhanced PSP field is more than an order of magnitude stronger for the parallel dipole orientation (\parallel) than for the perpendicular orientation (\perp). The emitted fluorescence intensity rapidly increases with the distance f . For the estimated changes in the distance of randomly oriented emitter attached to LLA, the simulated intensity increase for the distance switch from $f_{off} = 1.6$ nm to $f_{on} = 6.6$ nm is a factor of about 45. For the SLA aptamer with preferably parallel oriented dye in the closed hairpin conformation, slightly lower fluorescence signal change of about 40 is predicted when the distance changes from $f_{off} = 0.9$ nm to $f_{on} = 5.2$ nm.

Measurement of Plasmon Field-Enhanced Fluorescence Energy Transfer Aptamer Assay. As seen in Figure 4a, the resonant excitation of PSPs at λ_{ex} manifests itself as a narrow resonant dip in the reflectivity spectrum $R(\theta)$. Interestingly, the measured reflectivity spectra did not show significant shift of the SPR dip located at θ_{SPR} upon the binding of ATP which increases refractive index on the surface and also leads to its redistribution due to the conformation change of the aptamer. The lack of SPR signal to such variations can be ascribed to two effects. First, ATP exhibits low molecular weight (507.2 Da) which translates to weak increase in

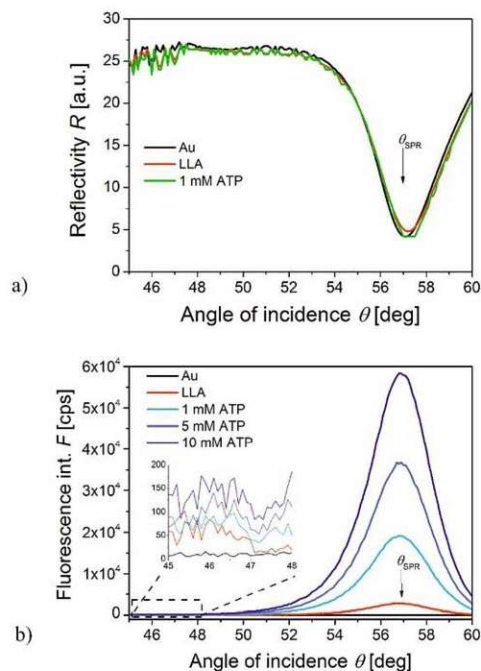


Figure 4. (a) Angular SPR reflectivity spectra $R(\theta)$ and (b) respective fluorescence intensity spectra $F(\theta)$ measured for a sensor surface in contact with HAB buffer spiked with the concentration of ATP of 0, 1, 5, and 10 mM. The gold sensor surface was functionalized with LLA.

refractive index that is proportional to $\delta\theta_{SPR}$. Second, the switching of the aptamer from its closed to open loop conformation by the capture of ATP should lead to counteracting small decrease in θ_{SPR} . Decrease of SPR angle by about $\delta\theta_{SPR} = 0.01\text{--}0.02^\circ$ was reported for swelling of polymer brushes with molecular weight 50–3000 kDa²⁶ which was attributed to increase in their thickness and accompanied decrease in refractive index. The switching of the aptamer structure should lead to similar effects, but as its molecular weight of 22.6 kDa is lower, the respective SPR changes are expected to be weaker.

In the surface plasmon field-enhanced fluorescence regime, the resonant coupling to PSPs leads to the excitation of attached Alexa Fluor 647 dyes which can be seen as a strong peak in the fluorescence intensity F centered at an angle θ slightly lower than that where SPR occurs (see Figure 4b). Interestingly, the maximum fluorescence intensity occurs at angle θ that is slightly lower than that where the minimum reflectivity occurs. Such small angular shift can be attributed to the interference between the laser beam, that directly reflects from the gold layer and undergoes a phase shift and the resonantly excited surface plasmon waves that are leaky to the substrate. When incubating the sensor surface with the ATP target analyte, an increase in the fluorescence signal F is observed. This is caused by a change in the aptamer conformation that leads to an increase in the distance of the emitter from the surface f and reduced effect of quenching. Experimental measurements with SLA show 10.3-fold increase in fluorescence intensity for 12 mM ATP in comparison to the measurement taken in the absence of analyte, while for LLA, a

stronger 23.3-fold increased fluorescence intensity was observed. For the SLA, this value is about 4-fold lower than predicted and for the LLA aptamer, the measured value is about 2-fold lower than predicted. These discrepancies can be attributed to inaccuracy of the model, particularly to the simplified means of determining the distances in the open and closed hairpin conformation and approximations used in the FDTD simulations where the size of the real emitter (of about 2 nm) was replaced by an infinitely small dipole.

Real-Time Detection of the Reversible Aptamer Interaction with Target Analyte. For the experimental observation of affinity interaction with tethered aptamers, the angle of incidence was set close to $\theta_{\text{SPR}} = 57^\circ$ (where the strongest fluorescence signal amplification occurs) and the fluorescence intensity was measured as a function of time $F(t)$. As can be seen from Figure 5, the injection of the HAB spiked

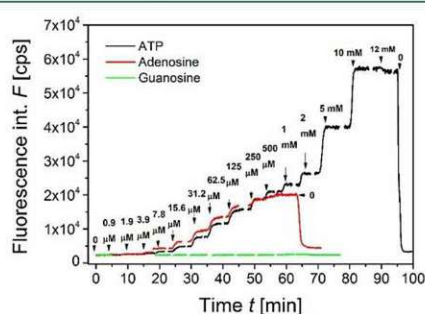


Figure 5. Example of the fluorescence signal $F(t)$ measured at a fixed angle $\theta = 57^\circ$ during titration of ATP, adenosine, and guanosine at concentration increments up to 12 mM in HAB buffer. Gold sensor surface was functionalized with LLA.

with ATP leads to a rapid increase in the fluorescence signal F . Increasing the ATP concentration from 0.9 μM to 12 mM leads to a gradual increase in equilibrium signal F . Exposure to the highest concentration followed by rinsing in buffer (without the analyte) resulted in a rapid dissociation of the ATP-aptamer complex that manifests itself as a drop of the fluorescence signal to the original baseline value F_0 . This observation confirms a fully reversible aptamer interaction for repeated measurements without regeneration. Moreover, virtually no bleaching of attached dyes was observed over the time course of the experiment. The aptamer assay showed a comparable reversible response for the detection of adenosine, but no observable response was recorded for the negative control—guanosine—which is a structural analogue of adenosine. The data for the long LLA ligand shown in Figure 5 were similar for the SLA (Figure S2).

Calibration Curves. From the data of the titration measurements, the equilibrium response F was obtained for each analyte concentration. The limit of detection (LOD) was determined as the concentration at which the calibration curve intersects with the value of the background signal F_0 plus 3 times the standard deviation, $3\sigma(F_0)$.

For SLA, the determined LOD for ATP was 108 μM and 24 μM for adenosine. This was greatly improved by the LLA where LOD values were ~ 1 –2 μM for both ATP and adenosine. The obtained detection limits of the sensor is within the reported values in the literature, that ranges over several orders of magnitude (ATP detection limits from 0.5

μM ²⁷ up to 0.65 mM²⁸) for a plethora of fluorescence detection schemes.^{29,30} Although our reported sensor may fall in the low sensitivity range, it is comparable to surface supported real-time detection sensors^{31,32} and has the added value of effortless reversible detection. As can be seen in Figure 6a, the baseline

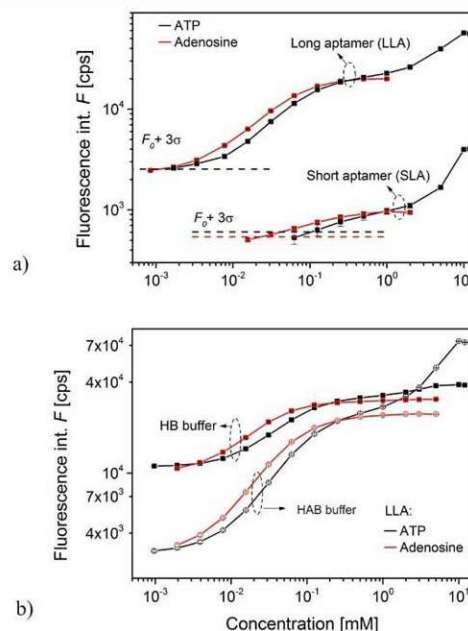


Figure 6. Calibration curves measured with SPFS detection principle for ATP and adenosine analytes. Each data point (ΔF) derived from triplicate titration measurements (an example shown in Figure 4). (a) Comparison of the response for LLA and SLA aptamers and analyte dissolved in HAB buffer. (b) Comparison of the response for LLA aptamer and analytes dissolved in HAB and HB buffers.

fluorescence intensity is higher for the interface with LLA compared to that for SLA. This can be attributed to its longer distance in the “off” aptamer state— f_{off} —(see Table S1) which is accompanied by higher emission rate (see Figure 3c). In addition, K_d values were determined from the calibration curves fitted with Langmuir isotherm model (presented in the Supporting Information) and the K_d for adenosine was of 90 μM for SLA and of 50 μM for LLA (Figures S3a,b). The calibration curves for ATP in both aptamers deviated from the Langmuir isotherm (Figure 6a). However, fitting the calibration curve for ATP concentrations up to 2 mM, where initial slight saturation was seen (Figure 5a), yields K_d values of 300 μM and 120 μM for SLA and LLA (Figure S3c,d), respectively. These values are probably increased by either the interaction of the strongly negatively charged molecule ATP with the surface-anchored aptamer that carries also negatively charged fluorophore, possibly affecting its orientation. It is worth of noting that the overall reduced affinity of fluorophore labeled aptamers with respect to the unmodified one was reported previously.^{33,34} Besides the molecular charge mentioned above, surface and label induced reduction in affinity of the aptamer, the competition of target-induced conformational change from the initial closed hairpin state is a likely contributor.

It was reported that the ATP binding aptamer can be described using a “conformational selection” recognition of ATP where the analyte-free state is more stable in high salt concentration, which leads to a deteriorated distinction of conformational changes when ATP is bound.³⁵ Therefore, the assay buffer (HAB) used in this study did not contain NaCl, in order to increase the contrast between aptamer conformations in analyte-free/hybridized and analyte bound states. However, it is important to observe the performance of the assay in buffers with compositions similar to samples relevant to applications in the field of medical diagnostics. For this purpose, HEPES buffer (HB) with salt concentration close to physiological conditions was used to evaluate LLA. Fluorescence intensity changes resulting from increasing analyte concentrations, in both HAB and HB, for both ATP and adenosine analytes can be seen in Figure 6b. The baseline fluorescence intensity F_0 of the sensor with HB is around 4-fold higher ($F_{0\text{HB}} \approx 11 \times 10^3$ cps and $F_{0\text{HAB}} \approx 3 \times 10^3$ cps); nevertheless the assay can be seen to perform similarly in terms of dynamic range for the detection of adenosine in both buffers. However, for ATP detection, saturation of sensor response is reached earlier in HB at 2 mM ATP, which is in contrast to 12 mM ATP for HAB and the peak intensity in HB is lower than for HAB. This decreased signal to background ratio and higher F_0 can be attributed to the influence of high salt concentration in HB, that leads to an analyte-free folded aptamer conformation and consequently lower structural change in the ATP bound state.

CONCLUSIONS

A DNA aptamer sequence specific to ATP was utilized in a plasmon field-enhanced reversible assay based on fluorescence energy transfer. The presented work demonstrates that the reversible interaction of a fluorophore-labeled aptamer with low-molecular-weight target analytes—adenosine and ATP—can be sensitively monitored in real time by plasmon field-enhanced fluorescence light intensity. The optical simulations qualitatively agree with the measured dependence of fluorescence light intensity on conformational changes of the used aptamers and they allowed ascribing the observed effects to variations in the fluorophore orientation and distance from the surface controlled by the molecular spacers. The plasmon field-enhanced fluorescence is shown to offer the advantage of continuous probing of aptamer capturing the target analyte for more than 1 h without bleaching of the dye, with a limit of detection of 1 μM . The observed design rules may provide leads to prepare more sensitive and robust assays that take advantage of versatile aptamer recognition elements and coupling with the confined field of surface plasmons in various optical configurations.

ASSOCIATED CONTENT

Supporting Information

The Supporting Information is available free of charge on the ACS Publications website at DOI: 10.1021/acssens.7b00131.

Summary of estimated distances between fluorophore and metallic surface for open and closed aptamer conformations, figures depicting the dihedral angle scan for SLA and LLA, fluorescence signal kinetics upon SLA interaction with ATP and adenosine, and fitting of calibration curves with Langmuir isotherm model in

order to determine equilibrium dissociation constant (PDF)

AUTHOR INFORMATION

Corresponding Author

*E-mail: jakub.dostalek@ait.ac.at.

ORCID

Chris Oostenbrink: 0000-0002-4232-2556

Bo Liedberg: 0000-0003-2883-6953

Jakub Dostálek: 0000-0002-0431-2170

Notes

The authors declare no competing financial interest.

ACKNOWLEDGMENTS

K.S. acknowledges financial support from the Austrian Federal Ministry for Transport, Innovation and Technology (GZ BMVIT-612.166/0001-III/II/2010). J.D. received support from the Tan Chin Tuan foundation, College of Engineering, Nanyang Technological University. A.T. acknowledges the Ph.D. program “BioTop - Biomolecular Technology of Proteins” (Austrian Science Fund, FWF Project W1224).

REFERENCES

- Bauch, M.; Toma, K.; Toma, M.; Zhang, Q.; Dostalek, J. Plasmon-Enhanced Fluorescence Biosensors: a Review. *Plasmonics* **2014**, *9* (4), 781–799.
- Lakowicz, J. R.; Ray, K.; Chowdhury, M.; Szmacinski, H.; Fu, Y.; Zhang, J.; Nowaczyk, K. Plasmon-Controlled Fluorescence: A New Paradigm in Fluorescence Spectroscopy. *Analyst* **2008**, *133* (10), 1308–1346.
- Khatua, S.; Paulo, P. M. R.; Yuan, H.; Gupta, A.; Zijlstra, P.; Orrit, M. Resonant Plasmonic Enhancement of Single-Molecule Fluorescence by Individual Gold Nanorods. *ACS Nano* **2014**, *8* (5), 4440–4449.
- Attridge, J. W.; Daniels, P. B.; Deacon, J. K.; Robinson, G. A.; Davidson, G. P. Sensitivity Enhancement of Optical Immunosensors by the Use of a Surface Plasmon Resonance Fluoroimmunoassay. *Biosens. Bioelectron.* **1991**, *6* (3), 201–214.
- Liebermann, T.; Knoll, W. Surface-Plasmon Field-Enhanced Fluorescence Spectroscopy. *Colloids Surf., A* **2000**, *171* (1–3), 115–130.
- Kinkhabwala, A.; Yu, Z.; Fan, S.; Avlasevich, Y.; Mullen, K.; Moerner, W. E. Large Single-Molecule Fluorescence Enhancements Produced by a Bowtie Nanoantenna. *Nat. Photonics* **2009**, *3* (11), 654–657.
- Anger, P.; Bharadwaj, P.; Novotny, L. Enhancement and Quenching of Single-Molecule Fluorescence. *Phys. Rev. Lett.* **2006**, *96* (11), 4.
- Bharadwaj, P.; Novotny, L. Spectral Dependence of Single Molecule Fluorescence Enhancement. *Opt. Express* **2007**, *15* (21), 14266–14274.
- Vasilev, K.; Knoll, W.; Kreiter, M. Fluorescence Intensities of Chromophores in Front of a Thin Metal Film. *J. Chem. Phys.* **2004**, *120* (7), 3439–3445.
- Wang, R. E.; Zhang, Y.; Cai, J.; Cai, W.; Gao, T. Aptamer-Based Fluorescent Biosensors. *Curr. Med. Chem.* **2011**, *18* (27), 4175–4184.
- Zhou, W.; Jimmy Huang, P.-J.; Ding, J.; Liu, J. Aptamer-Based Biosensors for Biomedical Diagnostics. *Analyst* **2014**, *139* (11), 2627–2640.
- Zhang, J.; Wang, L.; Zhang, H.; Boey, F.; Song, S.; Fan, C. Aptamer-Based Multicolor Fluorescent Gold Nanoprobes for Multiplex Detection in Homogeneous Solution. *Small* **2010**, *6* (2), 201–204.
- Wood, A. J.; Basuray, S.; Bok, S.; Gangopadhyay, K.; Gangopadhyay, S.; Grant, S. A. Enhanced DNA Detection Through

2.6. Plasmon Field-Enhanced Fluorescence Energy Transfer for Hairpin Aptamer Assay Readout

the Incorporation of Nanocones and Cavities Into a Plasmonic Grating Sensor Platform. *IEEE Sens. J.* **2016**, *16* (10), 3403–3408.

(14) Lee, S. E.; Chen, Q.; Bhat, R.; Petkiewicz, S.; Smith, J. M.; Ferry, V. E.; Correia, A. L.; Alivisatos, A. P.; Bissell, M. J. Reversible Aptamer-Au Plasmon Rulers for Secreted Single Molecules. *Nano Lett.* **2015**, *15* (7), 4564–4570.

(15) Wang, W.; Chen, C.; Qian, M.; Zhao, X. S. Aptamer biosensor for protein detection using gold nanoparticles. *Anal. Biochem.* **2008**, *373* (2), 213–219.

(16) Melaine, F.; Roupioz, Y.; Buhot, A. Gold Nanoparticles Surface Plasmon Resonance Enhanced Signal for the Detection of Small Molecules on Split-Aptamer Microarrays (Small Molecules Detection from Split-Aptamers). *Microarrays* **2015**, *4* (1), 41.

(17) Wu, C.; Yang, C. J.; Tan, W. Molecular Aptamer Beacons. In *Molecular Beacons*, Yang, C. J.; Tan, W., Eds.; Springer: Berlin, Heidelberg, 2013; pp 175–194.

(18) Sui, N.; Wang, L. N.; Xie, F. X.; Liu, F. Y.; Xiao, H. L.; Liu, M. H.; Yu, W. W. Ultrasensitive Aptamer-Based Thrombin Assay Based on Metal Enhanced Fluorescence Resonance Energy Transfer. *Microchim. Acta* **2016**, *183* (5), 1563–1570.

(19) Meng, C.; Dai, Z.; Guo, W. J.; Chu, Y. Y.; Chen, G. P. Selective and Sensitive Fluorescence Aptamer Biosensors of Adenosine Triphosphate. *Nanomater. Nanotechnol.* **2016**, *6*, 33.

(20) Xie, T. T.; Liu, Q.; Cai, W. P.; Chen, Z.; Li, Y. Q. Surface Plasmon-Coupled Directional Emission Based on a Conformational-Switching Signaling Aptamer. *Chem. Commun.* **2009**, *22*, 3190–3192.

(21) Huizenga, D. E.; Szostak, J. W. A DNA Aptamer That Binds Adenosine and ATP. *Biochemistry* **1995**, *34* (2), 656–665.

(22) Williams, M. L. CRC Handbook of Chemistry and Physics. *Occup. Environ. Med.* **1996**, *53* (7), 504.

(23) Flory, P. J.; Volkenstein, M. Statistical Mechanics of Chain Molecules. *Biopolymers* **1969**, *8* (5), 699–700.

(24) Murphy, M. C.; Rasnik, I.; Cheng, W.; Lohman, T. M.; Ha, T. Probing Single-Stranded DNA Conformational Flexibility Using Fluorescence Spectroscopy. *Biophys. J.* **2004**, *86* (4), 2530–2537.

(25) Hageneder, S.; Bauch, M.; Dostalek, J. Plasmonically Amplified Bioassay – Total Internal Reflection Fluorescence vs. Epifluorescence Geometry. *Talanta* **2016**, *156–157*, 225–231.

(26) Sarkar, D.; Somasundaran, P. Conformational Dynamics of Poly(acrylic acid). A Study Using Surface Plasmon Resonance Spectroscopy. *Langmuir* **2004**, *20* (11), 4657–4664.

(27) Xue, Q.; Wang, L.; Jiang, W. A Novel Label-Free Cascade Amplification Strategy based on Dumbbell Probe-Mediated Rolling Circle Amplification-Responsive G-Quadruplex Formation for Highly Sensitive and Selective Detection of NAD⁺ or ATP. *Chem. Commun.* **2013**, *49* (26), 2640–2642.

(28) Xu, J.; Wei, C. The Aptamer DNA-Templated Fluorescence Silver Nanoclusters: ATP Detection and Preliminary Mechanism Investigation. *Biosens. Bioelectron.* **2017**, *87*, 422–427.

(29) Ma, C.; Lin, C.; Wang, Y.; Chen, X. DNA-based ATP sensing. *TrAC, Trends Anal. Chem.* **2016**, *77*, 226–241.

(30) Perrier, S.; Bouilloud, P.; De Oliveira Coelho, G.; Henry, M.; Peyrin, E. Small Molecule Aptamer Assays based on Fluorescence Anisotropy Signal-Enhancer Oligonucleotides. *Biosens. Bioelectron.* **2016**, *82*, 155–161.

(31) Bogomolova, A.; Aldissi, M. Real-Time Aptamer Quantum Dot Fluorescent Flow Sensor. *Biosens. Bioelectron.* **2011**, *26* (10), 4099–4103.

(32) Liu, Z.; Chen, S.; Liu, B.; Wu, J.; Zhou, Y.; He, L.; Ding, J.; Liu, J. Intracellular Detection of ATP Using an Aptamer Beacon Covalently Linked to Graphene Oxide Resisting Nonspecific Probe Displacement. *Anal. Chem.* **2014**, *86* (24), 12229–12235.

(33) Cho, E. J.; Lee, J.-W.; Ellington, A. D. Applications of Aptamers as Sensors. *Annu. Rev. Anal. Chem.* **2009**, *2* (1), 241–264.

(34) Nielsen, L. J.; Olsen, L. F.; Ozalp, V. C. Aptamers Embedded in Polyacrylamide Nanoparticles: A Tool for in Vivo Metabolite Sensing. *ACS Nano* **2010**, *4* (8), 4361–4370.

(35) Xia, T.; Yuan, J.; Fang, X. Conformational Dynamics of an ATP-Binding DNA Aptamer: A Single-Molecule Study. *J. Phys. Chem. B* **2013**, *117* (48), 14994–15003.

2.7. Biosensor Platform for Parallel Surface Plasmon-Enhanced Epifluorescence and Surface Plasmon Resonance Detection

The following publication is reprinted under the Creative Commons CC-BY^f license.

Agnes T. Reiner, **Stefan Fossati**, Jakub Dostalek Biosensor platform for parallel surface plasmon-enhanced epifluorescence and surface plasmon resonance detection. *Sensors Actuators, B Chem.* 257, 594–601 (2018). <https://doi.org/10.1016/j.snb.2017.10.116>

Copyright © 2017 The Authors. Published by Elsevier B.V.

In this work, a novel bimodal approach is employed to study extracellular vesicles, a rapidly developing medical topic. These small lipid vesicles in the intercellular space have been overlooked for a long time due to their small size and the lack of analytical tools. While being too small to be visible, the vesicles are still much larger than the average biomolecule, which causes a much-reduced diffusion velocity. To facilitate diffusion towards the biosensor surface, the vesicles are decorated with magnetic nanobeads and driven towards the surface using a magnetic field applied through the thin glass substrate. Within the plasmon field, the magnetic beads then also serve as signal-enhancing labels.

In this work, Agnes Reiner and Stefan Fossati devised the multimodal reader concept. Stefan Fossati implemented the optical reader and provided the plasmonic substrates, prepared by LIL, NIL, and thermal evaporation. Agnes Reiner developed the biochemical assays and conducted most of the experiments. The work was carried out under the supervision of Jakub Dostalek.

^f <http://creativecommons.org/licenses/by/4.0/>



Research paper

Biosensor platform for parallel surface plasmon-enhanced epifluorescence and surface plasmon resonance detection



Agnes T. Reiner, Stefan Fossati, Jakub Dostalek*

BioSensor Technologies, AIT-Austrian Institute of Technology GmbH, Muthgasse 11, 1190 Vienna, Austria

ARTICLE INFO

Article history:

Received 27 June 2017
Received in revised form
15 September 2017
Accepted 20 October 2017
Available online 28 October 2017

Keywords:

Surface plasmon resonance
Plasmon enhanced fluorescence
Epifluorescence
Biosensor

ABSTRACT

For the first time, plasmonic diffraction grating is implemented for the combined direct and epifluorescence-based readout of assays in real-time. This plasmonic structure serves for grating-coupled surface plasmon resonance (SPR) monitoring of molecular binding-induced changes in the refractive index. In parallel, it allows to simultaneously perform plasmonically enhanced fluorescence (PEF) analysis of affinity binding of molecules that are labeled with fluorophores. This configuration offers facile readout of e.g. magnetic nanoparticle-enhanced assays which is not possible with more conventional Kretschmann geometry. The performance characteristics of this combined approach are discussed by using two types of assays. In the first assay a fluorophore-labeled protein with a medium molecular weight of 55 kDa was affinity captured on the plasmonic sensor grating. The associated PEF signal in this assay showed a signal-to-noise ratio that was 140-fold higher compared to that of the SPR detection channel. In the second assay, extracellular vesicles were detected by using antibodies against CD81 attached to the plasmonic grating. These vesicles were pre-concentrated by their coupling to magnetic nanoparticles with cholera toxin B chain. This assay exploited magnetic nanoparticles as labels enabling rapid collection of analyte at the sensor surface and for the enhancement of the SPR sensor response. In this case the label-free SPR detection channel outperformed the fluorescence-based detection, as the SPR signal-to-noise ratio was 2.4-fold higher than that of PEF.

© 2017 The Author(s). Published by Elsevier B.V. This is an open access article under the CC BY license (<http://creativecommons.org/licenses/by/4.0/>).

1. Introduction

Fluorescence is a widely used method in bioassays for sensitive detection of chemical and biological species. In order to advance their sensitivity, the fluorophores that are used as labels can be exposed to the confined field of surface plasmons [1,2]. These optical waves are resonantly excited at surfaces of metallic films and metallic nanoparticles and they originate from coupled collective oscillations of the charge density and the associated electromagnetic field. The combination of a surface plasmon-enhanced excitation rate at the fluorophore absorption wavelength, directional surface plasmon-coupled emission at the fluorophore emission wavelength, and an improved quantum yield was demonstrated to enhance the detected fluorescence intensity by a factor up to 10^3 [3]. Such interaction with the intense and confined surface plasmon field was exploited for amplification of the fluorescence signal associated to the affinity binding of labeled ana-

lyte biomolecules in bioassays and biosensors in order to improve their performance characteristics [4,5].

Besides plasmon-enhanced fluorescence (PEF) assays, the probing of molecular binding by surface plasmons allows for direct label-free detection of analytes. In surface plasmon resonance (SPR) biosensors, the affinity binding of analyte molecules increases the refractive index at a metallic sensor surface, which detunes the resonant coupling of light to surface plasmons and thus can be optically monitored as a shift of SPR. This method became an established tool in biomolecular interaction studies [6] and it is pursued for rapid and sensitive detection of chemical and biological analytes [7].

The possibility of parallel detection of SPR and PEF holds potential for more advanced detection schemes and molecular interaction studies. Up to now, the attenuated total reflection geometry (ATR) was dominantly used for the excitation of surface plasmons and it has been utilized for the combined SPR and PEF studies. It was reported for the SPR observation of functional bio-interfaces combined with enhanced sensitivity of fluorescence-based detection of low molecular weight analytes [8] or biomolecules present at minute concentrations in complex samples [9,10]. In addition, SPR and PEF was employed in the analysis of interaction

* Corresponding author.

E-mail address: jakub.dostalek@ait.ac.at (J. Dostalek).

<https://doi.org/10.1016/j.snb.2017.10.116>

0925-4005/© 2017 The Author(s). Published by Elsevier B.V. This is an open access article under the CC BY license (<http://creativecommons.org/licenses/by/4.0/>).

2.7. Biosensor Platform for Parallel Surface Plasmon-Enhanced Epifluorescence and Surface Plasmon Resonance Detection

between DNA polymerase, short oligonucleotide strands attached to a substrate, and labeled nucleotides that formed DNA duplexes [11]. Furthermore, the combination of fluorescence detection of enzyme linked immunoassays and SPR in a single instrument was demonstrated to be suitable for the analysis of target analytes over a broad dynamic range [12].

According to the knowledge of the authors, the combined SPR and PEF readout was implemented up to now only by using ATR configuration. The metallic diffraction grating-coupled SPR on periodically corrugated metallic surfaces provides an alternative means for the excitation and interrogation of surface plasmons, which found its applications in SPR biosensors [13] as well as in PEF detection in *epi*-fluorescence geometry configurations [14,15]. With respect to sensors utilizing ATR, diffraction gratings offer the advantage of simpler use that does not require optical matching of a sensor chip to a prism and it can be exploited in a format compatible with regular (fluorescence) microscopes. In addition, it was shown to enable the utilization of magnetic nanoparticle (MNP)-enhanced assays when a magnetic field gradient can be efficiently applied through a sensor chip in order to overcome diffusion-limited affinity binding kinetics and rapidly collect the pre-concentrated analyte at the sensor surface [16,17].

This work reports on SPR and PEF signal detection based on diffraction grating-coupled SPR and the epifluorescence geometry, which was not reported yet. We demonstrate that such a system can in parallel directly detect binding of biomolecules to the surface via SPR monitoring as well as by PEF when fluorophore labels are used. The performance characteristics of PEF and SPR modalities are investigated for the direct detection of medium size protein molecules and for MNP-enhanced analysis of larger extracellular vesicles (EVs).

2. Experimental

2.1. Materials

Positive photoresist Microposit S1805 was purchased from Shipley and its developer AZ 303 was acquired from Micro-Chemicals. Polydimethylsiloxane elastomer (PDMS) Sylgard 184 was obtained from Dow Corning and the UV-curable polymer Amonil MMS 10 was from AMO GmbH. Dithiolalkane aromatic PEG3 with hydroxyl endgroup (SPT-0013) and the dithiolalkane aromatic PEG6 with carboxyl endgroup (SPT0014A6) were purchased from SensoPath Technologies. N-(3-dimethylaminopropyl)-N'-ethylcarbodiimide hydrochloride (EDC), N-hydroxysuccinimide (NHS), ethanolamine and ethylenglycol, as well as acetic acid and sodiumacetate for the preparation of acetate buffer were bought from Sigma-Aldrich. Phosphate buffered saline (PBS) at a pH of 7.4 from Merck was used for the functionalization steps. PBS with addition of 0.05 % Tween 20 (Sigma-Aldrich) and 0.1 % bovine serum albumine (Thermo Fisher Scientific) (PBSTB) were used as running buffers in all detection experiments. The biotinylated mouse antibody (MG2b-57) was obtained from BioLegend and the mouse monoclonal antibody against human CD81 (1.3.3.22) from Santacruz Biotechnology. Streptavidin was from Thermo Fisher Scientific. Cholera toxin b-chain (CTB) from SBL Vaccin AB was biotinylated with EZ-link Sulfo-NHS-LC-Biotin (Thermo Fisher Scientific) and in parallel fluorescently labeled with Alexa Fluor 647 NHS ester (Thermo Fisher Scientific). MNPs with a diameter of 200 nm conjugated with streptavidin (fluidMAG-Streptavidin) were purchased from Chemicell. Prior to the use, streptavidin-coated MNPs were washed twice with PBSTB by applying a magnetic field for separation of the MNPs from the solution. EVs were generously provided from Sai Kiang Lim's group and their production and purification is described elsewhere [18].

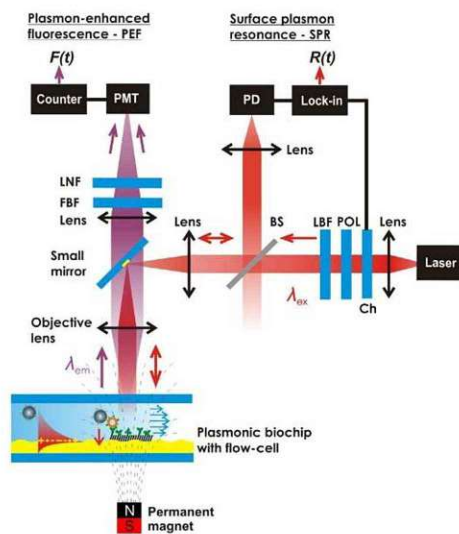


Fig. 1. Schematics of the platform for parallel surface plasmon-enhanced fluorescence and surface plasmon resonance detection (Ch – chopper, POL – polarizer, LBF – laser band-pass filter, BS – beam splitter, FBF – fluorescence band-pass filter, LNF – laser notch filter, $F(t)$ – fluorescence readout, $R(t)$ – SPR readout, PD – photodiode, PMT – photomultiplier).

2.2. Sensor chip preparation

A crossed relief grating was prepared by UV laser interference lithography and their multiple copies were made by soft lithography as described before [15]. Briefly, the used structure comprised of two superimposed crossed sinusoidal modulations with a period of $\Lambda = 434$ nm. The structure was cast to PDMS, which was cured over night at 60 °C before it was used as a working stamp. Cleaned BK7 glass substrates were coated with the UV-curable polymer Amonil MMS 10 by spin-coating at 3000 rpm for 120 s. Then, the PDMS working stamp was placed on the top of the Amonil layer and the structure cast to this polymer was irradiated by UV light (UV lamp Bio-Link 365, Vilber Lourmat). Finally, the PDMS stamp was detached from the cured Amonil MMS 10 leaving a copy of the master structure on the glass substrate. The grating copies were subsequently coated with 4 nm of chromium and 100 nm of gold by vacuum thermal evaporation (HHV AUTO 306 from HHV LTD) in vacuum better than 10^{-6} mBar. Each sensor chip consisted of an area with grating structure and an area with plain gold that was used for control measurements.

2.3. Optical system

The used optical system for the *in situ* detection of diffraction grating-coupled SPR and PEF was adopted based on our previous work [15] and it can be seen in Fig. 1. A beam emitted from a He-Ne laser (power of about 2 mW) at $\lambda_{ex} = 633$ nm subsequently travelled through a chopper, polarizer and laser band-pass filter (LBP, FL632.8-10 from Thorlabs). Then it passed through a beam splitter and it was focused by a lens (AC-254-040) on a mirror of 2 mm diameter, consisting of a 100 nm thick gold layer deposited on a BK7 glass slide. The mirror was oriented at 45 deg with respect to the incident beam. A lens (AC-254-040) collimated the reflected beam towards the sensor surface with relief gold diffraction grating mounted in its focal distance. A flow-cell was clamped to the gold sensor chip surface in order to contain aqueous samples. The flow-

2.7. Biosensor Platform for Parallel Surface Plasmon-Enhanced Epifluorescence and Surface Plasmon Resonance Detection

596

A.T. Reiner et al. / Sensors and Actuators B 257 (2018) 594–601

cell comprised of a flow chamber with a volume of $\sim 50 \mu\text{L}$ defined by a PDMS gasket and a transparent fused silica glass substrate with inlet and outlet ports. Upon its incidence at the gold grating surface, the laser beam at λ_{ex} was partially coupled to surface plasmons propagating along the gold surface and partially reflected. The reflected beam was focused back on the mirror by the objective lens and its intensity was detected by using a beam splitter and a photodiode connected to a lockin amplifier (7260 from EG&G). These means allowed the measurement of the detuning of SPR associated to the binding-induced refractive index variations. In addition, the enhanced field intensity at λ_{ex} was employed for the excitation of Alexa Fluor 647 (AF647) fluorophores that we used as labels in the fluorescence assays. The enhanced directional surface plasmon-coupled emission at $\lambda_{\text{em}} = 670 \text{ nm}$ was collimated by the objective lens, passed around the small mirror and was focused by a lens (AC-254-080, Thorlabs) to a photomultiplier (H6240-01, Hamamatsu) that was connected to a counter (53131A from Agilent). In order to separate light at the excitation wavelength λ_{ex} and the fluorescence beam at λ_{em} , a set of filters was used consisting of a notch filter (XNF-632.8-25.0 M from CVI Melles Griot) and two bandpass filters (FB670-10 from Thorlabs and 670FS10-25 from Andover Corporation Optical Filter). The output from the counter was recorded in counts per second (cps) by using software Wasplas developed at Max Planck Institute for Polymer Research in Mainz (Germany). It is worth of noting that the used implementation of SPR measurements allowed for measurements of bulk refractive index changes as small as 3×10^{-4} RIU. This value was determined as the ratio $\Delta n / (\sigma(R) / \Delta R_B)$ where $\sigma(R) = 3.6 \times 10^{-3}$ a.u. is the standard deviation of the reflectivity signal $R(r)$ and ΔR_B refers to the reflectivity change induced by the refractive index increase Δn due to the pumping of PBS spiked with 2 % ethylenglycol through the flow cell.

In the MNP-enhanced assays, a gradient magnetic field ∇B was applied through the sensor chip. A cylindrical permanent magnet (NdFeB with diameter of 10 mm and length of 35 mm from Neotexx) was approached to the grating sensor chip in order to expose its surface to the field gradient of about $\nabla B = 0.10 \text{ T mm}^{-1}$ [16]. By removing the magnet, the magnetic field gradient was switched off to $\nabla B = 0$.

2.4. Functionalization of sensor chips

The gold surface of the sensor chips was immersed in a 1 mM thiol solution in ethanol in order to form a mixed self-assembled monolayer (SAM). The solution comprised of a mixture of dithiol-PEG6 with carboxyl end group for later surface functionalization and dithiol-PEG3 with hydroxyl end group in order to form an antifouling background. The molar ratio of carboxyl to hydroxyl-terminated thiols was 1:9. After the overnight incubation, the sensor chips were thoroughly rinsed with ethanol, dried immediately in a stream of air and stored under argon gas.

The immobilization of either biotinylated unspecific antibodies or unconjugated specific antibodies against CD81 was performed *in situ* by amine coupling according to standard protocols. All solutions were flowed over the sensor surface at a constant speed of 45 $\mu\text{L}/\text{min}$. As a first step PBS was rinsed through the flow cell to reach a stable baseline in SPR signal. In order to calibrate the sensor, PBS spiked with 2 % ethylenglycol was flowed through, triggering a refractive index change of 2×10^{-3} refractive index units (2 mRIU). Afterwards, sodium acetate buffer with a pH-value of 5 was rinsed to adjust the pH for the consecutive amine coupling. The carboxyl groups on the surface were activated by flowing a mixture of 0.4 M EDC and 0.2 M NHS in water for 15 min. After rinsing the surface with sodium acetate buffer, the antibody, diluted in the same buffer at a concentration of 25 $\mu\text{g}/\text{mL}$, was flowed for 10 min. Finally, ethanolamine at 1 M and pH of 8.5 was used to inactivate all remaining carboxyl groups before the buffer was changed again to PBS.

2.5. Direct detection bioassay

Unspecific biotinylated antibodies were immobilized on the sensor surface by amine coupling and followed by the affinity binding of streptavidin and a fluorescently labeled biotin-CTB conjugate (see Fig. 2a). In these measurements PBSTB was used as running buffer and flowed over the sensor surface at a constant speed of 45 $\mu\text{L}/\text{min}$. First streptavidin at a concentration of 5 $\mu\text{g}/\text{mL}$ diluted in PBSTB was rinsed across the surface for 10 min. After washing with PBSTB, the biotinylated CTB that was also labeled with AF647 was pumped through the flow-cell at a concentration of 5 $\mu\text{g}/\text{mL}$.

2.6. Magnetic nanoparticle-enhanced bioassay

The MNP-enhanced bioassay for EV detection was performed as described in our previous work [17] with the addition of the AF647 labeling of the lipid-binding protein CTB. Briefly, 3 μg of mesenchymal stem cell-derived EVs were incubated with 250 ng of biotinylated and AF647-labeled CTB for 30 min at room temperature on a shaker. Then 10 μg of washed MNPs capped with streptavidin were added to the sample and incubated again at the same conditions (see Pre-incubation in Fig. 2b). Afterwards, the MNPs with bound EVs were washed twice with PBSTB and finally re-suspended in 1 mL buffer, leading to a concentration estimate of 3 μg total protein amount of vesicles per mL PBSTB or 520 fM based on the particle count determined by nanoparticle tracking analysis of the input EV sample. As control sample the MNPs were incubated only with the biotinylated and fluorescently labeled CTB. Then the control MNPs or MNP-bound EVs were collected on the sensor surface, which was first functionalized with antibodies specific for CD81, by rinsing the samples across the surface while a magnetic field gradient $\nabla B = 0.10 \text{ T mm}^{-1}$ was applied (see Affinity binding in Fig. 2b). After a 10 min incubation the magnetic field gradient was switched off $\nabla B = 0$ and the sensor surface was washed with

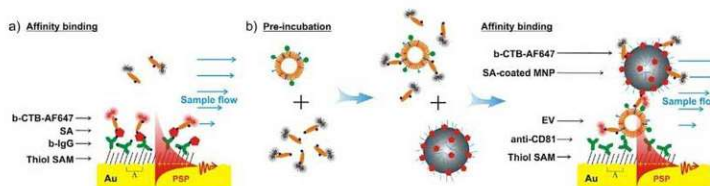


Fig. 2. Schematics of the assays used for testing of the sensing platform. a) The detection assay of medium sized CTB protein based on biotin-streptavidin affinity binding and fluorescent labeling with AF647. b) Extracellular vesicle (EV) assay consisting of the pre-incubation step and collection of the EVs at the sensor surface (MNPs – magnetic nanoparticles, b-CTB-AF647 – biotinylated cholera toxin b-chain conjugated with Alexa Fluor 647, SA – streptavidin, b-IgG – biotinylated unspecific antibody, anti-CD81 – specific antibody for CD81, SAM – self assembled monolayer, Au – gold, PSP – propagating surface plasmon, Λ – period).

2.7. Biosensor Platform for Parallel Surface Plasmon-Enhanced Epifluorescence and Surface Plasmon Resonance Detection

A.T. Reiner et al. / Sensors and Actuators B 257 (2018) 594–601

597

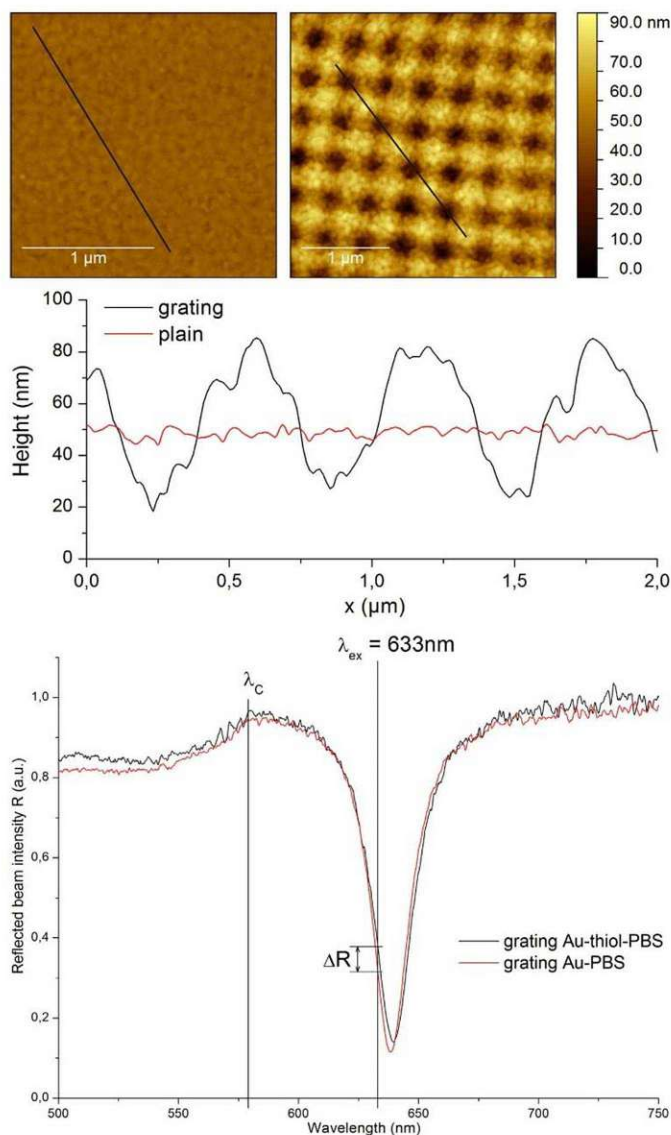


Fig. 3. a) Atomic force microscopy image of the plain (left) and grating (right) sensor surface after the coating with gold (scale bar corresponds to 1 μm). b) Height profiles of the plain and grating sensor surface of the indicated black lines in a). c) Wavelength reflectivity spectra for a normally incident beam at the sensor chip with a clamped flow-cell that was flooded with PBS before and after deposition of a mixed thiol SAM. The reflectivity change ΔR at a fixed wavelength of $\lambda_{ex} = 633$ nm is indicated.

PBSTB for 20 min. Due to the architecture of the setup and flow-cell, flushing shortly with running buffer at high speed was necessary to remove any unspecifically attached MNPs and aggregates.

3. Results and discussion

3.1. Characterization of GC-SPR sensor chips

The prepared sensor chip with or without the crossed grating corrugation carried a conformal 100 nm thick gold film. Atomic

force microscopy of these surfaces presented in Fig. 3a and b reveal that the periodicity of the two overlaid crossed sinusoidal modulations on grating area was about the targeted $\Lambda = 434$ nm, and the corrugation depth was 60 nm. This corrugation depth corresponds to the amplitude of the sinusoidal modulation in each perpendicular direction of about 15 nm. This value was showed before to be optimum for strong diffraction coupling to propagating surface plasmons (PSP) in the red part of the spectrum at an interface between gold and water [13]. The wavelength reflectivity spectra of the grating structured sensor chip, which was clamped to a flow-

2.7. Biosensor Platform for Parallel Surface Plasmon-Enhanced Epifluorescence and Surface Plasmon Resonance Detection

598

A.T. Reiner et al. / Sensors and Actuators B 257 (2018) 594–601

cell and flooded with PBS buffer, was measured by using a system reported before [17]. As visible in Fig. 3c, a narrow dip in the reflectivity spectrum occurs at the wavelength $\lambda_{\text{SPR}} = 638$ nm due to the first diffraction order excitation of PSPs on a periodically corrugated surface. The resonant wavelength λ_{SPR} can be controlled by varying the period Λ which was chosen in order to tune λ_{SPR} slightly above the excitation wavelength $\lambda_{\text{ex}} = 633$ nm that is further used in fluorescence measurements. After forming a mixed thiol SAM at the gold surface, the SPR shifts to a longer wavelength of $\lambda_{\text{SPR}} = 639$ nm due to the increase in the refractive index, as shown in Fig. 3c. The resonance wavelength shift of about 1 nm corresponds to the adlayer thickness of ~ 1 nm [19] which indicates that a compact mixed thiol SAM layer was formed on the gold surface. For the normally incident beam at λ_{ex} this shift is manifested as an increase in the reflectivity ΔR as its wavelength is coincident with the edge of the resonance dip.

In the further experiments, the gold grating structure was used for observing affinity binding events in two modes in parallel by using the optical setup showed in Fig. 1. Firstly, the direct SPR observation of molecular binding was implemented by measuring the reflectivity ΔR changes. An increase in the refractive index is manifested as a red shift in the SPR wavelength λ_{SPR} which is accompanied with an increase in the reflectivity at the chosen wavelength λ_{ex} (tuned to the edge of the resonance). Secondly, the enhanced intensity of the electromagnetic field associated with the resonance excitation of PSPs at λ_{ex} increases the excitation rate of AF647-labeled molecules bound to the surface. In addition, the same structure allows to exploit directional surface plasmon-coupled emission at the AF647 emission wavelength $\lambda_{\text{em}} = 670$ nm. The combination of these two effects offers means for the amplification of the fluorescence – PEF – signal $F(t)$ and *in situ* fluorescence monitoring of affinity binding events at the sensor surface [20]. Our previous work on PEF exploiting a similar grating configuration demonstrated an enhanced collection yield of emitted fluorescence photons at λ_{em} by a factor ~ 4 and about 40-times increased excitation rate at λ_{ex} with respect to a flat gold film [15]. Concerning the leakage losses to the substrate, we assume those are negligible as the fluorescence occurs on a gold film with a thickness of about 100 nm.

Two assays are carried out in order to demonstrate the performance of dual SPR and PEF readout and compare the sensitivity of these two detection modalities. Firstly, the combined SPR and PEF detection was used for the affinity binding of protein molecules in the close proximity to the gold sensor surface. Secondly, the implementation of SPR and PEF measurements for the detection of extracellular vesicles – EVs – is pursued with the aid of magnetic nanoparticles – MNPs – that allow for the efficient collection of such analytes at the sensor surface by application of a magnetic field gradient ∇B . For both experiments and readout modalities sensor chips with a plasmonic grating and a reference flat gold film were used.

3.2. Observation of affinity binding of protein analyte

Fig. 4 shows the SPR and PEF sensorgrams measured upon the preparation of the sensor surface architecture as well as for the affinity binding of biotinylated cholera toxin b chain (b-CTB). As seen in Fig. 2a, the surface of the sensor chip was functionalized with streptavidin (SA) and an additional layer of biotinylated antibody (b-IgG) was used between the gold surface and the SA layer in order to avoid the fluorescence quenching (that occurs at distances < 15 nm due to the Förster energy transfer [21]). The acquired sensorgrams include the fluorescence signal $F(t)$ and SPR reflectivity changes $\Delta R(t)$. For comparison, the molecular binding experiments were performed at two areas on the sensor chip: Fig. 4a shows the

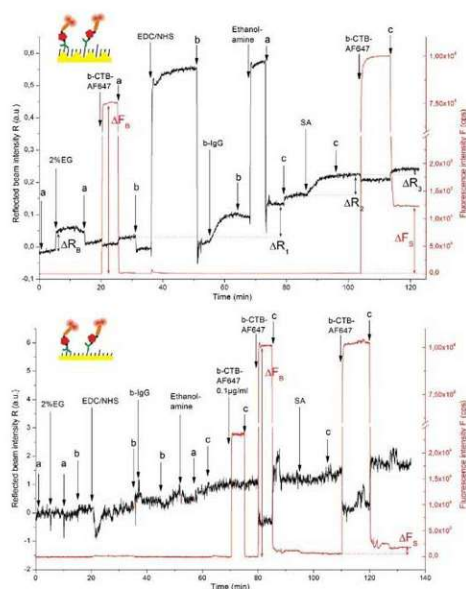


Fig. 4. SPR signal $R(t)$ and fluorescence signal $F(t)$ during amine coupling of a biotinylated unspecific antibody (b-IgG) and affinity binding of fluorescently labeled and biotinylated cholera toxin b-chain (b-CTB-AF647) on a grating gold chip (a) and a reference plain gold chip (b) as control. Insets on the top left show pictograms of the assay and the respective surface used. The signal responses to the affinity binding of molecules at the surface are indicated as ΔR or ΔF for SPR and fluorescence, respectively (a – PBS, b – acetate buffer pH = 5, c – PBSTB, EG – ethyleneglycol, b-IgG dissolved at 25 $\mu\text{g}/\text{mL}$, SA – streptavidin at 5 $\mu\text{g}/\text{mL}$).

sensor response at the grating surface and Fig. 4b at a reference flat area (where SPR is not generated).

Firstly, a baseline in the reflectivity $\Delta R(t)$ and fluorescence $F(t)$ signal was established upon a flow of PBS. Then, a PBS solution spiked with 2 % ethylene glycol was injected, followed by rinsing with PBS. This step was used to calibrate the SPR sensor channel by using the bulk refractive index change above the sensor surface which corresponds to about $\Delta n = 2 \times 10^{-3}$ refractive index units (RIU). The initial increase in the baseline signal, seen in Fig. 4a, didn't affect the results, because only the bulk change was used, and later the signal stabilized. As can be seen in Fig. 4a, this increase in the refractive index ($t = 5$ – 15 min) caused a change in the SPR signal $\Delta R_B = 0.06$ a.u. on a grating surface and no response was observed on a reference flat gold film (as presented in Fig. 4b). Similarly, the fluorescence detection channel was tested by a flow of b-CTB carrying AF647 tags (dissolved at a concentration of 5 $\mu\text{g}/\text{mL}$) over the gold grating (Fig. 4a, $t = 20$ – 25 min) and on a flat gold surface (Fig. 4b, $t = 80$ – 85 min) that did not carry SA moieties. A similar fluorescence signal increase in the range of $\Delta F_0 = 0.75$ – $1 \cdot 10^6$ cps was measured on both areas due to the excitation of fluorophores present in the bulk solution. The fluorescence signal F rapidly dropped back to the original baseline after the rinsing with PBS which indicates weak unspecific sorption to the surface.

Both grating and flat gold areas on the sensor chip were modified by b-IgG with the use of amine coupling followed by affinity binding SA. Fig. 4a shows the obtained sensorgram on a grating surface for the activation of carboxyl groups by a mixture of EDC/NHS ($t = 35$ – 50 min), covalent binding of b-IgG ($t = 55$ – 65 min), passivation of unreacted carboxyl groups with ethanolamine ($t = 70$ – 75 min), and binding of SA ($t = 85$ – 95 min). The same sequence and incubation times were performed in the

2.7. Biosensor Platform for Parallel Surface Plasmon-Enhanced Epifluorescence and Surface Plasmon Resonance Detection

flat area on the sensor chip and respective sensorgrams are presented in Fig. 4b. On the grating surface, the binding of b-IgG and SA increased the reflectivity signal by $\Delta R_1 = 0.10$ a.u. and $\Delta R_2 = 0.06$ a.u., respectively, while no measurable change was observed on a flat gold surface ($t = 20$ – 105 min). The observed reflectivity changes on the SPR grating area of the sensor chip correspond to the surface mass density of 1.2 ng/mm² for IgG and of 0.73 ng/mm² for SA which is comparable to values reported in literature [22,23].

After the immobilization of b-IgG and SA, a solution with CTB conjugated with biotin and AF647 tags (b-CTB-AF647, concentration of 5 μ g/mL) was flowed over the sensor surface for 10 min. On both grating area (Fig. 4a, $t = 105$ – 115 min) and reference flat area (Fig. 4a, $t = 110$ – 120 min) a weak drop in the reflectivity $R(t)$ occurs due to the absorption of the excitation light by fluorophores dissolved in the bulk solution. However, after the rinsing with buffer an increase in reflectivity of $\Delta R_3 = 0.02$ a.u. was measured on a grating while no measurable change occurred on a reference flat gold area. The SPR reflectivity response on the grating area due to b-CTB-AF647 binding showed a signal-to-noise ratio of $\Delta R_3/\sigma(R) \sim 5$. Contrary to the reflectivity measurement, the fluorescence detection channel $F(t)$ showed a much more pronounced signal. After the injection of b-CTB-AF647 a rapid increase in $F(t)$ is observed due to the dominant excitation of fluorophores in the bulk solution. After the 10 min incubation, the surface was rinsed with PBSTB and a strong change in fluorescence signal ΔF_5 caused by the affinity binding becomes visible. The fluorescence change yields $\Delta F_5 = 1.22 \times 10^5$ cps on the grating area and $\Delta F_5 = 1.2 \times 10^3$ cps on the reference flat area. The associated signal-to-noise ratio of fluorescence response on the grating area was ~ 700 . Hence, the accuracy of PEF readout outperforms the SPR on the grating surface by more than two orders of magnitude. Besides allowing for dual fluorescence and SPR detection, the used plasmonic grating enhanced the fluorescence signal originating from the grating surface compared to the flat surface by a factor of ~ 100 , which agrees with earlier published simulations and measurements of PEF using epifluorescence geometry [15].

3.3. Magnetic nanoparticle-enhanced observation of affinity binding of extracellular vesicles

Since the grating coupled SPR configuration and the epifluorescence geometry for PEF readout use only the front side of the sensor chip, there is free space at the back of the chip and flow-cell. This space was used for the applying a magnetic field gradient ∇B for the improved collection of the target analyte, that is affinity bound to MNPs, at the sensor surface. As we reported before, this approach allows to overcome the slow diffusion-limited mass transfer of the analyte [16,24]. Hence we incorporated the MNP-enhanced detection assay for EVs [17] into our optical setup for combined detection of SPR and PEF. It is worth of noting that in this second assay the target analyte, EVs, exhibit a larger size of about 100 nm compared to the previous assay in which a protein with a size of about several nanometers was detected.

In a pre-incubation step, the target EV analyte was first bound to MNPs via the lipid binding protein CTB with biotin tags, as illustrated in Fig. 2b. In order to achieve fluorescence detection of the EVs, CTB molecules were additionally labeled with AF647. For affinity binding of EVs at the sensor surface, the grating and reference flat areas were functionalized with antibodies specific for CD81 which is a protein present on the CTB-binding vesicles [18]. The immobilization of the anti-CD81 at the surface was accompanied with an SPR shift of $\Delta R = 0.13$ a.u. corresponding to the surface mass density of 1.6 ng/mm² (measured on the structured gold surface, sensorgram not shown), which is similar to the results discussed above.

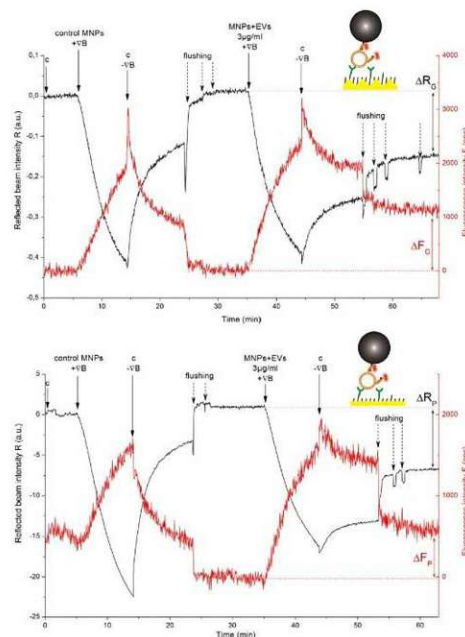


Fig. 5. SPR signal $R(t)$ and fluorescence signal $F(t)$ of a magnetic nanoparticle (MNP)-enhanced assay measurement on a grating gold chip (a) and a reference plain gold chip (b) as control. Insets on the top right show pictograms of the assay and the respective surface used. The application of the magnetic field for collection of MNPs and bound extracellular vesicles (EVs) is indicated as “+ ∇B ” and its removal as “- ∇B ”. The signal responses to the affinity binding of molecules to the surface are indicated as ΔR or ΔF for SPR and fluorescence, respectively (c – PBSTB).

Firstly PBSTB buffer was flowed over the gold grating (Fig. 5a) and reference flat (Fig. 5b) areas carrying anti-CD81 to establish a baseline ($t = 0$ – 5 min). Then the sensor surface was exposed to control MNPs in order to test for unspecific binding to the sensor surface (Fig. 5a and b, $t = 5$ – 15 min). These sensorgrams show that the SPR signal R decreased and fluorescence intensity F increased upon the accumulation of MNPs reacted with CTB-AF647 conjugate at the sensor surface, to which the MNP-CTB-AF647 mix without target EV analyte was pulled by the magnetic field gradient ∇B applied.

Interestingly, the SPR signal decrease is more pronounced on the reference plain gold area of the sensor chip than on that with grating. The reason is that the accumulated MNPs (with the size of about 200 nm) form a layer on the sensor surface that is substantially thicker than the probing depth of PSPs (< 100 nm). Therefore, the decrease in the reflected intensity is mostly due to the scattering and absorption by MNPs. On the flat gold surface the beam passes twice through this layer while on the grating surface only once as the majority of its intensity is transferred to the PSPs. Furthermore, MNPs in contact with the gold surface enhance the refractive index leading to a SPR signal increase R on the grating surface that counteracts the absorption of light intensity by the MNPs. In our previous work on the MNP-enhanced GC-coupled SPR biosensor [17] we monitored the wavelength reflectivity spectra over time and hence were able to discriminate the influence of light absorption and refractive index change occurring in vicinity to the gold surface. However, since we use a monochromatic light source for both fluorescence excitation and SPR measurements, this approach is not applicable for the parallel SPR and PEF measurements. The

2.7. Biosensor Platform for Parallel Surface Plasmon-Enhanced Epifluorescence and Surface Plasmon Resonance Detection

600

A.T. Reiner et al. / Sensors and Actuators B 257 (2018) 594–601

Table 1

Comparison of the signal-to-noise ratio obtained for the surface functionalization and the tested assays in the reflectivity and fluorescence channel on grating and plain gold sensing areas.

Assay	Readout type	Grating gold	Plain gold
b-IgG2b immobilization	SPR	23 ± 9 ^a	–
Anti-CD81 immobilization	SPR	40 ± 12 ^b	–
b-CTB-AF647 detection	SPR	5	–
	Fluorescence	700	18
MNP-enhanced detection of EVs	SPR	44	76
	Fluorescence	18	12

^a mean and standard deviation over 2 experiments.

^b mean and standard deviation over 3 experiments.

fluorescence signal change was observed at a similar level both on grating and plain gold as it mostly originates from a distance longer than the PSP probing depth and thus it is not plasmonically amplified.

After switching off the magnetic field gradient ∇B and rinsing the flow-cell with PBSTB (Fig. 5a and b, $t=15\text{--}35$ min) the unbound MNPs were quickly washed away. Due to the architecture of the instrument, flushing of the flow cell with running buffer was required to remove all unbound MNPs. These flushing steps are indicated in the sensorgrams by dashed arrows and present as sharp signal shifts. After flushing, SPR and PEF signals stabilized at the same level as before the MNP incubation, indicating that there was no unspecific binding to the functionalized surfaces.

Next the MNPs pre-incubated with the target EV analyte (at an estimated concentration of 3 μg total protein/mL or 520 fM) and CTB (conjugated with biotin and AF647) were collected at the sensor surface in the same manner as before for the control MNPs (Fig. 5a and b, $t=35\text{--}45$ min). Again a similar decrease in SPR was observable, but after switching off the magnetic field gradient and flushing with PBSTB (Fig. 5a and b, $t=45\text{--}65$ min) a reflectivity change of $\Delta R_G = 0.16$ a.u. on the grating gold area and $\Delta R_P = 7.72$ a.u. on the plain gold area was measured due to the affinity binding of EVs carried by MNPs to immobilized anti-CD81 antibodies. Since a decrease in the reflectivity R is observed on both grating and plain gold surfaces, it can be concluded that mainly the effect of light absorption and scattering by the MNPs is responsible for the signal change. Therefore, on the grating exhibiting SPR the reflectivity increase due to the analyte capture is overrun by the reflectivity decrease due to the MNPs. This counteraction also translates in the signal-to-noise ratio that is 1.7-fold lower for the grating gold (~ 44) compared to the plain gold (~ 76), see overview in Table 1. Hence the measurement on plain gold, which detects only light absorption by MNPs, performed better. In order to make use of the SPR signal change in addition to the light absorption and thus reaching higher signal-to-noise ratios, the coupling resonance needs to be tuned (e.g. by varying the grating period Λ) in a way that the resonance wavelength λ_{SPR} is shorter than the excitation wavelength λ_{ex} , resulting in a signal decrease upon binding of the target analyte to the sensor surface. It is worth of noting that a similar approach was adopted for the angular modulation of GC-SPR [24].

In the fluorescence channel a signal increase of $\Delta F_G = 1100$ cps and $\Delta F_P = 590$ cps for the grating and the plain gold chip, respectively, were observed due to binding of MNP-bound EVs to the sensor surface. The signal-to-noise ratio of ~ 18 on the grating gold and ~ 12 on the plain gold was reached with this assay, which implies a small signal improvement for the PSPs coupling with fluorophores. This also translates to the relatively small fluorescence enhancement of only 2-fold by PSPs. There are several explanations for the weak performance of the fluorescence channel for this type of assay. First, the monitored reflected beam intensity indicates that the binding of MNPs to the surface is accompanied with strong light absorption. This absorption likely decreases the intensity of light at the excitation wavelength λ_{ex} as well as at the emission

wavelength λ_{em} . The MNP-induced absorption at λ_{ex} leads to a less efficient excitation of PSPs, which again leads to lower levels of fluorescence signal amplification. Similarly for λ_{em} this effect disrupts the surface plasmon-coupled emission. In addition, the fluorescence photons emitted from a volume between gold and MNPs (see Fig. 2b) are partially blocked by these objects on both flat and grating surfaces.

Since the fluorescence enhancement in the grating coupled SPR and PEF sensor is inhibited by the presence of MNPs, a possible solution for signal improvement would be to remove the MNPs after the collection of the target analyte on the sensor surface. This could be achieved by dissociating the binding of the biotinylated CTB molecules and the SA coated MNPs and will be the subject of further studies. One solution could be to use desthiobiotin for the binding of EVs to the SA-MNPs. This type of biotin has a lower affinity to SA and therefore MNPs could be dissociated by replacement of desthiobiotin with biotin [23,25]. As free biotin has a higher affinity to SA compared to surface bound biotin [26], another very similar approach is to replace the biotin that is bound to the MNPs by addition of a high concentration of free biotin in solution. Furthermore, the sensitivity of the MNP-based assay for EV-detection could be improved by exploiting the surface plasmon-enhanced light scattering caused by MNPs, as it was demonstrated by Yang et al. [27].

4. Conclusions

Plasmonic grating was implemented for the combined label-free surface plasmon resonance (SPR) and plasmonically enhanced fluorescence (PEF) measurement of the affinity binding at the sensor surface by using epifluorescence geometry for the first time. These measurements can be performed on the same spot in parallel and in real-time and they allow for facile implementing magnetic nanoparticle-enhanced assays. The monitoring of the affinity binding of a medium sized protein that was labeled with Alexa Fluor 647 dyes showed a ~ 100 -fold fluorescence enhancement on the gold grating surface compared to a reference flat gold surface. The PEF readout outperformed SPR for this assay when the molecular binding occurs at distances of 15–20 nm from the metallic sensor surface and the respective signal-to-noise ratio was ~ 140 -fold higher. The reported geometry allows for the incorporation of magnetic nanoparticle (MNP)-enhanced assays for the detection of larger analytes, which exhibit slow diffusion that hinders their affinity binding to the sensor surface. The combined PEF and SPR readout was utilized for the detection of extracellular vesicles (EVs) with the size of about hundred nanometers. The MNPs offered means for efficient delivery and affinity binding of the target EV analyte at the sensor surface, but they substantially hindered the performance of the fluorescence-based assay. The SPR detection channel outperformed the PEF in the MNP-based assay and provided a 2.4-fold higher signal-to-noise ratio. For efficient PEF detection that takes advantage of MNPs, reversible coupling mechanism for the capture of the target analyte on MNPs should be

2.7. Biosensor Platform for Parallel Surface Plasmon-Enhanced Epifluorescence and Surface Plasmon Resonance Detection

adopted in order to detach them after the delivery and affinity binding of the target analyte at the sensor surface.

Conflict of interest

None.

Acknowledgments

ATR was supported by the Austrian Federal Ministry for Transport, Innovation and Technology (GZ BMVIT-612.166/0001-III/1/2010) via the International Graduate School Bio-Nano-Tech – a joint Ph.D. program of the University of Natural Resources and Life Sciences Vienna (BOKU), the Austrian Institute of Technology (AIT), and the Nanyang Technological University (NTU). SF acknowledges support from the European Union's Horizon 2020 Research and Innovation Programme under Grant agreement No. 633937, project ULTRAPLACAD.

References

- [1] M. Li, S.K. Cushing, N.Q. Wu, Plasmon-enhanced optical sensors: a review, *Analyst* 140 (2015) 386–406.
- [2] J.R. Lakowicz, K. Ray, M. Chowdhury, H. Szmajnski, Y. Fu, J. Zhang, et al., Plasmon-controlled fluorescence: a new paradigm in fluorescence spectroscopy, *Analyst* 133 (2008) 1308–1346.
- [3] A. Kinkhabwala, Z.F. Yu, S.H. Fan, Y. Avlasevich, K. Mullen, W.E. Moerner, Large single-molecule fluorescence enhancements produced by a bowtie nanoantenna, *Nat. Photonics* 3 (2009) 654–657.
- [4] J. Dostalek, W. Knoll, Biosensors based on surface plasmon-enhanced fluorescence spectroscopy, *Biointerphases* 3 (2008) Fd12–Fd22.
- [5] M. Bauch, K. Toma, M. Toma, Q.W. Zhang, J. Dostalek, Plasmon-Enhanced fluorescence biosensors: a review, *Plasmonics* 9 (2014) 781–799.
- [6] R. Gambari, G. Feriotto, C. Rutigliano, N. Bianchi, C. Mischiati, Biospecific interaction analysis (BIA) of low-molecular weight DNA-binding drugs, *J. Pharmacol. Exp. Ther.* 294 (2000) 370–377.
- [7] J. Homola, Surface plasmon resonance sensors for detection of chemical and biological species, *Chem. Rev.* 108 (2008) 462–493.
- [8] T. Liebermann, W. Knoll, P. Sluka, R. Herrmann, Complement hybridization from solution to surface-attached probe-oligonucleotides observed by surface-plasmon-field-enhanced fluorescence spectroscopy, *Colloid Surf. A* 169 (2000) 337–350.
- [9] Y. Wang, A. Brunsen, U. Jonas, J. Dostalek, W. Knoll, Prostate specific antigen biosensor based on long range surface plasmon-Enhanced fluorescence spectroscopy and dextran hydrogel binding matrix, *Anal. Chem.* 81 (2009) 9625–9632.
- [10] F. Yu, B. Persson, S. Lofas, W. Knoll, Attomolar sensitivity in bioassays based on surface plasmon fluorescence spectroscopy, *J. Am. Chem. Soc.* 126 (2004) 8902–8903.
- [11] G. Stengel, W. Knoll, Surface plasmon field-enhanced fluorescence spectroscopy studies of primer extension reactions, *Nucleic Acids Res.* 33 (2005) e69.
- [12] J. Breault-Turcot, H.P. Poirier-Richard, M. Couture, D. Pelechacz, J.F. Masson, Single chip SPR and fluorescent ELISA assay of prostate specific antigen, *Lab Chip* 15 (2015) 4433–4440.
- [13] J. Dostalek, J. Homola, M. Miler, Rich information format surface plasmon resonance biosensor based on array of diffraction gratings, *Sens. Actuators B Chem.* 107 (2005) 154–161.
- [14] X.Q. Cui, K. Tawa, K. Kintaka, J. Nishii, Enhanced fluorescence microscopic imaging by plasmonic nanostructures: from a 1D grating to a 2D nanohole array, *Adv. Funct. Mater.* 20 (2010) 945–950.
- [15] M. Bauch, S. Hageneder, J. Dostalek, Plasmonic amplification for bioassays with epi-fluorescence readout, *Opt. Express* 22 (2014) 32026–32038.
- [16] Y. Wang, J. Dostalek, W. Knoll, Magnetic nanoparticle-enhanced biosensor based on grating-coupled surface plasmon resonance, *Anal. Chem.* 83 (2011) 6202–6207.
- [17] A.T. Reiner, N.G. Ferrer, P. Venugopalan, R.C. Lai, S.K. Lim, J. Dostalek, Magnetic nanoparticle-enhanced surface plasmon resonance biosensor for extracellular vesicle analysis, *Analyst* (2017), <http://dx.doi.org/10.1039/c7an00469a>.
- [18] R.C. Lai, S.S. Tan, R.W. Yeo, A.B. Choo, A.T. Reiner, Y. Su, et al., MSC secretes at least 3 EV types each with a unique permutation of membrane lipid, protein and RNA, *J. Extracellular Vesicles* 5 (2016) 29828.
- [19] P. Adam, J. Dostalek, J. Homola, Multiple surface plasmon spectroscopy for study of biomolecular systems, *Sens. Actuators B Chem.* 113 (2006) 774–781.
- [20] S. Hageneder, M. Bauch, J. Dostalek, Plasmonically amplified bioassay – Total internal reflection fluorescence vs. epifluorescence geometry, *Talanta* 156–157 (2016) 225–231.
- [21] K. Sergelen, S. Fossati, A. Turupcu, C. Oostenbrink, B. Liedberg, W. Knoll, et al., Plasmon field-Enhanced fluorescence energy transfer for hairpin aptamer assay readout, *ACS Sens.* 2 (2017) 916–923.
- [22] J. Voros, The density and refractive index of adsorbing protein layers, *Biophys. J.* 87 (2004) 553–561.
- [23] W. Knoll, M. Zizlsperger, T. Liebermann, S. Arnold, A. Badia, M. Liley, et al., Streptavidin arrays as supramolecular architectures in surface-plasmon optical sensor formats, *Colloid Surf. A* 161 (2000) 115–137.
- [24] Y. Wang, W. Knoll, J. Dostalek, Bacterial pathogen surface plasmon resonance biosensor advanced by long range surface plasmons and magnetic nanoparticle assays, *Anal. Chem.* 84 (2012) 8345–8350.
- [25] J.D. Hirsch, L. Eslamizadeh, B.J. Filanowski, N. Malekzadeh, R.P. Haugland, J.M. Beechem, Easily reversible desthiobiotin binding to streptavidin, avidin, and other biotin-binding proteins: uses for protein labeling detection, and isolation, *Anal. Biochem.* 308 (2002) 343–357.
- [26] V.H. Perez-Luna, M.J. O'Brien, K.A. Opperman, P.D. Hampton, G.P. Lopez, L.A. Klumb, et al., Molecular recognition between genetically engineered streptavidin and surface-bound biotin, *J. Am. Chem. Soc.* 121 (1999) 6469–6478.
- [27] C.T. Yang, L. Wu, X.H. Liu, N.T. Tran, P. Ba, B. Liedberg, et al., Exploiting surface-Plasmon-Enhanced light scattering for the design of ultrasensitive biosensing modality, *Anal. Chem.* 88 (2016) 11924–11930.

Biographies

Agnes T. Reiner is a PhD candidate at the University for Natural Resources and Life Sciences in Vienna and the Nanyang Technological University in Singapore. She works at the AIT-Austrian Institute of Technology in Vienna and her research interests are extracellular vesicles, cancer diagnosis, and plasmonic biosensors.

Stefan Fossati is a PhD student at Vienna University of Technology and works at AIT-Austrian Institute of Technology in Vienna, Austria. His research focuses on optical biosensors and plasmonic nanostructures.

Jakub Dostalek currently serves as senior scientist at AIT-Austrian Institute of Technology in Vienna, Austria. He obtained his PhD degree from Charles University in Prague in 2006 and his research focuses on guided wave optics, plasmonics, optical sensors for medical diagnostics, and polymer-based biointerfaces.

2.8. Multiresonant Plasmonic Nanostructure for Ultrasensitive Fluorescence Biosensing

The following publication is reprinted under the Creative Commons Attribution 4.0[§] (CC BY 4.0) Public license.

Stefan Fossati, Simone Hageneder, Samia Menad, Emmanuel Maillart und Jakub Dostalek
Multiresonant plasmonic nanostructure for ultrasensitive fluorescence biosensing.
Nanophotonics **9**, 3673–3685 (2020). <https://doi.org/10.1515/nanoph-2020-0270>

© 2020 The Authors, published by de Gruyter

Surface plasmon resonance has proven to be a valuable tool for biochemical analysis. Supporting real-time label-free observation of affinity binding kinetics by monitoring the detuning of the plasmon resonance yields valuable information on the interaction between molecules.⁸² Furthermore, fluorescent labels attached to one component of the assay are routinely employed to improve sensitivity by orders of magnitude by plasmon enhanced fluorescence.⁴⁵ However, fluorescence assays allow only the observation of the last, labeled step in an assay. Combining real-time monitoring of the *in-situ* surface functionalization using SPR with a fluorescence readout channel enables more advanced detection schemes and molecular interaction studies.¹⁵⁵ To this date, the most widely used implementation of SPR is the ATR configuration, utilizing a bulky prism to couple the excitation beam to the surface plasmon, requiring a very specific optical readout configuration. In this chapter, a different approach for the excitation and observation of plasmonic absorption and fluorescence is followed. Using a corrugated metallic surface allows to excite surface plasmons by grating coupling and observation of fluorescence in an epifluorescence reader configuration. This optical configuration is used in a wide range of bioanalytical devices, including microarray readers, microplate readers, and even fluorescence microscopes. Therefore, this approach promises to extend the analytical capabilities of such devices by using tailored plasmonic substrates, which can be made by scalable manufacturing

[§] <http://creativecommons.org/licenses/by/4.0/>

technology, while achieving femtomolar sensitivity for multiplexed assays in an imaging format.

This work was mainly driven by Stefan Fossati, who developed the multi-diffractive grating architecture, carried out optimizations by FDTD simulations and the nanofabrication of the substrates. He furthermore developed the optical instrument and supervised the software development as well as fluorescence experiments. Samia Menad and Emmanuel Maillard contributed large parts of the measurement software. Simone Hageneder developed the bioassays and carried out parts of the experiments. The project was carried out under the supervision of Jakub Dostalek.

Supporting information to this article is included in the appendix, section 5.6.

Research article

Stefan Fossati, Simone Hageneder, Samia Menad, Emmanuel Maillart and Jakub Dostalek*

Multiresonant plasmonic nanostructure for ultrasensitive fluorescence biosensing

<https://doi.org/10.1515/nanoph-2020-0270>
Received May 6, 2020; accepted July 11, 2020

Abstract: A novel metallic nanostructure for efficient plasmon-enhanced fluorescence readout of biomolecular binding events on the surface of a solid sensor chip is reported. It is based on gold multiperiod plasmonic grating (MPG) that supports spectrally narrow plasmonic resonances centered at multiple distinct wavelengths. They originate from diffraction coupling to propagating surface plasmons (SPs) forming a delocalized plasmonic hotspot associated with enhanced electromagnetic field intensity and local density of optical states at its surface. The supported SP resonances are tailored to couple with the excitation and emission transitions of fluorophores that are conjugated with the biomolecules and serve as labels. By the simultaneous coupling at both excitation and emission wavelengths, detected fluorescence intensity is enhanced by the factor of 300 at the MPG surface, which when applied for the readout of fluorescence immunoassays translates to a limit of detection of 6 fM within detection time of 20 min. The proposed approach is attractive for parallel monitoring of kinetics of surface reactions in microarray format arranged on a macroscopic footprint. The readout by epi-fluorescence geometry (that inherently relies on low numerical aperture optics for the imaging of the arrays) can particularly take advantage of the reported MPG. In addition, the proposed MPG nanostructure can be

prepared in scaled up means by UV-nanoimprint lithography for future practical applications.

Keywords: fluorescence; multidiffractive gratings; optical biosensor; plasmonics; ultrasensitive assays.

1 Introduction

In a variety of optical biosensors, plasmonic nanomaterials become routinely employed for direct label-free analysis of biomolecules based on the measurement of specific binding-induced refractive index changes [1, 2]. In addition, we witness rapid progress in the implementation of plasmonic nanomaterials for the amplification of weak optical spectroscopy signal in other biosensor modalities relying on fluorescence, Raman scattering, and infrared absorption spectroscopy [3–5].

Plasmon-enhanced fluorescence (PEF) spectroscopy takes advantage of the increased intensity and local density of optical states accompanied with the resonant excitation of surface plasmons (SPs). These resonances originate from collective oscillations of electron density and associated electromagnetic field at the surface of metallic nanostructures. The coupling of SPs with fluorophores allows their lifetime, quantum yield, excitation rate, and far-field angular distribution of the emitted light to be efficiently manipulated [6–8]. These phenomena can be tailored to enhance the sensitivity of fluorescence-based assays where fluorophores are used as labels. Then, plasmonic nanostructures are deployed at the sensor surface to increase the signal-to-noise ratio of detected fluorescence signal that is attributed to the capture of the target analyte from the analyzed liquid sample. In general, detected fluorescence intensity can be enhanced by the combined coupling of SPs with fluorophores at their absorption λ_{ab} and emission λ_{em} wavelengths [9, 10]. This interaction can (i) increase the excitation rate at λ_{ab} , (ii) improve extraction yield of fluorescence light from the sensor surface by narrowing the angular emission range at λ_{em} towards the detector, and (iii) enhance quantum yield. The fact that the coupling with SPs occurs locally within their confined near-field allows only

*Corresponding author: **Jakub Dostalek**, Biosensor Technologies, Austrian Institute of Technology GmbH, Konrad-Lorenz-Straße 24, Tulln 3430, Austria; and FZU-Institute of Physics, Czech Academy of Sciences, Na Slovance 2, Prague 182 21, Czech Republic.
E-mail: Jakub.Dostalek@ait.ac.at. <https://orcid.org/0000-0002-0431-2170>

Stefan Fossati and Simone Hageneder: Biosensor Technologies, Austrian Institute of Technology GmbH, Konrad-Lorenz-Straße 24, Tulln 3430, Austria, E-mail: Stefan.Fossati@ait.ac.at (S. Fossati), Simone.Hageneder@ait.ac.at (S. Hageneder). <https://orcid.org/0000-0002-1109-0035> (S. Fossati)

Samia Menad and Emmanuel Maillart: Horiba France SAS, 14, Boulevard Thomas Gobert - Passage Jobin Yvon CS 45002, Palaiseau 91120, France, E-mail: samia.menad@gmail.com (S. Menad), emmanuel.maillart@horiba.com (E. Maillart)

Open Access. © 2020 Stefan Fossati et al., published by de Gruyter.  This work is licensed under the Creative Commons Attribution 4.0 Public License.

the fluorescence signal emitted in the close proximity to the sensor surface without increasing the background signal originating from the bulk to be selectively amplified.

The coupling of SPs with fluorophores scales with their near-field intensity strength, which is limited by Ohmic losses causing damping. Metallic nanostructures supporting SPs with decreased damping can provide stronger near-field intensity enhancement, which manifests itself as a spectrally narrower surface plasmon resonance (SPR) [11–13]. However, if the spectral window where SPs are resonantly excited becomes narrower than the Stokes shift of the used fluorophores, the combined coupling at absorption λ_{ab} and emission λ_{em} bands is not possible, potentially leading to a decrease of fluorescence enhancement.

Metallic nanoparticles supporting localized surface plasmons (LSPs) typically exhibit spectrally broad resonances that can be tuned to spectrally overlap with both λ_{ab} and λ_{em} of commonly used organic fluorophores [14]. This, however, holds true only for isolated or randomly arranged metallic nanoparticles, where the excitation of LSPs with an optical wave traveling from the far-field is weakly angular dependent. Periodic arrangement of nanoparticles allows narrowing SPR spectral bands by diffraction coupling of LSPs on individual nanoparticles giving rise to delocalized lattice modes that exhibit sharp dispersive spectral features [11, 12, 15–17]. A wide range of such nanoparticle architectures has been developed to control fluorescence [18–21], allowing the detection of even single molecules [22]. These systems nevertheless are typically suitable for research, and their utilization to practical applications is hampered by the requirement of nanoscale control of emitter placement at the metallic nanoparticle and complex techniques needed for their manufacturing. Besides LSPs, propagating surface plasmon (PSP) modes can be excited on continuous metal films. They exhibit less confined near-field profile compared to LSPs and are dispersive over a broad spectral range. When interacting with fluorophores, the dispersive nature of PSPs can be even exploited to angularly separate emission from fluorophores exhibiting different λ_{em} to distinct angles in the far-field by using the SP-coupled emission [23]. On continuous metal films, periodic corrugation can provide additional momentum in order to diffraction phase-match optical waves propagating in the far field with PSPs. These Bloch-like modes are delocalized along the surface with angular dispersive and narrow spectral characteristics, allowing the excitation of fluorophores at a certain angle, facilitating emission via PSPs, and outcoupling to propagating modes at different angles [24–26]. In order to overlap narrow plasmon resonances with multiple spectral windows, metallic nanoparticle assemblies supporting

hybrid SP modes can be used [27, 28]. They are formed by the coupling of multiple metallic nanostructures, and architectures supporting both LSP and PSP modes have been studied [29, 30]. These systems support multiple hybrid SP modes at distinct wavelengths; however, they typically confine electromagnetic near-field intensity at different locations on the structure and thus do not allow for the simultaneous probing of species placed in their proximity at respective spectral windows.

Plasmonic nanostructures can be prepared by a range of lithography techniques providing different level of control over their properties. While large areas of homogeneous flat metallic films are easily prepared by vapor deposition techniques [31], their optical properties are mostly determined by the choice of material. Metal island films, often created by vapor deposition [32], can support LSP modes with local hotspots exhibiting broad size distribution and lack of order. Colloidal lithography techniques allow the preparation of domains with ordered patterns of metallic nanostructures [33]. Electron beam lithography is often employed to create almost arbitrary morphology of metallic nanostructures with high precision [34]. However, it is still considered as complex and not well suited for cost-efficient large-scale production. Laser interference lithography (LIL), a method where interference pattern formed by overlapping coherent light beams is transferred to a photosensitive material, allows us to quickly and relatively inexpensively structure large areas with periodic corrugation such as holographic gratings, nanohole, or nanoparticle arrays [35, 36].

Nanoimprint lithography (NIL) represents another promising approach to address scalability in nanofabrication. Molds carrying a structure that can be prepared by more complex methods are then employed to repeated transfer of the target motives into an imprint resist [37]. The precise replication of patterns with feature size below 20 nm [38] paved the way towards the application in modern semiconductor manufacturing. In parallel, high-throughput NIL methods are developed to produce nanostructured surfaces, even on flexible substrates [39].

Herein, we report a new approach to plasmonic nanostructures supporting multiple tunable resonances with delocalized plasmonic hotspot along the surface and we tailor them for the simultaneous coupling with fluorophores at both their absorption and emission bands. It is based on multiperiod plasmonic gratings (MPGs) that are engineered to diffractively couple near-field SP field to far-field optical waves traveling at desired wavelengths and directions. The optical surfaces are prepared by UV-LIL that is combined with UV-NIL in order to open the door for potential scaled up preparation. The developed type of

MPGs is particularly beneficial for fluorescence biosensors with array detection format and *in situ* readout of reaction kinetics that relies on inherently low numerical aperture optics for the excitation and collecting of fluorescence light. We show that the developed structure offers strong enhancement of fluorescence signal by a factor of 300, enables the monitoring of affinity binding that is not masked by the bulk signal, and, when applied to an immunoassay, allows rapid detection of the target analyte at concentrations as low as 6 fM on multiple spots in microarray format.

2 Materials and methods

2.1 Materials

Microscope slides made of BK7 glass were purchased from Carl Roth (Germany) and used as substrates. The positive photoresist MICROPOSIT S1805 G2 and its developer AZ303 were bought from Microresist (Karlsruhe, Germany), and the nanoimprint resist Amonil MMS10 was acquired from Amo GmbH (Berlin, Germany). The silicone kit DOWSIL Sylgard 184 was purchased from Conrad GmbH (Wels, Austria). Dithiols with carboxylic head group (SPT-0014A6, COOH-OEG6-dithiol) and oligoethylene glycol head group (SPT-0013, OH-OEG3-dithiol) were from SensoPath Technologies (Bozeman, MT, USA). Antimouse IgG conjugated with Alexa Fluor 790 (AF790) came from Thermo Fisher Scientific-Life Technologies (Eugene, OR, USA). Phosphate buffered saline (PBS), 1-ethyl-3-(3-dimethylaminopropyl) carbodiimide (EDC), N-hydroxysuccinimide (NHS), ethanolamine, Tween 20, bovine serum albumin (BSA) and purified mouse IgG were acquired from Sigma-Aldrich Handels-GmbH (Vienna, Austria).

2.2 Preparation of MPG nanostructures

UV-LIL [40] was employed for the preparation of MPG nanostructures. Briefly, a laser beam with $\lambda = 325$ nm was collimated and expanded in order to perform the recording over an area of 1 cm^2 with homogenous intensity of about $15 \mu\text{W}/\text{cm}^2$. A glass or Si wafer substrate coated with a 500-nm thick film of positive photoresist S1805 was mounted into a Lloyd's mirror configuration to record sinusoidally modulated field intensity formed by the interference of two parts of the beam – one directly impinging at the resist layer and that other reflected by a UV mirror (Figure S1A). The period of the modulation Λ was controlled by changing the angle of the interfering beams θ . Multiple subsequent exposures of different periods Λ were performed in order to yield the target structure. In this work, the exposure of the period of $\Lambda_1 = 564$ nm was followed by two additional orthogonal exposures carried out with an interference field period set to $\Lambda_2 = \Lambda_3 = 583$ nm. Between each recording step, the substrate with resist layer was rotated by an azimuthal angle φ along the axis perpendicular to its surface. Next, the structure was etched into the photoresist by a developer and its topography was cast to polydimethylsiloxane (PDMS), which was used as a working stamp for the preparation of multiple copies by UV-NIL (Figure S1B). The PDMS was cured at room temperature for

48 h. For a small reduction of the pattern period, it is possible to cure the stamp at an elevated temperature of 60°C . The thermal shrinking of the cured working stamp after the cooling to room temperature reduces the pattern period Λ by about 1%. To prepare the plasmonic sensor chips by UV-NIL, glass slides were coated with a 130-nm layer of the nanoimprint resist Amonil MMS10, contacted with the working stamp, allowed to rest for 5 min, and were cured by UV cross-linker Bio-Link (Vilber Lourmat, Collégien, France) with 2 J cm^{-2} irradiation dose at 365 nm (Figure S1C). The PDMS stamp was finally demolded, and the corrugated glass substrates with casted MPG topography on their top were subsequently coated with 4-nm-thick Cr and 100-nm-thick Au layers by vacuum thermal evaporation instrument Auto306 from HHV Ltd (Crawley, UK).

2.3 Characterization of MPG nanostructures

The topography of MPG nanostructures was studied with atomic force microscope PicoPlus from Molecular Imaging (Arizona, USA). The spectrum of PSP modes that are optically excited on the gold-coated MPG structures was observed from reflectivity measurements with the structure clamped against a transparent flow cell that was flooded with water. The polychromatic light beam of a halogen lamp was collimated, polarized with a Glan polarizer, and made impinging at the MPG structure. For a beam incident normal to the surface, a beam splitter cube (CCM1-BS013 from Thorlabs, New Jersey, USA) was used to separate the incident and reflected beams. The reflected light beam was collected by an optical fiber and brought at the input of a spectrograph (Shamrock 303i from, Andor, New York, USA). As a reference, a flat gold-coated glass substrate was used.

2.4 Sensor chip and surface modification

Immediately after the deposition of thin metallic layers, the substrates were incubated in an ethanolic thiol solution of 0.1 mM COOH-OEG6-dithiol and 0.9 mM OEG3-dithiol overnight in order to form a self-assembled monolayer (SAM). After rinsing with ethanol and drying with a stream of compressed air, the prepared samples were stored in argon atmosphere at room temperature until further use to ensure their stability over weeks [41].

2.5 Optical reader

Readout of the binding of biomolecules labeled by a fluorophore on the sensor chip with MPG nanostructure and the investigation of the enhancement strength provided by this nanostructure were carried out using a setup with epi-illumination fluorescence geometry. It was designed to image an area of 4×4 mm on the sensor chip with MPG at a scientific EM-CCD camera (iXon 885K from Andor, Belfast, UK) by the optical system with a numerical aperture of $\text{NA} = 0.2$. A monochromatic beam emitted from diode laser iBeam Smart 785S with $\lambda_{\text{ex}} = 785$ nm from TOptica, Photonics AG (Gräfelfing, Germany) passed through a laser cleanup filter (BP λ_{ex} , LLO1-785 from Semrock, Rochester, NY, USA) and a spatial filter consisting of a $60\times$ microscope objective, a $40 \mu\text{m}$ pinhole, and recollimation lens (lens 1, AC-254-40-B from Thorlabs, Newton, NJ, USA). The central part of the expanded and collimated beam was polarized (POL,

LPVIS100 from Thorlabs, Newton, NJ, USA) and directed towards the sample by a dichroic mirror (DM) module. It comprised a DM (Di02-R785 from Semrock, Rochester, NY, USA) oriented by 45° with respect to the axis of the module, and its central area with 2-mm projected diameter was coated with 100-nm-thick gold serving as a central mirror (CM). The excitation beam at the wavelength of $\lambda_{\text{ex}} = 785$ nm was focused at the CM by a lens (lens 2, AC-254-35-B from Thorlabs, Newton, NY, USA), and the reflected beam was recollimated with another lens (lens 3, AC-254-40-B from Thorlabs, Newton, NJ, USA). The collimated excitation beam was made normally incident at the sensor chip surface that carried MPG nanostructure. The distance between the DM module and the sensor chip was set to the focal distance of lens 3. In this configuration, the reflected excitation beam λ_{ex} was focused again at the CM and reflected away from the detector arm. Contrary to the excitation beam λ_{ex} , the fluorescence light emitted from the sensor chip surface at longer wavelength λ_{em} propagated at deviated angles and thus the majority of its intensity passed through the DM module towards the detector. The surface of the sensor chip was imaged at the detector plane by an imaging lens (lens 4, AC-254-80-B from Thorlabs, Newton, NJ, USA). In the detector arm, a notch filter (NF03-785E-25 from Semrock, Rochester, NY, USA) and a fluorescence bandpass filter (FF01-810/10-25 from Semrock, Rochester, NY, USA) were used to suppress the intensity of the excitation beam that leaked through the dichroic filter with the CM. Fluorescence images were acquired with a scientific EM-CCD camera operated at -70°C and with EM gain set to 100. In-house-developed LabView software (LabView 2015, NI, Austin, TX, USA) was used to acquire image series and it comprised the data processing for determining the average signals on arrays of preselected spots and their progression over time.

2.6 Bioassay

For testing the analytical performance that is advanced by using sensor chips with the MPG nanostructure, a transparent flow cell was clamped on their top and the assembly was loaded to an optical fluorescence reader system. The flow cell consisted of a fused silica glass substrate with drilled input and output ports and a thin gasket cut from a 100- μm -thick PDMS sheet. The volume of the used flow chamber defined by the PDMS gasket was of several microliters, and aqueous samples were transported through the flow cell by using a peristaltic pump (from Ismatec, Switzerland).

The sensor chip carried a gold layer modified by a thiol SAM with carboxyl (COOH) and oligoethylene glycol (OEG) groups. In order to covalently couple protein ligands carrying amine groups, the COOH moieties on the thiol SAM were activated by a flow of an aqueous solution with 75 mg mL^{-1} EDC and 21 mg mL^{-1} NHS for 15 min. After rapid rinsing with acetate buffer of pH 4, mouse IgG dissolved (protein ligand) at a concentration of $50\text{ }\mu\text{g mL}^{-1}$ in acetate buffer was flowed through the sensor and allowed to react with the gold sensor chip surface for around 90 min. The unreacted COOH groups were passivated by a 1 M ethanolamine solution in H_2O , adjusted to pH 8.5. Immediately after the functionalization step, the sensor chip was used for the readout of model bioassay and liquid samples with increasing concentration of antimouse IgG conjugated with AF790 were sequentially flowed through the sensor (incubation time of 15 min for each concentration, followed by a rinsing step with buffer). All assay components were dissolved in PBS containing 0.05% Tween 20 and 1 mg mL^{-1} BSA.

2.7 Numerical simulations

The finite-difference time-domain method implemented in commercial software was employed from Lumerical Inc. (Canada). Optical near-field calculation of the electric field intensity distribution was performed at a wavelength that is coincident with the absorption band of the chosen emitter ($\lambda = 785$ nm). Fluorophore emission was studied by representing a fluorophore as an oscillating electric dipole. Both absorption $\vec{\mu}_{\text{ab}}$ and emission $\vec{\mu}_{\text{em}}$ dipoles were assumed randomly oriented, and the respective optical response was averaged over all their possible orientation and locations on the surface. A computation cell was defined with lateral dimensions of $20 \times 20\text{ }\mu\text{m}$ along the structure surface and height of $8\text{ }\mu\text{m}$ was used. Perfectly matched layer boundary conditions were applied to all boundaries. Cartesian coordinates were used and the axes in the plane of the structure are noted perpendicular (\perp) and parallel (\parallel) and the axis perpendicular to the structure as z . The emitter was placed 15 nm above the gold corrugated surface in the z direction. The wavelength-dependent refractive index of gold n_m was modeled by fitting a Drude-Lorentz model to data from the CRC Handbook on Chemistry and Physics while the refractive index of water as bulk medium was assumed nondispersive with $n_s = 1.332$. To study the spectrum of supported plasmonic modes, the MPG structure was illuminated with a plane wave source from above the bulk dielectric with refractive index n_s . Monitor planes were used 300 nm below and 700 nm above the surface to record the electrical field and calculate transmission and reflectivity. Furthermore, far-field distribution of the fluorescence emission in epi-fluorescence configuration was calculated by applying a far-field transformation to the reflectivity monitor.

3 Theory and experiment

The concept of MPG was pursued for the enhancement of fluorescence signal by using corrugation of a thin metal film with several encoded superimposed periodic modulations. These modulation components enable the precise design of the spectrum of excited plasmonic modes with

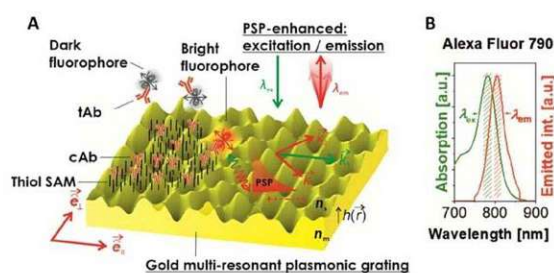


Figure 1: Concept of the MPG-based sensor readout. (A) Schematics of the surface of multiresonant MPG structure that carries a biointerface on its top to affinity capture fluorophore-labeled biomolecules that are probed by surface plasmon modes at its excitation and emission wavelengths. (B) Example of the absorption and emission spectra for selected fluorophore Alexa Fluor 790.

respect to the characteristics of the used fluorophores. Further, the structure was tailored for the amplification of fluorescence assays that utilize a near-infrared (NIR) fluorophore Alexa Fluor 790 (AF790) as a label. The MPG, schematically shown in Figure 1A, was implemented with grating periods suitable to resonantly excite PSPs on its surface at wavelengths that coincide with the excitation wavelength $\lambda_{\text{ex}} = 785$ nm and emission wavelength $\lambda_{\text{em}} = 810$ nm of AF790 (see respective absorption and emission peaks in Figure 1B). In the NIR wavelength range, the resonant excitation of PSPs at regular gold grating surfaces is manifested as a spectral dip in the reflectivity spectrum with a width of about $\Delta\lambda_{\text{FWHM}} = 15$ nm, which is substantially narrower than the Stokes shift of available fluorophore labels (including that for the chosen AF790 with $\lambda_{\text{em}} - \lambda_{\text{ab}} = 23$ nm). Therefore, the MPG was developed in order to support two distinct plasmonic resonances that provide enhanced intensity of PSP field at both excitation and emission wavelengths of AF790 in order to locally increase the excitation rate (at λ_{ex}) and take advantage of SP-mediated emission with diffractive outcoupling of fluorescence light trapped by PSPs (at λ_{em}) towards the detector. The importance of these contributions to amplify the measured fluorescence intensity is experimentally and theoretically demonstrated, and it is utilized for ultrasensitive fluorescence-based detection of biomolecules.

3.1 Topography of MPG structure

The MPG structure with three superimposed periodic corrugations was investigated and prepared by UV-LIL. A thin photoresist layer was sequentially exposed to series of sinusoidal patterns formed by two coherent interfering plane waves, and the final corrugation structure was yielded by its etching. The first recording of a shorter period $\Lambda_1 = 563$ nm was followed by two additional longer periods $\Lambda_2 = \Lambda_3 = 586$ nm that were rotated around the axis perpendicular to the surface by an azimuthal angle of $\varphi = 45^\circ$ and -45° (see Figure S1A). The superimposed interference field pattern is simulated in Figure 2A, and the respective etched corrugation profile can be described as the following height dependence:

$$h(\vec{r}) = \sum_{i=1}^3 a_i \sin\left(\frac{2\pi}{\Lambda_i} \vec{k}_i \cdot \vec{r}\right), \quad (1)$$

where a_i is the amplitude, Λ_i is the period of corrugation components, \vec{k}_i is the unit vector defining its orientation in the MPG plane ($i = 1, 2, 3$), and \vec{r} is the distance in the plane of the structure. Multiple substrates with identical corrugation profile were prepared by UV-NIL and coated with a 100-nm-thick Au film by vacuum thermal evaporation (Figure S1C). Atomic force microscopy was used to determine the topography of the prepared MPG, and the maximum

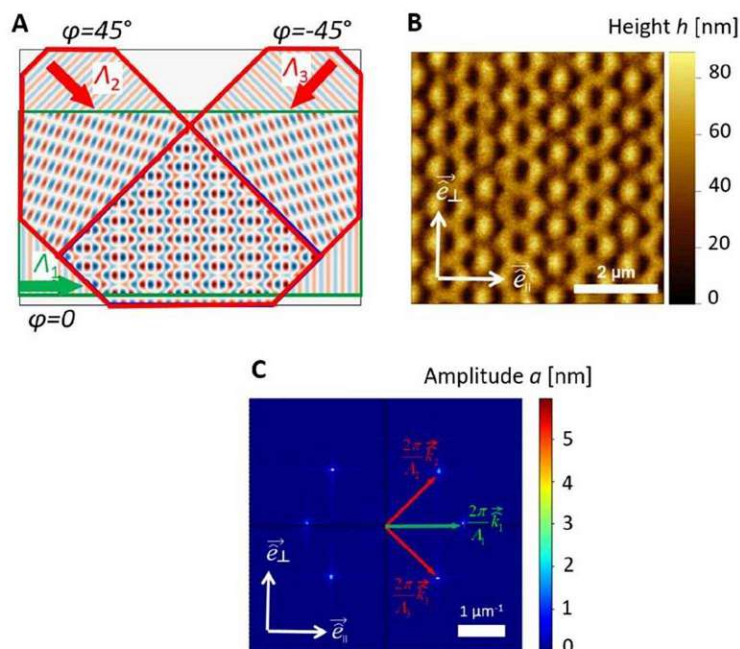


Figure 2: Designed MPG structure. (A) Orientation and periods of sequentially recorded overlaid sinusoidal corrugations by using UV-LIL method. (B) Measured topography of prepared MPG surface by AFM. (C) 2D FFT of the corrugation profile of the MPG structure. UV-LIL, UV-laser interference lithography; FFT, fast Fourier transform; AFM, atomic force microscopy.

corrugation depth of about 70 nm (difference in height of the topography) was observed, Figure 2B. The structure topography was further analyzed in more detail by 2D fast Fourier transform in order to reveal its periodic components. The obtained results are presented in Figure 2C, and they show clear peaks corresponding to recorded superimposed sinusoidal corrugations with periods Λ_1 , Λ_2 , and Λ_3 . The dependence of the respective orientation of \vec{k}_i vectors agrees with the azimuthal angles φ used in the recording process. The modulation amplitude for each corrugation was determined to be around $a_1 = a_2 = a_3 = 8$ nm. This value is close to that used for the first order diffraction coupling to PSPs on the gold surface in the NIR part of the spectrum as shown before in literature [42].

3.2 Diffraction coupling to SPs by MPG

Periodically corrugated metallic surfaces allow for the phase matching of optical waves propagating in the far field with the near-field PSPs traveling along these surfaces. In general, the investigated geometry of MPG with multiple harmonic components allows fulfilling the phase-matching condition via its individual spectral components or their combination. For shallow corrugations, the wavelength-dependent propagation constant of PSPs in transverse magnetic polarization can be approximated by that for plane metal surface:

$$\vec{k}_{SP} = \frac{2\pi}{\lambda} \text{Re} \left\{ \sqrt{\frac{n_m^2 \cdot n_s^2}{n_m^2 + n_s^2}} \right\} \left[\vec{e}_\perp \sin(\varphi) + \vec{e}_\parallel \cos(\varphi) \right], \quad (2)$$

where n_m and n_s are the refractive indices of the metal and the adjacent (water) dielectric, respectively, φ is azimuthal angle, and \vec{e}_\perp and \vec{e}_\parallel are the unit orthogonal vectors in the plane of the MPG. The momentum of the incident beam becomes phase matched with that of PSPs when the following condition holds:

$$\pm \vec{k}_{SP} = \frac{2\pi}{\lambda} n_s \cos(\theta) \left[\vec{e}_\perp \sin(\varphi) + \vec{e}_\parallel \cos(\varphi) \right] + \sum_{i=1}^3 m_i \frac{2\pi}{\Lambda_i} \vec{k}_i, \quad (3)$$

where θ and φ are the polar and azimuthal angles, respectively, of a plane wave traveling in the dielectric with a refractive index n_s , Λ_i is the period of corrugation components, \vec{k}_i is unit vectors defining its orientation in the MPG plane ($i = 1, 2, 3$), and integers (m_1, m_2, m_3) refer to a diffraction order.

The prepared gold-coated MPG structure was brought in contact with water exhibiting $n_s = 1.332$, and the specular reflectivity spectrum R_0 was measured for the

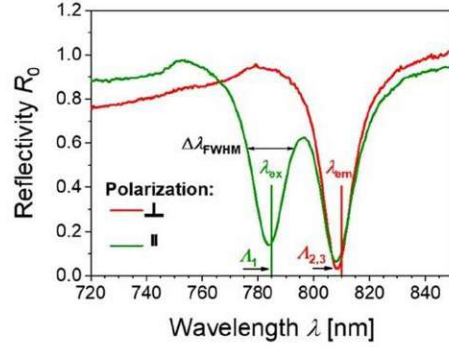


Figure 3: Plasmonic modes. Zero-order reflectivity spectrum measured for the normally incident beam at the MPG surface brought in contact with water ($n_s = 1.332$).

normally incident optical beam ($\theta = 0$, φ is arbitrary). As seen in Figure 3, it exhibits two narrow dips centered at wavelengths of 784 and 817 nm and the coupling strength to shorter wavelength resonance can be controlled by the polarization of the incident optical beam. For the parallel polarization, the SPR at shorter wavelength is strongly pronounced, while when rotating the polarization to the perpendicular direction, it diminishes. The longer wavelength SPR dip is not sensitive to polarization changes. This behavior clearly relates to the fact that the short wavelength SPR originates from the diffraction on the corrugation component Λ_1 (which is recorded with only one azimuthal orientation) while the longer wavelength resonance is associated to the corrugation components Λ_2 and Λ_3 (forming a crossed grating with two identical orthogonal corrugations). The spectral position of shorter and longer wavelength resonances observed in the specular zero-order reflectivity spectrum (R_0) can be ascribed by using equation (3) to first-order diffraction coupling. The resonance at 785 nm is associated with the excitation of PSPs via the order (1,0,0) and the one at 810 nm to (0,1,0) and (0,0,1). Interestingly, the higher order coupling is not apparent in the visible-NIR spectral window of measured specular reflectivity R_0 . It is worth of noting that the spectral position of short and long wavelength SPRs can be tuned by changing the respective periods Λ_1 and Λ_2/Λ_3 (see Figure S2A) and thus the reported MPG concept can be implemented for other emitters absorbing and emitting at different wavelengths λ_{ab} and λ_{em} , respectively. Moreover, the coupling strength of PSPs with optical wave that impinges from the far field depends on the modulation depth a_i and on the polarization of the incident field with respect to the grating vector as illustrated in Figure S2B.

3.3 Simulations of PEF on MPG

The MPG structure exhibits two distinct resonances that coincide with the absorption and emission wavelengths of the AF790 fluorophore λ_{ab} and λ_{em} , respectively. The coupling of this fluorophore with the enhanced intensity of electric field $|\vec{E}|^2$ of resonantly excited PSPs at these wavelengths was studied using numerical simulations. The fluorophore was represented as an infinitesimally small electric dipole placed at a distance of 15 nm from the gold surface, which was chosen with respect to a typical immunoassay experiment considering the size of immunoglobulin G antibodies ($13.7 \times 8 \times 4$ nm [43]) and the fact that it is above the distance where strong quenching occurs [44]. The fluorescence emission has dipole characteristics [45, 46], and it cannot be excited when the orientation of the electric field \vec{E} is perpendicular to the emitter absorption dipole $\vec{\mu}_{ab}$. In the reported experiments, fluorophores were conjugated to proteins by flexible molecular linkers with high degree of rotational freedom, which leads to randomizing its orientation in the fluorescence lifetime and consequently to an isotropic emission profile. Therefore, all possible orientations of the fluorophore absorption $\vec{\mu}_{ab}$ and emission $\vec{\mu}_{em}$ dipole were accounted for and averaged with respect to PSP electric field \vec{E} .

The excitation rate of a fluorophore is a function of the scalar product of the local electric field \vec{E} at λ_{ex} and absorption moment of the fluorophore $\vec{\mu}_{ab}$. Assuming the excitation rate is far below saturation, it can be expressed as $\propto |\vec{\mu}_{ab} \cdot \vec{E}|^2$ and thus being proportional to the electric field intensity enhancement $|\vec{E}/\vec{E}_0|^2$ accompanied with the resonant excitation of PSPs, which is strongest for the \vec{E} component perpendicular to the surface. It reaches value $|\vec{E}|^2/|\vec{E}_0|^2 = 160$ (normalized with the intensity of the incident field intensity $|\vec{E}_0|^2$) for the resonant coupling of light to PSPs at $\lambda_{ex} = 785$ nm and the distance of 15 nm from the surface after the averaging along the structure corrugation (see Figure S3). This electric field intensity enhancement yields the mean amplification of the excitation rate of the emitter with randomly oriented absorption moment $\vec{\mu}_{ab}$ of 53, compared to an emitter in a homogeneous medium, which is similar to the excitation rate enhancement reported for excitation in attenuated total reflection (ATR) configuration with Kretschmann geometry [47].

After the PSP-enhanced excitation of the fluorophore at λ_{ex} , its emission can also be mediated by these modes at λ_{em} as is analyzed further. These modes are generated upon the emission process by the near-field coupling and travel along the MPG surface. They become subsequently diffraction

outcoupled to far-field waves that propagate away from its surface in the perpendicular direction. The emission characteristics mediated by the coupling to PSPs were averaged over all lateral positions and orientations of emission moment $\vec{\mu}_{em}$ (assuming rapid rotation of fluorophore on the surface within the lifetime of its excited state). As shown in the simulated angular distribution of fluorescence intensity emitted to the far field above the MPG in Figure 4A, it exhibits a pattern with multiple narrow dispersive bands that are attributed to first-order diffraction on the corrugation components Λ_1 , Λ_2 , and Λ_3 , with corresponding diffraction order of $(\pm 1, 0, 0)$, $(0, \pm 1, 0)$, and $(0, 0, \pm 1)$, respectively. Clearly, these bands converge at the center, which consequently increases the probability of fluorescence emission to waves traveling at small polar angle θ . Assuming a fluorescence collecting cone corresponding to a numerical aperture of 0.2, the MPG structure redirects the fluorescence light, so the detected intensity is enhanced by a factor of 8.2 with respect to a dipole in a homogeneous medium, where the emission is omnidirectional, and a factor of 6.2 compared to a dipole on a flat gold surface. MPG shows an additional 30% improvement compared to previous work utilizing a crossed grating

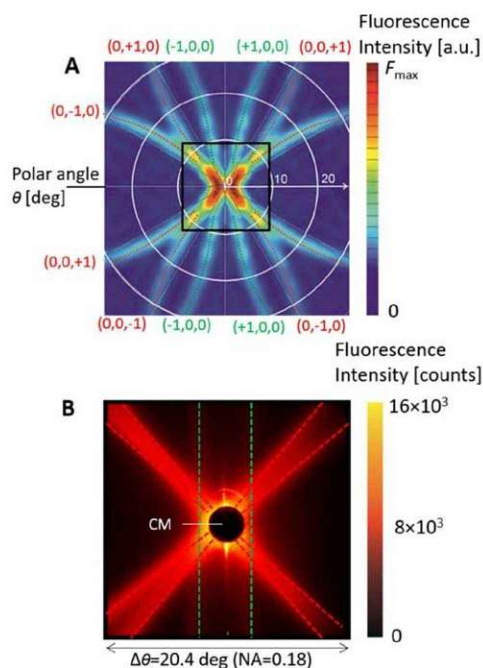


Figure 4: Surface plasmon-coupled emission at λ_{em} . (A) Simulated and (B) measured angular distribution of fluorescence light emitted from MPG surface with indicated diffraction orders.

that was tuned to couple to plasmons at the excitation wavelength only [48].

3.4 Experimental observation of PEF on MPG

In order to measure the fluorescence signal amplified by the developed MPG nanostructure, its gold surface was modified with a mixed thiol SAM carrying OEG and COOH groups. The OEG thiol in the mixed thiol SAM was used to provide protection against unspecific binding of proteins present in analyzed liquid sample, and the smaller fraction of thiols carrying the COOH end group was employed for the post-modification of the sensor surface with functional groups.

Firstly, mouse IgG conjugated with AF790 was covalently bound to the COOH moieties on the surface by using the amine coupling, and the angular distribution of fluorescence light emitted from MPG was measured. This experiment was performed using an in-house-developed fluorescence reader configured to image the back focal plane of the objective lens placed before the sensor chip with MPG (lens 3 in Figure S4, back focal plane cuts the CM as indicated). The imaged angular distribution of emitted fluorescence light was measured by an EM-CCD detector in the range from $\theta = -10.2$ to 10.2° , Figure 4B. This image shows six dispersive bands originating from first-order outcoupling of PSP-mediated fluorescence emission at λ_{em} at angles that agree with the simulations presented in Figure 4A.

Then, the configuration of the optical system of the reader was changed to image the surface of MPG to the EM-CCD detector to allow fluorescence readout of bioassays on the sensor chip. These measurements were carried out to evaluate the impact of individual components of the investigated MPG nanostructure to the fluorescence enhancement. The imaged area on the sensor chip was prepared so six different zones were coated with the same gold film and carrying the same surface density of IgG conjugated with AF790, see Figure 5A and D. The first reference zone was flat, the second and third zones were corrugated with only one component Λ_2 and Λ_3 , the fourth and fifth zones carried two superimposed components Λ_1 , Λ_2 and Λ_1 , Λ_3 , and the sixth zone comprised all components Λ_1 , Λ_2 , Λ_3 forming the full MPG structure. The sensor chip with all six zones carrying IgG-AF790 conjugates on their top was illuminated with a collimated and linearly polarized beam at λ_{ex} , and the intensity of emitted fluorescence light at λ_{em} was collected and imaged to the EM-CCD detector. In order to distinguish between the impact of plasmonically enhanced excitation at λ_{ex} and plasmon-coupled emission at λ_{em} , the polarization of the excitation beam

was rotated so the SPR at the excitation wavelength λ_{ex} was switched on and off (see Figure 3). The obtained fluorescence images are presented in Figure 5A–C. They show increased fluorescence signal in a circular illuminated area that is sliced to sections representing the six zones carrying different combinations of spatial components Λ_1 , Λ_2 , and Λ_3 . The fluorescence intensity was averaged over the surface of each zone, and the value measured outside the illuminated area was subtracted in order to compensate for stray light and a dark signal of the EM-CCD detector. Then, the intensity from structured zones was normalized with that measured on a reference flat surface, and the obtained enhancement factors are summarized in the table included in Figure 5E.

For the perpendicular polarization of the excitation beam \perp (which does not couple to surface PSPs at λ_{ex} via corrugation component Λ_1), the impact of MPG to the SP-coupled emission at λ_{em} was investigated. As Figure 5A shows, the presence of individual corrugations Λ_2 and Λ_3 provided the enhancement factor of collected fluorescence light intensity F of 3.7. On the zones when these components are overlaid with Λ_1 , this factor increases to 17, and when all the components $\Lambda_{1,2,3}$ are present, it raises to about 25. Let us note that the latter two enhancement values are substantially higher than the value predicted by simulations for the outcoupling of the emission occurring via PSPs at λ_{em} (factor of 6.2). This observation can be attributed to partial miss alignment of the excitation beam polarization which leads to weak coupling to PSPs at the excitation wavelength λ_{ex} , which amends the excitation rate of the attached fluorophores. For the parallel polarization of the excitation beam \parallel , the enhancement by individual corrugations Λ_2 and Λ_3 provided the same enhancement factor of 3.7. On the zones where these components are superimposed with Λ_1 , the enhancement factor of 248 was measured, which is about 67 times higher than on the surface without this component and which agrees well with the predicted contribution of the enhanced excitation rate at λ_{ex} of 53. On the zone where all components were present, additionally higher enhancement factor of 300 was determined with respect to the flat surface where both the excitation rate enhancement at λ_{ex} by Λ_1 and the improving of collection yield at λ_{em} by Λ_2 and Λ_3 are combined.

3.5 Readout of fluorescence immunoassay kinetics

The ability of the MPG nanostructure to enhance the performance characteristics of a fluorescence assay was

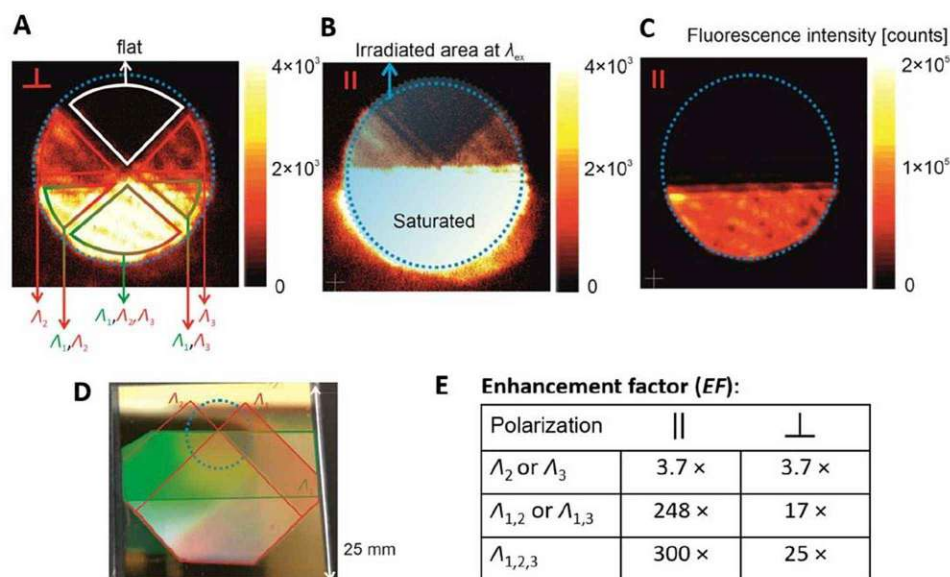


Figure 5: Experimentally determined fluorescence enhancement factors. Fluorescence images taken from an area, where different combinations of spatial MPG components are present. Polarization of the excitation beam was (A) orthogonal and (B,C) parallel to the grating Λ_1 . (D) Photograph of the prepared MPG with highlighted areas carrying different spectral components of MPG and (E) comparison of the respective enhancement factors with respect to that measured for the flat surface.

demonstrated for a microarray detection format. In this experiment, there was used the optical reader schematically shown in Figure 6A and a sensor chip with MPG nanostructure was interfaced with a flow-cell as indicated in Figure 6B. In this sensor configuration, the fluorescence signal F was measured as a function of time t from 21 circular spots defined on the sensor chip surface (see Figure S5). Each spot exhibited 220- μm diameter, and spot numbers 5, 8, 6, 9, 12, 10, 13, and 16 were defined on the sensor chip area in the flow cell chamber with the full MPG nanostructure coated with gold film. In addition, reference spots 1, 2, 3, 4, 7, 13, and 21 were placed outside the flow cell chamber, and reference spots 11, 15, 20, 14, 17, and 18 were defined inside the flow cell on the area with a flat gold film not carrying the MPG. The gold surface on the MPG inside the flow cell was functionalized by using the same mixed thiol SAM and amine-coupling strategy by mouse IgG molecules that were not labeled by a fluorophore. These biomolecules served as a ligand and allowed for affinity capture of target analyte (antimouse IgG conjugated with AF790) from the aqueous sample transported along the sensor surface through the flow cell chamber.

Initially, buffer was flowed through the sensor for at least 10 min until a stable baseline in the sensor response F_b was established for all sensing spots 1–21. Afterward, a series of samples spiked with a target analyte (antimouse

IgG conjugated with AF790) at concentrations between 10 fM and 10 nM was flowed over the sensor surface and its affinity binding at the array sensing spots was monitored through changes in the fluorescence signal F . The fluorescence signal deriving from each spot was averaged from the acquired images over its area and plotted by using in-house-developed LabView-based software. Variations in light source intensity were corrected by subtracting the signal of an illuminated reference spot outside the microfluidic channel from all other curves (spots 1, 2, 3, 4, 7, 13, and 21).

In a first step, the fluorescence signal was monitored for the affinity binding of high analyte concentrations (1 and 10 nM); therefore, the reader was configured for the monitoring of strong fluorescence intensities F (intensity of the excitation beam irradiating the sensor chip surface at λ_{ex} was $30 \mu\text{W cm}^{-2}$, irradiation time of 0.3 s, with image accumulation of 10). Figure 7A compares the fluorescence signal kinetics $F(t)$ for two spots on the surface with gold MPG (red-colored curves) and two reference spots with flat gold surface (green-colored curves) where baseline signal F_b was subtracted from the acquired signal. Each sample was flowed over the surface for 20 min followed by 10 min rinsing. These data reveal the affinity binding manifests itself as a gradual increase in the fluorescence signal ΔF until saturation is reached, then upon the rinsing step a

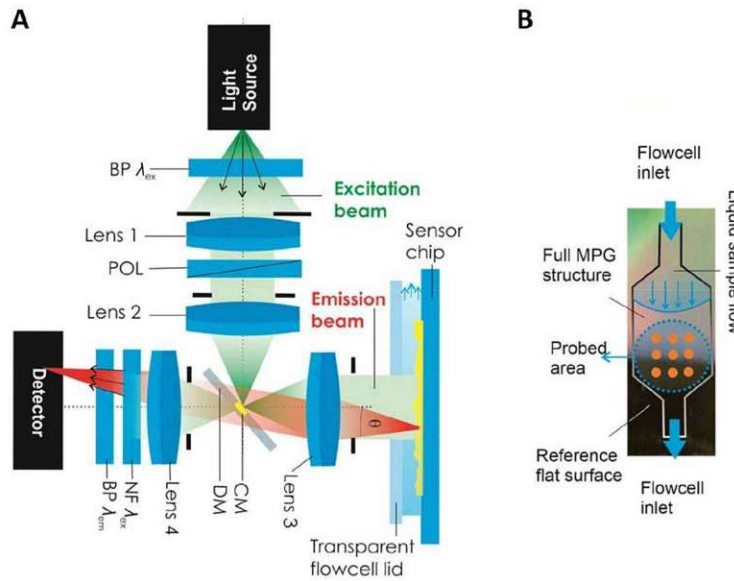


Figure 6: Optical biosensor reader. (A) Schematics of the optical configuration for the measurement of fluorescence signal kinetics from arrays of spots on the MPG sensor surface imaged to the detector. (B) Sensor chip with MPG structure that is interfaced with a flow cell and indication of the selected sensing spots. POL, polarizer; BP, bandpass filter; NF, notch filter; DM, dichroic mirror; CM, center mirror.

slow decrease in the fluorescence signal occurs due to dissociation of affinity bound molecules. The irradiation power at λ_{ex} was selected to prevent the fluorophore labels from bleaching within the reaction time. The sensor response ΔF to the analyzed sample was defined as a difference in the fluorescence signal

between the original baseline and after the 5 min rinsing. The measured data show that the MPG structure enhanced the fluorescence sensor response by a factor of 292 with respect to the flat surface, which is consistent with previous observations performed without the kinetics readout (see Figure 5).

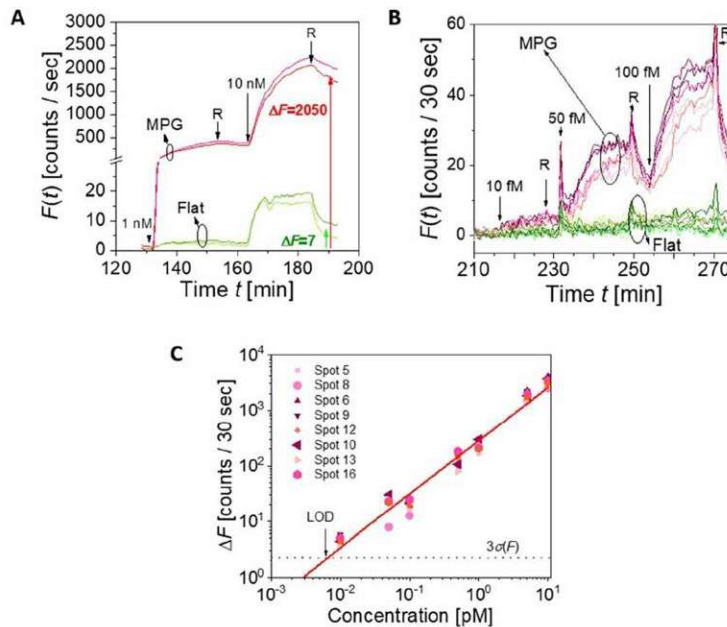


Figure 7: Biomolecular binding kinetics observed for a model IgG–anti-IgG on the MPG surface. The fluorescence reader was configured for detection of (A) high fluorescence intensities and (B) low fluorescence intensities for which the respective (C) calibration curve was established. The caption R states for the rinsing and red curves correspond to data measured on the MPG surface and green curves on the reference flat gold surface.

In a second step, the reader was configured for the monitoring of weak fluorescence signal in order to decrease the limit of detection (LOD) of the performed model assay (intensity of the excitation beam irradiating the sensor chip surface at λ_{ex} was raised to $265 \mu\text{W cm}^{-2}$, irradiation time 30 s, without accumulation of images). In Figure 7B, the kinetic measurement of the fluorescence signal $F(t)$ for the target analyte concentrations of 10, 50, and 100 fM is shown. For the spots on the nonstructured reference area (green-colored curves), no measurable change in signal was observed, while on the area structured with gold MPG, a clear increase in $F(t)$ for all shown concentrations is detected. The kinetics of the reaction presented in Figure 7B is qualitatively different from that in Figure 7A. The fluorescence signal intensity $F(t)$ faster saturates at already low concentrations where only a small fraction of available binding sites is occupied by the target analyte conjugated with AF790 and it also faster decreases upon the rising step. These effects are caused by the more pronounced bleaching occurring due to the more intense irradiation power at λ_{ex} .

From the measured kinetic data, the calibration curve presented in Figure 7C was established and the respective LOD was determined. The fluorescence response ΔF on the MPG structure was plotted against the analyte concentrations of 10 fM, 50 fM, 100 fM, 0.5 pM, 1 pM, and 5 pM in log-log scale and fitted by a linear function with a slope $S = 0.95 \text{ counts}/30 \text{ s}/\text{fM}$. The LOD was determined from the intersection of the fitted calibration curve with three times the standard deviation of the fluorescence background $3\sigma(F)$, where $\sigma(F) = 0.75 \text{ counts}/30 \text{ s}$. The achieved (average) LOD is 6 fM for the used measuring spot numbers 5, 8, 6, 9, 12, 10, 13, and 16. It should be noted that the imaged area of $4 \times 4 \text{ mm}$ can accommodate up to 270 of these spots, which can be used for parallel monitoring of biomolecular binding kinetics undisturbed by the background signal originating from the bulk, owing to the local enhancement of emitted fluorescence signal at the sensor chip surface.

4 Conclusions

A novel metallic nanostructure with a delocalized plasmonic hotspot and multiple SPR wavelengths is reported and its tailoring for PEF is discussed. It is based on a MPG that supports series of spectrally narrow (15 nm width) resonances associated with the diffraction coupling to PSP modes. These substrates were utilized for fluorescence immunoassay measurements, which show an enhancement factor of $300\times$ on the MPG surface with respect to a nonstructured surface carrying the same biointerface

architecture. This enhancement factor is about $2\times$ as high as previously reported by our group for single period crossed grating tuned for the excitation enhancement only [48] and more than $5\times$ higher than what has been reported for PEF with the ATR method and Kretschmann configuration [49]. In conjunction with a reader allowing spatially resolved monitoring of fluorescence intensity from multiple spots arranged in a footprint of 16 mm^2 , there is demonstrated the possibility of highly parallelized measurement of affinity binding kinetics that is not masked by the background single originating from the bulk and with high sensitivity enabling reaching the LOD of 6 fM. The reported LOD is about $66\times$ improved compared to similar assays reported by our previous work on single period crossed gratings and ATR-based PEF [49]. By changing the periods of the superimposed periodic structures, the proposed MPG concept can be utilized for arbitrary emitters in the red and infrared part of the spectrum (for a gold surface) or at shorter wavelengths (for silver or aluminum) covering a wide range of available fluorophore labels. In addition, the ability to translate the MPG preparation process to mass production compatible technologies such as UV-NIL in roll-to-roll format in conjunction with deploying of novel antifouling biointerface architectures [50] may open a pathway for future industrial applications (including analysis of trace amounts of diseases biomarkers in bodily fluids, which is a topic for the follow-up work).

Abbreviations

AF790	Alexa Fluor 790 fluorescent dye
CM	Central mirror
DM	Dichroic mirror
EBL	Electron beam lithography
LIL	Laser interference lithography
LSP	Localized surface plasmon
MPG	Multi-period plasmonic grating
NA	Numerical aperture
PEF	Plasmon-enhanced fluorescence
PSP	Propagating surface plasmon
SAM	Self-assembled monolayer
SP	Surface plasmon
SPR	Surface plasmon resonance
UV-NIL	UV-nanoimprint lithography
UV-LIL	UV-laser interference lithography

Author contribution: All the authors have accepted responsibility for the entire content of this submitted manuscript and approved submission.

Research funding: S.F., S.H., S.M. E.M., and J.D. received support from the European Union's Horizon 2020 research and the innovation program under Grant agreement no.

633937, project ULTRAPLACAD. In addition, S.H., S.F., and J.D. were partially supported by the Austrian Research Promotion Agency (FFG) with Grant agreement no. 861578 (ERANET project PLABAN), and J.D. acknowledges support from the ESIF and MEYS (Project 'FZU researchers, technical and administrative staff mobility' – CZ.02.2.69/0.0/0.0/18_053/0016627).

Conflict of interest statement: The authors declare no conflicts of interest regarding this article.

References

- [1] B. Liedberg, C. Nylander, and I. Lunström, "Surface plasmon resonance for gas detection and biosensing," *Sens. Actuators*, vol. 4, pp. 299–304, Jan. 1983.
- [2] J. Homola, *Surface Plasmon Resonance Based Sensors*, 2006.
- [3] M. F. Cardinal, E. Vander Ende, R. Hackler, et al., "Expanding applications of SERS through versatile nanomaterials engineering," *Chem. Soc. Rev.*, vol. 46, no. 13, pp. 3886–3903, 2017.
- [4] Y. Jeong, Y. M. Kook, K. Lee, and W. G. Koh, "Metal enhanced fluorescence (MEF) for biosensors: general approaches and a review of recent developments," *Biosens. Bioelectron.*, 2018. <https://doi.org/10.1016/j.bios.2018.04.007>.
- [5] M. Li, S. K. Cushing, and N. Wu, "Plasmon-enhanced optical sensors: a review," *Analyst*, vol. 140, no. 2, pp. 386–406, 2015.
- [6] G. W. Ford and W. H. Weber, "Electromagnetic interactions of molecules with metal surfaces," *Phys. Rep.*, vol. 113, no. 4, pp. 195–287, 1984.
- [7] J. R. Lakowicz, K. Ray, M. Chowdhury, H. Szmajcinski, Y. Fu, J. Zhang, and K. Nowaczyk, "Plasmon-controlled fluorescence: a new paradigm in fluorescence spectroscopy," *Analyst*, vol. 133, no. 10, pp. 1308–1346, 2008.
- [8] E. Fort and S. Grésillon, "Surface enhanced fluorescence," *J. Phys. D Appl. Phys.*, vol. 41, no. 1, p. 013001, 2008.
- [9] J. R. Lakowicz, K. Ray, M. Chowdhury et al., "Plasmon-controlled fluorescence: a new paradigm in fluorescence spectroscopy," *Analyst*, vol. 133, no. 10, pp. 1308–1346, 2008.
- [10] F. D. Stefani, K. Vasilev, N. Bocchio, N. Stoyanova, and M. Kreiter, "Surface-plasmon-mediated single-molecule fluorescence through a thin metallic film," *Phys. Rev. Lett.*, vol. 94, no. 2, pp. 1–4, 2005.
- [11] B. Auguié and W. L. Barnes, "Collective resonances in gold nanoparticle arrays," *Phys. Rev. Lett.*, vol. 101, no. 14, p. 143902, Sep. 2008.
- [12] M. Bauch and J. Dostalek, "Collective localized surface plasmons for high performance fluorescence biosensing," *Opt. Express*, vol. 21, no. 17, p. 20470, Aug. 2013.
- [13] E. Petryayeva and U. J. Krull, "Localized surface plasmon resonance: nanostructures, bioassays and biosensing-A review," *Anal. Chim. Acta*, vol. 706, no. 1, pp. 8–24, 2011.
- [14] Y. Chen, K. Munechika, and D. S. Ginger, "Dependence of fluorescence intensity on the spectral overlap between fluorophores and plasmon resonant single silver nanoparticles," *Nano Lett.*, vol. 7, no. 3, pp. 690–696, Mar. 2007.
- [15] G. Vecchi, V. Giannini, and J. Gómez Rivas, "Shaping the fluorescent emission by lattice resonances in plasmonic crystals of nanoantennas," *Phys. Rev. Lett.*, vol. 102, no. 14, Apr. 2009, <https://doi.org/10.1103/physrevlett.102.146807>.
- [16] Y. Wang, L. Wu, T. I. Wong, et al., "Directional fluorescence emission co-enhanced by localized and propagating surface plasmons for biosensing," *Nanoscale*, vol. 8, no. 15, pp. 8008–8016, Apr. 2016.
- [17] V. G. Kravets, A. V. Kabashin, W. L. Barnes, and A. N. Grigorenko, "Plasmonic surface lattice resonances: a review of properties and applications," *Chem. Rev.*, vol. 118, pp. 1–72, 2018.
- [18] P. Biagioni, J.-S. Huang, and B. Hecht, "Nanoantennas for visible and infrared radiation," *Reports Prog. Phys.*, vol. 75, no. 2, p. 024402, Feb. 2012.
- [19] A. Devilez, B. Stout, and N. Bonod, "Compact metallo-dielectric optical antenna for ultra directional and enhanced radiative emission," *ACS Nano*, vol. 4, no. 6, pp. 3390–3396, Jun. 2010.
- [20] T. Coenen, E. J. R. Vesseur, A. Polman, and A. F. Koenderink, "Directional emission from plasmonic Yagi-Uda antennas probed by angle-resolved cathodoluminescence spectroscopy," *Nano Lett.*, vol. 11, no. 9, pp. 3779–3784, Sep. 2011.
- [21] T. Kosako, Y. Kadoya, and H. F. Hofmann, "Directional control of light by a nano-optical Yagi-Uda antenna," *Nat. Photonics*, vol. 4, no. 5, pp. 312–315, May 2010.
- [22] A. B. Taylor and P. Zijlstra, "Single-molecule plasmon sensing: current status and future prospects," *ACS Sensors*, vol. 2, no. 8. American Chemical Society, pp. 1103–1122, Aug. 2017.
- [23] J. R. Lakowicz, J. Malicka, I. Gryczynski, and Z. Gryczynski, "Directional surface plasmon-coupled emission: a new method for high sensitivity detection," *Biochem. Biophys. Res. Commun.*, vol. 307, no. 3, pp. 435–439, 2003.
- [24] I. I. Smolyaninov, Y. J. Hung, and C. C. Davis, "Fluorescence enhancement by surface gratings," *Opt. InfoBase Conf. Pap.*, vol. 14, no. 22, pp. 10825–10830, 2007.
- [25] A. Nicol and W. Knoll, "Characteristics of fluorescence emission excited by grating-coupled surface plasmons," *Plasmonics*, vol. 13, no. 6, pp. 2337–2343, 2018.
- [26] K. Tawa, H. Hori, K. Kintaka, K. Kiyosue, Y. Tatsu, and J. Nishii, "Optical microscopic observation of fluorescence enhanced by grating-coupled surface plasmon resonance," *Opt. Express*, vol. 16, no. 13, p. 9781, Jun. 2008.
- [27] E. Prodan, "A hybridization model for the plasmon response of complex nanostructures," *Science (80-)*, vol. 302, no. 5644, pp. 419–422, Oct. 2003.
- [28] S. A. Safabadi Tali and W. Zhou, "Multiresonant plasmonics with spatial mode overlap: overview and outlook," *Nanophotonics*, vol. 8, no. 7, pp. 1199–1225, Jul. 2019.
- [29] J. Parsons, E. Hendry, C. P. Burrows, B. Auguié, J. R. Sambles, and W. L. Barnes, "Localized surface-plasmon resonances in periodic nondiffracting metallic nanoparticle and nanohole arrays," *Phys. Rev. B Condens. Matter Mater. Phys.*, vol. 79, no. 7, 2009, <https://doi.org/10.1103/physrevb.79.073412>.
- [30] J. S. Pang, I. G. Theodorou, A. Centeno, et al., "Tunable three-dimensional plasmonic arrays for large near-infrared fluorescence enhancement," *ACS Appl. Mater. Interfaces*, vol. 11, no. 26, 23083–23092, Jul. 2019.
- [31] K. M. McPeak, S. V. Jayanti, S. J. P. Kress, et al., "Plasmonic films can easily be better: rules and recipes," *ACS Photonics*, vol. 2, no. 3, pp. 326–333, 2015.
- [32] R. Gupta, M. J. Dyer, and W. A. Weimer, "Preparation and characterization of surface plasmon resonance tunable gold and

- silver films," *J. Appl. Phys.*, vol. 92, no. 9, pp. 5264–5271, Nov. 2002.
- [33] B. Ai, Y. Yu, H. Möhwald, G. Zhang, and B. Yang, "Plasmonic films based on colloidal lithography," *Adv. Colloid Interface Sci.*, vol. 206. Elsevier B.V., pp. 5–16, 2014.
- [34] T. H. P. Chang, M. Mankos, K. Y. Lee, and L. P. Muray, "Multiple electron-beam lithography," *Microelectron. Eng.*, vols. 57–58, pp. 117–135, Sep. 2001.
- [35] C. Lu and R. H. Lipson, "Interference lithography: a powerful tool for fabricating periodic structures," *Laser Photonics Rev.*, vol. 4, no. 4, pp. 568–580, 2010.
- [36] A. Rodriguez, A. Echeverría, M. Ellman, et al., "Laser interference lithography for nanoscale structuring of materials: from laboratory to industry," *Microelectron. Eng.*, vol. 86, nos. 4–6, pp. 937–940, Apr. 2009.
- [37] H. Schiff, "Nanoimprint lithography: an old story in modern times? A review," *J. Vac. Sci. Technol. B Microelectron. Nanom. Struct.*, vol. 26, no. 2, pp. 458–480, Mar. 2008.
- [38] S. V. Sreenivasan, "Nanoimprint lithography steppers for volume fabrication of leading-edge semiconductor integrated circuits," *Microsyst. Nanoeng.*, vol. 3, no. 1, pp. 1–19, 2017.
- [39] N. Kooy, K. Mohamed, L. T. Pin, and O. S. Guan, "A review of roll-to-roll nanoimprint lithography," *Nanoscale Res. Lett.*, vol. 9, no. 1, pp. 1–13, Jun. 2014.
- [40] I. Khan, H. Keshmiri, F. Kolb, T. Dimopoulos, E. J. W. List-Kratochvil, and J. Dostalek, "Multidiffractive broadband plasmonic absorber," *Adv. Opt. Mater.*, vol. 4, no. 3, pp. 435–443, 2016.
- [41] K. Jans, K. Bonroy, K. De Palmas, et al., "Stability of mixed PEO-thiol SAMs for biosensing applications," *Langmuir*, vol. 24, no. 8, pp. 3949–3954, 2008.
- [42] P. Adam, J. Dostálek, and J. Homola, "Multiple surface plasmon spectroscopy for study of biomolecular systems," *Sens. Actuators B Chem.*, vol. 113, no. 2, pp. 774–781, Feb. 2006.
- [43] Y. H. Tan, M. Liu, B. Nolting, J. G. Go, J. Gervay-Hague, and G. Liu, "A nanoengineering approach for investigation and regulation of protein immobilization," *ACS Nano*, vol. 2, no. 11, pp. 2374–2384, Nov. 2008.
- [44] K. Sergelen, S. Fossati, A. Turupcu, et al., "Plasmon field-enhanced fluorescence energy transfer for hairpin aptamer assay readout," *ACS Sensors*, vol. 2, no. 7, pp. 916–923, 2017.
- [45] F. Michelotti and E. Sepe, "Anisotropic fluorescence emission and photobleaching at the surface of one-dimensional photonic crystals sustaining Bloch surface waves. I. Theory," *J. Phys. Chem. C*, vol. 123, no. 34, pp. 21167–21175, Aug. 2019.
- [46] E. Sepe, A. Sinibaldi, N. Danz, P. Munzert, and F. Michelotti, "Anisotropic fluorescence emission and photobleaching at the surface of one-dimensional photonic crystals sustaining Bloch surface waves. II. Experiments," *J. Phys. Chem. C*, vol. 123, no. 34, pp. 21176–21184, Aug. 2019.
- [47] M. Bauch, K. Toma, M. Toma, Q. Zhang, and J. Dostalek, "Plasmon-enhanced fluorescence biosensors: a review," *Plasmonics*, vol. 9, no. 4, pp. 781–799, Aug. 2014.
- [48] M. Bauch, S. Hageneder, and J. Dostalek, "Plasmonic amplification for bioassays with epi-fluorescence readout," *Opt. Express*, vol. 22, no. 26, p. 32026, 2014.
- [49] S. Hageneder, M. Bauch, and J. Dostalek, "Plasmonically amplified bioassay - total internal reflection fluorescence vs. epifluorescence geometry," *Talanta*, vols. 156–157, pp. 225–231, Aug. 2016.
- [50] D. Kotlarek, M. Vorobii, W. Ogieglo, W. Knoll, C. Rodriguez-Emmenegger, and J. Dostálek, "Compact grating-coupled biosensor for the analysis of thrombin," *ACS Sensors*, vol. 4, no. 8, pp. 2109–2116, 2019.

Supplementary material: The online version of this article offers supplementary material (<https://doi.org/10.1556/nanoph-2020-0270>).

3. Summary and Outlook

In this work, novel multimodal biosensor concepts are pursued to push forward the capabilities of biosensor applications in the sensitive detection of chemical and biological species and in biomolecular interaction analysis. They are based on nanophotonic surfaces that enable the implementation of novel functionalities in established optical technologies and provide the basis for a new type of sensor devices, particularly in conjunction with additional electronic sensing principles. Plasmonic resonances, supported by the nanostructured metallic surface, are utilized for probing of target molecular species, rendering means for the direct detection based on induced refractive index changes, plasmon enhanced fluorescence (PEF), and surface-enhanced Raman spectroscopy (SERS). New architectures and fabrication methods have been devised to serve in high-performance sensors that overcome the need of using particularly cost-extensive and complex fabrication processes.

One of the best-studied plasmonic surface architectures, a thin gold film prepared by thermal evaporation, has been employed to investigate new approaches for plasmonic biosensors. The interaction of fluorescent molecules with the electromagnetic nearfield at a gold surface has been studied in section 2.6 and an aptamer-based sensor for the continuous monitoring of adenosine triphosphate as a small model analyte has been developed. The strong distance dependence of observed fluorescence intensity within ~10 nanometers from the metallic surface, caused by the interplay between quenching by metal-induced energy transfer and plasmon-enhanced fluorescence, allows to observe the conformational change of a hairpin aptamer assay with an unprecedented 23-fold increase of fluorescence upon sensor saturation while maintaining sensor response times to analyte concentration within minutes. Furthermore, propagating plasmons at a flat gold film, used as the gate electrode of a graphene field-effect transistor, have been used to implement a novel multimodal sensor device that allows the simultaneous monitoring of surface mass accumulation and change electrical surface properties at the electrode. The instrument presented in chapter 2.5 has been used to investigate the layer-by-layer assembly of polyelectrolytes and revealed a remarkable difference in the kinetics of SPR and electronic

3. Summary and Outlook

response, which would be difficult to reliably observe by conventional separate experiments. With the results of the new observation method, a detailed model for the assembly process of polyelectrolyte multilayers has been derived. In both projects, prism coupling has been used to excite surface plasmons, but this approach severely limits possible applications, as dedicated instruments with a prism in ATR configuration are required. To allow integration of plasmonic enhancement in established optical biosensor architectures, several surface architectures have been developed that allow the coupling to plasmons from normal incidence and plasmonic fluorescence enhancement for epifluorescence reader configurations.

A novel nanomesh-on-mirror architecture, prepared by colloidal lithography and a thin film transfer, is presented in chapter 2.1 and it exhibits a rich spectrum of modes with different angular dispersion properties. This photonic material exhibits good short distance ordering with hexagonal symmetry and can potentially be prepared on large areas. A non-dispersive cavity mode with a high Q-factor, strongly concentrating the electromagnetic field in the spacer layer, was identified and makes this type of architecture an excellent candidate for applications in solar cells. Another nanomesh-based surface architecture, including a thermoresponsive hydrogel as an active element, has been employed for biosensor applications in chapter 2.2. By embedding metallic nanoparticles in the pores formed by nanoholes of a perforated metal film on hydrogel, a plasmonic hotspot is generated at the pore by coupling between LSP of the particle and nanoholes. With the recognition elements of the biosensor immobilized in the hydrogel matrix, highly efficient transport of the analyte to the plasmonic hotspot is facilitated. Remarkably, the transition from the collapsed or dry state to the swollen state allows using the hydrogel as a temperature-regulated valve or even as an active pump in this architecture. The working principle has successfully been demonstrated by the capture and label-free detection of IgG as model protein by SPR and the detection of 4-mercaptobenzoic acid using the SERS modality. The architecture holds potential for scaled-up production, as it is manufactured by nanoimprinting and thermal evaporation, both compatible with wafer processing. Hydrogel as a matrix for the biointerface with large binding capacity, high diffusion rates, and good fouling properties has also been employed on nanoparticle arrays. The hot spots generated by LSP are small compared to the overall sensor surface thus efficient transport

3. Summary and Outlook

of analyte to the surface is required. In the work presented in chapter 2.3, gold nanoparticles have been capped with photocrosslinkable hydrogel coatings using high-contrast 4-beam lithography. After an incubation phase in the swollen state where the hydrogel effectively covers the whole sensor surface, the hydrogel cushions are collapsed around the particles, moving the captured analytes into the plasmonic nearfield, where optical methods like PEF and SERS can take advantage of the locally high field intensity.

While the nanophotonic surface architectures discussed up to now offer remarkable performance characteristics and can be reasonably well produced in a research environment, several challenges complicate the transition to practical applications at an industrial scale. Most notably, most of the discussed architectures expose a mix of surface materials to the analyte carrying medium. This is problematic, as the unspecific adhesion of compounds contained in the medium is one of the most limiting factors of a biosensor. As the chemical properties of the surface materials (including metals, oxides, and polymers) can be very different, the development of passivation strategies accommodating all of them is very challenging. Furthermore, coupled systems like the presented nanomesh-on-mirror architecture or coupled nanohole-nanoparticle resonators are very sensitive to variations in the geometry, particularly the gap distance, and require precise replication that can be difficult to achieve with high-throughput methods and is also affected by artifacts generated by metal deposition processes.¹⁰⁴ These issues have been addressed by utilizing propagating plasmons modes excited by diffractive coupling on corrugated metal surfaces. Shallow holographic gratings offer excellent coupling efficiencies (with more than 90% absorption³⁸) at spectrally narrow resonances that can be precisely tuned by the grating period. Such gratings have been generated by UV-laser-interference-lithography (UV-LIL) and biosensor substrates have been replicated by nanoimprint lithography in a highly reproducible manner. It is noteworthy that multiple gratings with different periods, amplitude, and orientation can be superimposed on the same surface by multiple exposures.¹⁴⁸ This versatile approach allows to implementation of a variety of interesting nanophotonic surfaces for different applications. In contrast to prism coupling, diffractive coupling typically occurs at the illumination side with weak coupling efficiency through the film.¹⁴⁸ In some cases, for example, for highly scattering media, illumination from the backside would be desirable. In chapter 2.4, a method is presented that allows label-free sensing on a multi-diffractive grating with backside excitation. To achieve cross-coupling,

3. Summary and Outlook

a second period with approximately half of the period of the excitation grating is used to open an optical bandgap in the PSP dispersion relation by Bragg-scattering. The PSP on the opposite interfaces of the film generally do not phase match and thus cannot couple, however, the branches of the split resonances originating from the Bragg-scattering can be adjusted to allow cross-coupling by adjusting the modulation depth of the scattering grating. Interestingly, the change of refractive index of the medium does not directly shift the wavelength of the coupled resonances but rather modulates the relative coupling strength in distinct resonances observed in the reflectivity spectra. By monitoring the relative coupling strength, this approach yielded similar sensitivity as regular grating coupled SPR. A substrate consisting of a gold layer modulated by a crossed grating coupling the excitation light to PSP offers a fluorescence enhancement factor of ~ 100 for an epifluorescence reader, as observed in chapter 2.7. By monitoring the reflected excitation beam, an additional SPR-based readout channel has been established that substantially extends the capabilities of the device. This bimodal approach allows to not only evaluate the final fluorescence signal of an assay but to monitor all assay steps when conducted in a microfluidic system. The sensitivity of fluorescence assays can be further increased by advanced light management. Frequently, fluorescence enhancement strategies focus on the increase of field intensity at the dye excitation wavelength, which is the most important factor. However, the collection efficiency of the optical system is often limited by geometrical constraints and only a small fraction of the generated fluorescent photons is detected. Superimposed gratings, however, allow generating plasmon modes tuned for the excitation and the emission wavelength, taking advantage of plasmon mediated emission that allows shaping of the emission beam. This offers means to further increase the plasmonic enhancement of the fluorescence signal to 300-fold and allowed to push the LOD of a spatially multiplexed fluorescent immunoassay to 6 fM while monitoring the binding kinetic in a time-resolved measurement on a relatively large area of 4 x 4 mm, as demonstrated in chapter 2.8. This high sensitivity, combined with large field of view and the ability to monitor binding affinities hold the potential for new applications in personal medicine, where multiple biomarkers are analyzed in parallel to improve the diagnostic value. Adding the affinity information generates a whole new parameter for bioinformatic analysis that is not available in conventional microarrays.

3. Summary and Outlook

Concluding, in this work, a variety of nanophotonic structures have been prepared, characterized, and evaluated for their suitability for biosensor applications. The investigated geometries include flat metallic layers, corrugated metallic layers, nanoparticle arrays, and coupled 3D architectures. An active component in the form of thermoresponsive hydrogel has been included in some of the architectures not only as an optical tunable element but also as an antifouling biinterface and even as a functional microfluidic actuator. Multi-diffractive grating structures have been identified as robust and versatile architecture that allows both refractometric sensing and plasmonic enhancement of fluorescence with competitive performance to established technologies. Moreover, the approach to potentially integrate novel readout modalities into well-established analytical methods opens opportunities for the development of novel assays and protocols. It has been shown that widely used epifluorescence readers can perform label-free detection with minor modification when a grating substrate is used. Furthermore, for the first time, SPR and electronic sensing have been integrated into a single device that allowed to gain novel insight into the surface processes by simultaneous observation of mass accumulation and change of electrical properties. This new capability can improve the performance of future biosensor systems by providing additional, multimodal information that could help to reduce unspecific sensor response. Furthermore, the strong enhancement of fluorescence will allow designing biosensors that utilize the available fluorescence emission more efficiently, allowing expand the measurement result from a matrix of fluorescence intensities at the end of the assay, to a collection of time series in the fluorescent and the refractometric channel that can be used to mitigate ambiguities now encountered by cross-reactions, inconsistent spot size and other artifacts. This additional information could be used to further improve the diagnostic value of biomedical assays.

4. References

1. Corman, V. M. *et al.* Detection of 2019 novel coronavirus (2019-nCoV) by real-time RT-PCR. *Eurosurveillance* **25**, 2000045 (2020).
2. van Kasteren, P. B. *et al.* Comparison of seven commercial RT-PCR diagnostic kits for COVID-19. *J. Clin. Virol.* **128**, 104412 (2020).
3. Arnaout, R. *et al.* The Limit of Detection Matters: The Case for Benchmarking Severe Acute Respiratory Syndrome Coronavirus 2 Testing. *Clin. Infect. Dis.* (2021). doi:10.1093/cid/ciaa1382
4. Tchou, J. *et al.* Monitoring serum HER2 levels in breast cancer patients. *Springerplus* **4**, (2015).
5. Srinivasan, B. & Tung, S. Development and Applications of Portable Biosensors. *J. Lab. Autom.* **20**, 365–389 (2015).
6. Vörös, J. *et al.* Optical grating coupler biosensors. *Biomaterials* **23**, 3699–3710 (2002).
7. Kozma, P., Kehl, F., Ehrentreich-Förster, E., Stamm, C. & Bier, F. F. Integrated planar optical waveguide interferometer biosensors: A comparative review. *Biosens. Bioelectron.* **58**, 287–307 (2014).
8. Skivesen, N. *et al.* Photonic-crystal waveguide biosensor. *Opt. Express* **15**, 3169 (2007).
9. Shafiee, H. *et al.* Nanostructured Optical Photonic Crystal Biosensor for HIV Viral Load Measurement. *Sci. Reports 2014 41* **4**, 1–7 (2014).
10. Homola, J., Yee, S. S. & Gauglitz, G. Surface plasmon resonance sensors: review. *Sensors Actuators B Chem.* **54**, 3–15 (1999).
11. Su Jin Lee, † *et al.* ssDNA Aptamer-Based Surface Plasmon Resonance Biosensor for the Detection of Retinol Binding Protein 4 for the Early Diagnosis of Type 2 Diabetes. *Anal. Chem.* **80**, 2867–2873 (2008).
12. Bauch, M., Hageneder, S. & Dostalek, J. Plasmonic amplification for bioassays with epi-fluorescence readout. *Opt. Express* **22**, 32026 (2014).
13. Pollet, J. *et al.* Fast and accurate peanut allergen detection with nanobead enhanced optical fiber SPR biosensor. *Talanta* **83**, 1436–1441 (2011).
14. Taitt, C. R., Anderson, G. P., Lingerfelt, B. M., Feldstein, M. J. & Ligler, F. S. Nine-Analyte Detection Using an Array-Based Biosensor. *Anal. Chem.* **74**, 6114–6120 (2002).
15. Escobedo, C., Brolo, A. G., Gordon, R. & Sinton, D. Flow-Through vs Flow-Over: Analysis of Transport and Binding in Nanohole Array Plasmonic Biosensors. *Anal. Chem.* **82**, 10015–10020 (2010).

16. Rizzo, R. *et al.* Bloch surface wave label-free and fluorescence platform for the detection of VEGF biomarker in biological matrices. *Sensors Actuators B* **255**, 2143–2150 (2018).
17. Kurosawa, H. & Iwanaga, M. Optical-signal-enhancing metasurface platforms for fluorescent molecules at water-transparent near-infrared wavelengths. *RSC Adv.* **7**, 37076–37085 (2017).
18. Elsherif, M., Hassan, M. U., Yetisen, A. K. & Butt, H. Glucose Sensing with Phenylboronic Acid Functionalized Hydrogel-Based Optical Diffusers. *ACS Nano* **12**, 2283–2291 (2018).
19. Aizawa, M., Morioka, A., Suzuki, S. & Nagamura, Y. Enzyme immunosensor: III. Amperometric determination of human chorionic gonadotropin by membrane-bound antibody. *Anal. Biochem.* **94**, 22–28 (1979).
20. Fang, Z., Wu, W., Lu, X. & Zeng, L. Lateral flow biosensor for DNA extraction-free detection of salmonella based on aptamer mediated strand displacement amplification. *Biosens. Bioelectron.* **56**, 192–197 (2014).
21. Qiu, W. *et al.* Carbon nanotube-based lateral flow biosensor for sensitive and rapid detection of DNA sequence. *Biosens. Bioelectron.* **64**, 367–372 (2015).
22. Mukama, O. *et al.* An ultrasensitive and specific point-of-care CRISPR/Cas12 based lateral flow biosensor for the rapid detection of nucleic acids. *Biosens. Bioelectron.* **159**, 112143 (2020).
23. Peto, T. *et al.* COVID-19: Rapid antigen detection for SARS-CoV-2 by lateral flow assay: A national systematic evaluation of sensitivity and specificity for mass-testing. *EClinicalMedicine* **36**, 100924 (2021).
24. Grant, B. D. *et al.* SARS-CoV-2 Coronavirus Nucleocapsid Antigen-Detecting Half-Strip Lateral Flow Assay Toward the Development of Point of Care Tests Using Commercially Available Reagents. *Anal. Chem.* **92**, 11305–11309 (2020).
25. Atanasov, P. & Wilkins, E. Biosensor for continuous glucose monitoring. *Biotechnol. Bioeng.* **43**, 262–266 (1994).
26. Bobrowski, T. & Schuhmann, W. Long-term implantable glucose biosensors. *Curr. Opin. Electrochem.* **10**, 112–119 (2018).
27. Wisniewski, N., Moussy, F. & Reichert, W. M. Characterization of implantable biosensor membrane biofouling. *Fresenius. J. Anal. Chem.* **366**, 611–621 (2000).
28. Russo, M. J. *et al.* Antifouling Strategies for Electrochemical Biosensing: Mechanisms and Performance toward Point of Care Based Diagnostic Applications. *ACS Sensors* **6**, 1482–1507 (2021).
29. Emilsson, G. *et al.* Strongly stretched protein resistant poly(ethylene glycol) brushes prepared by grafting-to. *ACS Appl. Mater. Interfaces* **7**, 7505–7515 (2015).
30. Liu, B. *et al.* Design and mechanisms of antifouling materials for surface plasmon resonance sensors. *Acta Biomater.* **40**, 100–118 (2016).

4. References

31. Zou, Q., Kegel, L. L. & Booksh, K. S. Electrografted diazonium salt layers for antifouling on the surface of surface plasmon resonance biosensors. *Anal. Chem.* **87**, 2488–2494 (2015).
32. Vaisocherová, H. *et al.* Rapid and sensitive detection of multiple microRNAs in cell lysate by low-fouling surface plasmon resonance biosensor. *Biosens. Bioelectron.* **70**, 226–231 (2015).
33. Liu, Z. *et al.* Modification of thin film composite polyamide membranes with 3D hyperbranched polyglycerol for simultaneous improvement in their filtration performance and antifouling properties. *J. Mater. Chem. A* **5**, 23190–23197 (2017).
34. Hageneder, S. *et al.* Responsive Hydrogel Binding Matrix for Dual Signal Amplification in Fluorescence Affinity Biosensors and Peptide Microarrays. *ACS Appl. Mater. Interfaces* **13**, 27645–27655 (2021).
35. *Handbook of Biofunctional Surfaces.* (Jenny standord Publishing, 2013).
36. Banerjee, I., Pangule, R. C. & Kane, R. S. Antifouling Coatings: Recent Developments in the Design of Surfaces That Prevent Fouling by Proteins, Bacteria, and Marine Organisms. *Adv. Mater.* **23**, 690–718 (2011).
37. Sharma, S., Byrne, H. & O’Kennedy, R. J. Antibodies and antibody-derived analytical biosensors. *Essays Biochem.* **60**, 9 (2016).
38. Fossati, S., Hageneder, S., Menad, S., Maillart, E. & Dostalek, J. Multiresonant plasmonic nanostructure for ultrasensitive fluorescence biosensing. *Nanophotonics* **9**, 3673–3685 (2020).
39. Nguyen, H. H., Lee, S. H., Lee, U. J., Fermin, C. D. & Kim, M. Immobilized Enzymes in Biosensor Applications. *Mater. 2019, Vol. 12, Page 121* **12**, 121 (2019).
40. Bolduc, O. R., Pelletier, J. N. & Masson, J.-F. SPR Biosensing in Crude Serum Using Ultralow Fouling Binary Patterned Peptide SAM. *Anal. Chem.* **82**, 3699–3706 (2010).
41. Ellington, A. D. *et al.* An Aptamer-Based Quartz Crystal Protein Biosensor. *Anal. Chem.* **346**, 4488 (1990).
42. Hong, C. C., Chang, P. H., Lin, C. C. & Hong, C. L. A disposable microfluidic biochip with on-chip molecularly imprinted biosensors for optical detection of anesthetic propofol. *Biosens. Bioelectron.* **25**, 2058–2064 (2010).
43. Langmuir, I. The Adsorption of Gases on Plane Surfaces of Glass, Mica and Platinum. *J. Am. Chem. Soc.* **40**, 1361–1403 (1918).
44. Breault-Turcot, J., Poirier-Richard, H.-P., Couture, M., Pelechacz, D. & Masson, J.-F. Single chip SPR and fluorescent ELISA assay of prostate specific antigen. *Lab Chip* **15**, 4433–4440 (2015).
45. Lakowicz, J. R. *et al.* Plasmon-controlled fluorescence: a new paradigm in fluorescence spectroscopy. (2008). doi:10.1039/b802918k
46. Chen, C. *et al.* Recent advances in electrochemical glucose biosensors: a

- review. **3**, 4473 (2013).
47. Ferreira, P. C. *et al.* Wearable electrochemical sensors for forensic and clinical applications. *TrAC Trends Anal. Chem.* **119**, 115622 (2019).
 48. Wang, D., Noël, V. & Piro, B. Electrolytic gated organic field-effect transistors for application in biosensors—A review. *Electron.* **5**, (2016).
 49. Pohanka, M. The piezoelectric biosensors: Principles and applications, a review. *Int. J. Electrochem. Sci.* **12**, 496–506 (2017).
 50. Seplveda, B. *et al.* Optical biosensor microsystems based on the integration of highly sensitive Mach-Zehnder interferometer devices. *J. Opt. A Pure Appl. Opt.* **8**, (2006).
 51. Jin, G. *et al.* Development of biosensor based on imaging ellipsometry and biomedical applications. (2010). doi:10.1016/j.tsf.2010.12.175
 52. *Surface Plasmon Resonance Based Sensors.* **4**, (Springer Berlin Heidelberg, 2006).
 53. Anker, J. N. *et al.* Biosensing with plasmonic nanosensors. *Nat. Mater.* **7**, 442–453 (2008).
 54. Zhao, Y., Tong, R. jie, Xia, F. & Peng, Y. Current status of optical fiber biosensor based on surface plasmon resonance. *Biosens. Bioelectron.* **142**, 111505 (2019).
 55. Jang, H. S. *et al.* Optical fiber SPR biosensor with sandwich assay for the detection of prostate specific antigen. *Opt. Commun.* **282**, 2827–2830 (2009).
 56. Mitchell, J. S., Wu, Y., Cook, C. J. & Main, L. Sensitivity enhancement of surface plasmon resonance biosensing of small molecules. *Anal. Biochem.* **343**, 125–135 (2005).
 57. Liu, J. & Lu, Y. Adenosine-Dependent Assembly of Aptazyme-Functionalized Gold Nanoparticles and Its Application as a Colorimetric Biosensor. *Anal. Chem.* **76**, 1627–1632 (2004).
 58. Yu, L. & Li, N. Noble Metal Nanoparticles-Based Colorimetric Biosensor for Visual Quantification: A Mini Review. *Chemosens. 2019, Vol. 7, Page 53* **7**, 53 (2019).
 59. Resch-Genger, U., Grabolle, M., Cavaliere-Jaricot, S., Nitschke, R. & Nann, T. Quantum dots versus organic dyes as fluorescent labels. *Nat. Methods* **5**, 763–775 (2008).
 60. Bauch, M., Toma, K., Toma, M., Zhang, Q. & Dostalek, J. Plasmon-Enhanced Fluorescence Biosensors: a Review. *Plasmonics* **9**, 781–799 (2014).
 61. *Principles of Fluorescence Spectroscopy.* (Springer US, 2006). doi:10.1007/978-0-387-46312-4
 62. Vaisocherová-Lísalová, H. *et al.* Low-fouling surface plasmon resonance biosensor for multi-step detection of foodborne bacterial pathogens in

- complex food samples. *Biosens. Bioelectron.* **80**, 84–90 (2016).
63. Reiner, A. T. *et al.* Magnetic nanoparticle-enhanced surface plasmon resonance biosensor for extracellular vesicle analysis. *Analyst* **142**, 3913–3921 (2017).
64. Shi, D. *et al.* Isothermal and rapid detection of pathogenic microorganisms using a nano-rolling circle amplification-surface plasmon resonance biosensor. *Biosens. Bioelectron.* **62**, 280–287 (2014).
65. Lai, W., Wei, Q., Xu, M., Zhuang, J. & Tang, D. Enzyme-controlled dissolution of MnO₂ nanoflakes with enzyme cascade amplification for colorimetric immunoassay. *Biosens. Bioelectron.* **89**, 645–651 (2017).
66. Kashiwakuma, T. *et al.* Detection of hepatitis C virus specific core protein in serum of patients by a sensitive fluorescence enzyme immunoassay (FEIA). *J. Immunol. Methods* **190**, 79–89 (1996).
67. Armbruster, D. A. & Pry, T. Limit of Blank, Limit of Detection and Limit of Quantitation. *Clin. Biochem. Rev.* **29**, S49 (2008).
68. Gorgannezhad, L., Umer, M., Islam, M. N., Nguyen, N. T. & Shiddiky, M. J. A. Circulating tumor DNA and liquid biopsy: Opportunities, challenges, and recent advances in detection technologies. *Lab Chip* **18**, 1174–1196 (2018).
69. Alberghina, D., Giannetto, C., Vazzana, I., Ferrantelli, V. & Piccione, G. Reference intervals for total protein concentration, serum protein fractions, and albumin/globulin ratios in clinically healthy dairy cows. *J. Vet. Diagnostic Investig.* **23**, 111–114 (2011).
70. Wood, R. W. On a remarkable case of uneven distribution of light in a diffraction grating spectrum. *Proc. Phys. Soc. London* **18**, 269–275 (1902).
71. Fano, U. The Theory of Anomalous Diffraction Gratings and of Quasi-Stationary Waves on Metallic Surfaces (Sommerfeld's Waves). *J. Opt. Soc. Am.* **31**, 213 (1941).
72. Otto, A. Excitation of nonradiative surface plasma waves in silver by the method of frustrated total reflection. *Zeitschrift für Phys.* **216**, 398–410 (1968).
73. Kretschmann, E. & Raether, H. Radiative Decay of Non Radiative Surface Plasmons Excited by Light. *Zeitschrift für Naturforsch. - Sect. A J. Phys. Sci.* **23**, 2135–2136 (1968).
74. Knoll, W. INTERFACES AND THIN FILMS AS SEEN BY BOUND ELECTROMAGNETIC WAVES. *Annu. Rev. Phys. Chem.* **49**, 569–638 (1998).
75. Genevet, P., Capasso, F., Aieta, F., Khorasaninejad, M. & Devlin, R. Recent advances in planar optics: from plasmonic to dielectric metasurfaces. *Optica* **4**, 139 (2017).
76. Kotsifaki, D. G. & Chormaic, S. N. Plasmonic optical tweezers based on nanostructures: Fundamentals, advances and prospects. *Nanophotonics* **8**, 1227–1245 (2019).

77. Fu, Y. & Zhou, X. Plasmonic Lenses: A Review. *Plasmonics* **5**, 287–310 (2010).
78. Koch, U. *et al.* A monolithic bipolar CMOS electronic–plasmonic high-speed transmitter. *Nat. Electron.* **3**, 338–345 (2020).
79. Emboras, A. *et al.* Electrically controlled plasmonic switches and modulators. *IEEE J. Sel. Top. Quantum Electron.* **21**, 276–283 (2015).
80. Burla, M. *et al.* 500 GHz plasmonic Mach-Zehnder modulator enabling sub-THz microwave photonics. *APL Photonics* **4**, 56106 (2019).
81. Yuan, M. *et al.* Terahertz Spoof Surface Plasmonic Logic Gates. *iScience* **23**, 101685 (2020).
82. Špačková, B., Wrobel, P., Bocková, M. & Homola, J. Optical Biosensors Based on Plasmonic Nanostructures: A Review. *Proc. IEEE* **104**, 2380–2408 (2016).
83. Yu, F. Surface Plasmon Fluorescence Spectroscopy and Surface Plasmon Diffraction in Biomolecular Interaction Studies. *Prism* (2004).
84. Akkilic, N., Geschwindner, S. & Höök, F. Single-molecule biosensors: Recent advances and applications. *Biosensors and Bioelectronics* **151**, 111944 (2020).
85. Maier, S. A. *Plasmonics: Fundamentals and applications. Plasmonics: Fundamentals and Applications* (2007). doi:10.1007/0-387-37825-1
86. Kedenburg, S., Vieweg, M., Gissibl, T. & Giessen, H. Linear refractive index and absorption measurements of nonlinear optical liquids in the visible and near-infrared spectral region. *Opt. Mater. Express* **2**, 1588 (2012).
87. Johnson, P. B. & Christy, R. W. Optical constants of transition metals: Ti, V, Cr, Mn, Fe, Co, Ni, and Pd. *Phys. Rev. B* **9**, 5056–5070 (1974).
88. Chu, M.-W. *et al.* Probing Bright and Dark Surface-Plasmon Modes in Individual and Coupled Noble Metal Nanoparticles Using an Electron Beam. *Nano Lett.* **9**, 399–404 (2008).
89. Dallapiccola, R., Dubois, C., Gopinath, A., Stellacci, F. & Negro, L. D. Near-field excitation and near-field detection of propagating surface plasmon polaritons on Au waveguide structures. *Appl. Phys. Lett.* **94**, 243118 (2009).
90. Lavers, C. R. & Wilkinson, J. S. A waveguide-coupled surface-plasmon sensor for an aqueous environment. *Sensors Actuators B Chem.* **22**, 75–81 (1994).
91. Krenn, J. R. *et al.* Direct observation of localized surface plasmon coupling. *Phys. Rev. B* **60**, 5029 (1999).
92. Khan, I. *et al.* Multidiffractive Broadband Plasmonic Absorber. *Adv. Opt. Mater.* **4**, 435–443 (2016).
93. Mie, G. Beiträge zur Optik trüber Medien, speziell kolloidaler Metallösungen. *Ann. Phys.* **330**, 377–445 (1908).

4. References

94. Grand, J. *et al.* Optical Extinction Spectroscopy of Oblate, Prolate and Ellipsoid Shaped Gold Nanoparticles: Experiments and Theory. *Plasmon. 2006* **12** 1, 135–140 (2006).
95. Mayer, K. M. & Hafner, J. H. Localized Surface Plasmon Resonance Sensors. *Chem. Rev.* **111**, 3828–3857 (2011).
96. Petryayeva, E. & Krull, U. J. Localized surface plasmon resonance: Nanostructures, bioassays and biosensing-A review. *Anal. Chim. Acta* **706**, 8–24 (2011).
97. Quilis, N. G., Sharma, N., Fossati, S., Knoll, W. & Dostalek, J. Responsive Polymer Networks and Brushes for Active Plasmonics. in *Polymer and Biopolymer Brushes* 687–707 (John Wiley & Sons, Inc., 2017). doi:10.1002/9781119455042.ch24
98. Raether, H. Surface-Plasmons on Smooth and Rough Surfaces and on Gratings. *Springer Tracts in Modern Physics* **111**, 1–133 (1988).
99. McPeak, K. M. *et al.* Plasmonic Films Can Easily Be Better: Rules and Recipes. *ACS Photonics* **2**, 326–333 (2015).
100. Gupta, R., Dyer, M. J. & Weimer, W. A. Preparation and characterization of surface plasmon resonance tunable gold and silver films. *J. Appl. Phys.* **92**, 5264–5271 (2002).
101. Auguie, B. & Barnes, W. L. Collective Resonances in Gold Nanoparticle Arrays. *Phys. Rev. Lett.* **101**, 143902 (2008).
102. Stelling, C., Fossati, S., Dostalek, J. & Retsch, M. Surface plasmon modes of nanomesh-on-mirror nanocavities prepared by nanosphere lithography. *Nanoscale* **10**, 17983–17989 (2018).
103. Escobedo, C. On-chip nanohole array based sensing: A review. *Lab Chip* **13**, 2445–2463 (2013).
104. Shen, Y. *et al.* Plasmonic gold mushroom arrays with refractive index sensing figures of merit approaching the theoretical limit. *Nat. Commun.* **4**, 2381 (2013).
105. Prodan, E. A Hybridization Model for the Plasmon Response of Complex Nanostructures. *Science (80-.)*. **302**, 419–422 (2003).
106. Brown, L. V., Sobhani, H., Lassiter, J. B., Nordlander, P. & Halas, N. J. Heterodimers: Plasmonic Properties of Mismatched Nanoparticle Pairs. *ACS Nano* **4**, 819–832 (2010).
107. Kaniber, M. *et al.* Surface plasmon resonance spectroscopy of single bowtie nano-antennas using a differential reflectivity method. *Sci. Reports* **2016** **6** 1–10 (2016).
108. Hentschel, M., Dregely, D., Vogelgesang, R., Giessen, H. & Liu, N. Plasmonic Oligomers: The Role of Individual Particles in Collective Behavior. *ACS Nano* **5**, 2042–2050 (2011).
109. Pang, J. S. *et al.* Tunable Three-Dimensional Plasmonic Arrays for Large

- Near-Infrared Fluorescence Enhancement. *ACS Appl. Mater. Interfaces* **11**, 23083–23092 (2019).
110. Hackett, L. P. *et al.* Spectrometer-Free Plasmonic Biosensing with Metal–Insulator–Metal Nanocup Arrays. *ACS Sensors* **3**, 290–298 (2018).
111. MacDonald, K. F. & Zheludev, N. I. Active plasmonics: current status. *Laser Photon. Rev.* **4**, 562–567 (2010).
112. Gehan, H. *et al.* Design and optical properties of active polymer-coated plasmonic nanostructures. *J. Phys. Chem. Lett.* **2**, 926–931 (2011).
113. Tokarev, I. & Minko, S. Tunable plasmonic nanostructures from noble metal nanoparticles and stimuli-responsive polymers. *Soft Matter* **8**, 5980–5987 (2012).
114. Jiang, N., Zhuo, X. & Wang, J. Active Plasmonics: Principles, Structures, and Applications. *Chem. Rev.* **118**, 3054–3099 (2018).
115. Anac, I. *et al.* Optical characterization of co-nonsolvency effects in thin responsive PNIPAAm-based gel layers exposed to ethanol/water mixtures. *Macromol. Chem. Phys.* **211**, 1018–1025 (2010).
116. Harmon, M. E., Kuckling, D. & Frank, C. W. Photo-cross-linkable PNIPAAm copolymers. 2. Effects of constraint on temperature and pH-responsive hydrogel layers. *Macromolecules* **36**, 162–172 (2003).
117. Junk, M. J. N., Ilke, A., Menges, B. & Jonas, U. Analysis of optical gradient profiles during temperature- and salt-dependent swelling of thin responsive hydrogel films. *Langmuir* **26**, 12253–12259 (2010).
118. Hale, G. M. & Querry, M. R. Optical Constants of Water in the 200-nm to 200- μ m Wavelength Region. *Appl. Opt. Vol. 12, Issue 3, pp. 555-563* **12**, 555–563 (1973).
119. Toma, M., Jonas, U., Mateescu, A., Knoll, W. & Dostalek, J. Active control of SPR by thermoresponsive hydrogels for biosensor applications. *J. Phys. Chem. C* **117**, 11705–11712 (2013).
120. George, S. M., Tandon, S. & Kandasubramanian, B. Advancements in Hydrogel-Functionalized Immunosensing Platforms. *ACS Omega* **5**, 2060–2068 (2020).
121. Rodriguez, E. A. *et al.* The growing and glowing toolbox of fluorescent and photoactive proteins. *Trends Biochem. Sci.* **42**, 111 (2017).
122. Wu, B., Piatkevich, K. D., Lionnet, T., Singer, R. H. & Verkhusha, V. V. Modern fluorescent proteins and imaging technologies to study gene expression, nuclear localization, and dynamics. *Curr. Opin. Cell Biol.* **23**, 310–317 (2011).
123. Zheng, Q. *et al.* Ultra-stable organic fluorophores for single-molecule research. *Chem. Soc. Rev.* **43**, 1044–1056 (2014).
124. Song, L., Hennink, E. J., Young, I. T. & Tanke, H. J. Photobleaching kinetics of fluorescein in quantitative fluorescence microscopy. *Biophys. J.* **68**, 2588–

- 2600 (1995).
125. Chance, R. R., Miller, A. H., Prock, A. & Silbey, R. Fluorescence and energy transfer near interfaces: The complete and quantitative description of the Eu⁺³/mirror systems. *J. Chem. Phys.* **63**, 1589–1595 (1975).
 126. Gregor, I., Chizhik, A., Karedla, N. & Enderlein, J. Metal-induced energy transfer. *Nanophotonics* **8**, 1689–1699 (2019).
 127. Lakowicz, J. R. Radiative decay engineering 3. Surface plasmon-coupled directional emission. *Anal. Biochem.* **324**, 153–169 (2004).
 128. Ruckstuhl, T., Enderlein, J., Jung, S. & Seeger, S. Forbidden light detection from single molecules. *Anal. Chem.* **72**, 2117–2123 (2000).
 129. Bauch, M. & Dostalek, J. Collective localized surface plasmons for high performance fluorescence biosensing. *Opt. Express* **21**, 637–644 (2013).
 130. Shu, Q. Q. & Hansma, P. K. Fluorescent apparent quantum yields for excited molecules near dielectric interfaces. *Thin Solid Films* **384**, 76–84 (2001).
 131. Campion, A., Gallo, A. R., Harris, C. B., Robota, H. J. & Whitmore, P. M. Electronic energy transfer to metal surfaces: a test of classical image dipole theory at short distances. *Chem. Phys. Lett.* **73**, 447–450 (1980).
 132. Fort, E. & Grésillon, S. Surface enhanced fluorescence. *J. Phys. D. Appl. Phys.* **41**, 013001 (2008).
 133. Barnes, W. L., Dereux, A. & Ebbesen, T. W. Surface plasmon subwavelength optics. *Nature* **424**, 824–830 (2003).
 134. Lakowicz, J. R. *et al.* Radiative decay engineering: 2. Effects of silver island films on fluorescence intensity, lifetimes, and resonance energy transfer. *Anal. Biochem.* **301**, 261–277 (2002).
 135. Enderlein, J. & Ruckstuhl, T. The efficiency of surface-plasmon coupled emission for sensitive fluorescence detection. *Opt. Express* **13**, 8855 (2005).
 136. Kinkhabwala, A. *et al.* Large single-molecule fluorescence enhancements produced by a bowtie nanoantenna. *Nat. Photonics* **2009 311** **3**, 654–657 (2009).
 137. Zhang, W. *et al.* Giant and uniform fluorescence enhancement over large areas using plasmonic nanodots in 3D resonant cavity nanoantenna by nanoimprinting. *Nanotechnology* **23**, 225301 (2012).
 138. Kravets, V. G., Kabashin, A. V., Barnes, W. L. & Grigorenko, A. N. Plasmonic Surface Lattice Resonances: A Review of Properties and Applications. *Chem. Rev.* **118**, 5912–5951 (2018).
 139. Neubrech, F., Huck, C., Weber, K., Pucci, A. & Giessen, H. Surface-Enhanced Infrared Spectroscopy Using Resonant Nanoantennas. *Chem. Rev.* **117**, 5110–5145 (2017).
 140. Langer, J. *et al.* Present and future of surface-enhanced Raman scattering. *ACS Nano* **14**, 28–117 (2020).

141. Nguyen, H. H., Park, J., Kang, S. & Kim, M. Surface plasmon resonance: A versatile technique for biosensor applications. *Sensors (Switzerland)* **15**, 10481–10510 (2015).
142. Sandhyarani, N. Surface modification methods for electrochemical biosensors. in *Electrochemical Biosensors* 45–75 (Elsevier, 2019). doi:10.1016/B978-0-12-816491-4.00003-6
143. Morales, M. A. & Halpern, J. M. Guide to Selecting a Biorecognition Element for Biosensors. *Bioconjug. Chem.* **29**, 3231–3239 (2018).
144. www.biocore.com.
145. www.bionavis.com.
146. www.bruker.com.
147. Piliarik, M., Vala, M., Tichý, I. & Homola, J. Compact and low-cost biosensor based on novel approach to spectroscopy of surface plasmons. *Biosens. Bioelectron.* **24**, 3430–3435 (2009).
148. Adam, P., Dostálek, J. & Homola, J. Multiple surface plasmon spectroscopy for study of biomolecular systems. *Sensors Actuators, B Chem.* **113**, 774–781 (2006).
149. Bocková, M., Slabý, J., Špringer, T. & Homola, J. Advances in Surface Plasmon Resonance Imaging and Microscopy and Their Biological Applications. *Annu. Rev. Anal. Chem.* **12**, 151–176 (2019).
150. Belushkin, A., Yesilkoy, F. & Altug, H. Nanoparticle-Enhanced Plasmonic Biosensor for Digital Biomarker Detection in a Microarray. *ACS Nano* **12**, 4453–4461 (2018).
151. Hu, W., Chen, H., Shi, Z. & Yu, L. Dual signal amplification of surface plasmon resonance imaging for sensitive immunoassay of tumor marker. *Anal. Biochem.* **453**, 16–21 (2014).
152. Foudeh, A. M., Daoud, J. T., Faucher, S. P., Veres, T. & Tabrizian, M. Sub-femtomole detection of 16s rRNA from Legionella pneumophila using surface plasmon resonance imaging. *Biosens. Bioelectron.* **52**, 129–135 (2014).
153. Morlay, A., Piat, F., Mercey, T. & Roupioz, Y. Immunological detection of Cronobacter and Salmonella in powdered infant formula by plasmonic label-free assay. *Lett. Appl. Microbiol.* **62**, 459–465 (2016).
154. Tu, L. *et al.* Label-free and real-time monitoring of single cell attachment on template-stripped plasmonic nano-holes. *Sci. Rep.* **7**, (2017).
155. Hageneder, S., Bauch, M. & Dostalek, J. Plasmonically amplified bioassay - Total internal reflection fluorescence vs. epifluorescence geometry. *Talanta* **156–157**, 225–231 (2016).
156. Kambhampati, D., Nielsen, P. E. & Knoll, W. Investigating the kinetics of DNA–DNA and PNA–DNA interactions using surface plasmon resonance-enhanced fluorescence spectroscopy. *Biosens. Bioelectron.* **16**, 1109–1118 (2001).

4. References

157. Wang, Y. *et al.* A novel aptasensor based on silver nanoparticle enhanced fluorescence. *Biosens. Bioelectron.* **32**, 76–81 (2012).
158. Punj, D. *et al.* Self-Assembled Nanoparticle Dimer Antennas for Plasmonic-Enhanced Single-Molecule Fluorescence Detection at Micromolar Concentrations. *ACS Photonics* **2**, 1099–1107 (2015).
159. Brolo, A. G. *et al.* Enhanced Fluorescence from Arrays of Nanoholes in a Gold Film. *J. Am. Chem. Soc.* **127**, 14936–14941 (2005).
160. Tang, F., Ma, N., Wang, X., He, F. & Li, L. Hybrid conjugated polymer-Ag@PNIPAM fluorescent nanoparticles with metal-enhanced fluorescence. *J. Mater. Chem.* **21**, 16943–16948 (2011).
161. Wu, W., Shen, J., Banerjee, P. & Zhou, S. A Multifunctional Nanoplatfrom Based on Responsive Fluorescent Plasmonic ZnO-Au@PEG Hybrid Nanogels. *Adv. Funct. Mater.* **21**, 2830–2839 (2011).
162. Lee, S. H., Bantz, K. C., Lindquist, N. C., Oh, S.-H. & Haynes, C. L. Self-Assembled Plasmonic Nanohole Arrays. *Langmuir* **25**, 13685–13693 (2009).
163. Stranik, O., McEvoy, H. M., McDonagh, C. & MacCraith, B. D. Plasmonic enhancement of fluorescence for sensor applications. *Sensors Actuators B Chem.* **107**, 148–153 (2005).
164. Valsecchi, C., Gomez Armas, L. E. & Weber de Menezes, J. Large Area Nanohole Arrays for Sensing Fabricated by Interference Lithography. *Sensors* **19**, 2182 (2019).
165. Kooy, N., Mohamed, K., Pin, L. T. & Guan, O. S. A review of roll-to-roll nanoimprint lithography. *Nanoscale Res. Lett.* **9**, 1–13 (2014).
166. Taflove, A. & Hagness, S. C. *Computational Electrodynamics: The Finite-Difference Time-Domain Method, Third Edition.* Artech House (2005).
167. Ai, B., Yu, Y., Möhwald, H., Zhang, G. & Yang, B. Plasmonic films based on colloidal lithography. *Advances in Colloid and Interface Science* **206**, 5–16 (2014).
168. Toma, K., Knoll, W. & Dostalek, J. Long range surface plasmon-coupled fluorescence emission for biosensor applications. *2011 Int. Work. Biophotonics, BIOPHOTONICS 2011* **19**, 97–106 (2011).
169. Quilis, N. G. *et al.* UV-Laser Interference Lithography for Local Functionalization of Plasmonic Nanostructures with Responsive Hydrogel. *J. Phys. Chem. C* **124**, 3297–3305 (2020).
170. Schiff, H. Nanoimprint lithography: An old story in modern times? A review. *J. Vac. Sci. Technol. B Microelectron. Nanom. Struct.* **26**, 458–480 (2008).
171. Gisbert Quilis, N. *et al.* Tunable laser interference lithography preparation of plasmonic nanoparticle arrays tailored for SERS. *Nanoscale* **10**, 10268–10276 (2018).
172. Bauch, M. New enhancement strategies for plasmon-enhanced fluorescence biosensors. (2014).

4. References

173. Stefan Fossati. A resonant plasmonic structure for fluorescence spectroscopy. (2015).
174. Saito, M. *et al.* Novel gold-capped nanopillars imprinted on a polymer film for highly sensitive plasmonic biosensing. *Anal. Chem.* **84**, 5494–5500 (2012).
175. Ahn, M. S., Chung, T. & Jeong, K. H. Structural coloration of transmission light through self-aligned and complementary plasmonic nanostructures. *Nanoscale* **10**, 6313–6317 (2018).
176. Zhou, W., Huang, P.-J. J., Ding, J. & Liu, J. Aptamer-based biosensors for biomedical diagnostics. *Analyst* **139**, 2627–2640 (2014).
177. E. Wang, R., Zhang, Y., Cai, J., Cai, W. & Gao, T. Aptamer-Based Fluorescent Biosensors. *Curr. Med. Chem.* **18**, 4175–4184 (2011).

5. Appendix

5.1. Supporting Information – Surface Plasmon Modes of Nanomesh-on-Mirror Nanocavities prepared by Nanosphere Lithography

The following supporting information is reprinted with the permission of the Royal Society of Chemistry.

Christian Stelling, Stefan Fossati, Jakub Dostalek, and Markus Retsch Surface plasmon modes of nanomesh-on-mirror nanocavities prepared by nanosphere lithography. *Nanoscale* 10, 17983–17989 (2018). <https://doi.org/10.1039/c8nr05499a>

Copyright © The Royal Society of Chemistry 2018

5.1. Supporting Information – Surface Plasmon Modes of Nanomesh-on-Mirror Nanocavities prepared by Nanosphere Lithography

Electronic Supplementary Material (ESI) for Nanoscale.
This journal is © The Royal Society of Chemistry 2018

Supporting Information: Surface Plasmon Modes of Nanomesh-on-Mirror

Nanocavities Prepared by Nanosphere Lithography

Christian Stelling,¹ Stefan Fossati,² Jakub Dostalek,^{2*} Markus Retsch^{1*}

¹ Department of Chemistry, University of Bayreuth, 95447 Bayreuth, Germany

² Biosensor Technologies, AIT-Austrian Institute of Technology GmbH, Konrad-Lorenz-Strasse 24 | 3430 Tulln,
Austria

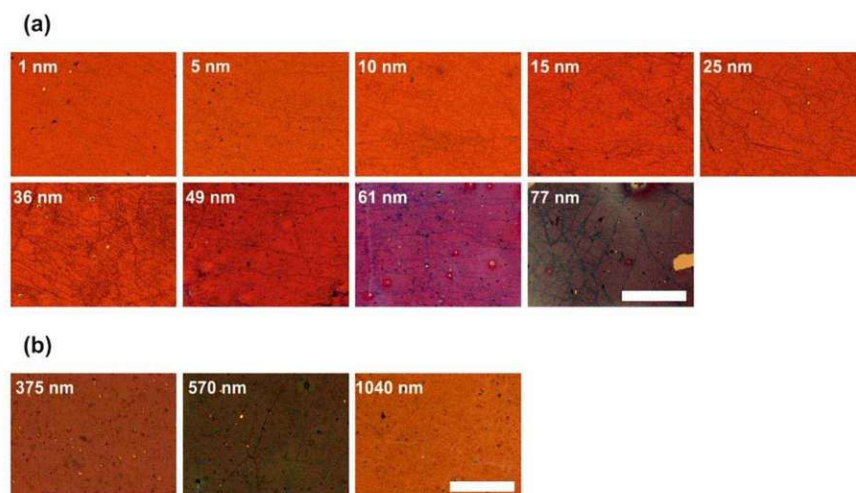


Figure S1. Optical microscopy images of MIM structures with (a) distinct spacer thicknesses and (b) distinct lattice periods. Scale bars are 500 μm .

S1

5.1. Supporting Information – Surface Plasmon Modes of Nanomesh-on-Mirror Nanocavities prepared by Nanosphere Lithography

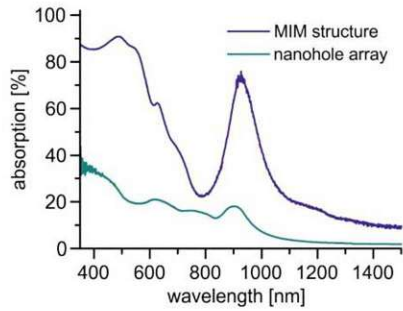


Figure S2. Measured absorption (1-reflectance) of a MIM structure with $p = 570$ nm, $t_{\text{gold}} = 100$ nm, $t_{\text{gap}} = 50$ nm and $t_{\text{hole}} = 90$ nm compared to an isolated gold nanohole array with $p = 570$ nm.

S2

5.1. Supporting Information – Surface Plasmon Modes of Nanomesh-on-Mirror Nanocavities prepared by Nanosphere Lithography

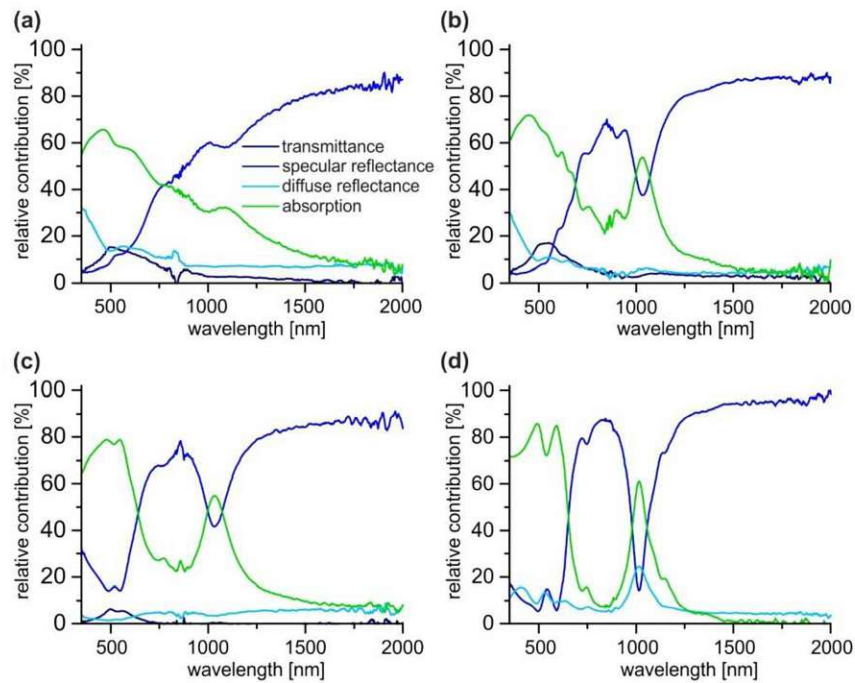


Figure S3. Influence mirror thickness. Transmittance, specular reflectance, diffuse reflectance and absorption for MIM structures with $p = 570$ nm, $t_{\text{gap}} = 30$ nm, $t_{\text{hole}} = 80$ nm and (a) $t_{\text{gold}} = 13$ nm (b) $t_{\text{gold}} = 21$ nm (c) $t_{\text{gold}} = 40$ nm (d) $t_{\text{gold}} = 100$ nm.

S3

5.1. Supporting Information – Surface Plasmon Modes of Nanomesh-on-Mirror Nanocavities prepared by Nanosphere Lithography

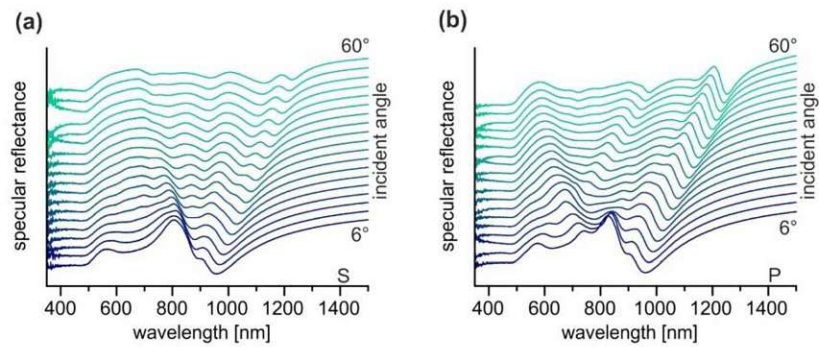


Figure S4. Angle-resolved reflectance measurements with (a) s-polarized and (b) p-polarized light of an isolated gold nanohole array with $p = 570$ nm.

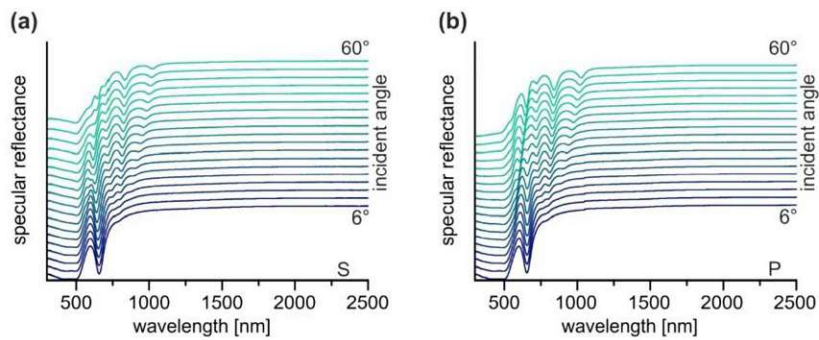


Figure S5. Angle-resolved reflectance measurements with (a) s-polarized and (b) p-polarized light of a MIM structure with $p = 375$ nm, $t_{\text{gold}} = 100$ nm, $t_{\text{gap}} = 40$ nm and $t_{\text{hole}} = 90$ nm.

S4

5.1. Supporting Information – Surface Plasmon Modes of Nanomesh-on-Mirror Nanocavities prepared by Nanosphere Lithography

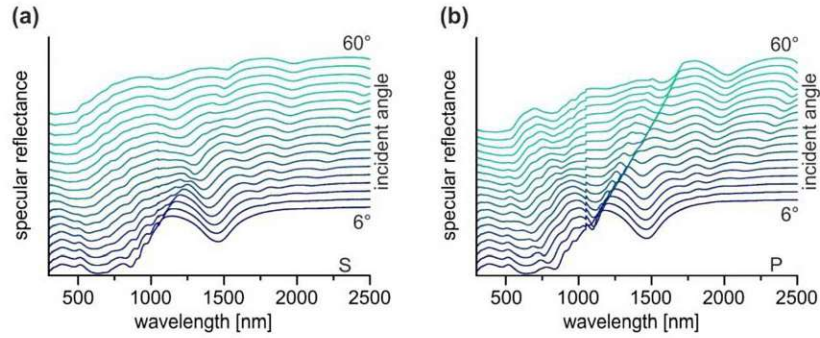


Figure S6. Angle-resolved reflectance measurements with (a) s-polarized and (b) p-polarized light of a MIM structure with $p = 1040$ nm, $t_{\text{gold}} = 100$ nm, $t_{\text{gap}} = 40$ nm and $t_{\text{hole}} = 90$ nm.

5.1. Supporting Information – Surface Plasmon Modes of Nanomesh-on-Mirror Nanocavities prepared by Nanosphere Lithography

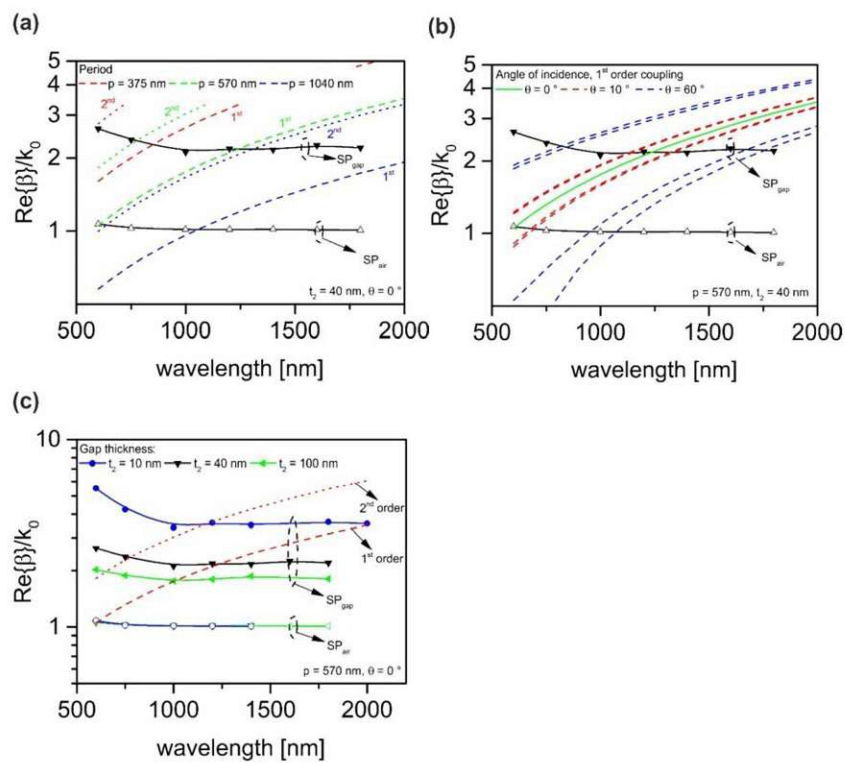


Figure S7. Analytically derived dispersion curves of the two SPP modes present in the MIM structures. (a) Influence of the lattice period at normal incidence. (b) Influence of the angle of incidence for $p = 570$ nm. Assumed coupling via all (0,1), (1,0), (1,1), (0,1), (1,0) and (1,1) orders. The plane of incidence was assumed to be parallel with (0,1) and (0,1) orders. (c) Influence of the spacer thickness for $p = 570$ nm at normal incidence. β is the propagation constant of guided modes, k_0 is the light wavenumber in vacuum.

5.1. Supporting Information – Surface Plasmon Modes of Nanomesh-on-Mirror Nanocavities prepared by Nanosphere Lithography

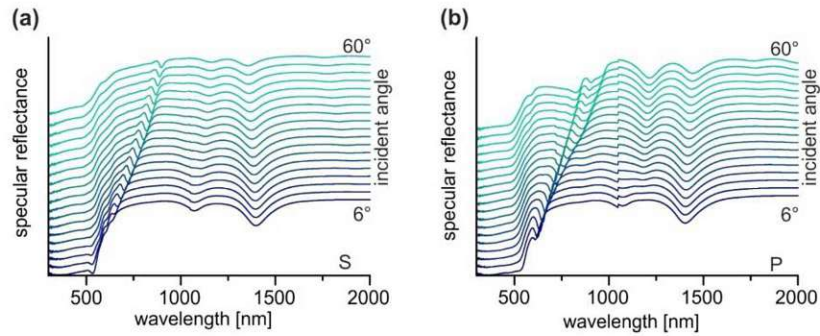


Figure S8. Angle-resolved reflectance measurements with (a) s-polarized and (b) p-polarized light of a MIM structure with $p = 570$ nm, $t_{\text{gold}} = 100$ nm, $t_{\text{gap}} = 1$ nm and $t_{\text{hole}} = 90$ nm.

S7

5.1. Supporting Information – Surface Plasmon Modes of Nanomesh-on-Mirror Nanocavities prepared by Nanosphere Lithography

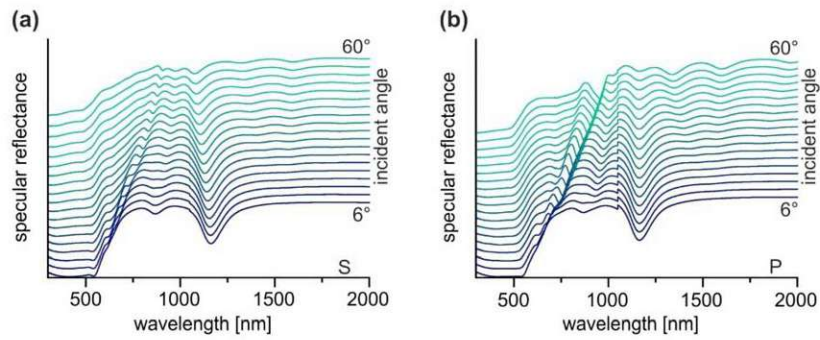


Figure S9. Angle-resolved reflectance measurements with (a) s-polarized and (b) p-polarized light of a MIM structure with $p = 570$ nm, $t_{\text{gold}} = 100$ nm, $t_{\text{gap}} = 15$ nm and $t_{\text{hole}} = 90$ nm.

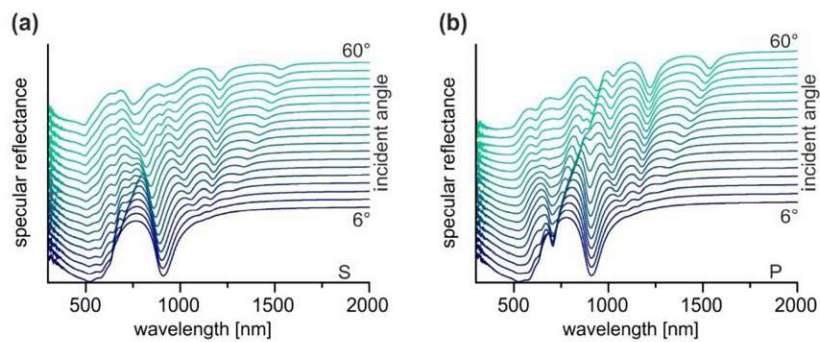


Figure S10. Angle-resolved reflectance measurements with (a) s-polarized and (b) p-polarized light of a MIM structure with $p = 570$ nm, $t_{\text{gold}} = 100$ nm, $t_{\text{gap}} = 50$ nm and $t_{\text{hole}} = 90$ nm.

S8

5.1. Supporting Information – Surface Plasmon Modes of Nanomesh-on-Mirror Nanocavities prepared by Nanosphere Lithography

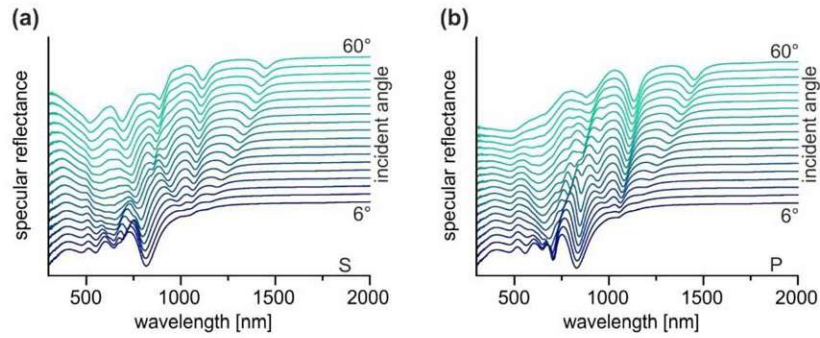


Figure S11. Angle-resolved reflectance measurements with (a) s-polarized and (b) p-polarized light of a MIM structure with $p = 570$ nm, $t_{\text{gold}} = 100$ nm, $t_{\text{gap}} = 77$ nm and $t_{\text{hole}} = 90$ nm.

5.1. Supporting Information – Surface Plasmon Modes of Nanomesh-on-Mirror Nanocavities prepared by Nanosphere Lithography

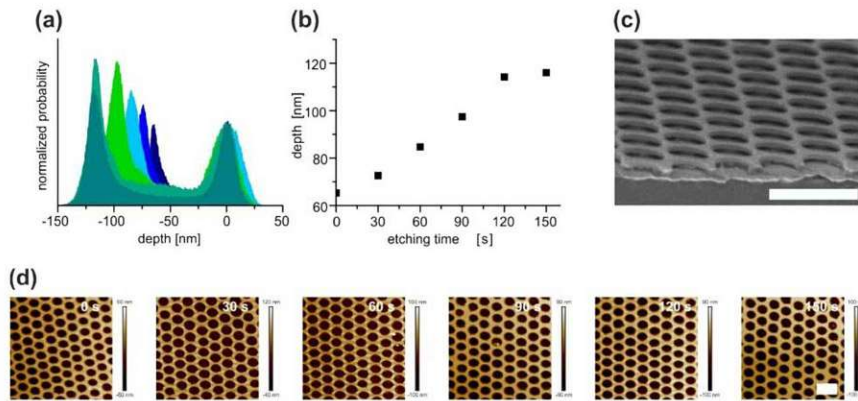


Figure S12. Plasma etching of MIM structure. (a) Depth profile of the MIM structure measured with AFM after consecutive etching steps. (b) Depth of the plasma etched MIM structure with increasing etching time. (c) Side-view SEM image of the MIM structure etched for 150 s. (d) AFM images of the MIM structure after each etching step, Scale bars are 1 μm .

5.1. Supporting Information – Surface Plasmon Modes of Nanomesh-on-Mirror Nanocavities prepared by Nanosphere Lithography

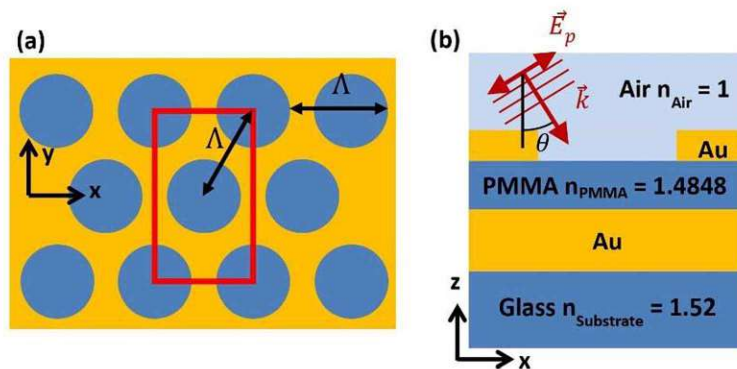


Figure S13. Schematic of geometry used in FDTD simulation for hexagonal nanomeshes with a rectangular unit cell. (a) Top view. The red rectangle indicates simulation volume with Bloch boundary conditions. A vertical cross-section is shown in (b) with the definition of the angle of incidence θ and E-field orientation E_0 for p-polarization.

S11

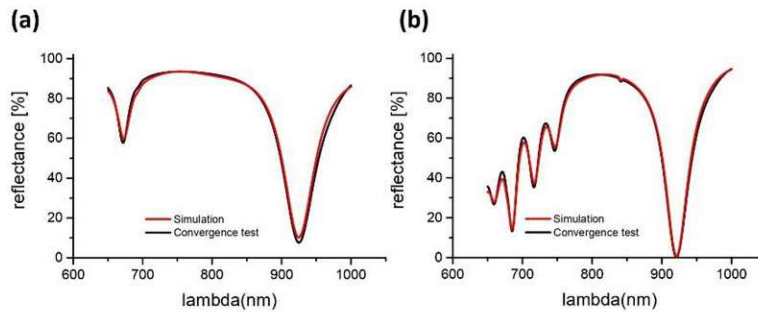


Figure S14. Convergence of the simulation was tested by increase of the mesh resolution. Simulations were run with a uniform mesh of $(x,y,z) = (5 \text{ nm}, 5 \text{ nm}, 2 \text{ nm})$ unit cell size. The Mesh size was reduced to $(x,y,z) = (2 \text{ nm}, 2 \text{ nm}, 2 \text{ nm})$ for selected configurations to confirm the convergence of results. Here, the convergence test for the shorter wavelength part of the spectrum is shown for the geometry used to study near-field distribution in Figure 4 for (a) normal incident light and (b) excitation with $\theta = 22^\circ$ angle of incidence.

5.2. Supporting Information – Actuated Plasmonic Nanohole Arrays for Sensing and Optical Spectroscopy Applications

The following supporting information is reprinted with the permission of the Royal Society of Chemistry.

Daria Kotlarek, Stefan Fossati, Priyamvada Venugopalan, Nestor Gisbert Quilis, Jiří Slabý, Jiří Homola, Médéric Lequeux, Frédéric Amiard, Marc Lamy de la Chapelle, Ulrich Jonas, and Jakub Dostálek Actuated plasmonic nanohole arrays for sensing and optical spectroscopy applications. *Nanoscale* 12, 9756–9768 (2020).
<https://doi.org/10.1039/d0nr00761g>

Copyright © The Royal Society of Chemistry 2020

5.2. Supporting Information – Actuated Plasmonic Nanohole Arrays for Sensing and Optical Spectroscopy Applications

Electronic Supplementary Material (ESI) for Nanoscale.
This journal is © The Royal Society of Chemistry 2020

Supporting information

Actuated Plasmonic Nanohole Arrays for Sensing and Optical Spectroscopy Applications

Daria Kotlarek^a, Stefan Fossati^b, Priyamvada Venugopalan^{a,b,c}, Nestor Gisbert Quilis^b, Jiří Slabý^d, Jiří Homola^d, Médéric Lequeux^e, Frédéric Amiard^f, Marc Lamy de la Chapelle^f, Ulrich Jonas^g, Jakub Dostálek^a

^a Biosensor Technologies, AIT-Austrian Institute of Technology GmbH, Konrad-Lorenz-Straße 24, 3430 Tulln an der Donau, Austria. E-mail: Jakub.dostalek@ait.ac.at.

^b CEST Kompetenzzentrum für elektrochemische Oberflächentechnologie GmbH, TFZ, Wiener Neustadt, Viktor-Kaplan-Strasse 2, 2700 Wiener Neustadt, Austria

^c Current address: NYU Abu Dhabi, Saadiyat Campus, P.O. Box 129188, Abu Dhabi, United Arab Emirates

^d Institute of Photonics and Electronics, Academy of Sciences of the Czech Republic, Chaberská 57, 18251, Praha 8, Czech Republic

^e Université Paris 13, Sorbonne Paris Cité, Laboratoire CSPBAT, CNRS, (UMR 7244), 74 rue Marcel Cachin, 93017 Bobigny, France

^f Institut des Molécules et Matériaux du Mans (IMMM - UMR CNRS 6283), Avenue Olivier Messiaen, 72085 Le Mans cedex 9, France

^g Macromolecular Chemistry, Department Chemistry-Biology, University of Siegen, Adolf Reichwein-Strasse 2, Siegen 57076, Germany

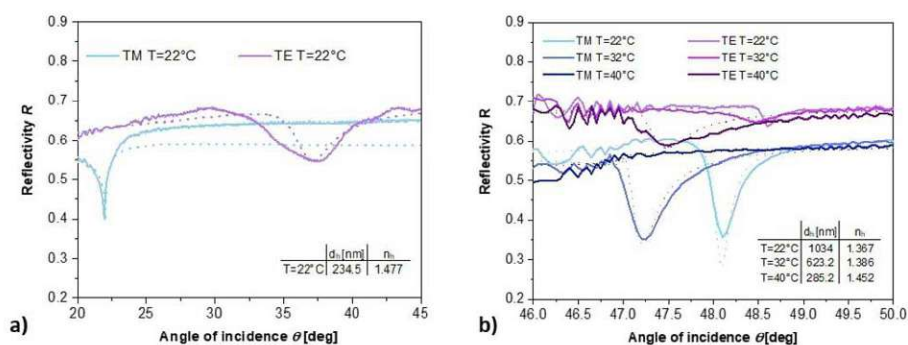


Figure S1. Measurement of thickness and the refractive index of a flat pNIPAAm-based polymer layer on a gold surface a) in a dry state and b) in water by using optical waveguide spectroscopy. Solid lines represent the measured angular scans and dashed curves are the fitted data.

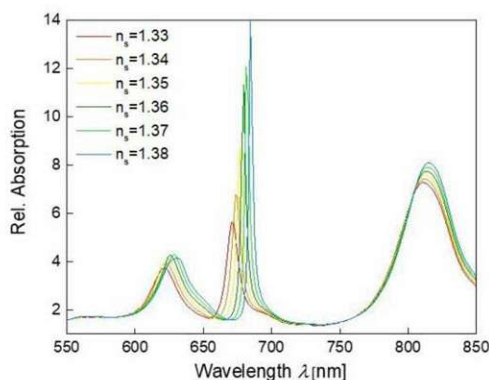


Figure S2. Simulated absorption spectra for the structure NHA+NP for the varied refractive index of superstrate n_s , the substrate refractive index was of $n_s=1.47$, the gap distance between NP and NHA was set as $g=50$ nm, the period was $A=460$ nm, diameter averaged between $D=100-120$ nm, height $h=50$ nm.

5.3. Supporting Information – UV-Laser Interference Lithography for Local Functionalization of Plasmonic Nanostructures with Responsive Hydrogel

The following supportin information is reprinted under the terms of the Creative Commons CC-BY^h license.

Nestor Gisbert Quilis, Simone Hageneder, **Stefan Fossati**, Simone K. Auer, Priyamvada Venugopalan, Anil Bozdogan, Christian Petri, Alberto Moreno-Cencerrado, Jose Luis Toca-Herrera, Ulrich Jonas, and Jakub Dostalek UV-Laser Interference Lithography for Local Functionalization of Plasmonic Nanostructures with Responsive Hydrogel. *J. Phys. Chem. C* **124**, 3297–3305 (2020). <https://doi.org/10.1021/acs.jpcc.9b11059>

Copyright © 2020 American Chemical Society

^h <http://creativecommons.org/licenses/by/4.0/>, Appendix 5.7.2

Supporting Information

UV-Laser Interference Lithography for Local Functionalization of Plasmonic Nanostructures with Responsive Hydrogel

Nestor Gisbert Quilis^a, Simone Hageneder^a, Stefan Fossati^a, Simone K. Auer^a, Priyamvada Venugopalan^{a,b†}, Anil Bozdogan^b, Christian Petri^c, Alberto Moreno-Cencerrado^d, Jose Luis Toca-Herrera^d, Ulrich Jonas^c and Jakub Dostalek^{a}*

^aBioSensor Technologies, AIT-Austrian Institute of Technology GmbH, Konrad-Lorenz-Strasse 24, 3430 Tulln, Austria

^bCEST Kompetenzzentrum für elektrochemische Oberflächentechnologie GmbH, TFZ, Wiener Neustadt, Viktor-Kaplan-Strasse 2, 2700 Wiener Neustadt, Austria

^cMacromolecular Chemistry, Department Chemistry-Biology, University of Siegen, Adolf Reichwein-Strasse 2, Siegen 57076, Germany

^dInstitute for Biophysics, Department of Nanobiotechnology, University of Natural Resources and Life Sciences Vienna (BOKU), Muthgasse 11, Vienna 1190, Austria

S1

Observation of the interference field profile formed by the phase mask. A thin layer of the S1805 positive photoresist (diluted 1:2 with propylene glycol monomethyl ether acetate) with a thickness of 120 nm was deposited by spin-coating (4500 rpm, 45 s) on top of a BK7 substrate. Afterward, the sample was mounted in a home-built set-up together with the phase mask to verify the recording pattern. The distance of the photoresist-coated substrate in respect with the phase mask (recording plane) was kept to 5.6 mm. At this distance the first order diffraction gratings overlap at the center of the mask for a $\Lambda=690$ nm. Thus, the samples were irradiated once to 27 mJ cm^{-2} and developed for 35 sec.

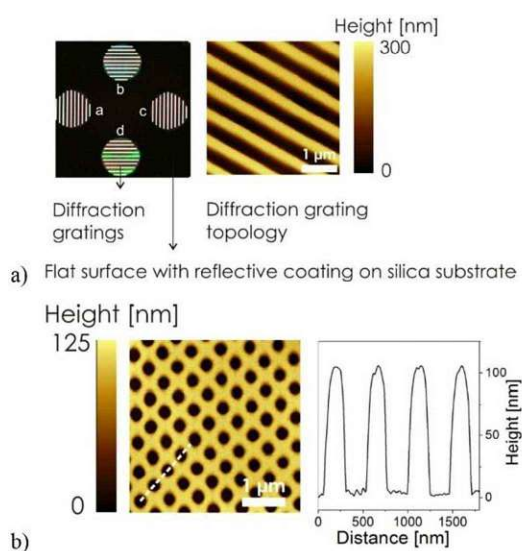


Figure S1. (a) Schematics of the prepared phase mask with orientation of the transmission gratings (left) and their topography obtained by AFM (right). (b) Recorded interference pattern into the S1805 positive photoresist using the prepared phase mask.

S2

Plasmon-enhanced fluorescence readout of model assay

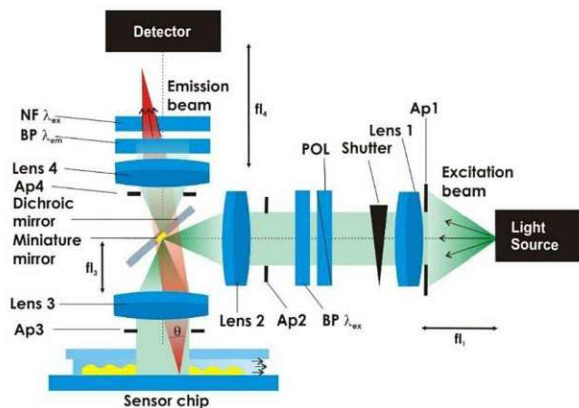


Figure S2. Schematics of the optical setup configuration of the reader that enables in situ readout of fluorescence signal kinetics from the sensing spots on a sensor chip: NF – notch filter, BP – bandpass filter, Ap – aperture, POL – polarizer, fl – focal length.

5.3. Supporting Information – UV-Laser Interference Lithography for Local Functionalization of Plasmonic Nanostructures with Responsive Hydrogel

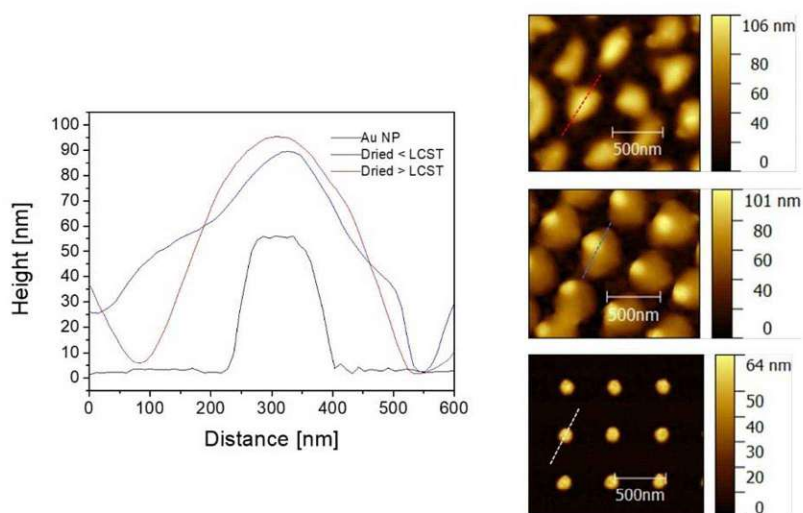


Figure S3. Cross-sections of representative areas of AFM topography showed in Figure 5 for bare gold nanoparticles (black curve), gold nanoparticles capped with pNIPAAm-based hydrogel dried below its LCST (blue curve) and above its LCST (red curve) and associated AFM images.

S4

5.4. Supporting Information – Dual Monitoring of Surface Reactions in Real Time by Combined Surface Plasmon Resonance and Field-Effect Transistor Interrogation

The following supporting information is reprinted under the ACS AuthorChoice publishing agreementⁱ.

Patrik Aspermaier, Ulrich Ramach, Ciril Reiner-Rozman, Stefan Fossati, Bernadette Lechner, Sergio E. Moya, Omar Azzaroni, Jakub Dostalek, Sabine Szunerits, Wolfgang Knoll, and Johannes Bintinger Dual Monitoring of Surface Reactions in Real Time by Combined Surface-Plasmon Resonance and Field-Effect Transistor Interrogation. *J. Am. Chem. Soc.* **142**, 11709–11716 (2020). <https://doi.org/10.1021/jacs.9b11835>

Copyright © 2020 American Chemical Society

ⁱ <http://creativecommons.org/licenses/by/4.0/>, Appendix 5.7.2

5.4. Supporting Information – Dual Monitoring of Surface Reactions in Real Time by Combined Surface Plasmon Resonance and Field-Effect Transistor Interrogation

Dual Monitoring of Surface Reactions in Real-time by Combined Surface-Plasmon Resonance and Field-Effect Transistor Interrogation

Patrik Aspermaier^{†,‡,§,°}, Ulrich Ramach^{‡,°}, Ciril Reiner-Rozman[†], Stefan Fossati[†], Bernadette Lechner[†], Sergio E. Moya[~], Omar Azzaroni^{||}, Jakub Dostalek[†], Sabine Szunerits[§], Wolfgang Knoll^{†,‡}, Johannes Binteringer^{†,*}

[†]: Austrian Institute of Technology, Biosensor Technologies, Konrad-Lorenz-Strasse 24, 3430 Tulln, Austria

[‡]: CEST Competence Center for Electrochemical Surface Technologies, Konrad-Lorenz-Strasse 24, 3430 Tulln, Austria

[~]: CIC biomaGUNE, Paseo Miramon 182 C, 20014 San Sebastian, Spain

[§]: Univ. Lille, CNRS, Centrale Lille, ISEN, Univ. Valenciennes, UMR 8520 - IEMN, 59000 Lille, France

^{||}: Instituto de Investigaciones Fisicoquímicas Teóricas y Aplicadas (INIFTA)–Departamento de Química, Facultad de Ciencias Exactas, Universidad Nacional de La Plata–CONICET, Suc. 4, CC 16, La Plata, Argentina

[°] Patrik Aspermaier and Ulrich Ramach contributed equally.

Table of Contents

I. Theoretical framework	3
a) Development of the theoretical framework	3
b) Implementation of the theory for explanation of the experimental results	8
• Bulk changes.....	8
• Surface charge accumulation (σ_a)	9
• Influence of gate-surface distance	11
• Capacitive (σ_i).....	12
II. Complementary experiments	15
• Different deposition rates at positive and negative applied potentials:.....	16
• Voltage Drop across the PEM.....	18
III. Experimental procedure	19
• Preparation of the rGO-FETs	19
• Preparation of the SPR Au-slides.....	20
• Preparation of the polyelectrolyte solutions	20
• Experimental setup and details.....	21
• Readout software for electrical and optical measurements	22
IV. Materials and hardware	23
Hardware.....	23
Chemicals	23
V. References	24

I. Theoretical framework

a) Development of the theoretical framework

This chapter aims at a comprehensive evaluation of the electronic EG-FET read-out for LBL assembly. Figure S1 (middle) shows the measurement of the layer-by-layer assembly from the manuscript. Figure S1 (left) shows the corresponding raw data. The baseline correction was performed by linear assumption of a baseline drift and subtraction, resulting in ΔI_{DS} . The resulting ΔI_{DS} after the rinsing steps for each polyelectrolyte layer are shown in Figure S1 (right) to illustrate the stability of the system over 8 layers in a duration of more than 3 hours under continuous flow.

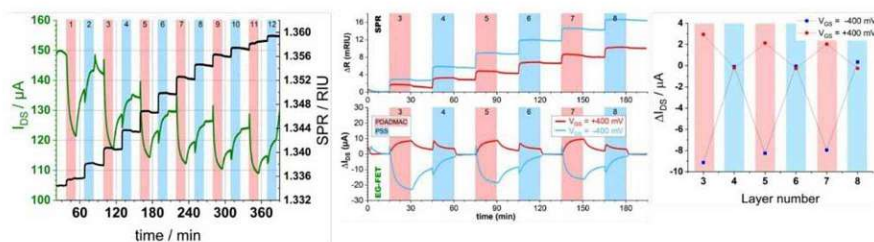


Figure S1. *left:* raw data for -400 mV V_{GS} , *middle:* baseline corrected data of selected layers as shown in Figure 3; *right:* ΔI_{DS} after rinsing of each corresponding PEM extracted from data shown in Figure 3.

A detailed EG-FET and SPR response to the PDADMAC and PSS layer formations are shown in Figure S2. For the fast reactions in this Figure it is important to comment that the rapid responses cannot originate from flow variation due to the peristaltic pump used, as the pump needs about 3-5 min to flush the PEM into the flow cell, thus changing of the pump solution was performed significantly before these observed kinetics.

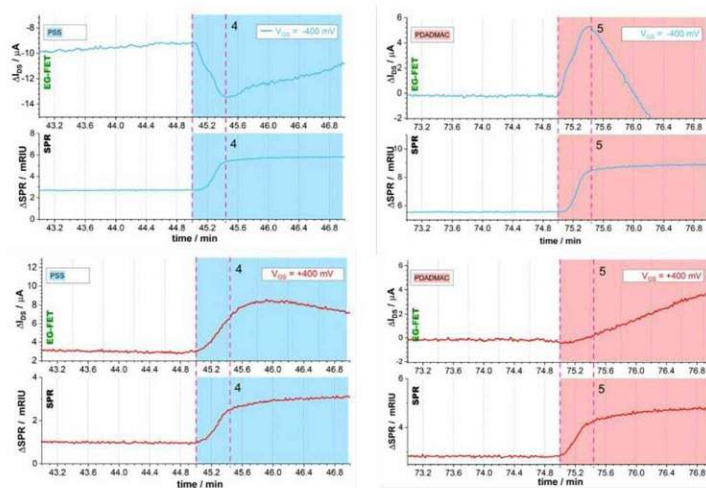


Figure S2. Magnification for the first minutes of each layer deposition from Figure S1 (middle), showing the overlap of two effects both exhibiting exponential behavior with different time constants.

5.4. Supporting Information – Dual Monitoring of Surface Reactions in Real Time by Combined Surface Plasmon Resonance and Field-Effect Transistor Interrogation

The discussion of the signal obtained from SPR/EG-FET measurements is based on three observations and considerations of sensing mechanisms regarding the sources of the convoluted signal output, which are described in the next section based on the theoretical framework depicted in this section, ascribing the effects to a) bulk changes, b) surface charge accumulation, and c) capacitive effects. For understanding the underlying effects, a few basic formulations and definitions have to be established.

The observed current I_{DS} for the linear region of EG-FET devices can be formulated as:

$$I_{DS} = \frac{W}{L} C_i \mu (V_{GS} - V_T) V_{DS} \quad V_{DS} \ll (V_{GS} - V_T) \quad (\text{Eq.S1})$$

Where W is the FET's channel width, L the channel length, C_i the insulating layer capacitance (from Gate to channel), μ is the charge carrier mobility, V_{GS} the applied Gate voltage, V_T the threshold voltage, and V_D the applied voltage between Source and Drain electrodes. Emerging from the basic FET equation (Eq.S1), the time dependency (Eq.S2) of the separate variables is studied in regard to their dependencies to sensing mechanisms.

$$\frac{\partial I_{DS}}{\partial t} = \frac{W}{L} \frac{\partial C_i}{\partial t} \frac{\partial \mu}{\partial t} \left(V_{GS} - \frac{\partial V_T}{\partial t} \right) V_{DS} \quad (\text{Eq.S2})$$

Time dependence of charge carrier mobility $\frac{\partial \mu}{\partial t}$ is the change of charge carrier mobility over time. It depends on several factors, a significant one of those is the effective electric Field, which is described by the Poisson's equation for the effective voltage of the FET channel in the x-coordinate from Gate to channel:¹

$$F_x = \sqrt{\frac{2}{\epsilon \epsilon_r} \int_0^V e \rho(V) \partial V}; \quad (\text{Eq.S3})$$

where ϵ_r is the relative permittivity, ϵ the absolute permittivity, e is unit charge, and $\rho(V)$ is the charge density. Here we also need to introduce the surface charge density σ , which we divide in two components:

$$\sigma = \sigma_i + \sigma_a \quad (\text{Eq.S4})$$

where σ_i is the charge density induced to the surface by electric forces and σ_a is the charge density, originating from adsorption of molecules to the surface. Therefore, changes of the surface charge density originating from the electrolyte, namely bulk and capacitive effects, are ascribed to σ_i , while changes of the surface charge potential by direct adsorption of mass are ascribed to σ_a . The Poisson equation clearly shows that the change of surface charge density influences the electric field. On the other hand, it can be understood that similarly also for changes in the electric field, the surface charge density will be modified (the induced part σ_i).

The effective potential at the EG-FET surface by propagation of the electric field is lower than the applied voltage at the gate V_{GS} due to a voltage drop depending on the distance from the electrode and the distribution of dielectric media on the propagation path and can be described by:^{1,2}

$$V_{GS,eff} = \frac{Q_{ind}}{C_i} + V_{fb} = \frac{\epsilon \epsilon_r F_x(0)}{C_i} + V_{fb} \quad (\text{Eq.S5})$$

depending on the flat band voltage V_{fb} which is the difference of the work function of the materials at the interface ($\Phi_{rGO} - \Phi_{KCl}$) that can be obtained by electrochemical means, leading to the evaluation of $V_{GS,eff}$ at the surface. The described C_i is the insulator capacitance. For measurements without a gate-electrode (see Figure S4), this part of the equation is 0, therefore $V_{GS,eff} = V_{fb}$. A change of the potential drop at the liquid/solid interface will change $V_{GS,eff}$ and hence the measured signal.

The interface of the electrolyte to the semiconductor with an applied capacitance is described by the **Mott-Schottky** equation:³

$$\frac{1}{C^2} = \frac{2}{\epsilon \epsilon_0 A^2 q N_d} \left(V - V_{fb} - \frac{k_B T}{q} \right) \quad (\text{Eq.S6})$$

N_d , the doping density, leads to a change of the FET-mobility due to surface binding of σ and can be obtained from capacitive as well as resistance-based measurements. Doping generally refers to the introduction of impurities into a semiconductor, but in the Mott-Schottky concept it also describes the addition of electrons or holes (by the removal of electrons) into the rGO film.

The indirect way to explain N_d is by describing the surface charge density, which does not take the following parameters into account – e.g. the sign of the charge, the polarity, binding affinity, etc. – but rather offers a very general description of charge distribution and its effect on the EG-FET. Although not all of these parameters regarding the interaction of the polymers with the rGO are known, the relation between doping density and surface charge distribution can still be obtained from Eq.S5, using C_{obs} for determination via the differential capacitance $C = \frac{d\sigma}{d\psi}$, using the surface potential ψ . The surface potential is described by linearization of the Poisson-Boltzmann equation and after rearrangement yields the Debye-Hückel model for the surface charge to surface potential relationship:^{4,5}

$$\psi = \frac{\sigma}{\epsilon \epsilon_0 \kappa} \quad (\text{Eq.S7})$$

which is valid for ionic liquids at interfaces taking into account the Grahame equation for the surface potential distribution, with the reciprocal of κ being the Debye length λ_D :

$$\kappa = \frac{1}{\lambda_D} = \sqrt{\frac{2 z^2 e^2 n_0}{\epsilon k_B T}}, \quad (\text{Eq.S8})$$

where z is the valency of the ions and n_0 is the concentration of ions in an infinite distance from the surface. Also, here the surface charge density is used to describe the surface potential.

The contribution by adsorption which corresponds to σ_a is determined by the introduction of holes n or electrons e^- in the rGO-channel. Without V_{GS} the graphene channel current is determined by:⁶

$$I_{DS} = V_{DS} \cdot \frac{W}{L} \cdot n \cdot e^- \cdot \mu_{eff} \quad (\text{Eq.S9})$$

where the mobility is governed by Matthiessen's rule: $\mu_{eff} = (\mu_{lattice}^{-1} + \mu_{impurity}^{-1} + \mu_{adsorption}^{-1})^{-1}$ showing that the response signal is defined by lattice and doping parameters as well as the introduction of charge carriers.

In summary, the mobility, defined by these variables ($\psi, \rho, \sigma, V_{GS,eff}, \mu_{adsorption}$), is related to the charge density by Eq.S10.

The **time-dependence of the mobility** can be described as:¹

$$\frac{\partial \mu}{\partial t} = \frac{\partial \alpha_p / \partial t}{e \rho} \quad (\text{Eq.S10}),$$

with ρ being the charge density and α_p the conductivity for a certain p .

Relating these observations to the approach to describe the surface charge density via $\sigma = \sigma_i + \sigma_a$, we can conclude that the mobility is determined by both the induced and the adsorbed surface charge. The charge carrier mobility in the EG-FET channel is determined by the change of

5.4. Supporting Information – Dual Monitoring of Surface Reactions in Real Time by Combined Surface Plasmon Resonance and Field-Effect Transistor Interrogation

conductivity (measured by I_{DS}) in the transistor and is directly given by the dependency of surface charge densities to the applied electric field:

$$\mu = \frac{1}{\rho_i e d V_{GS}} \quad (\text{Eq.S11}),$$

where ρ_i is the induced charge carrier density at $V_{GS} = 1V$.

Time dependence of threshold voltage $\frac{\partial V_T}{\partial t}$

For the threshold voltage the time dependence originates from changes in the semiconductor material and from the applied potential. V_T is usually obtained by linear fits of the $I_{DS}V_{GS}$ transfer characteristics; for p- or n-type FETs it is the voltage at which the semiconductor is responding to V_{GS} . This comes from the intrinsic semiconductor and dielectric properties modulated by μ and C_i and are therefore included in the parts above and below. For reduced graphene oxide, which is exerts ambipolar behavior of the transfer characteristics, V_T is not considered as a separate physical quantity, rather than a measured factor used for qualitative determination of I_{DS} from the transfer characteristics and will not be considered independently in this discussion.

Time dependence of capacitance $\frac{\partial C_i}{\partial t}$

Changes of capacitance over time will be evaluated in this section. The capacitance is defined by:

$$Q = C \cdot U \quad (\text{Eq.S12}),$$

giving the general dependency of charges Q to the applied voltage U (for the FET this is V_{GS}). For a certain geometry of a parallel plated capacitor with the use of a classical dielectrics, the capacitance can be calculated by the distance d between the plates (here the rGO and gate-electrodes), the area A and the dielectric permittivity ϵ :

$$C = \epsilon_0 \epsilon_r \frac{A}{d} \quad (\text{Eq.S13})$$

Since the Applied V_{GS} , the thickness and area of the system are constant during measurements, capacitive changes of the system can originate only from variations in permittivity ϵ_r or the surface charge σ . In our theoretical framework we assume ϵ_r of the system constant at any given time during layer deposition. The adsorbed surface charge σ_a leads to a minute change of the capacitance, which is then constant after mass adsorption (as seen from SPR). For the induced surface charge density σ_i , the time-dependent capacitance is given by the differential capacitance as described in electrochemistry by:

$$C = \frac{\partial \sigma}{\partial \psi} \quad (\text{Eq.S14}),$$

where C , σ and ψ are capacitance, surface charge and electric surface potential.

As shown in Eq.S7, the capacitance only has a time-dependence if the permittivity ϵ_r and/or the Debye length λ_D vary. Capacitive effects play a crucial role in EG-FET configured biosensors and in literature are often used as the

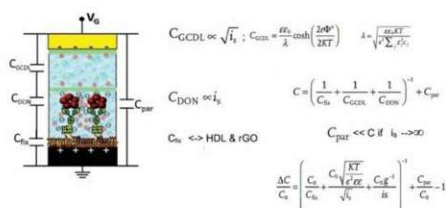


Figure S3. Schematic illustration of the capacitive sensing approach, splitting the system capacitance into serial terms regarding the layers. The dependencies on the ionic strength are shown on the right side.¹¹

S6

5.4. Supporting Information – Dual Monitoring of Surface Reactions in Real Time by Combined Surface Plasmon Resonance and Field-Effect Transistor Interrogation

primary source of the signal, the so called capacitive sensing (Torsi et al)⁷. It has been demonstrated that capacitive sensing does not suffer from Debye-screening limitations⁸ and coupled with advanced surface modification principles can lead to the enhancement of the biosensor signal, even down to the single molecule detection level.⁹

A good description for the capacitive effects was given by the Torsi group and concludes a strong dependency of the EG-FET signal to the ionic strength of the buffer solution and the charges originating from the donation layer,^{10,11} which in their case is a biomolecule-functionalized architecture, while for a LbL approach with polyelectrolytes it is also the polymeric layer and the thereby induced screening charge ions. The dependencies are shown in Figure S3 (modified from the Torsi group).¹¹ The effects originating from capacitive sensing can, for simplification, also be described by their influence on the channel material solely, deriving an expression from Ohm's law:

$$j_{DS} = \sigma F \quad (\text{Eq.S15})$$

where j_{DS} is the drain current density and F the field from source to drain. Furthermore, we ascribe the capacitive effects to modulations of the channel via the integral of induced surface charge density:¹²

$$I_{DS} = -WdL \int_{V_{GS}}^{V_{GS}-V_{DS}} \sigma(V) dV \quad (\text{Eq.S16})$$

With d being the thickness of the polymer film. As shown in the chapter for charge carrier mobility, C_i influences the mobility of the rGO layer and can therefore be used as the measuring quantity in the proper system configuration.

Relating these observations to the approach for the surface charge density $\sigma = \sigma_i + \sigma_a$, we can conclude that the capacitance, in contrast to the mobility, varies by the induced surface charge and does not change after each layer deposition, once adsorbed surface charge σ_a is established on the layer.

b) Implementation of the theory for explanation of the experimental results

Using the insights from the previous section we now want to focus on the outcome from the EG-FET/SPR system for LbL deposition as shown in the main article and Figure S1. This section will focus on the effects of a) bulk changes, b) adhered surface charge density σ_s , and c) capacitive effects influencing the induced surface charge density σ_i .

- Bulk changes

One Monomer of each polyelectrolyte has one charge (1eV). For PDADMAC, a monomer has 160 g/mol of molecular weight, the polymer has an average weight of 100 kDa. Therefore, 1 mg/ml of PDADMAC in 100 mM KCl as used in the experiment has a monomer concentration of 625 μM , which equals 60.2 Coulomb for a liter of solution. The sensing area of the cell has a volume of 5 μL , so 300 μC of charge should be introduced into the system at any given time. The ionic strength of the KCl buffer with PDADMAC is 100.625 mM in comparison to 100 mM for the washing steps, a difference of less than one percent.

For PSS, a monomer has 206 g/mol of molecular weight, whereas the polymer has an average weight less or equal than 70 kDa. Therefore, 1 mg/ml of PSS in 100 mM KCl has a monomer concentration of 475 μM , which equals 47.75 Coulomb for a liter of the solution. The sensing area of the cell has a volume of 5 μL , so 238 μC of charge should be introduced into the system at any given time. The ionic strength of the KCl buffer with PSS is 100.475 mM in comparison to 100 mM for the washing steps, a difference of less than one percent.

This yields changes in ionic strength of about 0.5%, which has a minute effect on the capacitive behavior of the system and the gating effect of the transistor. In relation to the signals obtained during sensing, bulk effects can therefore be neglected.

5.4. Supporting Information – Dual Monitoring of Surface Reactions in Real Time by Combined Surface Plasmon Resonance and Field-Effect Transistor Interrogation

- Surface charge accumulation (σ_a)

The current I_{DS} is determined by the resistance of the channel which is inversely connected to the mobility of the transistor material (here rGO) by Ohm's law:¹³

$$R = \frac{1}{\mu C_i \frac{w}{L} (V_{GS} - V_T)} \quad (\text{Eq.S17})$$

This holds true because I_{DS} is generated by flow through the transistor layer and not through the applied polymeric layers ($R > 1 \text{ M}\Omega$ for both polyelectrolytes), a resistance several order of magnitude higher than the conducting material. Therefore, polyelectrolyte conductivity can be neglected.

The basic sensing principle for reduced graphene oxide (rGO) biosensors is based on binding or adsorption of analytes to the rGO surface or to the biorecognition units functionalized on the rGO. The principle of such direct sensors is in use, e.g. in graphene based chemiresistors¹⁴ or EG-FETs.

To conduct zero-capacitance measurements our simultaneous SPR/EG-FET setup could not be used, as a gold substrate, which again would introduce capacitive effects, is required for SPR measurements.

Thus, the zero-capacitance measurement setup consists of a two-terminal configuration in which the gate-material was changed from an Au-coated glass slide to a non-coated glass-slide. As the gate was left floating the capacitance is also 0. The results from the measurement are shown in Figure S4. For PDADMAC adsorption and the corresponding washing step the EG-FET signal from the zero-capacitance experiment is in good agreement with the signal from SPR in the standard configuration (Figure S1). In contrast, while PSS adsorption can hardly be observed from the EG-FET signal in the zero-capacitance experiment the post-PSS rinsing steps can again be readily measured. We speculate that this effect for PSS is ascribed to repulsion of PSS from the surface, because the intrinsic negative charge of rGO (like PSS).¹⁵

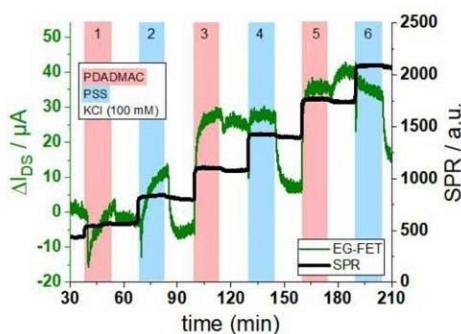


Figure S4. zero-capacitance EG-FET response realized by replacing the gate-electrode with a non-conductive substrate, thus leading to $\sigma = \sigma_a$, comparable with the SPR response from Figure S1.

Exponential fits for the adsorption time constants (t_{on}) of SPR and EG-FET responses for polyelectrolytes, have been evaluated. Obtained time constants are shown in Figure S6.

5.4. Supporting Information – Dual Monitoring of Surface Reactions in Real Time by Combined Surface Plasmon Resonance and Field-Effect Transistor Interrogation

The difference in the time constants for SPR and zero-capacitance EG-FET (two terminal configuration) signals are due to non-existing applied gate voltage (floating gate) and are shown in Figure S6. The lack of applied voltage changes the surface potential and, as shown in Eq.S5 and Eq.S6, also the affinity to the surface and mobility of the rGO. Furthermore, the time kinetics for additional layers of the applied

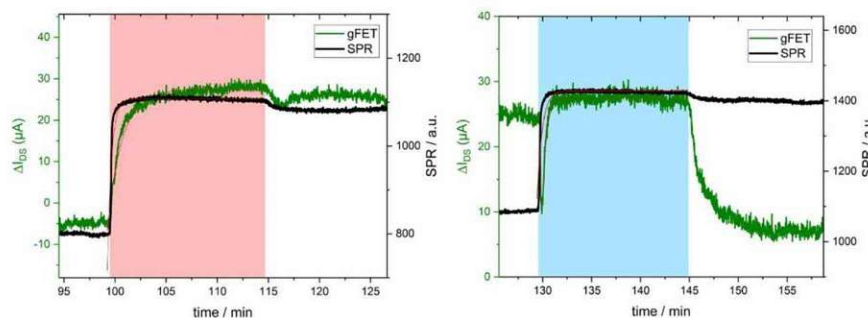


Figure S5. Comparison of the EG-FET responses (green) in a non-capacitive setup with the responses from the SPR signal (black). *left:* shows the third layer, PDADMAC and *right:* shows the fourth layer, PSS

polyelectrolytes converge towards the signals obtained by SPR with increasing number of layers.

The discrepancy between initial layers and later deposited layers can be attributed due to incomplete layer formation for seed layers.

Strikingly, a much better agreement for the time constants obtained from zero-capacitance measurements to SPR (Figure S6) is observed than for time constants from the combined SPR/EG-FET system (Figures S1 and S2). As a result, we conclude that responses obtained from zero-capacitance measurement are attributed to the adsorbed surface charge density σ_s (Eq.S4).

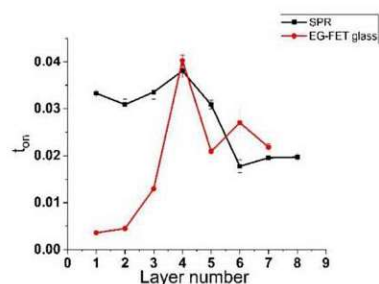


Figure S6. obtained time constants t_{on} from the exp. Fits of the zero-capacitance measurement

5.4. Supporting Information – Dual Monitoring of Surface Reactions in Real Time by Combined Surface Plasmon Resonance and Field-Effect Transistor Interrogation

- Influence of gate-surface distance

To further support these claims, the flow-cell gasket thickness was increased by a factor of 10, thereby decreasing the overall capacitance of the system (Eq.S13) by the same factor.

It was shown that the capacitive effects are diminished, the measurement is similar to the results obtained by using a non-conductive Gate-electrode (Figure S4). Albeit the capacitive effect still plays a minute roll in this measurement, the advantage of simultaneous SPR measurement, yields a direct comparison of the binding constants shown in Figure S7b. The flow channel thickness is defined by the height of the gasket between the gold slide (gate electrode) and the drain-source electrodes.

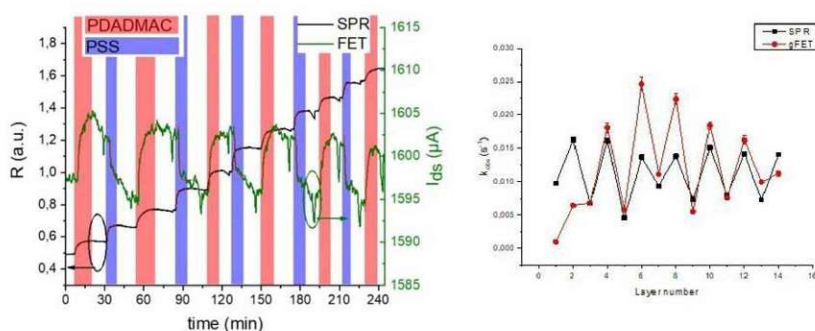


Figure S7. *left:* LbL measurement of SPR/EG-FET with a gasket of 3mm thickness. *right:* time-constants of the exponential fits evaluated from SPR and EG-FET measurements (*left*) in a).

Figure S7b demonstrates that the time constants of this architecture are in good agreement to the time constants obtained from SPR measurements. Therefore, according to Eq.S4, decreasing the capacitance enables the observation of the adsorbed surface charge density, as the term σ_i , induced surface charge density, converges to 0, and results in comparable time constants between EG-FET and SPR readouts.

- Capacitive (σ_i)

The induced surface charge density σ_i can be obtained by the subtraction of the adsorbed surface charge density σ_a from the total surface charge density σ , as proposed in Eq.S4. Therefore, the measurement in Figure S4 was subtracted from the submitted measurement in Figure S1 with equivalence factors for normalization of 1,4 for PDADMAC (L5) and 2,9 for PSS (L4), to compensate the differences in sensor fabrication, shown in Figure S8.

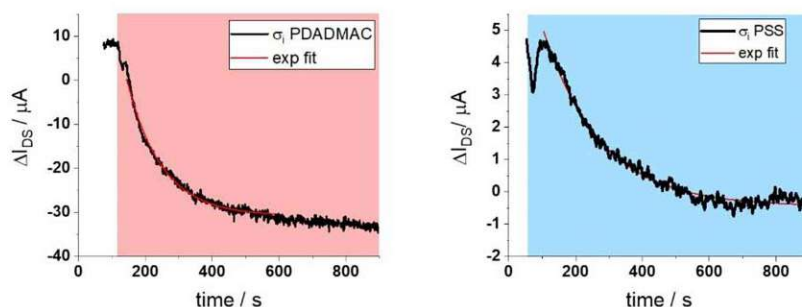


Figure S8. *left:* Subtracted EG-FET response curve for PDADMAC layer deposition and *right:* subtracted response curve for PSS layer deposition.

Slow responses are directly related to ion diffusion in PEM, as discussed in Figure S4: σ_i

As argumentized in the main manuscript the slow responses, for which we demonstrated their origin by the zero-capacitance experiment in the previous section to σ_i , are directly connected to ion diffusion in the PEM layers. To evaluate the tendency for ion diffusion of the separate layers at different V_G we introduced an arbitrary kinetic ratio ξ which is obtained by exponential fitting of the response signals obtained by the subtracted data shown in Figure S8, eliminating the influence of σ_a with the corresponding wash-off kinetics.

We defined this ratio by: $\xi = t_{on}/t_{off}$, where t_{on} is the time constant in the fit from Figure S8 and t_{off} is the time constant from the corresponding wash-off step. The full fitting data is found in Table S1.

5.4. Supporting Information – Dual Monitoring of Surface Reactions in Real Time by Combined Surface Plasmon Resonance and Field-Effect Transistor Interrogation

Table S1. t_{on} and t_{off} values for PDADMAC and PSS for positive and negative gate voltage V_{GS}

(s ⁻¹)	PSS		PDADMAC	
	+ 400mV	- 400mV	+ 400mV	- 400mV
L3 t_{on}			0.0044	0.0049
L3 t_{off}			0.0035	0.0031
L4 t_{on}	0.0055	0.0040		
L4 t_{off}	0.015	0.016		
L5 t_{on}			0.0051	0.0058
L5 t_{off}			0.0035	0.0032
L6 t_{on}	0.0047	0.0039		
L6 t_{off}	0.016	0.020		
L7 t_{on}			0.0052	0.0051
L7 t_{off}			0.0037	0.0038
L8 t_{on}	0.0037	0.0039		
L8 t_{off}	0.017	0.013		

Furthermore, the charge carrier density at the channel-electrolyte interface $Q(V)$ in the accumulation regime of the semiconductor ($V < V_{fb}$). Can then be calculated by:

$$Q(V) = - \int_{-V_{fb}}^V C(V) \partial V \quad (\text{Eq.S18}),$$

as demonstrated by the Berggren group.¹⁶

Such evaluations for charge distribution and similar studies also for diffusion processes not obtained by EG-FET platforms where until now, but always by means of electrochemistry (CV or EIS). However, the suitability of EG-FET systems as complementary tools for electrochemistry has been proposed before.¹⁷ The discussed quantities can also be described by the chemical potential, which in turn is related to the surface potential at a solid/electrolyte interface. For single ion species this thermodynamic approach leads to:¹⁸

$$\bar{\mu}_i = \mu_i^0 + \left[\frac{R z_i q}{k_B} (\psi_2 - \psi_1) \right] + z_i q \psi \quad (\text{Eq.S19}),$$

where μ_i^0 is the chemical standard potential, R the molar gas constant, ψ_1 the potential at the solid interface, ψ_2 the potential at the liquid interface. This demonstrates that the applied theoretical framework could also be reformulated using the chemical potentials throughout the system rather than the surface potentials and charge density, which could be a useful mean for the description of more complex chemical experiments performed by the EG-FET/SPR setup where the charge of the analytes is not sufficient for a comprehensive explanation and the chemical activity has to be considered thoroughly. The concept itself is visualized in Figure S9.

5.4. Supporting Information – Dual Monitoring of Surface Reactions in Real Time by Combined Surface Plasmon Resonance and Field-Effect Transistor Interrogation

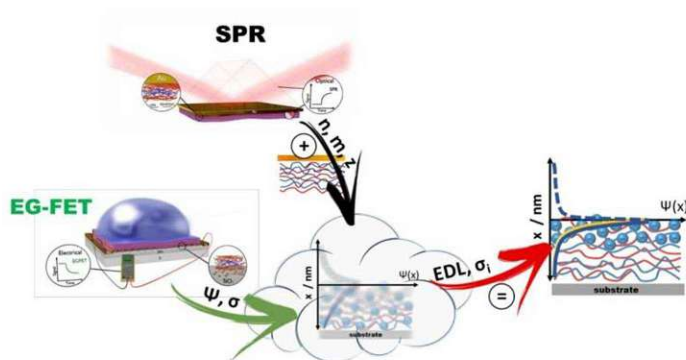


Figure S9. Concept of the EG-FET and SPR signal fusion to obtain a detailed information about the surface charge density. Superimposed surface phenomena can be separated by the simultaneous real-time observation with a bifunctional sensor and the subsequent demodulation.

II. Complementary experiments

This chapter describes additional experiments and illustrates different data representations to justify the developed theoretical framework on the EG-FET/SPR system.

The experiments were performed using a constant flow rate of 100 $\mu\text{l}/\text{min}$ and 1 mg/ml PDADMAC and PSS concentrations in 0.1 M KCl electrolyte solutions. All EG-FET experiments were performed at $V_{\text{DS}} = 0.05$ V using the same PDADMAC/PSS solutions as for SPR measurements.

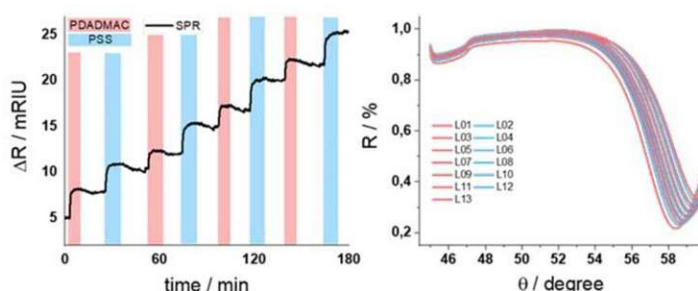


Figure S10. LBL SPR investigations, *left*: kinetic measurement in SPR flow cell using 20 mM KCl and a concentration of 1 mg/ml of PDADMAC and PSS solutions, *right*: corresponding angular scans and the shift of the resonance angle after the completed layer deposition.

Results for measurements with 20mM KCl are shown in Figure S10. To promote LbL assembly the gold surface was activated by UV/ozone treatment beforehand. The initial separated EG-FET experiments were carried out in a flowcell with an Ag/AgCl wire as gating electrode. For the EG-FET/SPR approach, the gating electrode was replaced by the SPR Au-slide with 2 nm Cr adhesion layer and 50 nm Au layer. All kinetic SPR sensor measurements were calibrated with standard glucose solutions to relate the observed changes in SPR reflectivity to refractive index variations.

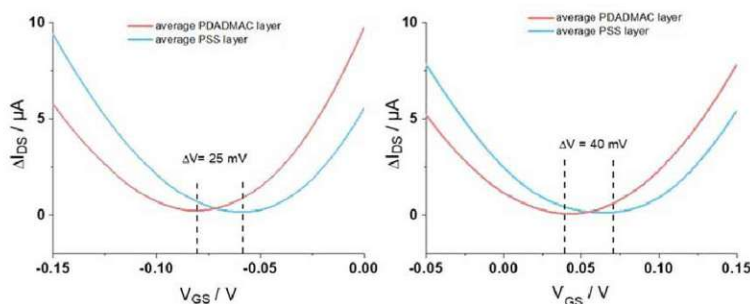


Figure S11. Influence of different ionic strength solutions on the $I_{\text{DS}}V_{\text{GS}}$ output curves. *left*: $I_{\text{DS}}V_{\text{GS}}$ measurement in 20 mM KCl using a 1 mg/ml PDADMAC/PSS solution, *right*: $I_{\text{DS}}V_{\text{GS}}$ measurements in 500 mM KCl electrolyte solution using a 1mg/ml PDADMAC/PSS solution. The Dirac point shift V_i corresponds to the ionic strength of the electrolyte solution.

S15

5.4. Supporting Information – Dual Monitoring of Surface Reactions in Real Time by Combined Surface Plasmon Resonance and Field-Effect Transistor Interrogation

Dirac points are the minimum of the drain source current I_{DS} and are represented as an average of several $I_{DS}V_{GS}$ scans after each layer deposition. The resulting Dirac shift is a result of the effective electrostatic gating caused by differently charged polyelectrolytes and depends on the ionic strength of the electrolyte solution, shown in Figure S11. The effect of ionic strength on SPR data, which influences the layer thickness, is shown in Figure S12.

- Different deposition rates at positive and negative applied potentials:

Figure S12 shows the different PEM growth rates for positive and negative applied gate potentials. It has been previously shown in literature that the rate of deposition of the PEM can be controlled via the application of an external electric field. This effect is observed below voltages which would lead to electrolysis of water, for higher voltages the contribution of electrolysis is dominant.

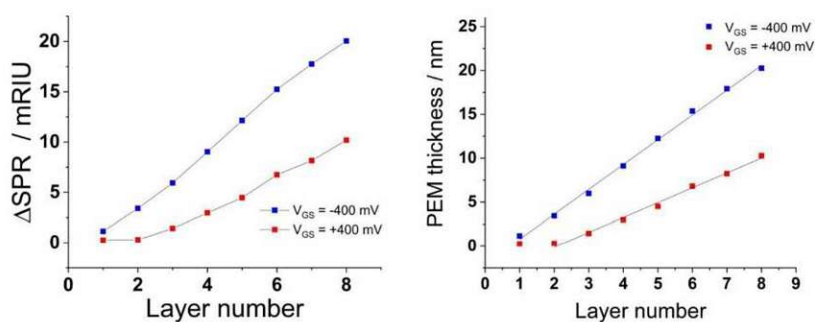


Figure S12. *left:* SPR response to the LbL growth at different applied gate voltages, *right:* PEM layer growth at different applied gate voltages V_{GS} , including a linear fit.

For $V_{GS} = \pm 400 \text{ mV}$ electrolysis of water only plays a minute role. The polarizability of charged polymers is much higher than water at such low potentials, the polymer chains exhibit instantaneous response to the electrostatic attraction by V_{GS} .¹⁹ Hence, electrophoretic deposition occurs and the electrostatic compensation process between cationic and anionic polyelectrolytes is stronger, resulting in thicker films as seen by the SPR signals which can be seen in Figure S12. Since the same potential strength with different signum was applied for our experiment, the difference of both measurements can therefore be explained by the different polarizability of PDADMAC and PSS at positive and negative potentials. The mean layer growth d_p for the applied gate voltage $V_{GS} = -400 \text{ mV}$ is $2,82 \pm 0,06 \text{ nm}$ and for $V_{GS} = +400 \text{ mV}$ is $1,69 \pm 0,06 \text{ nm}$ according to Eq.1 and the accumulating layers are plotted in Figure S12 (right).

5.4. Supporting Information – Dual Monitoring of Surface Reactions in Real Time by Combined Surface Plasmon Resonance and Field-Effect Transistor Interrogation

Figure S13 shows the raw data including leakage current of the combined EG-FET/SPR measurement in one measurement chamber at simultaneous data acquisition. As can be seen, the leakage current is several orders of magnitude smaller than the electric response signal. We deem it therefore to be neglectable.

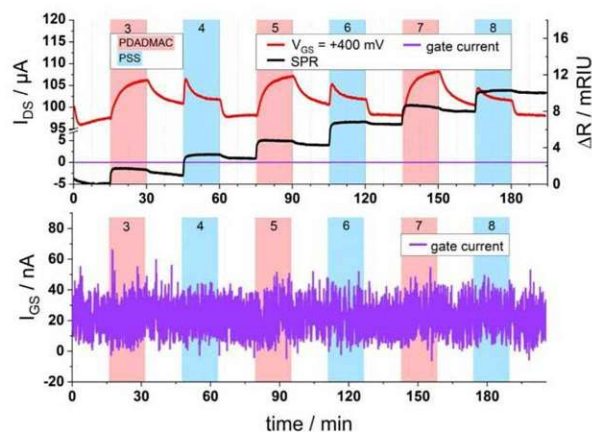


Figure S13. *top:* Raw data of the SPR/EG-FET measurement including leakage current (gate current). *bottom:* Zoom in of the leakage current. EG-FET chips have a leakage current in the order of $\sim 0.02\%$ of the total measured current thus making leakage current irrelevant for measurements.

The I_{D5} shifts at a fixed gate voltage V_{GS} are in accordance with the change in $I_{D5}V_{GS}$ -curves due to the adsorption of PEM layers, which is visualized in Figure S14. The deposition of a PSS layer leads to a right shift of the Dirac point V_i , causing an increase of the current I_{D5} , if the working point is adjusted via the gate voltage V_{GS} to a negative slope along the transfer characteristic.

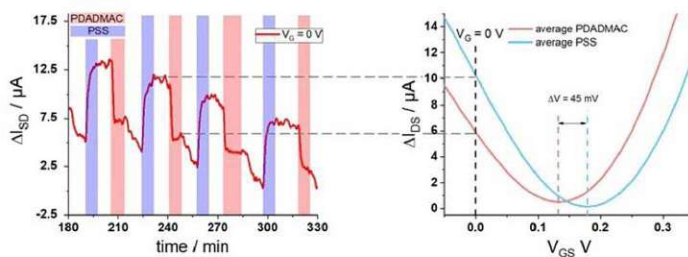


Figure S14. *left:* time resolved $I_{D5}(t)$ measurement of the LbL process and the corresponding *right:* $I_{D5}V_{GS}$ curves after layer deposition. The working point for $I_{D5}(t)$ measurements is determined by the adjusted gate voltage V_{GS} prior to the measurement.

S17

5.4. Supporting Information – Dual Monitoring of Surface Reactions in Real Time by Combined Surface Plasmon Resonance and Field-Effect Transistor Interrogation

The $I_{DS}V_{GS}$ scan cannot be observed at the same time as the $I_D(t)$ measurements, because the gate voltage needs to be modulated to record transfer characteristics, while the time-resolved measurement requires a constant gate current. Therefore, the Dirac point shift V_i is just a momentary snapshot, while $I_D(t)$ allows kinetic analysis.

- Voltage Drop across the PEM

The voltage drop across the PEM was calculated with the measured drain source current I_{GS} across the KCl ion solution which can be seen in Figure S15. With the initial state of the configuration, where

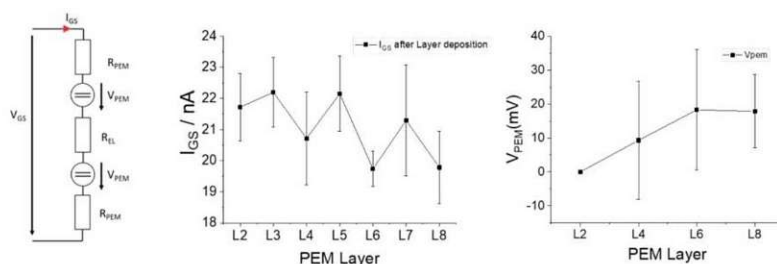


Figure S15. *left:* Electrical equivalent circuit to represent the resistance between the gate electrode and the rGO EG-FET. *middle:* The resulting gate source current $I_{GS}(t)$ after each layer deposition exemplary demonstrated at $V_{GS} = +400$ mV. The total current I_{GS} variation upon layer formation is very low, but still indicates the different voltage drops across the PSS or PDADMAC layer. *right:* Voltage drop across every polyelectrolyte double layer.

$R_{PEM} = 0$, the voltage drop is entirely across the electrolyte. The voltage drop after each polyelectrolyte double layer is calculated with Eq.S20.

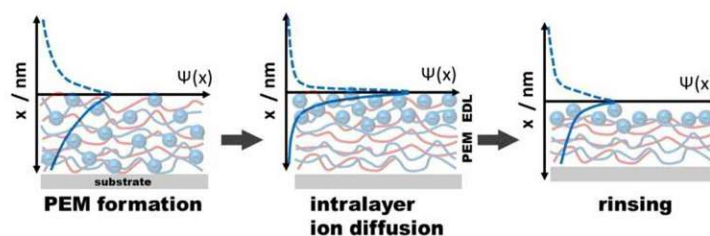


Figure S16. Surface potential Ψ as a function of the distance to the sensing surface. Upon Layer formation, surface charge density increases, hence the surface potential is modulated. The initial state after the first precursor layer are shown on the left, the adsorption of a new layer is shown in the middle and the polyelectrolyte washing off is shown in the rinsing graph.

$$V_{PEM} = V_{GS} \frac{R_{PEM}}{R_{Total}} = V_{GS} \frac{R_{PEM}}{R_{el} + 2 R_{PEM}} \quad (\text{Eq.S20})$$

S18

III. Experimental procedure

- Preparation of the rGO-FETs

First, Micrux chips (schematically shown in Figure S17a) are sonicated in a 1 % HELMANEX(III) Milli-Q® cleaning solution for 15 minutes, then rinsed with Milli-Q®, sonicated again and finally rinsed with pure EtOH and sonicated again. The chips are then thoroughly rinsed with Milli-Q® water and put into an absolute ethanol solution with 2%v/v APTES for 1 hour. Subsequently, the chips are cleaned with absolute ethanol, gently blow dried put in an oven at 120°C for 1 hour. After cooling down to room temperature, a 12.5 µg/ml solution of graphene oxide in Milli-Q® water is drop-casted on the chips and incubated for 2 hours at room temperature. The chips are then thoroughly rinsed again with Milli-Q® water.

For the thermo-chemical reduction of the graphene oxide to reduced graphene oxide (rGO), the chips are placed into a glass petri dish with 1 ml of hydrazine monohydrate and sealed with chemically and thermally resistant Kapton tape. After 4 hours at 80°C the chips are removed from the oven, cooled to room temperature and subsequently washed with Milli-Q® water and isopropanol. Next the chips are put into a vacuum oven at 200°C for an additional thermal reduction step. After 2 hours, the rGO-FETs are controlled once again by checking the resistance before being used.

SEM images of reduced graphene oxide deposited on interdigitated electrodes to obtain a drain-source channel for FET sensors, 90 interdigitated electrode pairs with a distance of 10 µm, corresponding to a total channel width of 490 µm, can be seen in Figure S17b.

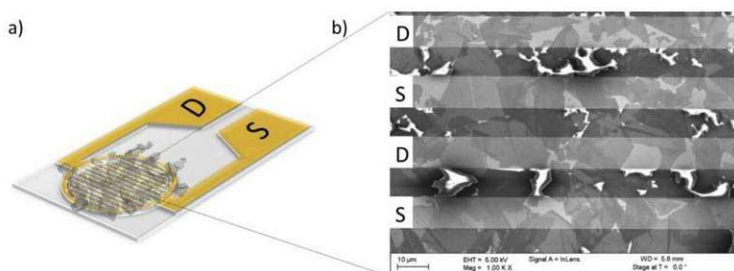


Figure S17. a) shows the glass substrate with the interdigitated electrodes, coated with reduced graphene oxide (rGO) as channel material. b) Scanning electron microscopy image of the rGO. The interdigitated electrodes have a distance of 10 µm and are alternating connected to drain and source, forming the channel of the EG-FET.

The electrical characterization of the rGO EG-FET is given by the transfer characteristic of the finalized device, shown in Figure S18. The influence on the scanning direction is shown in a slight shift of the Dirac point V_i , representing the hysteresis of the reduced graphene oxide upon field-effect probing direction.

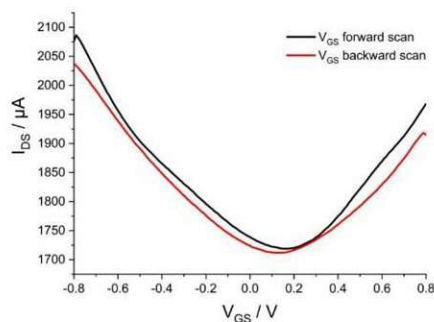


Figure S18: The transfer characteristics of the rGO EG-FET is used to characterize the sensor electrically. The drain source current I_{DS} is modulated upon applying an electric field by the gate electrode. The hysteresis of the Dirac point shift V_i upon different gate voltage V_{GS} scanning directions can be observed.

- Preparation of the SPR Au-slides

Standard microscope glass slides are placed into a 1% HELMANEX (III) aqueous solution and sonicated for 15 minutes. Then, the slides are cleaned with Milli-Q® water, put into pure ethanol and sonicated for an additional 15 minutes. Subsequently, the slides are placed on a slide holder which is mounted into a physical-vapor-deposition chamber. 2 nm Cr and then 50 nm Au (99.999%) are evaporated at roughly 1×10^{-6} mbar at evaporation rates of about 0.1 Å/s. After the evaporation, the glass slides are stored in an Argon atmosphere until being used. The slides are cut to appropriate size before measuring.

- Preparation of the polyelectrolyte solutions

PDADMAC and PSS solutions are prepared in concentrations of 1 mg/ml in KCl solutions with different ionic strengths (20 mM, 100 mM, 500 mM). This step is done one day before the measurement in order to give the polyelectrolytes enough time to unfold.

KCl solutions are prepared at different ionic strengths by dissolving the proper amount of KCl in Milli-Q® water.

5.4. Supporting Information – Dual Monitoring of Surface Reactions in Real Time by Combined Surface Plasmon Resonance and Field-Effect Transistor Interrogation

- Experimental setup and details

For the simultaneous measurement of SPR and EG-FET the experimental setup is configured as follows:

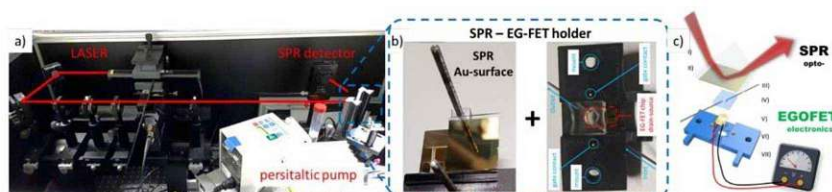


Figure S19. Experimental setup a) combined EG-FET/SPR setup, b) closeup of the EG-FET/SPR holder *left*: SPR prism with gold slide *right*: assembled microfluidic cell consisting of a PDMS-gasket, 3D printed holder, inlet and outlet, a commercial Micrux chip (IDE1) and the gate pins. c) Schematic drawing of the experimental setup consisting of the optical SPR part: I) prism II) 50 nm gold slide which also acts as the gate electrode for the electronic – EG-FET part: III) in- and outlet IV) PDMS flow cell V) interdigitated electrode chip VI) contact pins for gate electrode VII) 3D printed holder.

The SPR system in Kretschmann configuration was described in previous work.²⁰ Briefly, the collimated beam of a He-Ne laser ($\lambda = 633$ nm, power 10 mW), passes a linear (Glan) polarizer and a chopper before it is made incident on a prism and the reflected beam is detected using a photodiode and a lock-in amplifier. To allow for angular scans, prism and detector are mounted on a 2-circle goniometer maintaining $\vartheta - 2\vartheta$ configuration. A SPR substrate, a glass slide coated with 50 nm of gold, is optically matched to the prism with immersion oil. Then, a gasket made of PDMS with flow cell with an embedded microfluidic channel as shown in Figure S20a, is placed on the SPR surface. To form a microfluidic channel, the glass substrate carrying the EG-FET channel is placed on top and pressed on to seal the flow cell. The flow cell with a channel height of 400 μm and a channel width in the sensing chamber of 3.5 mm has a volume of 5 μL (Figure S20b). The SPR surface is electrically contacted to form the gate electrode of the EG-FET.

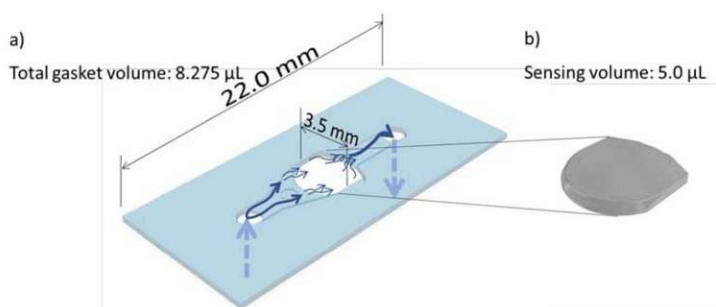


Figure S20. a) Gasket design for the SPR/EG-FET combination. The flow channel height is 400 μm , with a sensing area diameter of 3.5 mm, leading to a measurement volume of 5 μL , shown in b)

The flow cell has the following dimensions: 400 μm height, 3.5 mm diameter, 5 μL sensing volume.

5.4. Supporting Information – Dual Monitoring of Surface Reactions in Real Time by Combined Surface Plasmon Resonance and Field-Effect Transistor Interrogation

- Readout software for electrical and optical measurements

Beside the development of the novel sensing platform, a software tool including a graphical user interface (GUI) was created to adjust the measurement parameters and log all measured and calculated values.

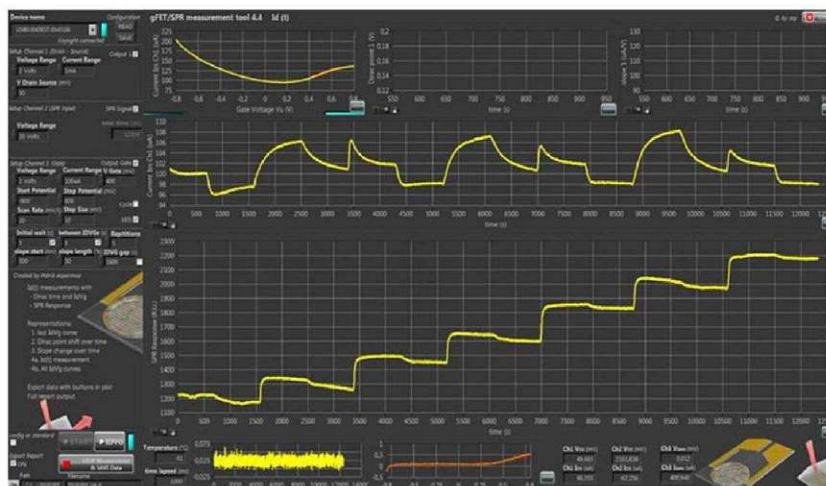


Figure S21. Layout of the measurement software. An $I_{DS}V_{GS}$ curve can be seen in the top frame, followed by a time-resolved EG-FET measurement and a time-resolved SPR measurement. The leakage current is shown at the bottom graph. All measured values are automatically exported to a spreadsheet once the measurement is finished.

IV. Materials and hardware

Hardware

BK7 glass (Hecht Assistent)
Chrome (99,9%) (MaTeCK)
Metal evaporator (HHV Ltd. FL400 AUTO 306)
Gold 99,999% Au Granular 10g (MaTeCK)
Multi-meter (Fluke)
U2722A USB Modular Source Measurement Unit (Keysight)
Peristaltic pump (ISMATEC ISM935C)
Molybdenum evaporation boats (HHV Ltd)
Heating oven (Thermo Scientific)
Kapton Tape (Amazon)
Tygon® 3350 tubing (ID = 0,64 mm, L = 300mm) (VWR)
Ultrasonicator ELMA S180H (Elmasonic)
Optical Microscope HR800 des Raman Systems (Horiba)
Ultimaker Cura S5 (Ultimaker)
High-refractive-index oil (Cargille Inc.)
Micrux chips IDE-1 (MicruX Technologies)
Chopper (Signal Recovery Model 197)
Lock-in amplifier (Model 5210, EG&G Princeton Applied Research)
Photodiode (ResTec)
2-circle goniometer (Huber Diffraktionstechnik)
Laser (JDS Uniphase 1125P)

Chemicals

(3-Aminopropyl)triethoxysilane (99 %, Sigma Aldrich)
Helmanex(III) solution (VWR)
Ethanol absolute (99,8 %, VWR)
Graphene Oxide Water Dispersion (0.4 wt% Concentration, Graphenea)
Hydrazine monohydrate (64-65 %, reagent grade 98 %, Sigma Aldrich)
Potassium Chloride (≥ 99 %, Sigma Aldrich)
Poly(diallyldimethylammonium chloride, PDADMAC, low molecular weight, average weight <100.000 Da, Sigma Aldrich)
Sodium 1-pyrenesulfonate (97 %, Sigma Aldrich)
Poly(sodium 4-styrenesulfonate, PSS, low molecular weight, average weight ~ 70.000 Da, Sigma Aldrich)

All chemicals and materials were used as received without further purification.

V. References

- (1) Tanase, C.; Meijer, E.; Blom, P.; De Leeuw, D. Local Charge Carrier Mobility in Disordered Organic Field-Effect Transistors. *Org. Electron.* **2003**, *4* (1), 33–37.
- (2) Casalini, S.; Bortolotti, C. A.; Leonardi, F.; Biscarini, F. Self-Assembled Monolayers in Organic Electronics. *Chem. Soc. Rev.* **2017**, *46* (1), 40–71.
- (3) Cardon, F.; Gomes, W. On the Determination of the Flat-Band Potential of a Semiconductor in Contact with a Metal or an Electrolyte from the Mott-Schottky Plot. *J. Phys. Appl. Phys.* **1978**, *11* (4), L63.
- (4) Lowe, B. M.; Skylaris, C.-K.; Green, N. G.; Shibuta, Y.; Sakata, T. Molecular Dynamics Simulation of Potentiometric Sensor Response: The Effect of Biomolecules, Surface Morphology and Surface Charge. *Nanoscale* **2018**, *10* (18), 8650–8666.
- (5) Scherer, P.; Fischer, S. *Theoretical Molecular Biophysics*; Biological and Medical Physics, Biomedical Engineering; 2010.
- (6) Chen, Y.; Zhang, H.; Feng, Z.; Zhang, H.; Zhang, R.; Yu, Y.; Tao, J.; Zhao, H.; Guo, W.; Pang, W.; Duan, X.; Liu, J.; Zhang, D. Chemiresistive and Gravimetric Dual-Mode Gas Sensor toward Target Recognition and Differentiation. *ACS Appl. Mater. Interfaces* **2016**, *8* (33), 21742–21749. <https://doi.org/10.1021/acsami.6b02682>.
- (7) Macchia, E.; Picca, R. A.; Manoli, K.; Franco, C. D.; Blasi, D.; Sarcina, L.; Ditaranto, N.; Cioffi, N.; Österbacka, R.; Scamarcio, G.; Torricelli, F.; Torsi, L. About the Amplification Factors in Organic Bioelectronic Sensors. *Mater. Horiz.* **2020**, *7* (4), 999–1013. <https://doi.org/10.1039/C9MH01544B>.
- (8) Palazzo, G.; De Tullio, D.; Magliulo, M.; Mallardi, A.; Intranuovo, F.; Mulla, M. Y.; Favia, P.; Vikholm-Lundin, I.; Torsi, L. Detection Beyond Debye's Length with an Electrolyte-Gated Organic Field-Effect Transistor. *Adv. Mater.* **2015**, *27* (5), 911–916.
- (9) Macchia, E.; Manoli, K.; Holzer, B.; Franco, C. D.; Ghittorelli, M.; Torricelli, F.; Alberga, D.; Mangiatordi, G. F.; Palazzo, G.; Scamarcio, G.; Torsi, L. Single-Molecule Detection with a Millimetre-Sized Transistor. *Nat. Commun.* **2018**, *9* (1), 1–10. <https://doi.org/10.1038/s41467-018-05235-z>.
- (10) Macchia, E.; Giordano, F.; Magliulo, M.; Palazzo, G.; Torsi, L. An Analytical Model for Bio-Electronic Organic Field-Effect Transistor Sensors. *Appl. Phys. Lett.* **2013**, *103* (10), 166_1.
- (11) Manoli, K.; Magliulo, M.; Mulla, M. Y.; Singh, M.; Sabbatini, L.; Palazzo, G.; Torsi, L. Printable Bioelectronics to Investigate Functional Biological Interfaces. *Angew. Chem. Int. Ed.* **2015**, *54* (43), 12562–12576.
- (12) Shirinskaya, A.; Horowitz, G.; Rivnay, J.; Malliaras, G. G.; Bonnassieux, Y. Numerical Modeling of an Organic Electrochemical Transistor. *Biosensors* **2018**, *8* (4), 103.
- (13) Texas Instruments, Application Report, SLVA771, June 2016, Fu, J. *Fundamentals of On-Resistance in Load Switches*. <http://www.ti.com/lit/an/slva771/slva771.pdf> (accessed 2020-05-01)
- (14) Kim, Y.-T.; Lee, S.; Park, S.; Lee, C. Y. Graphene Chemiresistors Modified with Functionalized Triphenylene for Highly Sensitive and Selective Detection of Dimethyl Methylphosphonate. *RSC Adv.* **2019**, *9* (58), 33976–33980.
- (15) Li, M.; Liu, C.; Xie, Y.; Cao, H.; Zhao, H.; Zhang, Y. The Evolution of Surface Charge on Graphene Oxide during the Reduction and Its Application in Electroanalysis. *Carbon* **2014**, *66*, 302–311. <https://doi.org/10.1016/j.carbon.2013.09.004>.
- (16) Kergoat, L.; Herlogsson, L.; Piro, B.; Pham, M. C.; Horowitz, G.; Crispin, X.; Berggren, M. Tuning the Threshold Voltage in Electrolyte-Gated Organic Field-Effect Transistors. *Proc. Natl. Acad. Sci.* **2012**, *109* (22), 8394–8399.
- (17) Tibaldi, A.; Fillaud, L.; Anquetin, G.; Woytasik, M.; Zrig, S.; Piro, B.; Mattana, G.; Noël, V. Electrolyte-Gated Organic Field-Effect Transistors (EGOFETs) as Complementary Tools to Electrochemistry for the Study of Surface Processes. *Electrochem. Commun.* **2019**, *98*, 43–46.
- (18) Eijkel, J. C.; van den Berg, A. Nanofluidics and the Chemical Potential Applied to Solvent and Solute Transport. *Chem. Soc. Rev.* **2010**, *39* (3), 957–973.

5.4. Supporting Information – Dual Monitoring of Surface Reactions in Real Time by Combined Surface Plasmon Resonance and Field-Effect Transistor Interrogation

- (19) Ko, Y. H.; Kim, Y. H.; Park, J.; Nam, K. T.; Park, J. H.; Yoo, P. J. Electric-Field-Assisted Layer-by-Layer Assembly of Weakly Charged Polyelectrolyte Multilayers. *Macromolecules* **2011**, *44* (8), 2866–2872.
- (20) Hageneder, S.; Bauch, M.; Dostalek, J. Plasmonically Amplified Bioassay – Total Internal Reflection Fluorescence vs. Epifluorescence Geometry. *Talanta* **2016**, *156–157*, 225–231. <https://doi.org/10.1016/j.talanta.2016.05.023>.

5.5. Supporting Information – Plasmon Field-Enhanced Fluorescence Energy Transfer for Hairpin Aptamer Assay Readout

The following supporting information is reprinted under the Creative Commons CC-BY^j license.

Khulan Sergelen, **Stefan Fossati**, Aysegül Turupcu, Chris Oostenbrink, Bo Liedberg, Wolfgang Knoll, and Jakub Dostálek Plasmon field-enhanced fluorescence energy transfer for hairpin aptamer assay readout. *ACS Sensors* 2, 916–923 (2017). <https://doi.org/10.1021/acssensors.7b00131>

Copyright © 2017 American Chemical Society

^j <http://creativecommons.org/licenses/by/4.0/>,

Supporting Information

Plasmon field-enhanced fluorescence energy transfer for hairpin aptamer assay readout

*Khulan Sergelen^{†,‡}, Stefan Fossati[†], Aysegül Turupcu[‡], Chris Oostenbrink[‡], Bo Liedberg[‡],
Wolfgang Knoll,[†] and Jakub Dostálek^{†,*}*

[†] BioSensor Technologies, AIT-Austrian Institute of Technology, Muthgasse 11, 1190 Vienna, Austria

^{*} Nanyang Technological University, Centre for Biomimetic Sensor Science, School of Materials Science and Engineering, 50 Nanyang Drive, Singapore 637553

[‡] University of Natural Resources and Life Sciences, Institute of Molecular Modeling and Simulation, Muthgasse 18, 1190 Vienna, Austria

Table of Contents:

Table S1. Calculated possible lengths of aptamer linkers between metallic surface and Alexa Fluor 647 dye

Figure S1. Dihedral angle scan of f_{off} states for SLA and LLA

Figure S2. Fluorescence signal kinetics of SLA binding with ATP and Adenosine

Figure S3. Dissociation constants K_d of adenosine and ATP for SLA and LLA aptamers

S-1

5.5. Supporting Information – Plasmon Field-Enhanced Fluorescence Energy Transfer for Hairpin Aptamer Assay Readout

Calculated possible lengths of aptamer linkers between metallic surface and Alexa Fluor 647 dye

		min, nm	random, nm	max, nm
SLA	f_{off}	0	0.9	4.7
	f_{on}		3.8	15.3
LLA	f_{off}	0	1.6	9.6
	f_{on}		5.7	35.5

Table S1. Summary of distance values determined for the length of aptamer linkers separating Alexa Fluor 547 dye from metallic surface in both SLA and LLA aptamers in their off f_{off} and on f_{on} states. The minimum in f_{off} set at 0 is due to the possible collapsing of the dye on the metallic surface, resulting in complete quenching. The values for random (freely rotating polymer-ssDNA stretch) was determined using the random coil model with the function $\sqrt{N} \cdot a$, where N is the polymer units and a the length between each unit. Values of a for ssDNA subunits was 0.63 nm^1 and all other bonds 0.15 nm . The value maximum is defined as $N \cdot a$, of a maximum extended polymer.

S-2

Dihedral angle scan of f_{off} states for SLA and LLA

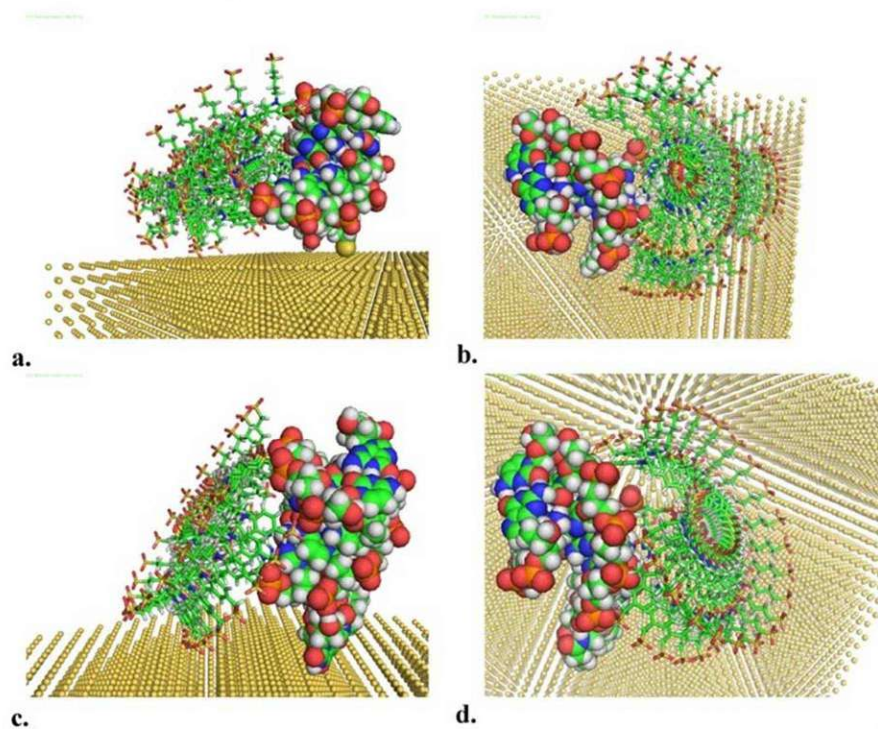


Figure S1. Dihedral scans of SLA (a. and b.) and LLA (c. and d.) aptamers in the f_{off} state. The rotational freedom of the Alexa Fluor 647 dye (sticks) attached to 5' end of complementary 14 base linker DNA (colored spheres) anchored onto a gold film (yellow spheres), is demonstrated. The Alexa Fluor 647 dye in the SLA linker shows more restricted rotational freedom, as seen in a. side view and b. top view, compared to the LLA attached dye as seen in c. side view and d. top view.

S-3

Fluorescence signal kinetics of SLA binding with ATP and Adenosine

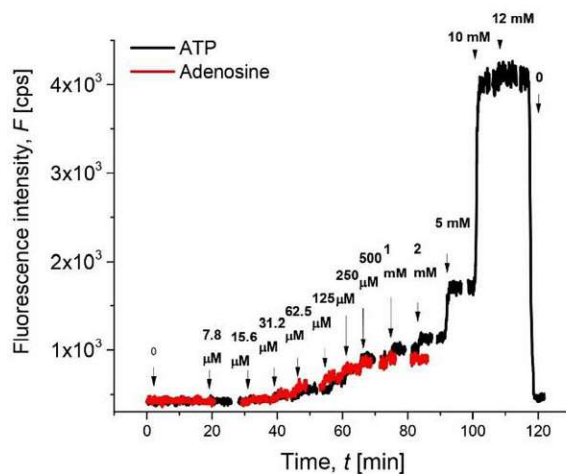
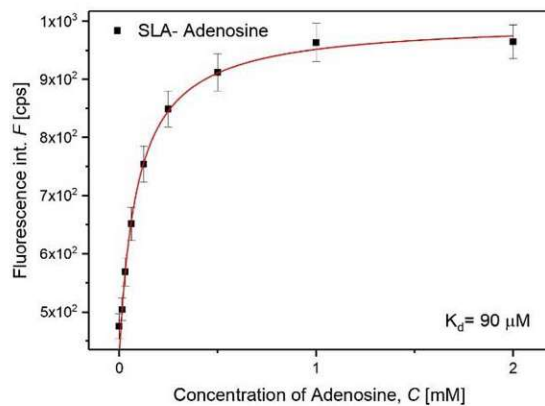


Figure S2. Real-time fluorescence signal $F(t)$ measured at a fixed angle $\theta=57$ deg upon sequential injection of ATP and adenosine at concentrations 0-12 mM in HAB buffer for gold sensor surface functionalized with SLA.

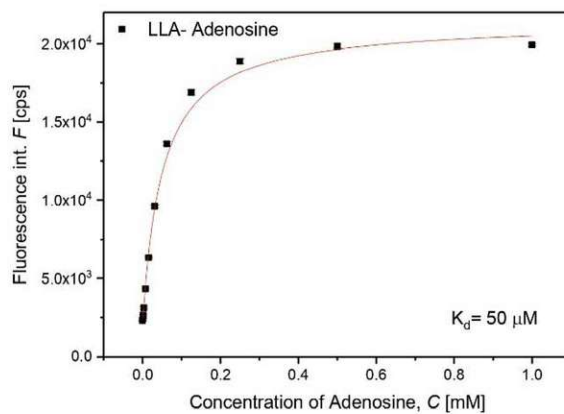
S-4

5.5. Supporting Information – Plasmon Field-Enhanced Fluorescence Energy Transfer for Hairpin Aptamer Assay Readout

Dissociation constants K_d of adenosine and ATP for SLA and LLA aptamers

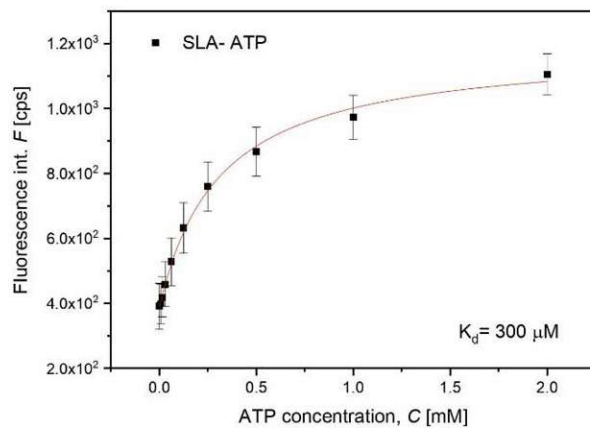


a.

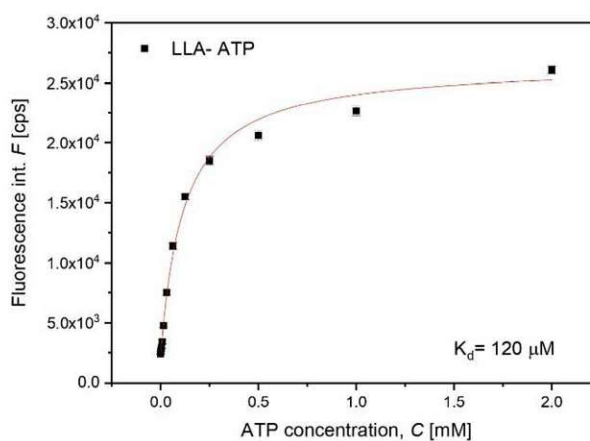


b.

S-5



c.



d.

Figure S3. Calibration curves established from changes in fluorescence intensity F as a result of increasing concentrations of analytes adenosine (a. and b.) and ATP (c. and d.). Dissociation constants (K_d) are determined by fitting with Langmuir isotherm model.

S-6

5.5. Supporting Information – Plasmon Field-Enhanced Fluorescence Energy Transfer for Hairpin Aptamer Assay Readout

REFERENCES

1. Murphy, M. C.; Rasnik, I.; Cheng, W.; Lohman, T. M.; Ha, T. Probing Single-Stranded DNA Conformational Flexibility Using Fluorescence Spectroscopy. *Biophysical Journal* **2004**, *86* (4), 2530-2537.

S-7

5.6. Supporting Information – Multiresonant Plasmonic Nanostructure for Ultrasensitive Fluorescence Biosensing

The following publication is reprinted under the Creative Commons Attribution 4.0^k (CC BY 4.0) Public license.

Stefan Fossati, Simone Hageneder, Samia Menad, Emmanuel Maillart und Jakob Dostalek Multiresonant plasmonic nanostructure for ultrasensitive fluorescence biosensing. *Nanophotonics* **9**, 3673–3685 (2020). <https://doi.org/10.1515/nanoph-2020-0270>

© 2020 The Authors, published by de Gruyter

^k <http://creativecommons.org/licenses/by/4.0/>

Supporting Information

Stefan Fossati, Simone Hageneder, Samia Menad, Emmanuel Maillart, Jakub Dostalek*

Multi-resonant plasmonic nanostructure for ultrasensitive fluorescence biosensing

Fabrication process

The multi-period plasmonic grating – MPG – nanostructures were prepared using a series of nanolithography steps. UV-laser interference lithography – UV-LIL – was employed to generate a master structure in photoresist layer on the top of a glass substrate by using multiple exposures of an interference field followed by etching with a developer. Lloyd's mirror configuration was used as shown in Figure S1A to record an interference field formed by two overlapping plane waves. Precise control of the pattern period Λ is achieved by adjusting the angle θ while the modulation depth is adjusted by the exposure time and development parameters.

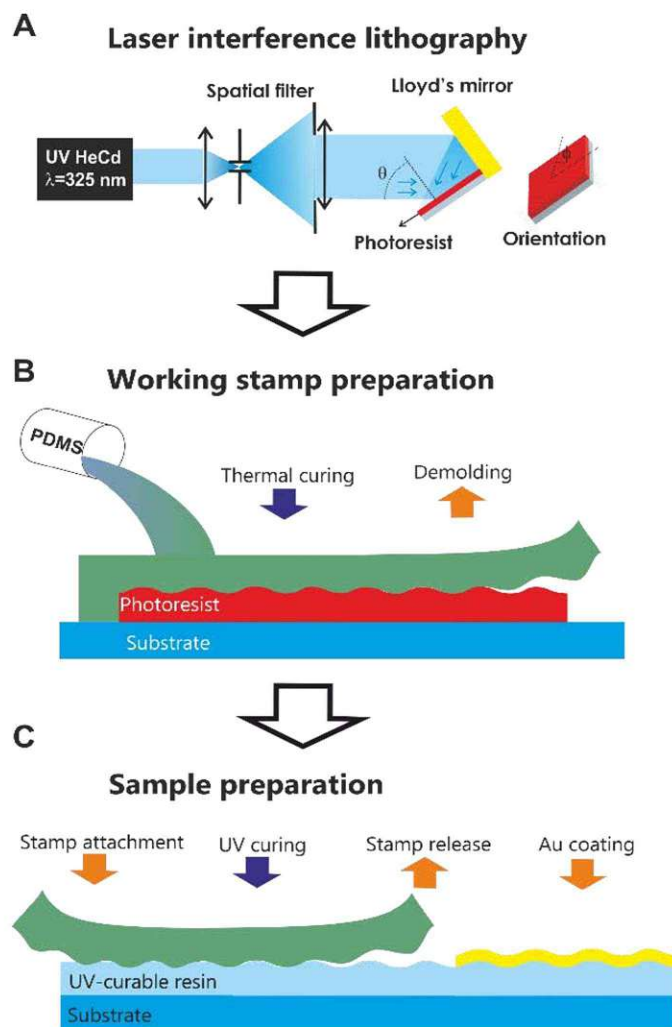


Figure. S12: A) UV-LIL setup in Lloyd's mirror configuration, where the photoresist layer (red) is exposed to the interference pattern formed by two overlaid parts of the expanded collimated UV laser beam. Between multiple exposures, the sample is rotated around its normal axis by an azimuthal angle ϕ . B) Working stamp preparation by casting the prepared MPG topography to PDMS for C) UV-nanoimprint lithography replication, where the stamp is imprinted in thin layer of imprint resist, followed by curing with UV light before demolding of the PDMS working stamp.

5.6. Supporting Information – Multiresonant Plasmonic Nanostructure for Ultrasensitive Fluorescence Biosensing

Since preparation of higher numbers of MPG structures with identical parameters by using UV-LIL is impractical, UV-nanoimprint lithography – UV-NIL – was employed to replicate the master structure. First, a working stamp was prepared by casting the master structure to polydimethylsiloxane (PDMS) that was cured at controlled temperature (Figure S1B). After the curing, the stamp is demolded and used to replicate the pattern to nanoimprint resist (Amonil) on a glass substrate. Such copies with MPG topography were subsequently coated with a 100 nm gold film by vacuum thermal evaporation (Figure S1C).

Optical properties of grating coupled plasmon resonances

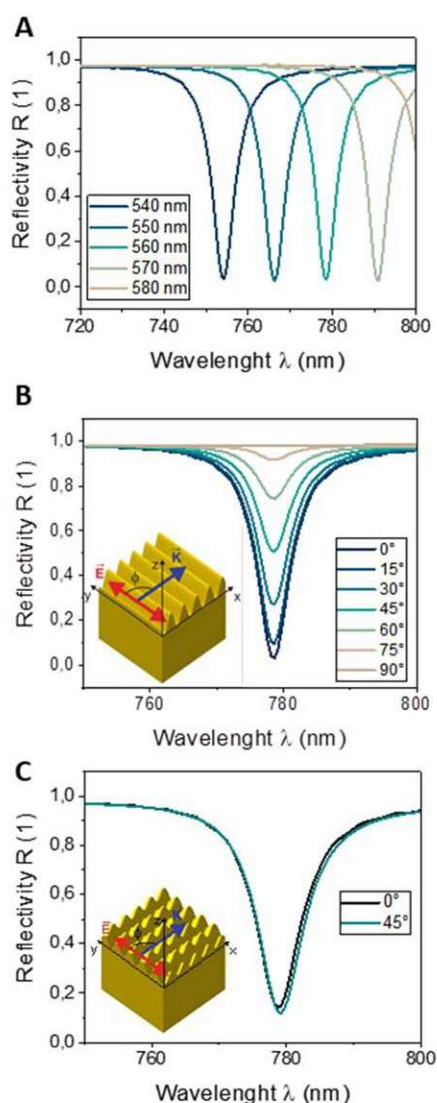


Figure S2: (A) Change of the spectral position of SPR with grating period for a single sinusoidal grating, 15 nm modulation depth, and gold – water interface. Coupling efficiency dependence on the polar angle φ between grating vector and electric field vector is shown for linear gratings in (B) and for crossed grating in (C).

Plasmon near-field intensity profile

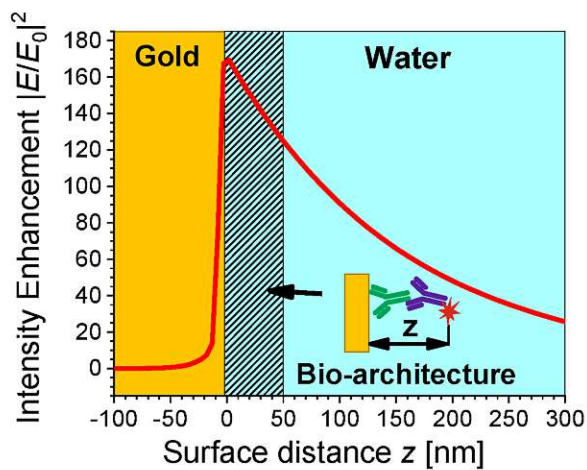


Figure. S3: Distance dependence of the local electrical field enhancement averaged over the MPG along the axis perpendicular to the surface.

Measurement of fluorescence angular distribution

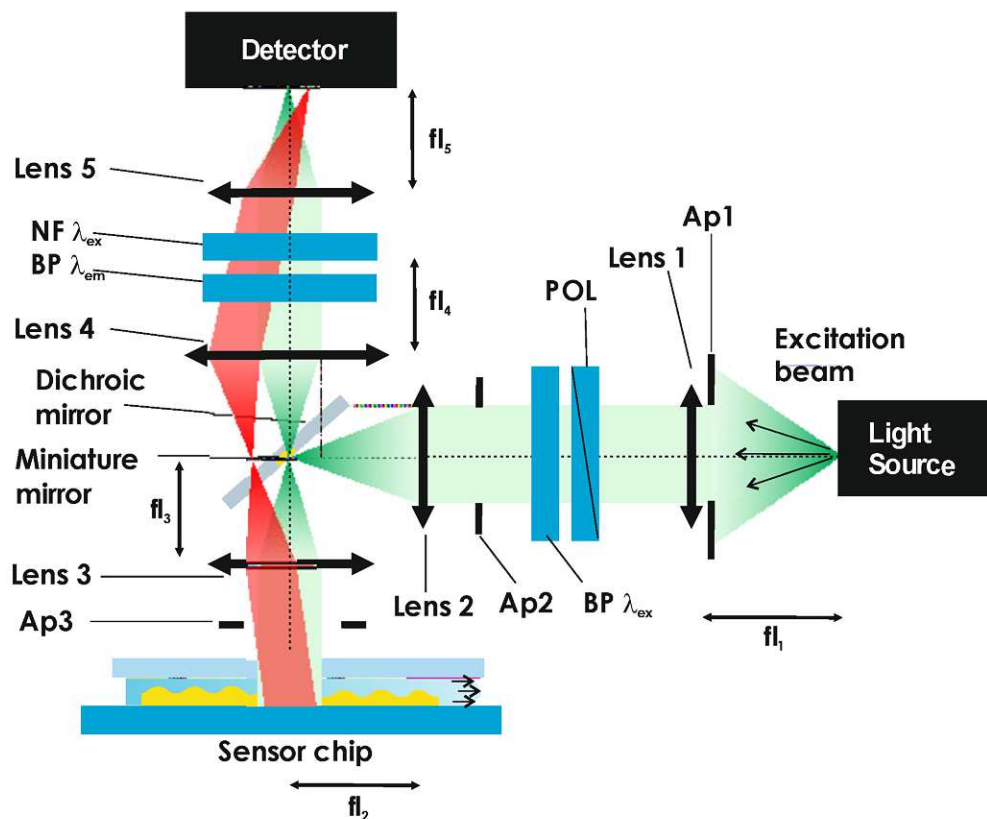
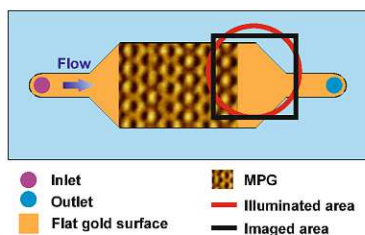


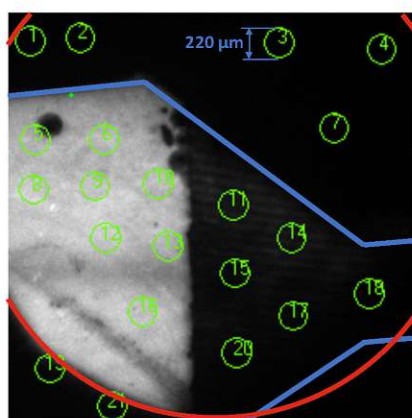
Figure. S4: The reader configured to image the back-focal plane of the objective lens, where the miniature mirror is located, by an additional lens (Lens 5).

Experimental observation of a fluorescence assay

A



B



Class	Spots
Dark reference	19, 21
Illuminated but not functionalized	1, 2, 3, 4, 7
MPG functionalized	5, 6, 8, 9, 10, 12, 13, 16
Flat gold functionalized	11, 14, 15, 17, 18, 20

Figure. S5: A) A schematic of the sensor chip with part of its area structured with gold-coated MPG and part of its area carrying flat gold surface that is clamped against a microfluidic flow-cell. The illuminated area is indicated by a red circle, the imaged area by a black square. In B) a fluorescence image obtained during the measurement in Figure 7 b) after titration up to 50 pM target analyte concentration is shown. The microfluidic channel is indicated in blue, the illuminated area with a red circle and the spots averaged to calculate the fluorescence signal are indicated in green.

NIL reproducibility

Reproducibility of the UV-NIL process was tested on 5 samples prepared using a PDMS stamp. The spectra were acquired in air to prevent contamination, before the samples were chemically modified (therefore the spectral positions differ from those presented in Figure 3 measured in contact with water). The spectral position of the resonances deviate by less than 2 nm, significantly smaller value than the resonance width.

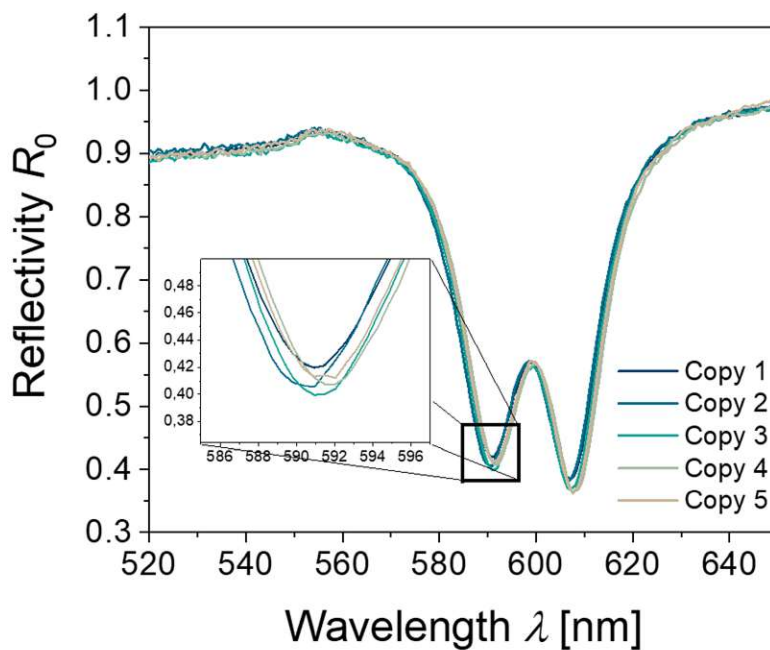


Figure S6: Reflectivity spectra acquired from 5 nanoimprinted samples from the same master structure

Collection efficiency enhancement

A key challenge in making sensitive fluorescence assays is the collection efficiency of emitted fluorescence light for practical optical systems. For a freely rotating fluorophore in homogeneous medium, the emission is assumed to be isotropic despite the orientation sensitive absorption characteristics of the electrical dipole model, due to the random change of orientation during fluorescence lifetime. For an optical system with a given numerical aperture $NA = n \sin \theta$ the collection only part of fluorescence light emitted to a cone with half angle θ can be collected. In the case of isotropic emission, the fraction can be determined analytically by calculating the ratio of the surface of the emission cone to the overall surface.

$$A_{collected} = \int_0^\theta \int_0^{2\pi} \sin\theta \, d\phi \, d\theta = 2\pi (1 - \cos\theta) \quad (1)$$

$$CE = \frac{A_{collected}}{A_{sphere}} = \frac{A_{collected}}{4\pi} = \frac{1}{2}(1 - \cos\theta) \quad (2)$$

For the MPG structure, collection efficiency was determined by calculating the farfield emission of a dipole in 15 nm distance from the surface. Four polar orientations of the dipole ($0^\circ, 45^\circ, 90^\circ, 135^\circ$) with respect to the linear grating were considered. The emitted power to a cone of opening angle θ perpendicular to the interface was computed by numerical integration. A similar calculation was performed for an emitter on a flat gold surface. In this work, an optical system with numerical aperture $NA=0.2$ was used to image a large sample area in a flow cell. Collection efficiencies for this system were calculated and are shown in Figure S7.

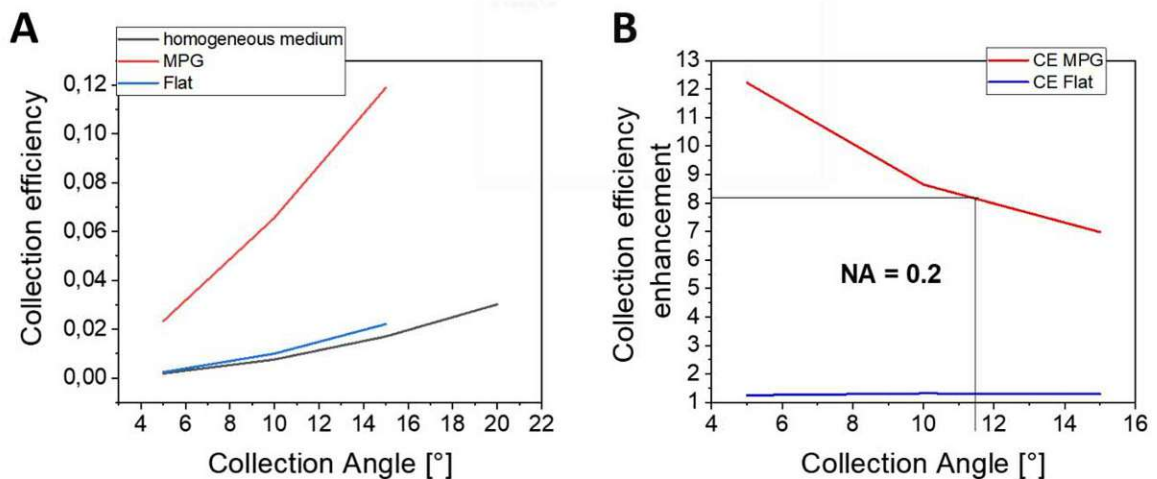


Figure S7: (A) Collection efficiency of an optical system with $NA = 0.2$ opt for an emitter located in a homogeneous medium (black), on a flat gold surface (blue) and on the MPG structure (red). (B) Enhancement of collection efficiency with respect to emitter in homogeneous medium for MPG and flat surfaces.

5.7. Copyright Agreements and Permissions

5.7.1. Nanoscale

URI: <https://doi.org/10.1039/c8nr05499a>

Date: 2.11.2021

The screenshot shows a web page for a journal article. At the top left, it says 'Issue 37, 2018' and 'From the journal: Nanoscale'. The main title is 'Surface plasmon modes of nanomesh-on-mirror nanocavities prepared by nanosphere lithography'. Below the title are the authors: Christian Stelling, Stefan Fossati, Jakub Dostalek, and Markus Retsch. There is a 'Check for updates' button. The abstract starts with 'Metal-insulator-metal (MIM) structures show great potential for numerous photonic applications...'. On the right side, there is a sidebar with tabs for 'About', 'Cited by', and 'Related'. Under 'About', it lists the authors and the journal: 'C. Stelling, S. Fossati, J. Dostalek and M. Retsch, *Nanoscale*, 2018, 10, 17983 DOI: 10.1039/C8NR05499A'. Below this, there is a copyright notice: 'To request permission to reproduce material from this article, please go to the Copyright Clearance Center request page. If you are an author contributing to an RSC publication, you do not need to request permission provided correct acknowledgement is given. If you are the author of this article, you do not need to request permission to reproduce figures and diagrams provided correct acknowledgement is given. If you want to reproduce the whole article in a third-party publication (excluding your thesis/dissertation for which permission is not required) please go to the Copyright Clearance Center request page. Read more about how to correctly acknowledge RSC content.'

5.7.2. ACS AuthorChoice/Editors' Choice via Creative Commons CC-BY Usage Agreement

23.8.2021 https://pubs.acs.org/page/policy/authorchoice_ccby_termsfuse.html
https://pubs.acs.org/page/policy/authorchoice_ccby_termsfuse.html 1/9

the Terms and Conditions of this Agreement. ACS and You are collectively referred to in this Agreement as "the Parties").

1. SCOPE OF GRANT

ACS grants You a non-exclusive and nontransferable permission to access and use this ACS article subject to the terms and conditions set forth in this Agreement.

2. PERMITTED USES

a. ACS grants You the rights in the attached Creative Commons Attribution 4.0 International license.

Consistent with the Creative Commons Attribution 4.0 license we note that any use of the article is subject to the following conditions:

- i. The authors' moral right to the integrity of their work under the Berne Convention (Article 6bis) is not compromised.
- ii. Where content in the article is identified as belonging to a third party, it is your responsibility to ensure that any reuse complies with copyright policies of the owner.

3. TERMINATION

ACS reserves the right to limit, suspend, or terminate your access to and use of the ACS Publications Division website and/or all ACS articles immediately upon detecting a breach of this License.

4. COPYRIGHTS; OTHER INTELLECTUAL PROPERTY RIGHTS

Except as otherwise specifically noted, ACS is the owner of all right, title and interest in the content of this ACS article, including, without limitations, graphs, charts, tables illustrations, and copyrightable supporting information. This ACS article is protected under the Copyright Laws of the United States Codified in Title 17 of the U.S. Code and subject to the Universal Copyright Convention and the Berne Copyright Convention. You agree not to remove or obscure copyright notices. You acknowledge that You have no claim to ownership of any part of this ACS article or other proprietary information accessed under this Agreement. The names "American Chemical Society," "ACS" and the titles of the journals and other ACS products are trademarks of ACS.

5. DISCLAIMER OF WARRANTIES; LIMITATION OF LIABILITY

ACS warrants that it is entitled to grant this Agreement.

EXCEPT AS SET FORTH IN THE PRECEDING SENTENCE, ACS MAKES NO WARRANTY OR REPRESENTATION OF ANY KIND, EXPRESS OR IMPLIED, WITH RESPECT TO THIS ACS ARTICLE INCLUDING, BUT NOT LIMITED TO WARRANTIES AS TO THE ACCURACY OR COMPLETENESS OF THE ACS ARTICLE, ITS QUALITY, ORIGINALITY, SUITABILITY, SEARCHABILITY, OPERATION, PERFORMANCE, COMPLIANCE WITH ANY COMPUTATIONAL PROCESS, MERCHANTABILITY OR FITNESS FOR A PARTICULAR PURPOSE.

ACS SHALL NOT BE LIABLE FOR: EXEMPLARY, SPECIAL, INDIRECT, INCIDENTAL, CONSEQUENTIAL OR OTHER DAMAGES ARISING OUT OF OR IN CONNECTION WITH THE AGREEMENT GRANTED HEREUNDER, THE USE OR INABILITY TO USE ANY ACS PRODUCT, ACS'S PERFORMANCE UNDER THIS AGREEMENT, TERMINATION OF THIS AGREEMENT BY ACS OR THE LOSS OF DATA, BUSINESS OR GOODWILL EVEN IF ACS IS ADVISED OR AWARE OF THE POSSIBILITY OF SUCH DAMAGES. IN NO EVENT SHALL THE TOTAL AGGREGATE LIABILITY OF ACS OUT OF ANY BREACH OR TERMINATION OF THIS AGREEMENT EXCEED THE TOTAL AMOUNT PAID BY YOU TO ACS FOR ACCESS TO THIS ACS ARTICLE FOR THE CURRENT YEAR IN WHICH SUCH CLAIM, LOSS OR DAMAGE OCCURRED, WHETHER IN CONTRACT, TORT OR OTHERWISE, INCLUDING, WITHOUT LIMITATION, DUE TO NEGLIGENCE.

The foregoing limitations and exclusions of certain damages shall apply regardless of the success or effectiveness of other remedies. No claim may be made against ACS unless suit is filed within one (1) year after the event giving rise to the claim.

6. GENERAL

This Agreement sets forth the entire understanding of the Parties. The validity, construction and performance of this Agreement shall be governed by and construed in accordance with the laws of the District of Columbia, USA without reference to its conflicts of laws principles. You acknowledge that the delivery of the ACS article will occur in the District of Columbia, USA. You shall pay any taxes lawfully due

from it, other than taxes on ACS's net income, arising out of your use of this ACS article and/or other rights granted under this Agreement.

7. ACCEPTANCE

You warrant that You have read, understand, and accept the terms and conditions of this Agreement. ACS reserves the right to modify this Agreement at any time by posting the modified terms and conditions on the ACS Publications Web site. Any use of this ACS article after such posting shall constitute acceptance of the terms and conditions as modified.

Creative Commons Attribution 4.0 International Public License

By exercising the Licensed Rights (defined below), You accept and agree to be bound by the terms and conditions of this Creative Commons Attribution 4.0 International Public License ("Public License"). To the extent this Public License may be interpreted as a contract, You are granted the Licensed Rights in consideration of Your acceptance of these terms and conditions, and the Licensor grants You such rights in consideration of benefits the Licensor receives from making the Licensed Material available under these terms and conditions.

Section 1 – Definitions

a. **Adapted Material** means material subject to Copyright and Similar Rights that is derived from or based upon the Licensed Material and in which the Licensed Material is translated, altered, arranged, transformed, or otherwise modified in a manner requiring permission under the Copyright and Similar Rights held by the Licensor. For purposes of this Public License, where the Licensed Material is a musical work, performance, or sound recording, Adapted Material is always produced where the Licensed Material is synched in timed relation with a moving image.

b. **Adapter's License** means the license You apply to Your Copyright and Similar Rights in Your contributions to Adapted Material in accordance with the terms and conditions of this Public License.

c. **Copyright and Similar Rights** means copyright and/or similar rights closely related to copyright including, without limitation, performance, broadcast, sound recording, and Sui Generis Database Rights, without regard to how the rights are labeled or categorized. For purposes of this Public License, the rights specified in Section 2(b)(1)-(2) are not Copyright and Similar Rights.

- d. **Effective Technological Measures** means those measures that, in the absence of proper authority, may not be circumvented under laws fulfilling obligations under Article 11 of the WIPO Copyright Treaty adopted on December 20, 1996, and/or similar international agreements.
- e. **Exceptions and Limitations** means fair use, fair dealing, and/or any other exception or limitation to Copyright and Similar Rights that applies to Your use of the Licensed Material.
- f. **Licensed Material** means the artistic or literary work, database, or other material to which the Licensor applied this Public License.
- g. **Licensed Rights** means the rights granted to You subject to the terms and conditions of this Public License, which are limited to all Copyright and Similar Rights that apply to Your use of the Licensed Material and that the Licensor has authority to license.
- h. **Licensor** means the individual(s) or entity(ies) granting rights under this Public License.
- i. **Share** means to provide material to the public by any means or process that requires permission under the Licensed Rights, such as reproduction, public display, public performance, distribution, dissemination, communication, or importation, and to make material available to the public including in ways that members of the public may access the material from a place and at a time individually chosen by them.
- j. **Sui Generis Database Rights** means rights other than copyright resulting from Directive 96/9/EC of the European Parliament and of the Council of 11 March 1996 on the legal protection of databases, as amended and/or succeeded, as well as other essentially equivalent rights anywhere in the world.
- k. **You** means the individual or entity exercising the Licensed Rights under this Public License. **Your** has a corresponding meaning.

Section 2 – Scope

a. License grant.

1. Subject to the terms and conditions of this Public License, the Licensor hereby grants You a worldwide, royalty-free, non-sublicensable, non-exclusive, irrevocable license to exercise the Licensed Rights in the Licensed Material to:
 - A. reproduce and Share the Licensed Material, in whole or in part; and
 - B. produce, reproduce, and Share Adapted Material.
2. Exceptions and Limitations. For the avoidance of doubt, where Exceptions and Limitations apply to Your use, this Public License does not apply, and You do not need to comply with its terms and conditions.
3. Term. The term of this Public License is specified in Section 6(a).
4. Media and formats; technical modifications allowed. The Licensor authorizes You to exercise the

Licensed Rights in all media and formats whether now known or hereafter created, and to make technical modifications necessary to do so. The Licensor waives and/or agrees not to assert any right or authority to forbid You from making technical modifications necessary to exercise the Licensed Rights, including technical modifications necessary to circumvent Effective Technological Measures. For purposes of this Public License, simply making modifications authorized by this Section 2(a)(4) never produces Adapted Material.

5. Downstream recipients

A. Offer from the Licensor – Licensed Material. Every recipient of the Licensed Material automatically receives an offer from the Licensor to exercise the Licensed Rights under the terms and conditions of this Public License.

B. No downstream restrictions. You may not offer or impose any additional or different terms or conditions on, or apply any Effective Technological Measures to, the Licensed Material if doing so restricts exercise of the Licensed Rights by any recipient of the Licensed Material.

6. No endorsement. Nothing in this Public License constitutes or may be construed as permission to assert or imply that You are, or that Your use of the Licensed Material is, connected with, or sponsored, endorsed, or granted official status by, the Licensor or others designated to receive attribution as provided in Section 3(a)(1)(A)(i).

b. Other rights.

1. Moral rights, such as the right of integrity, are not licensed under this Public License, nor are publicity, privacy, and/or other similar personality rights; however, to the extent possible, the Licensor waives and/or agrees not to assert any such rights held by the Licensor to the limited extent necessary to allow You to exercise the Licensed Rights, but not otherwise.

2. Patent and trademark rights are not licensed under this Public License.

3. To the extent possible, the Licensor waives any right to collect royalties from You for the exercise of the Licensed Rights, whether directly or through a collecting society under any voluntary or waivable statutory or compulsory licensing scheme. In all other cases the Licensor expressly reserves any right to collect such royalties.

Section 3 – License Conditions

Your exercise of the Licensed Rights is expressly made subject to the following conditions.

a. Attribution

1. If You Share the Licensed Material (including in modified form), You must:

A. retain the following if it is supplied by the Licensor with the Licensed Material:

- i. identification of the creator(s) of the Licensed Material and any others designated to receive attribution, in any reasonable manner requested by the Licensor (including by pseudonym if designated);
 - ii. a copyright notice;
 - iii. a notice that refers to this Public License;
 - iv. a notice that refers to the disclaimer of warranties;
 - v. a URI or hyperlink to the Licensed Material to the extent reasonably practicable;
- B. indicate if You modified the Licensed Material and retain an indication of any previous modifications; and
- C. indicate the Licensed Material is licensed under this Public License, and include the text of, or the URI or hyperlink to, this Public License.
2. You may satisfy the conditions in Section 3(a)(1) in any reasonable manner based on the medium, means, and context in which You Share the Licensed Material. For example, it may be reasonable to satisfy the conditions by providing a URI or hyperlink to a resource that includes the required information.
3. If requested by the Licensor, You must remove any of the information required by Section 3(a)(1)(A) to the extent reasonably practicable.
4. If You Share Adapted Material You produce, the Adapter's License You apply must not prevent recipients of the Adapted Material from complying with this Public License.

Section 4 – Sui Generis Database Rights

Where the Licensed Rights include Sui Generis Database Rights that apply to Your use of the Licensed Material:

- a. for the avoidance of doubt, Section 2(a)(1) grants You the right to extract, reuse, reproduce, and Share all or a substantial portion of the contents of the database;
- b. if You include all or a substantial portion of the database contents in a database in which You have Sui Generis Database Rights, then the database in which You have Sui Generis Database Rights (but not its individual contents) is Adapted Material; and
- c. You must comply with the conditions in Section 3(a) if You Share all or a substantial portion of the contents of the database. For the avoidance of doubt, this Section 4 supplements and does not replace Your obligations under this Public License where the Licensed Rights include other Copyright and Similar Rights.

Section 5 – Disclaimer of Warranties and Limitation of Liability

- a. **Unless otherwise separately undertaken by the Licensor, to the extent possible, the Licensor offers the Licensed Material as-is and as-available, and makes no representations or warranties of any kind concerning the Licensed Material, whether express, implied, statutory, or other. This includes, without limitation, warranties of title, merchantability, fitness for a particular purpose, non-infringement, absence of latent or other defects, accuracy, or the presence or absence of errors, whether or not known or discoverable. Where disclaimers of warranties are not allowed in full or in part, this disclaimer may not apply to You.**
- b. **To the extent possible, in no event will the Licensor be liable to You on any legal theory (including, without limitation, negligence) or otherwise for any direct, special,**

indirect, incidental, consequential, punitive, exemplary, or other losses, costs, expenses, or damages arising out of this Public License or use of the Licensed Material, even if the Licensor has been advised of the possibility of such losses, costs, expenses, or damages. Where a limitation of liability is not allowed in full or in part, this limitation may not apply to You.

c. The disclaimer of warranties and limitation of liability provided above shall be interpreted in a manner that, to the extent possible, most closely approximates an absolute disclaimer and waiver of all liability.

Section 6 – Term and Termination

a. This Public License applies for the term of the Copyright and Similar Rights licensed here. However, if You fail to comply with this Public License, then Your rights under this Public License terminate automatically.

b. Where Your right to use the Licensed Material has terminated under Section 6(a), it reinstates:

1. automatically as of the date the violation is cured, provided it is cured within 30 days of Your discovery of the violation; or
 2. upon express reinstatement by the Licensor. For the avoidance of doubt, this Section 6(b) does not affect any right the Licensor may have to seek remedies for Your violations of this Public License.
- c. For the avoidance of doubt, the Licensor may also offer the Licensed Material under separate terms or conditions or stop distributing the Licensed Material at any time; however, doing so will not terminate this Public License.
- d. Sections 1, 5, 6, 7, and 8 survive termination of this Public License.

Section 7 – Other Terms and Conditions

a. The Licensor shall not be bound by any additional or different terms or conditions communicated by You unless expressly agreed.

b. Any arrangements, understandings, or agreements regarding the Licensed Material not stated herein are separate from and independent of the terms and conditions of this Public License.

Section 8 – Interpretation

a. For the avoidance of doubt, this Public License does not, and shall not be interpreted to, reduce, limit, restrict, or impose conditions on any use of the Licensed Material that could lawfully be made without permission under this Public License.

b. To the extent possible, if any provision of this Public License is deemed unenforceable, it shall be automatically reformed to the minimum extent necessary to make it enforceable. If the provision cannot be reformed, it shall be severed from this Public License without affecting the enforceability of the remaining terms and conditions.

c. No term or condition of this Public License will be waived and no failure to comply consented to unless expressly agreed to by the Licensor.

d. Nothing in this Public License constitutes or may be interpreted as a limitation upon, or waiver of, any privileges and immunities that apply to the Licensor or You, including from the legal processes of any jurisdiction or authority.

Posted: 03/06/20

Curriculum Vitae

STEFAN FOSSATI

Date of Birth: [REDACTED]
Place of Birth: Vienna, Austria
Citizenship: Austrian
Address: [REDACTED]
[REDACTED]
Österreich

Phone: [REDACTED]
Email: stefan.fossati@ait.ac.at



Professional Career:

2015 – now Junior Scientist, AIT – Austrian Institute of Technology GmbH, Vienna, Austria
2012 – 2015 Development engineer, Magtor Group, Vienna, Austria
2008 – 2009 Research Assistant, Stefan-Meyer-Institute, Vienna, Austria

Education:

2015 – now PhD candidate, Institute for Applied Physics, Vienna University of Technology
2004 – 2015 Study of Technical physics at Vienna University of Technology
1998 – 2003 TGM HTL Wien 20, Elektronik - Technologie der Medien.

Degrees:

2015 MSc., Technical Physics, University of Technology, Vienna, Austria .
Thesis: A resonant plasmonic structure for fluorescence spectroscopy, Supervisor: Prof. C. Eisenmenger-Sittner, J. Dostalek

Publications

Stefan Fossati published 12 publications, 1 book chapter and authored 1 patent.

Teaching and synergistic activities:

He served as teaching assistant for laboratory courses at Vienna University of Technology and as lecturer for laboratory courses at the University of Applied Science IMC Krems.